

IN VIVO DIFFUSION WEIGHTED MAGNETIC RESONANCE  
SPECTROSCOPY IN MULTIPLE SCLEROSIS

by

Emily Turner Wood

A dissertation submitted to Johns Hopkins University in conformity with the  
requirements for the degree of Doctor of Philosophy

Baltimore, Maryland

March, 2015

© 2015 Emily Turner Wood

All Rights Reserved

## Abstract

Multiple sclerosis (MS) is a complex CNS disease in which inflammation, demyelination and neuroaxonal degeneration are concurrent processes. MS therapies developed to date are directed at the immune-mediated, inflammatory destruction of myelin – axonal degeneration is ongoing and not specifically targeted. In vivo techniques to measure axonal degeneration could be useful in developing neuroprotective agents.

This dissertation explores the capacity of diffusion weighted spectroscopy (DWS) for measuring axonopathy in patients in vivo. DWS is a magnetic resonance technique that measures the diffusivity of metabolites, such as N-acetyl aspartate (NAA), in vivo, allowing compartment specific assessment of disease-related changes. Here we developed and optimized the DWS technique for use with patients on clinical scanners so that we could study NAA diffusivity in MS patients.

In order to establish reliability parameters for DWS, comprehensive DWS data sets of the human corpus callosum were acquired and the *inter*- and *intra*-subject variability of empirical and modeled diffusion properties of NAA was investigated. Reproducibility analysis and power calculations demonstrated that a difference of 10% in NAA diffusivity could be detected with group sizes as small as 21 patients at 3T with a sequence that runs in under 20 minutes

Cross-sectional study of MS patients and healthy controls revealed lower diffusion of NAA parallel to the long axis of axons in the corpus callosum of patients. This result demonstrated that, by detecting reduced diffusion of NAA parallel to axons in white matter, DWS may be capable of distinguishing axonal disruption in MS in the setting of increased parallel diffusion of water, which is commonly observed in MS but

pathologically nonspecific.

A longitudinal study of DWS in patients with stable and active disease replicated the previous cross-sectional findings and found that active MS patients had lower NAA parallel diffusivity at 6 months while stable patients remained constant. Additionally, water diffusion and volumetric measures did not detect changes in active MS patients during this period. As NAA diffusivity measurements reflect specifically on the intra-axonal space, these data suggest that NAA diffusivity is a read-out of axonal health in a background of multiple pathological processes in MS.

**Supervisor:**

Daniel S. Reich, M.D., Ph.D.

*Chief*

Translational Neuroradiology Unit, National Institutes of Neurological Disorders and Stroke, National Institutes of Health

**Committee:**

Amy J. Bastian, Ph.D.

*Professor*

Departments of Neuroscience and Neurology, Johns Hopkins University School of Medicine

*Staff Scientist*

Kennedy Krieger Institute

Peter C.M. van Zijl, Ph.D.

*Professor*

Departments of Radiology & Radiological Science and Biophysics and Biophysical Chemistry, Johns Hopkins University School of Medicine

*Director*

F.M. Kirby Research Center for Functional Brain Imaging, Kennedy Krieger Institute

Adam I. Kaplin, M.D., Ph.D.

*Assistant Professor*

Departments of Psychiatry & Behavioral Sciences and Neurology, Johns Hopkins University School of Medicine

## **Dedication**

This dissertation is dedicated to the mentorship and memory of Dr. Steve Hsiao. His brilliance, honesty, humor, and kindness continue to inspire me. In his too short time, he was tirelessly committed to fostering young scientists with the hope that all of us would experience the joyous curiosity and awe that he felt every day. His two sons were a daily focus of wonder, adoration and great stories. I miss him very much.

## Acknowledgments

First and foremost, I could not have completed this dissertation without the support of my husband and family who have allowed me to indulge my scientific curiosity and work toward a fulfilling career.

The work of this dissertation took place between multiple institutions with collaborations across Maryland and the Atlantic. I would like to thank Danny Reich who has been my adviser, mentor and friend. Danny has created a working environment that allows individuals to explore their interests and goals. From the beginning, Danny fostered my independence and supported me in my scientific pursuits. He helped me to succeed and he allowed me to fail without guilt or remorse. Without question, the most educational and beneficial parts of my graduate school experience have been failures. I have also had the pleasure of witnessing the transformation of Danny from student (Neuroradiology Fellow) to chief. His commitment to betterment is inspiring.

I had the honor of working with, learning from and becoming friends with Itamar Ronen. Thank you, Itamar, for teaching me about diffusion weighted spectroscopy and for teaching me how to be a collaborator. I am so happy to call you a colleague.

I had the privilege of working at in the Neuroimmunology Branch at NINDS (NIH). Henry McFarland and Steve Jacobson are excellent scientists and really decent people. I would like to thank everyone from their labs, especially Emily Leibovitch who taught me how to work with marmosets. Thank you to the branch clinicians and support staff, Irene Cortese, Joan Ohayon, Kaylan Fenton, Rose Ebinger, Helen Griffith, Ann Mayfield, and Freddy Reyes for making it possible for me to work with so many well-cared for patients. Donna Thomas and Ilesha Baskins make it look easy to work for the government.

I have been inspired and supported by my lab, the Translational Neuroradiology Unit: Pascal Sati, Govind Nair, Maria Gaitán, Colin Shea, Roger Stone, Luca Massacesi, Isabela Borges, Martina Absinta, Ilena George, Pietro Maggi, Katherine Gao, Blake Jones, Anshika Bakshi, Blake Dewey, Joe Guy, Sonya Steele, Michael Cotterell, Luisa Vuolo, Varun Sethi. In particular, I owe thanks to Manori De Alwis and Breona Mabry for their excellent work during their NIH Summer Internships. They were a great help and it was a pleasure to watch them grow as scientists.

Additionally, the staff of the NIH Clinical Center MRI facility were instrumental with both data collection and moral support.

Ece Ercan is a wonderful collaborator and graduate school confidant. She always knew what I was going through.

I was also fortunate to work with people in the Johns Hopkins School of Medicine departments of Radiology and Neurology as well as folks at the F.M. Kirby Center for Functional Brain Imaging and the Kennedy Krieger Institute. Thank you to Peter van Zijl, Peter Calabresi, Dan Harrison, Peter Barker, Richard Edden, and Jon Farrell who all spent time helping and mentoring me. Terri Brawner, Kathleen Kahl, Ivana Kusevic, Heather Hall, Candace Herbster, and Joe Gillen are the people who make the Kirby Center function properly and were incredibly helpful to me. Thank you to Stephanie Syc and Michaela Siego for recruiting and testing patients.

Finally, I would like to thank Dzung Pham, Pi-Lou Bazin, Jerry Prince, and Navid Shiee for their image analysis expertise and immense patience with all of my questions.

# Table of Contents

<b>Abstract</b>	<b>ii</b>
<b>Dedication</b>	<b>v</b>
<b>Acknowledgments</b>	<b>vi</b>
<b>Table of Contents</b>	<b>viii</b>
<b>List of Tables</b>	<b>xiii</b>
<b>List of Figures</b>	<b>xv</b>
<b>1 Diffusion weighted spectroscopy in Multiple sclerosis: An Introduction</b>	<b>1</b>
1.1 <i>Preface</i>	1
1.2 <i>Background and motivation</i>	1
1.3 <i>Dissertation Outline</i>	4
<b>2 An Overview of Multiple Sclerosis</b>	<b>6</b>
2.1 <i>Epidemiology &amp; Clinical Course</i>	6
2.2 <i>Pathophysiology</i>	8
2.2.1 Immunology	8
2.2.2 Pathogenesis	11
2.2.3 Disease modifying therapies in MS	12
2.2.4 Pathology of MS plaques	14
2.2.5 Pathology of Progressive MS	18
2.3 <i>Neuro-axonal degeneration</i>	19
2.3.1 Programmed axonal degeneration	19
2.3.2 Axonal degeneration in MS	22
2.3.3 Axonal degeneration in animal models of MS	24
2.4 <i>Conclusions</i>	25



<b>3</b>	<b>MS &amp; Nuclear Magnetic Resonance</b>	<b>26</b>
<b>3.1</b>	<b><i>What can NMR tell us about MS?</i></b>	<b>29</b>
3.1.1	A brief and hand-wavy (non-mathematical) introduction to nuclear magnetic resonance imaging principles	29
3.1.2	T <sub>1</sub> -weighted imaging	33
3.1.3	T <sub>2</sub> -weighted/FLAIR imaging	37
3.1.4	Tissue segmentation and brain atrophy	38
3.1.5	Contrast enhancing lesions (CELs)	40
<b>3.2</b>	<b><i>Diffusion Weighted Imaging</i></b>	<b>44</b>
3.2.1	Brownian Motion	45
3.2.2	Restricted Diffusion	48
3.2.3	The Diffusion Tensor & Tractography	51
3.2.4	DTI in MS	55
3.2.5	DTI in animal models of MS	59
<b>3.3</b>	<b><i>Magnetic Resonance Spectroscopy</i></b>	<b>64</b>
3.3.1	MRS Technical overview	66
3.3.2	NAA in MS	67
<b>3.4</b>	<b><i>MRI for diagnosis, prognosis and drug development in MS</i></b>	<b>71</b>
<b>4</b>	<b>Diffusion weighted spectroscopy: Theory &amp; Models</b>	<b>74</b>
<b>4.1</b>	<b><i>Measuring molecular diffusion in cells</i></b>	<b>74</b>
4.1.1	Molecular diffusion in solution	74
4.1.2	Molecular crowding in cells	75
4.1.3	Molecular crowding and NMR methods	81
4.1.4	Compartmentation – intra- vs. extra-cellular	82
<b>4.2</b>	<b><i>Diffusion of N-acetyl aspartate in vivo (humans and animals)</i></b>	<b>83</b>
4.2.1	Measurements of NAA diffusivity in vivo	83
4.2.2	Using NAA diffusion to study microstructure	87
4.2.3	Diffusion weighted NMR with ultra-short diffusion times	89
<b>4.3</b>	<b><i>Modeling diffusion in impermeable cylinders</i></b>	<b>90</b>
<b>4.4</b>	<b><i>Conclusions</i></b>	<b>99</b>

<b><u>5</u></b>	<b><u>Diffusion weighted spectroscopy methods</u></b>	<b>100</b>
<b>5.1</b>	<b><i>Hardware</i></b>	<b>100</b>
<b>5.2</b>	<b><i>Magnetic resonance image acquisition and processing</i></b>	<b>101</b>
5.2.1	T1-weighted Images	101
5.2.2	FLAIR images	104
5.2.3	DTI Images	105
<b>5.3</b>	<b><i>Diffusion weighted spectroscopy acquisition and processing</i></b>	<b>106</b>
5.3.1	Acquisition	106
5.3.2	DWS Post-Processing	114
5.3.3	Modeled analysis of DWS data	116
<b>5.4</b>	<b><i>Conclusions</i></b>	<b>121</b>
<b><u>6</u></b>	<b><u>Reproducibility and optimization of in vivo Diffusion weighted spectroscopy of the human corpus callosum at 3T and 7T</u></b>	<b>123</b>
<b>6.1</b>	<b><i>Introduction</i></b>	<b>123</b>
<b>6.2</b>	<b><i>Methods</i></b>	<b>126</b>
6.2.1	Subjects	126
6.2.2	Data acquisition	126
6.2.3	Spectra processing	130
6.2.4	Derivation of NAA diffusion measures	131
6.2.5	Inter-subject variability analysis	133
6.2.6	Intra-subject variability analysis	133
6.2.7	Statistical analyses	134
<b>6.3</b>	<b><i>Results</i></b>	<b>135</b>
6.3.1	Diffusion weighted spectra and model fit	135
6.3.2	Inter-subject variability	138
6.3.3	Intra-Subject Variability	141
6.3.4	Inter-subject variability with optimized b-value scheme	148
6.3.5	Reproducibility and sample size analysis	149
<b>6.4</b>	<b><i>Discussion</i></b>	<b>151</b>
6.4.1	Intra- and inter-subject variability of DWS Measures	152
6.4.2	Effect of number of spectral averages	153

6.4.3	Effect of b-value range	154
6.4.4	Effect of b-value scheme on intra-subject variability	155
6.4.5	Limitations of the study	156
6.4.6	Conclusion	157
<b>6.5</b>	<b><i>Other contributors to this work</i></b>	<b>157</b>
6.5.1	Affiliations	157

## **7 Investigating Axonal Damage in Multiple Sclerosis by Diffusion Tensor**

<b><u>Spectroscopy</u></b>		<b>158</b>
<b>7.1</b>	<b><i>Introduction</i></b>	<b>158</b>
<b>7.2</b>	<b><i>Materials &amp; Methods</i></b>	<b>160</b>
7.2.1	Subjects & hardware	160
7.2.2	Structural images	161
7.2.3	Diffusion weighted spectroscopy	162
7.2.4	Statistics	164
<b>7.3</b>	<b><i>Results</i></b>	<b>164</b>
<b>7.4</b>	<b><i>Discussion</i></b>	<b>169</b>
<b>7.5</b>	<b><i>Other contributors to this work</i></b>	<b>174</b>
7.5.1	Affiliations	174

## **8 Following neurodegeneration in MS with Diffusion Spectroscopy –**

<b><u>Longitudinal analysis of MS Patients at 3T</u></b>		<b>175</b>
<b>8.1</b>	<b><i>Introduction</i></b>	<b>175</b>
<b>8.2</b>	<b><i>Methods</i></b>	<b>179</b>
8.2.1	Subjects	179
8.2.2	Structural image acquisition and processing	180
8.2.3	DWS volume of interest & acquisition	182
8.2.4	DWS data processing	185
8.2.5	Statistics	186
<b>8.3</b>	<b><i>Results</i></b>	<b>188</b>
8.3.1	Demographics and example cases	188
8.3.2	Cross-sectional analysis	189

8.3.3	Longitudinal Analysis	193
<b>8.4</b>	<b><i>Discussion</i></b>	<b>195</b>
<b>8.5</b>	<b><i>Conclusion</i></b>	<b>198</b>
<b>9</b>	<b><u>Conclusions</u></b>	<b>200</b>
<b>9.1</b>	<b><i>Multiple sclerosis and neuro-axonal degeneration</i></b>	<b>200</b>
<b>9.2</b>	<b><i>Magnetic resonance and multiple sclerosis</i></b>	<b>201</b>
<b>9.3</b>	<b><i>Diffusion weighted spectroscopy</i></b>	<b>204</b>
<b>9.4</b>	<b><i>Measuring axonal degeneration in multiple sclerosis with diffusion weighted spectroscopy</i></b>	<b>206</b>
<b>9.5</b>	<b><i>Summation, limitations and possible future directions</i></b>	<b>210</b>
<b>10</b>	<b><u>References</u></b>	<b>212</b>
<b>10.1</b>	<b><i>Permissions</i></b>	<b>212</b>
<b>10.2</b>	<b><i>Bibliography</i></b>	<b>221</b>
<b>11</b>	<b><u>Curriculum Vitae</u></b>	<b>260</b>

## List of Tables

Table 2.1 Histopathological characteristics of multiple sclerosis lesions .....	16
Table 3.1.A summary of DTI results in a representative subset of DTI studies of multiple sclerosis.....	58
Table 4.1. Summary of NMR studies of in vivo N-acetyl aspartate diffusion.(Diffusivity: $\mu\text{m}^2/\text{ms}$ ) .....	83
Table 5.1. Scanner parameters .....	101
Table 5.2. T <sub>1</sub> -weighted image parameters .....	102
Table 5.3. FLAIR image parameters.....	104
Table 5.4. DTI Parameters .....	105
Table 5.5 DWS sequence parameters by experiment.....	113
Table 6.1. Important abbreviations .....	125
Table 6.2. Subject Demographics.....	126
Table 6.3. Scanner and structural image acquisition parameters.....	128
Table 6.4 DWS acquisition parameters.....	129
Table 6.5. Diffusion weighting parameters (b-values) used for each scanner strength and direction. (Perpendicular b-values are twice those of parallel.).....	130
Table 6.6 Average, standard deviation and coefficient of variation for $D_{\text{model}}$ , $D_{\text{par}}$ , $D_{\text{avg}}$ , $D_{\text{perp}}$ , and $\sigma_{\phi}$ values calculated based on complete datasets acquired from subjects at 3T and 7T. ....	138
Table 6.7 List of b-value schemes with the number of spectral averages used for equivalent acquisition time comparisons in Figure 6.8. ....	145

Table 6.9 Repeatability and sample size values for b-value scheme $g_{247}$ .....	150
Table 7.1 Subject demographics – no significant differences between patients and controls.....	164
Table 7.2. Mean imaging and spectroscopy measures for MS patients and healthy controls.....	165
Table 8.1 Patient Demographics.....	188

## List of Figures

- Figure 2.1. Axonal injury related to an inflammatory demyelinating lesion in MS. Reprinted from “Axonal loss in the pathology of MS: consequences for understanding the progressive phase of the disease” by C. Bjartmar et al., 2003, Journal of Neurological Sciences, 206, page 166. Copyright 2003 by Elsevier. Reprinted with permission. .... 21
- Figure 3.1. First published MR images of multiple sclerosis. Reprinted from “Nuclear Magnetic Resonance Imaging of the Brain in Multiple Sclerosis” by I.R. Young et al., 1981, The Lancet, 318(8255), page 1064. Copyright 1981 by Elsevier. Reprinted with permission..... 27
- Figure 3.2. Spin and precession of a proton in an external magnetic field ( $B_0$ ). The solid arrow represents the magnetic moment or pole around which the proton spins (movement shown as a light gray spin circle). The dotted-line straight arrow represents the direction of  $B_0$  around which the nuclear magnetic moment precesses (movement shown as dotted-line spin circle) Reprinted from Basic Concepts in NMR Spectroscopy (page 4) by K.V.R Chary et al., 2008, Dordrecht, The Netherlands: Springer. Copyright 2008 by Springer. Reprinted with permission. .... 30
- Figure 3.3 Nutation of a spin net magnetic moment vector (bold arrow) onto the transverse (XY) plane with application of radiofrequency field  $H_1$ . Adapted from Carr & Purcell, Physical Review 94:3, 1954, Figure 3. A,B,C,D. Adapted from “Effects of Diffusion on Free Precession in Nuclear Magnetic Resonance Experiments” by H.Y. Carr and E.M. Purcell, 1954, Physical Review, 94(3), page 632. Copyright 1954 by American Physical Society. Adapted with permission..... 31
- Figure 3.4. (next page) Axial MRI slices of a healthy subject (A, C & E) and a multiple sclerosis patient (B, D & F). (A & B)  $T_1$ -weighted magnetization prepared rapid gradient echo images

(MPRAGE). (C & D) Tissue segmentation maps from the TOADS algorithm – white = white matter, orange = cortical gray matter, maroon = CSF, red = lesion, light orange & yellow = deep gray matter structures. (E & F) T<sub>2</sub>-weighted fluid attenuated inversion recovery (FLAIR) images..... 34

Figure 3.5. Skull-stripped T1-weighted images before (A & B) and after (C & D) injection of gadolinium contrast agent. 28-year-old female patient with multiple sclerosis. Contrast enhancing lesion (red arrows). Axial (A & C) and sagittal (B & D) images..... 41

Figure 3.6. Brownian motion in 3D. Adapted from “Brownian Motion” by T.J. Sullivan, Wikipedia, 2007. Retrieved from [http://commons.wikimedia.org/wiki/File:Wiener\\_process\\_3d.png](http://commons.wikimedia.org/wiki/File:Wiener_process_3d.png). ..... 45

Figure 3.7 (next page) Ensemble average of a simulation of 10,000 particles in a 3 dimensional random walk in impermeable cylinders. A. The root mean square displacement (RMSD) for diffusion parallel (blue) and perpendicular (red) to the long axis of the cylinders versus diffusion time ( $T_{diff}$ ). Panels B-E show histograms of the particle displacement for  $T_{diff} = 0.6$  ms (B & D) and  $T_{diff} = 60$  ms (C & E). In B & C, both the simulated parallel displacement (blue) and the calculated free diffusion (black) are shown. D & E demonstrate the simulated perpendicular displacement (red), the confining geometry (diameter of the cylinder) (black dotted), and the autocorrelation function ..... 46

Figure 3.8. Molecular diffusion in restricting environments. Shown is a simplified rendering of a cross-section of axons - looking down the end of the cylinders. A is pointing to restricted diffusion within axons where the molecules are largely confined by the cell membranes. B shows the somewhat obstructed diffusion of molecules moving through the extracellular space. C shows the path of molecules diffusing across membranes - a much slower process. Reprinted from “Looking into the functional architecture of the brain with diffusion MRI” by D. Le Bihan, 2003, Nature Reviews Neuroscience, 4(6), page 470. Copyright 2003



by Nature Publishing Group. Reprinted with permission. ....	50
Figure 3.9. An ellipsoid where axis directions or orientations are described by eigenvectors ( $v_1$ , $v_2$ , $v_3$ ) and the magnitude or length of each axis is described by the eigenvalues ( $\lambda_1$ , $\lambda_2$ , $\lambda_3$ ). .....	52
Figure 3.10 Fiber Assignment by Continuous Tracking (FACT). Reprinted from “Three-dimensional tracking of axonal projections in the brain by magnetic resonance imaging” by S. Mori et al., 1999, Annals of Neurology 45(2), page 266. Copyright 2001 by John Wiley and Sons. Reprinted with permission. ....	54
Figure 3.11. DTI color map of a healthy volunteer. Colors designates primary eigenvector direction – red = right-left; blue = foot-head; green = anterior-posterior. Brightness = FA. ...	56
Figure 3.12. Axons in white matter. Green = axons/axoplasm; yellow = myelin bilayers; blue dots = water molecules; magenta dots = N-acetyl aspartate molecules; orange ovals = voltage-gated sodium channels; white = extracellular space; violet arrows demonstrate direction of parallel and perpendicular diffusion with respect to the axon orientation. ....	65
Figure 3.13. An in vivo proton magnetic resonance spectroscopy spectrum from the brain of a healthy volunteer at 7T. NAA is the largest peak in the spectrum at 2 ppm. ....	68
Figure 4.1. (next page) (A&B) Cross-section of axons and modeled neurofilaments ( electron micrographs, scale bar = 0.5 $\mu\text{m}$ ). (A) Node of Ranvier as evidenced by lack of myelin and dense cytoskeletal undercoating (arrow head). Microtubules are the small circular structures (red arrows). Neurofilaments appear as dense spots (blue arrows). Vesicular organelles, such as mitochondria (green arrow), are throughout. (B) Myelinated internode with denser neurofilaments and fewer microtubules and organelles than the nearby node of Ranvier. (C) The neurofilament network can be visualized as interconnecting cross bridges connecting to each other and other organelles, such as the mitochondria shown here (quick-freeze deep-	

etch axon). A&B are reprinted from “Regional modulation of neurofilament organization by myelination in normal axons” by S.T. Hsieh et al., 1994, Journal of Neuroscience 14(11), page 6395. Copyright 1994 by the Society for Neuroscience. Reprinted with permission. C is reprinted form “Gene Targeting Studies Begin to Reveal the Function of Neurofilament Proteins” by N. Hirokawa and S. Takeda, 1998, The Journal of Cell Biology, 143(1), page 1. Copyright 1998 by the Rockefeller University Press. Reused with permission (non-commercial). ..... 76

Figure 4.2. Molecular crowding and volume exclusion. The yellow boxes represent cells filled with macromolecules (black dots). In (A), the small molecule will have many collisions with macromolecules, but it can sample the remaining 70% of the cytosol that is not occupied by macromolecules. In (B), the macromolecules have been marked with an open circle, which represents the radius of the molecule of interest. This molecule will not be able to pass between closely spaced macromolecules and, therefore, will not be able to sample the cytoplasm. Adapted from “The Influence of Macromolecular Crowding and Macromolecular Confinement on Biochemical Reactions in Physiological Media” by A.P. Minton, 2001, The Journal of Biological Chemistry, 276(14), page 10578. Copyright 2001 by the American Society of Biochemistry and Molecular Biology. Adapted with permission. .... 80

Figure 4.3 ADC and  $\lambda_{||}$  (when available) for the studies listed in Table 4.1. .... 87

Figure 4.4 Geometric models of axonopathy used for simulations. .... 92

Figure 4.5 NAA (A & B) and water (C & D) motion-probability propagators for each of the axon geometry models shown in Figure 4.4. (A & C) Plot of number of spins versus displacement perpendicular to the axis of the axon cylinders. The dotted line box represents the cylinder diameter. (B & D) Plot of spin counts versus displacement parallel to the axon length. The black curve shows free Gaussian diffusion. .... 93

Figure 4.6 NAA kurtosis excess (KE) values for the perpendicular and parallel motion-probability propagator distributions. ....	95
Figure 4.7. NAA diffusivity values of modeled diffusion in a variety of geometries. ....	96
Figure 4.8. Water kurtosis measures. ....	97
Figure 4.9. Water diffusivity measures of modeled diffusion in a variety of geometries. ....	98
Figure 5.1. Image processing pipeline implemented in MIPAV/JIST. ....	103
Figure 5.2. A. 3D reconstruction of brain viewed from above right showing placement of teal sVOI in anterior corpus callosum (healthy volunteer). B. Anatomical drawing of brain viewed from above with gray matter cut away on the right side to illustrate the right-left course of corpus callosum fibers. Black arrow points to approximate location of VOI in the anterior CC. (Adapted from Eye, Brain and Vision, by D. Hubel, 1988, retrieved from <a href="http://hubel.med.harvard.edu/book/b34.htm">http://hubel.med.harvard.edu/book/b34.htm</a> .) ....	107
Figure 5.3. PRESS localization sequence with diffusion weighting. ....	108
Figure 5.4. Coronal and sagittal views of DWS VOI placement and angulation from the scanner console at 7T. Red box = VOI, white box = location of water measured in spectrum due to chemical shift displacement from NAA, yellow box = shim volume. ....	109
Figure 5.5. DWS gradient directions for 7T Hopkins data. The DWS VOI is represented by white cuboid outline and the 6 orthogonal gradient directions are shown in the right bottom on various VOI views. Red-orange lines represent DTI tractography tracts seeded within the VOI. ....	110
Figure 5.6. Parallel ([1,0,0]) and perpendicular ([0,-1,1]) gradient directions with respect to VOI for 2-direction acquisitions. ....	111
Figure 5.7. (Left) a coronal slice of a DTI color map where brightness represents FA; colors show	

primary orientation of fibers (red: LR, blue: FH, green: AP); primary eigenvectors ( $E1$ ) are displayed for voxels in the CC. (Right) Illustration of angles between the  $E1$ s and the diffusion weighting directions used for metabolite diffusion. (Adapted from “Axonal and glial microstructural information obtained with diffusion weighted magnetic resonance spectroscopy at 7T” by I. Ronen et al., *Frontiers in Integrative Neuroscience*, 7(13). Open access article distributed under the terms of the Creative Commons Attribution License.) 116

Figure 5.8 Modeled diffusion using the Random Walk Simulator (Landman et al. 2010) with 10,000 molecules intracellular,  $D = 0.7\mu\text{m}^2/\text{s}$ , cylinder lattice with radius= $7\mu\text{m}$ . Diffusion parallel = blue, diffusion perpendicular = red. Diffusion perpendicular to the cylinders has a smaller apparent diffusion constant (slope) than the parallel diffusion..... 118

Figure 5.9. Histogram of angles between the parallel gradient  $[0, -1, 0]$  and the  $E1$ s (left) and the perpendicular gradient  $[1, 0, -1]$  and the  $E1$ s (right). By convention angles are with respect to the azimuthal, zero degrees is with respect to a plane orthogonal to the primary fiber direction. From a healthy volunteer, 3T data. .... 120

Figure 5.10 Modeled analysis of DWS data. The primary eigenvector information is taken from the DTI image to produce histograms of the eigenvector angles with respect to the diffusion weighted spectroscopy gradients. The histograms can be combined with the signal attenuation data for each direction and (A) fit them to find the diffusion of total NAA or (B) fit these data with a micro dispersion parameter. (Adapted from “Axonal and glial microstructural information obtained with diffusion weighted magnetic resonance spectroscopy at 7T” by I. Ronen et al., *Frontiers in Integrative Neuroscience*, 7(13). Open access article distributed under the terms of the Creative Commons Attribution License.) 121

Figure 6.1 Placement of sVOI (yellow box) on coronal (left) and sagittal (right) T1-weighted slices. Directions of parallel and perpendicular gradients for DWS are illustrated as the orange and

purple solid lines, respectively. ....	127
Figure 6.2 Schematic description of the method in which data subsets are randomly selected from the full data set of a single session of a specific subject. ....	132
Figure 6.3 Typical spectra acquired at 3T with diffusion-weighting in the parallel ( $g_{[-1,0,0]}$ ) and perpendicular( $g_{[0,-1,1]}$ ) directions are shown in panels A and C, respectively. Spectra acquired at 7T with the same gradient directions are shown in panels B and D. Line broadening of 5 Hz was applied to all of the spectra for display purposes.....	136
Figure 6.4 Logarithm of the diffusion weighted signal measured with the diffusion weighting applied along the $[0,-1,1]$ and $[-1,0,0]$ directions as a function of b-value (measured in $s/mm^2$ ). Panels A and C show the monoexponential fits used to calculate the parallel ( $D_{par}$ ) and perpendicular ( $D_{perp}$ ) diffusivity values from one data set acquired at 3T (A) and one acquired at 7T (C). Panels B and D show the same data fitted to the model described in the text, which yields the cytosolic diffusivity $D_{model}$ and the standard deviation of the axonal angular dispersion $\sigma_\phi$ .....	137
Figure 6.5 Inter-subject and inter-session variability of all diffusivity values ( $D_{par}$ , $D_{perp}$ , $D_{avg}$ and $D_{model}$ ), calculated based on complete datasets acquired from 3 subjects at 3T (left panel) and three subjects at 7T (right panel). Box-and-whisker plots show the inter-session variability of diffusivity measures for each subject.....	140
Figure 6.6 Diffusivity measures from all subjects and all sessions obtained from the experiments performed at 3T and 7T. ....	141
Figure 6.7 Mean diffusivity values and standard deviations obtained from the jackknife-like resampling procedure applied to the data acquired from one subject at 3T (A-H) and one subject at 7T (I-O). The solid symbols in panels A-D and I-L show the diffusivity measures obtained for a given number of acquisitions, averaged first over 100 jackknife evaluations	

and then over the 5 sessions. The shaded areas show the standard deviations of the means across the 5 sessions. Panels E-H and M-O show the standard deviations of the diffusivity measures shown in the upper panels, similarly obtained first by evaluating the standard deviations of the jackknife results from a single session, and then averaging them across sessions. The shaded areas show the standard deviation of the standard deviations across the 5 sessions. .... 143

Figure 6.8 (next page) Mean diffusivity values obtained from all 5 sessions are shown as a function of the highest b-value used. Error bars correspond to the inter-session standard deviation. Panels A-D are one subject scanned at 3T. Panels E-H are one subject scanned at 7T. .... 145

Figure 6.9 The coefficients of variation for  $D_{\text{model}}$  (panels A & C) and  $D_{\text{avg}}$  (panels B & D) obtained from a single session subject acquired at 3T (panels A & B) and 7T (panels C & D), shown as a function of number of total spectra acquired for different b-value schemes Table 6.7. .... 147

Figure 6.10 Inter-subject and inter-session variability of all diffusivity values ( $D_{\text{par}}$ ,  $D_{\text{perp}}$ ,  $D_{\text{avg}}$ , and  $D_{\text{model}}$ ) calculated for the  $g_{247}$  b-value scheme, a subset of b-values from the maximum datasets, acquired from 3 subjects at 3T (left panel) and three subjects at 7T (right panel). Box-and-whisker plots show the inter-session variability of diffusivity measures for each subject. .... 148

Figure 6.11 Plots of standard deviation versus mean for the  $D_{\text{model}}$  (A) and  $D_{\text{avg}}$  (B) diffusivity measures at 3T and 7T. .... 149

Figure 6.12 Number of subjects required to detect difference (in percent of mean) with significance level of  $\alpha = 0.05$  and power of  $1-\beta = 0.80$  using the  $g_{1357}$  b-value scheme for 3T and  $g_{247}$  b-value scheme for 7T. .... 150

Figure 7.1. Voxel location and spectra. **a**, sagittal and **c**, coronal T1-weighted images demonstrating voxel location in red. **b**, DTI axial color map. **d**, non-diffusion weighted spectrum (black) and diffusion weighted spectra with gradient direction primarily parallel to fiber tract (red & blue). ..... 163

Figure 7.2. tNAA/tCr , a measure of NAA concentration, was negatively correlated with age for both patients and healthy controls. .... 167

Figure 7.3. NAA  $\lambda_{||}$  and avgDTI water  $\lambda_{||}$  for multiple sclerosis patients (MS) and healthy controls (HC) ( \*p < 0.05, \*\*p < 0.001, error bars represent 95% confidence intervals). ..... 167

Figure 7.4. Comparison of water mean diffusivity values calculated with the single-voxel DTI analysis scheme versus the conventional averaging of voxels after the tensors have been found. .... 168

Figure 7.5. Parallel diffusivity ( $\lambda_{||}$ ) of NAA and water. a, NAA  $\lambda_{||}$  was negatively correlated with avgDTI water  $\lambda_{||}$  (all subjects,  $R^2 = 0.16$ ,  $p = 0.02$ ). ..... 169

Figure 7.6. NAA parallel diffusivity ( $\lambda_{||}$ ) is correlated with clinical severity of disease ( $\rho = -0.61$ ,  $p = 0.015$ ). EDSS = Expanded Disability Status Scale. .... 169

Figure 8.1 A. DWS VOI placement on anterior CC (yellow) and splenium (green). B. Coronal view of anterior CC VOI on DTI color map overlaid with the primary eigenvector (color denote direction of primary eigenvector: red = RL, green = AP, blue = FH). C & D. Diffusion weighted spectra acquired parallel [1,0,0] and perpendicular [0,-1,1] to the CC fibers. b-values measured in s/mm<sup>2</sup>. .... 184

Figure 8.2 Logarithm of the diffusion-weighted signal measured from one active MS patient with the diffusion weighting applied along the parallel ([1,0,0], red triangles) and perpendicular ([0,-1,1], blue triangles) directions as a function of b-value (measured in s/mm<sup>2</sup>). **A**, the

monoexponential fits used to calculate the parallel ( $D_{par}$ ) and perpendicular ( $D_{perp}$ ) diffusivity values. **B**, the same data fitted to the model described in the text, which yields the cytosolic diffusivity  $D_{model}$  and the standard deviation of the axonal angular dispersion  $\sigma_{\phi}$ ..... 187

Figure 8.3 **A**. Average brain volume (% intracranial volume) across scans versus age for all subjects, MS=red triangles, HV=blue circles. \*\*\*MS  $R^2 = 0.36$ ,  $p < 0.001$  (red line); \*HV  $R^2 = 0.46$ ,  $p = 0.01$  (blue line). **B**. Average water mean diffusivity ( $\mu m^2/s$ ) across scans versus brain volume (%ICV) for all subjects. \*\*\*MS  $R^2 = 0.36$ ,  $p < 0.001$ ; \*HV  $R^2 = 0.36$ ,  $p < 0.05$ . ..... 189

Figure 8.4 **A**. Water mean diffusivity and NAA  $D_{model}$  for healthy volunteers and MS patients, \*\* $p < 0.01$ . **B**. NAA  $D_{model}$  versus water mean diffusivity for MS patients and healthy volunteers (ns). ..... 190

Figure 8.5 Lesion load for stable and active MS patients. Left: volume of lesion segmented in corpus callosum volume of interest. ns. Right: lesion load as percent of total brain white matter, ns. .... 191

Figure 8.6 **A**. NAA  $D_{model}$  was negatively correlated with lesion load (% white matter),  $R^2 = 0.16$ , \* $p < 0.05$ . **B**. Water fractional anisotropy was negatively correlated with lesion load (% white matter),  $R^2 = 0.19$ , \*\* $p < 0.01$ . **C**. Water mean diffusivity was positively correlated with lesion load (% white matter),  $R^2 = 0.18$ , \* $p < 0.05$ . **D**. Water perpendicular diffusivity was positively correlated with lesion load (% white matter),  $R^2 = 0.19$ , \*\* $p < 0.01$ ..... 192

Figure 8.7 MS disease duration. **A**. Disease duration for stable and active MS patients, ns. **B**. Mean diffusivity versus age in MS patients, #non-significant trend  $RC = 0.003 \mu m^2/ms/year$ ,  $R^2 = 0.10$ ,  $p = 0.07$ . **C**. Change in water mean diffusivity over 6 months versus disease duration (ns,  $p = 0.15$ ). **D**. Change in  $D_{model}$  over 6 months versus disease duration (ns) ... 193

Figure 8.8. Difference in measurement between baseline and 6 months for stable and active MS



patients. For healthy controls, scans were 0-1 months apart. **A.** NAA diffusivity (modeled analysis), \*p < 0.05 for stable ≠ active, \*p < 0.05 for active ≠ 0. **B.** Brain volume (%=total brain/total intracranial volume), no significant differences (ns). **C.** Water mean diffusivity (MD), \*\*p < 0.01 for stable ≠active, \*p < 0.05 for stable ≠ 0. **D.** Water fractional anisotropy, ns. .... 194

# **1 DIFFUSION WEIGHTED SPECTROSCOPY IN MULTIPLE SCLEROSIS: AN INTRODUCTION**

## ***1.1 Preface***

Multiple sclerosis is a chronic disease of the brain and spinal cord that kills nerve cells and their insulation, called myelin. It is a common cause of weakness, loss of sensation and thinking difficulties in young people. While some drugs can reduce the inflammation in this disease, nerve cells and myelin continue to die. In order to develop new drugs to prevent this from occurring, new techniques for measuring nerve cells and myelin in the living brain need to be developed. With this in mind, diffusion weighted spectroscopy, an advanced magnetic resonance technique, was developed and tested in multiple sclerosis patients with the twin goals of monitoring potential therapies and contributing to the current understanding of how the disease develops and takes its toll.

## ***1.2 Background and motivation***

Multiple sclerosis is a chronic, immune-mediated, demyelinating and neurodegenerative disease of the central nervous system that affects approximately 2.1 million individuals worldwide (Miller & Leary 2007; Hauser & Oksenberg 2006). Neuro-axonal degeneration is an important determinant of clinical status in multiple sclerosis, especially for those patients with the chronic, progressive form of the disease (Bjartmar & Trapp 2001; Trapp et al. 1998; Tallantyre et al. 2009). Currently, there are no drug therapies dedicated to neuroprotection for patients with multiple sclerosis (or other neurological diseases) (Ellwardt & Zipp 2014; Noseworthy 2003), and there are few in vivo measures of neuro-axonal health. The long-term effects of neurodegeneration can

be detected in the form of tissue loss (atrophy) (Gao et al. 2014; Fisher et al. 2008), but ongoing neurodegeneration, manifested as neurons that are damaged but still intact, is exceedingly difficult to measure. Sensitive and specific in vivo measures of axonal damage would greatly benefit prognostication and therapy development and assessment in multiple sclerosis.

To date, the disease modifying therapies available to patients with multiple sclerosis are targeted at the immune-mediated and inflammatory aspects of the disease. This focus on inflammation – and not neurodegeneration – is likely due, in large part, to many critical research contributions in multiple sclerosis pathophysiology that have been made over centuries that demonstrate a role for the immune system. An additional explanation for the imbalance of drug targets is that inflammatory relapses are relatively easily quantitated while clinical progression due to neurodegeneration is insidious and difficult to measure. Therefore, it is more straightforward to design a clinical trial of efficacy with drugs that primarily target inflammation. This explanation is highlighted by the role that contrast-enhanced magnetic resonance imaging has played in multiple sclerosis drug therapy.

Magnetic resonance imaging has been central to the development of disease-modifying therapies in multiple sclerosis (McFarland 2010). Soon after magnetic resonance imaging was applied to clinical medicine, it was found that lesions were visible on brain images in patients with multiple sclerosis (Young et al. 1981). Subsequently, it was discovered that administration of contrast agents could be combined with magnetic resonance techniques to detect new, active lesions in patients with high sensitivity and specificity (Katz et al. 1993; Miller et al. 1998). As lesion activity is associated with clinical relapse and disease progression, contrast enhanced magnetic resonance imaging came to be used as a surrogate marker of disease activity in multiple

sclerosis and as a secondary outcome in many phase 2 and phase 3 clinical trials (McFarland et al. 2002). In this way, magnetic resonance imaging of contrast-enhancing lesions helped to bring a number of multiple sclerosis disease-modifying therapies to the market.

The heterogeneity of multiple sclerosis renders measuring neurodegeneration very difficult. At the clinical level, patients experience very different courses from one another. At the level of the patient, every relapse may manifest differently, and brain imaging will exhibit lesions disseminated in both space and time. At the tissue level, many combinations of a group of pathological processes may be found in a lesion: blood brain barrier breakdown, invasion by various immune cells (T-cells, B-cells, macrophages, etc.), demyelination, remyelination, gliosis, axon transection and axon degeneration as illustrated by end-bulbs, changes in neuro-filament staining, etc. Even with optimized, high resolution, high-field magnetic resonance water images (e.g. 0.5mm isotropic resolution at 7 tesla), any white matter lesion voxel will likely encompass multiple pathological processes and fibers involved in multiple brain function processes.

Diffusion weighted spectroscopy is a magnetic resonance technique that combines features of diffusion tensor imaging and magnetic resonance spectroscopy, allowing measurement of the diffusion properties of intracellular, cell-type-specific metabolites (Upadhyay et al. 2008; Ellegood et al. 2010; Kan et al. 2012; Ronen et al. 2013; P. C. M. van Zijl et al. 1994). As such, diffusion weighted spectroscopy of an intraneuronal metabolite, N-acetyl aspartate, may provide specific information about axonal microstructure and consequently serve as a useful marker of axonal integrity in the complex mixture of pathologies that characterizes multiple sclerosis (inflammation, demyelination, edema, gliosis, axonopathy).

Prior to this work, diffusion weighted spectroscopy had been studied in a small

number of healthy humans and animal models. Here we developed and optimized the diffusion weighted spectroscopy technique for use with patients on clinical scanners so that we could study N-acetyl aspartate diffusivity in two populations of multiple sclerosis patients.

### **1.3 *Dissertation Outline***

This dissertation advances diffusion weighted spectroscopy as an in vivo technique for studying disease progression and pathophysiology in the human neurological disease, multiple sclerosis. Multiple sclerosis is a highly heterogeneous and widely studied disease. **Chapter 2** provides a brief overview of recent knowledge in the vast field of multiple sclerosis including epidemiology, pathology, pathophysiology and current therapies. Additionally, chapter 2 discusses axonal degeneration broadly and with respect to multiple sclerosis. **Chapter 3** provides some background for understanding the physical underpinnings of the magnetic resonance techniques discussed in this work. Diffusion weighted imaging, magnetic resonance spectroscopy and diffusion weighted spectroscopy are introduced in the context of multiple sclerosis.

While diffusion weighted spectroscopy is not widely used, both the concept of measuring molecular diffusion in biology and the technique are not brand new. In **chapter 4**, the theories surrounding in vivo molecular diffusion are presented, and work to date in diffusion weighted spectroscopy of N-acetyl aspartate is summarized. Additionally, a computational simulation of diffusion in cylinders is implemented, using the Random Walk Simulator software (Landman et al. 2010), to model N-acetyl aspartate and water diffusion in axon-like geometries (cylinders).

**Chapter 5** presents the specific methods used for experiments detailed in chapters 6-8.

**Chapter 6** presents the first reproducibility and reliability study of diffusion weighted spectroscopy in humans. Based on this work, suggestions are given for data acquisition and processing to optimize scan time and reliability using scanners at fields of both 3 tesla and 7 tesla. Furthermore, power calculations are provided for planning future studies with diffusion weighted spectroscopy. A manuscript detailing this work has recently been submitted for publication.

**Chapter 7** describes the results of the first study of diffusion weighted spectroscopy *in patients*. In this cross-sectional study, we examined the diffusion properties of N-acetyl aspartate and water, using both diffusion weighted spectroscopy and diffusion tensor imaging performed on an ultra-high-field (7 tesla) MRI scanner, in the corpus callosum of multiple sclerosis cases and healthy controls. This work was published in the *The Journal of Neuroscience* in 2012 (Wood et al. 2012).

**Chapter 8** extends the results from chapters 6 and 7 in several ways. A longitudinal assessment of diffusion weighted spectroscopy in patients with multiple sclerosis is detailed. These data were acquired on clinical scanners and analyzed with a model that combines information from concurrently acquired diffusion tensor images to account for the macroscopic curvature of white matter fibers and estimate the cytosolic diffusivity of N-acetyl aspartate. A manuscript describing this work is in preparation.

**Chapter 9** addresses the implications and limitations of this work and offers concluding remarks regarding possible future directions.

## **2 AN OVERVIEW OF MULTIPLE SCLEROSIS**

### ***2.1 Epidemiology & Clinical Course***

Multiple sclerosis (MS) is a common, chronic demyelinating and neurodegenerative disease with profound impact on individuals and their families and communities. After trauma, MS is the most common cause of neurologic disability in young adults in North America and Europe – in these regions, the prevalence of MS is between 1 in 500 and 1 in 1500 people (Miller & Leary 2007; Hauser & Oksenberg 2006). MS tends to strike adults in the prime of their lives, during a time when they are raising families and experiencing high career productivity. By 10 years after disease onset, 50% of patients are unable to perform household and employment responsibilities (Trapp & Nave 2008).

Patients with MS experience different clinical courses. The majority of newly diagnosed patients are around 30 years old, 2-3:1 female:male, and have a relapsing-remitting (RR) form of the disease characterized by episodes of acute neurological deterioration between periods of partial to complete recovery. This phase of the disease, and relapses in particular, are associated with focal, inflammatory white matter lesions that can be visualized with magnetic resonance imaging (MRI). After 10-20 years, approximately 65% of RRMS patients develop the secondary progressive (SP) form of the disease (Miller & Leary 2007). In another course of the disease, 10-15% of newly diagnosed MS patients have a primary progressive (PP) form of MS, which is split evenly between males and females. The average age of clinical onset of PPMS is 40 years, similar to the average age of conversion from RRMS to SPMS. Both progressive forms of the disease tend to manifest as spinal cord disease and are characterized by

steady clinical progression (Miller & Leary 2007; Compston & Coles 2008). Around two thirds of MS patients die from their disease or from the increased risk of infection and associated complications. The median time from disease onset to death is 30 years, which represents a reduced life expectancy of 5-10 years for people with MS.

MS is a disease of the entire central nervous system. Consequently, patients can present with a wide range of symptoms and signs. As vision loss is a disturbing and noticeable occurrence for most people, optic neuritis, which typically presents as a unilateral painful loss of vision, is the presenting symptom of many patients who go on to be diagnosed with MS. Inflammatory, demyelinating lesions throughout the corticospinal tract will cause weakness, increased spinal reflexes, and other upper motor neuron signs. Similarly, unilateral sensory deficits are commonly due to lesions disrupting the dorsal column-medial lemniscus pathway or spinothalamic tracts. As expected, tremor, limb incoordination, and gait ataxia are typically associated with lesions in the cerebellum and cerebellar pathways while lesions in brainstem can be associated with dysarthria, vertigo, diplopia, and paroxysmal symptoms. Lesions in the cerebral cortex and white matter can be more difficult to associate with particular symptoms but have been considered to be the primary cause of cognitive and affective deficits that are common to MS patients (Compston & Coles 2008). The time course of MS is also highly heterogeneous but tends to follow patterns. A typical MS relapse or exacerbation comes on quickly - over the course of hours - and lasts for days to weeks.

As there are no pathognomonic signs or symptoms of MS, diagnosis is based on a set of criteria that reflect the chronicity and expansive CNS territory of the disease. The most recent diagnostic criteria were set out by the International Panel on Diagnosis of Multiple Sclerosis and are referred to as the McDonald 2010 criteria. Diagnosis of relapsing remitting MS requires evidence of demyelinating activity in more than 1 area of



the CNS occurring at more than 1 time point (Katz Sand & Lublin 2013; Polman et al. 2011). These requirements are referred to, respectively, as “dissemination in space” and “dissemination in time.” Dissemination in space can be satisfied by clinical evidence of two demyelinating attacks with different symptoms or MRI evidence of two lesions in different sites in the CNS – specifically in the periventricular, juxtacortical, infratentorial, or spinal cord sites. Likewise, dissemination in time is established with clinical evidence of two distinct episodes or MRI scans that demonstrate lesions at different stages. Under the McDonald 2010 criteria, it is possible to make the diagnosis of RRMS with a high degree of sensitivity and specificity with a single clinic visit and MRI scan (Klawiter 2013). Making the diagnosis of primary progressive MS is slightly more complicated. PPMS diagnosis requires 1 year of disease progression, which can be determined retrospectively or prospectively. Additionally, the patient must have 2 of the following: 1) at least 1 lesion at a characteristic location for MS in the intracranial CNS; 2) at least 2 lesions in the spinal cord; or 3) CSF positive for oligoclonal bands or an elevated IgG index. Oligoclonal bands are found in approximately 90% of MS patients (See section 2.2.1, regarding B-cells).

## **2.2 Pathophysiology**

### **2.2.1 Immunology**

A large portion of the thousands of articles and chapters written about MS begin with a phrase like: "multiple sclerosis is an inflammatory, demyelinating disease of the central nervous system". Here, I will briefly discuss the major immunological players contributing to inflammation in MS. While there is a great deal of evidence to support an important role for CD4+ T-cells in MS, there is no smoking gun in this disease – all the big contenders in the specific or adaptive immune system have been implicated in

various stages and types of MS pathophysiology.

Where the innate immune system acts rapidly and broadly, adaptive immunity is targeted to specific invaders and keeps memories of prior attacks and defense strategies. The basis for this adaptive, precise defense mechanism is the use of antigen-specific receptors on lymphocytes – T- and B-cells. These individualized receptors are created through an elegant scheme of gene rearrangement, selection for functional receptors, selection against self-reactive receptors and tolerance. This scheme is both tightly regulated and different for every single person. T-cells can be divided into two main groups based on their receptor type – CD4+ and CD8+. When CD4+ T-cells are presented with an antigen on an MHC class II molecule and become activated, they will produce cytokines, mostly proinflammatory, that can activate a wide range of cells. Importantly, MHC class II molecules exist almost exclusively on specialized antigen-presenting cells (APCs) and present antigens picked up from outside the APC (exogenous). CD8+ T-cells can be activated by antigens presented on an MHC class I molecule resulting in cytotoxic attack of the presenting cell. MHC class I molecules can be expressed by any nucleated cell and present endogenous antigens that have infected the cell. Therefore, to a large extent, the type of pathogen – intracellular (e.g. viruses) versus extracellular (e.g. bacteria) – can be known from the MHC class molecule that presents the antigen fragment and the T-cells type that is activated (Parkin & B. Cohen 2001).

There is wide ranging evidence that CD4+ T-cells play a key role in MS pathogenesis. Firstly, CD4+ lymphocytes are almost never seen in the healthy CNS and yet are present in and around MS plaques (Sospedra & Martin 2005). Experimental Autoimmune Encephalomyelitis (EAE) is an animal model of MS that is elicited by combined activations of the innate and adaptive immune responses. White matter

antigens are injected with inflammatory adjuvants that activate the innate immune mechanisms and tend to induce autoimmune disease. In this way, autoimmunity toward white matter is stimulated, resulting in neurological impairments and acute lesions that resemble MS in mice, rats, and marmosets ('t Hart et al. 2011; Maggi et al. 2014). CD4+ T-cells are prevalent in EAE and myelin-specific T-cells can induce white matter autoimmunity when transferred to naïve animals (Pettinelli & McFarlin 1981). Additionally, genome wide associated studies of large groups of patients with and without MS have demonstrated HLA-DR and -DQ genes, which are associated with MHC class II molecules, confer risk for MS. Finally, CD4+ T-cells, which are referred to as T helper cells, can be classified further into Th1 and Th2 based on the pattern of cytokines that they secrete. Th1 cells secrete cytokines that induce T-cell proliferation, lower the threshold for the CD8+ T-cell cytotoxic response, activate macrophages and inhibit the Th2 response. Th2 cells secrete cytokines associated with allergies including B-cell class switching to IgE and eosinophil activation in addition to dampening the Th1 response (Parkin & B. Cohen 2001). As MS pathophysiology reflects possible over-activation of the Th1 response, this is another way in which CD4+ T-cells are implicated in MS pathogenesis.

While CD4+ T-cells have garnered a lot of attention, CD8+ T-cells may be better positioned to cause damage in MS. CD8+ T-cells are directly cytotoxic to cells bearing their specific antigen presented on MHC class I molecules. Since most cells that reside in the CNS, other than microglia, are unable to present MHC class II (Sospedra & Martin 2005), the MHC class I (CD8+) response is expected. In MS lesions, CD8+ T-cells tend to be much more prevalent than CD4+ (Batoulis et al. 2010). There is in vivo and ex vivo evidence that CD8+ T-cells will destroy neurons and axons presenting MHC class I (Neumann 2003). Finally, in MS lesions, the number of CD8+ T-cells has been

correlated with the extent of axon damage (Bitsch et al. 2000; Kutzelnigg & Lassmann 2014).

B-cells produce antibodies against invading pathogens. Antibodies can neutralize toxins, prevent adherence of pathogens to mucosal surface, opsonize bacteria, activate the innate immune system (e.g. complement), and sensitize pathogens for cytotoxic killing by T-cells (Parkin & B. Cohen 2001). It has long been known that B-cells are active in MS as they are found to expand clonally and produce oligoclonal IgG (aka oligoclonal bands) in the CSF of patients with MS (Franciotta et al. 2008). More recently, B-cell follicles – specialized immune structures – have been found in the meninges of SPMS patients and have been associated with more severe cortical pathology (Serafini et al. 2004; Magliozzi et al. 2007). Additionally, a number of disease modifying therapies for MS have direct effects on B-cells, suggesting that B-cells play an important role in MS pathophysiology (Krumbholz et al. 2012).

### **2.2.2 Pathogenesis**

The pathogenesis of multiple sclerosis remains largely unknown. There is a consensus view that inflammation directed at myelin arises in certain people when various combinations of environmental factors, genetic background, and immunological profiles coalesce. This line of reasoning is supported by the vast heterogeneity of MS disease features and courses as well as the fact that, after hundreds of years of study, a singular explanatory origin has yet to be found.

Immunologically, the main ideas that have been set forth as possible pathogenic mechanisms for MS involve infectious agents and the hypotheses of molecular mimicry and bystander activation. Under the molecular mimicry hypothesis, autoreactive T- and B-cells are established by cross-reactivity with antigenic determinants that are shared by

infectious and self-agents. Bystander activation assumes that autoreactive cells are activated by the nonspecific inflammatory response to infection. For instance, T-cells could be activated by T-cell-receptor-independent mechanisms such as cytokines, superantigens or molecular pattern recognition. Alternatively, host antigens could be exposed in the adjuvant context of infection-induced inflammation (Sospedra & Martin 2005; Ascherio et al. 2012). These auto-immunogenic mechanisms are, by no means, mutually exclusive within or between people. And, it is conceivable that a wide range of pathogens, especially neurotropic viruses such as the herpes viruses (particularly Epstein-Barr virus), could provide the cross-reactive antigenic determinants or the inflammatory environment that would promote these processes. Important research is being done to understand this process.

### **2.2.3 Disease modifying therapies in MS**

The pharmacological therapies that have been developed for use in patients with multiple sclerosis act primarily on the immune system, and each has a different mechanism of action. These medicines have dramatically changed the landscape of how MS is viewed as a disease – for many patients, MS (at least in its early stages) is now a chronic, largely controllable disease. Furthermore, by studying how these therapies work, we have learned a great deal about the pathophysiology of the disease. Before briefly discussing some of the disease modifying therapies (DMTs) used in multiple sclerosis, the corticosteroids should be mentioned. These drugs have, by far, the longest track record for treating patients with MS and are the first line in patients with a relapse or exacerbation. Corticosteroids have vast effects throughout the immune system because they both act at multiple cellular levels and influence a wide range of cells. In the case of MS, it seems that the most prominent mechanism of action is the rapid,

specific non-genomic effects that occur on the cell membrane within minutes to hours of drug administration (Gold et al. 2001). These changes help to reseal the blood brain barrier and block leukocyte trafficking into the CNS (Frohman et al. 2007).

Corticosteroids have been shown to decrease the duration of relapses and short term disability measures (Filippini et al. 2000). However, corticosteroids have not demonstrated any long term effects on clinical disease progression – often measured with annualized relapse rate (ARR) or rate of Expanded Disability Scale Score (EDSS) changes. For this reason, corticosteroids are not considered to be MS DMTs.

Interferon- $\beta$  (IFN- $\beta$ ) preparations and glatiramer acetate (GA) were the first DMTs on the market for MS treatment. Both seem to have their chief effects on lymphocytes. IFN- $\beta$  acts somewhat broadly to modulate B- and T-cell activity away from the pro-inflammatory state while decreasing BBB permeability and altering cytokine expression (Freedman 2013). Phase 3 trials and many long-term (on the order of 5-6 years) studies undertaken since IFN- $\beta$  was approved have demonstrated decreased annualized relapse rate (ARR) and fewer new and enhancing lesions and less brain atrophy on MRI (Kappos et al. 2009; Paolillo et al. 2002). GA is a mixture of synthetic polypeptides that may be able to bind MHC class II molecules thereby blocking the active site for myelin-associated self-antigens. In so doing, it may activate regulatory T-cells, as opposed to cytotoxic T-cells, to migrate to the CNS (Freedman 2013). GA has also been shown to decrease the ARR and numbers of new and enhancing lesions (Noseworthy 2003).

Natalizumab is a humanized monoclonal antibody that binds an integrin on leukocytes so that these cells cannot interact with and cross endothelial cells to get from the blood into the CNS (Noseworthy & Kirkpatrick 2005). Natalizumab has been associated with impressive reductions in ARR – around 68% - as well as with

devastating side effects due to progressive multifocal leukoencephalopathy (PML) (Freedman 2013). PML is an inflammatory white matter disease caused by the JC virus and seen in immunocompromised individuals. Due to increased vigilance among physicians including regular monitoring (every 6-12 months) for JC virus, the incidence of PML in MS patients taking Natalizumab may be on the decline.

Fingolimod is the first oral drug to be approved for MS treatment and probably acts by preventing T-cell egress from lymph nodes. With few lymphocytes leaving the lymph nodes, there are fewer able to enter the CNS. Fingolimod may reduce the ARR by as much as 50% compared to placebo (Kappos et al. 2010) and by 33% compared to IFN- $\beta$  (J. A. Cohen et al. 2010). There are a number of immunomodulatory therapies for relapsing remitting MS in the pipeline including teriflunomide, dimethyl fumarate and daclizumab. Laquinimod is an emerging therapy with immune system effects that may also be axon protective due to increased production of brain-derived neurotrophic factor (Saidha et al. 2012). For the most part, disease-modifying therapies used in MS treatment, which are primarily anti-inflammatory, are not effective in the progressive phase of the disease due to a lower overall degree of inflammation (Leary & Thompson 2005).

#### **2.2.4 Pathology of MS plaques**

The pathological descriptions of brains and tissue from patients with multiple sclerosis go back, at least, to Jean-Marie Charcot. In 1868, he described white matter plaques under the microscope, where he saw a central vein surrounded by sparse “cylindres d’axe” in various states of myelination being encompassed by glial “fibrilles” (Charcot 1868). These plaques are the hallmark of pathology in MS. At autopsy, plaques or lesions can be seen on gross sections as sharply demarcated, focal, dark areas in the

otherwise light white matter. Histologically, lesions display many processes and features including: inflammation, injured oligodendrocytes, myelin debris, astrogliosis, neuro- and axonal and neurodegeneration, and remyelination. With immunohistochemistry to help illuminate the lineage and phase of various cell types, lesions can be described in great detail, and some patterns have emerged.

Pathologists categorize MS lesions according to location (e.g., white or gray matter), stage (acute or chronic), and features, such as the type of immune cells that are present as well as the myelination state (Table 2.1). Acute lesions are those that are actively inflamed. General features of acute active white matter lesions are: hypercellularity with evenly distributed macrophages full of myelin debris on a background of CD8+ greater than CD4+ (cytotoxic>helper) T-cells (Popescu et al. 2013); relative axonal sparing with axons in various states of demyelination, and injury seen as beaded axons or end-bulbs (Trapp et al. 1998); activated astrocytes are typically hypertrophic with many fibrillary processes forming a suspensory network; oligodendrocyte injury varying from loss of oligodendroglia to the presence of remyelinating oligodendrocytes (Lucchinetti et al. 1999). The type of myelin degradation products present in macrophages can more precisely determine the stage of an active lesion: minor myelin proteins such as myelin oligodendrocyte glycoprotein are digested first followed by major myelin proteins such as proteolipid protein, which are more hydrophobic and abundant (Brück et al. 1995).

Acute multiple sclerosis lesions exhibit a high degree of variability in terms of topography, type of inflammatory process, and degree of oligodendrocyte and other cell-type destruction. Four lesion patterns, which may reflect the heterogeneity of disease mechanisms in MS, have been noticed and described (Lucchinetti et al. 2000) (Table 2.1, *Acute Active Plaques*). Type I lesions are dominated by T-cell infiltrates and



macrophage-mediated tissue destruction. Type II lesions make up the majority pattern of active lesions and are notable for antibody and complement-mediated destruction of myelin and oligodendroglia. The next largest segment, type III lesions appear as hypoxia-like injury, which may be due to inflammatory toxins. Finally, Type IV, which comprise around 1% of the lesions studied, display evidence of primary oligodendrocyte susceptibility (Popescu et al. 2013; Compston & Coles 2008). Together, patterns I and II make up nearly three quarters of MS lesions and show the typical perivenular T-cell/complement autoimmune response. While the issue is debated, there is evidence that individual MS patients present a single lesion type suggesting that these histological patterns are representative of distinct, heterogeneous pathophysiological mechanisms specific to the patient (Lucchinetti et al. 2000). Alternatively, some research indicates that these different lesions types do exist in the same patient and that the lesion types are actually stages of lesion maturation (Barnett & Prineas 2004). In any case, there is agreement in the field that great heterogeneity exists between MS lesions.

*Table 2.1 Histopathological characteristics of multiple sclerosis lesions*

	<b>Lesion</b>	<b>Histological Patterns</b>
<b>White Matter</b>	<b>Acute Active</b>	<u><i>Type I:</i></u> (15%) sharp demarcation; perivascular; equal loss of all myelin components; no complement; background of T-cells, macrophages & microglia
		<u><i>Type II:</i></u> (58%) sharp demarcation; perivascular; equal loss of all myelin components; immunoglobulin & complement on myelin; macrophages phagocytosing complement-opsonized myelin
		<u><i>Type III:</i></u> (26%) ill-defined border; oligodendrocyte apoptosis, maybe due to toxic injury of vasculature and/or mitochondria; greater loss of periaxonal myelin parts (MAG, CNPase);

		<u>Type IV</u> : (1%) non-apoptotic oligodendrocyte death.
	<i>Chronic / Slowly expanding</i>	<u>Active</u> : sharply demarcated with myelin-laden macrophages at edges
		<u>Inactive</u> : sharply demarcated; hypocellular with loss of axons, oligodendrocytes and inflammatory infiltrates
	<i>Remyelinated</i>	<u>Active</u> : present within pattern I and II active lesions
		<u>Shadow</u> : “completely” remyelinated; may blend into NAWM; more susceptible to further inflammatory attacks
<i>Gray Matter</i>	<i>Cortical</i>	<u>Subpial</u> : extend from the pial surface to cortical layers 3,4, or entire width; may involve several gyri
		<u>Intracortical</u> : small, perivascular and confined within cortex with sparing of both superficial cortex and adjacent WM
		<u>Leukocortical</u> : involve both gray and WM at the GM-WM junction with sparing of superficial cortex

Over time, most MS lesions become less inflamed and edematous, as some tissue is lost and resorbed and astrogliotic fibrillary scars fill the void. Those plaques that lose all signs of inflammatory activity are referred to as inactive in comparison to those that continue to have smoldering activity of myelin-laden macrophages at their outer rim (Popescu et al. 2013; Lassmann 2011). Lesion remyelination differs in extent and time course across patients. Remyelination can begin during the acute active lesion process and may continue indefinitely. Frequently, remyelination is seen at the edge of chronic lesions. Rarely, lesions called “shadow plaques” will have nearly complete remyelination (Goldschmidt et al. 2009). In some chronic active lesions, there is a continuous cycle of re- and demyelination. In type I and II active lesions, in which oligodendrocytes are not

the primary target, oligodendrocyte precursor cells are more likely to be present and remyelination is more common (Lucchinetti et al. 1999).

While MS is typically described as a white matter disease, recent studies have shown that MS cortical lesions are demyelinating, frequent and inflammatory (Lucchinetti et al. 2011). Pathologists have divided cortical lesions into three types based on their topography with respect to the cortical layers (described in Table 2.1, cortical lesions): subpial, intracortical and leukocortical. One of the most prominent MS cortical lesion subtypes – confluent, band-like, subpial lesions – have been seen exclusively in multiple sclerosis (Fischer et al. 2013; Lassmann 2014) and no other neuro-inflammatory or neuro-infectious disease. On examination, most acute cortical lesions contain T-cell infiltrates, and many demonstrate macrophage-associated demyelination. Additionally, cortical lesions are often situated near and may be related to meningeal inflammation (Lucchinetti et al. 2011).

### **2.2.5 Pathology of Progressive MS**

On pathology, PPMS displays all the typical features of MS including inflammation, demyelinating plaques and reactive astrocytic scarring. But, instead of new, focal white matter plaques, PPMS is characterized by microglial activation, diffuse white matter axonal injury, and cortical demyelination and neurodegeneration (Rovaris et al. 2005; Filippi et al. 2003; Narayana et al. 2004; Kutzelnigg et al. 2005; Lucchinetti & Brück 2004). In RRMS, remyelination, or attempted remyelination, and axonal functional compensation are key features of inflammatory lesions. In the progressive phase of the disease, in both SPMS and PPMS, functional compensation has been exhausted, there is lack of trophic support, and oxidative stress begins to take its toll on mitochondria leading to widespread, gradual neurodegeneration (Lassmann et al. 2012). Chronically

demyelinated axons degenerate due to lack of myelin-derived trophic support and overwhelmed energy supplies (Bjartmar et al. 2003). Interestingly, the BBB is relatively closed in PPMS so that the inflammation that is present may be unreachable by most disease modifying therapies (Kutzelnigg & Lassmann 2014).

## **2.3 *Neuro-axonal degeneration***

Due to their tremendous length, axons face many challenges and stresses that are not encountered by any other cell-type, or even the neuronal soma. Some of the challenges associated with extreme length and, necessarily, large volume are long distance antero- and retrograde transport, great metabolic demands, signaling between distant organelles, greater risk for mechanical damage, and affiliations with glia for myelin and neurotrophic support (Coleman 2013). Until recently, it was assumed that the process of axon degeneration occurred haphazardly due to disrupted metabolic communications from the soma after death of the neuronal soma or following axon transection. Recent research has demonstrated that axonal degeneration is a programmed autonomous destruction process distinct from neuronal cell body apoptosis and necrosis (Yan et al. 2010). Axonal degeneration is prominent in MS and weighs heavily in the progression of clinical disability. Still, the etiology of axonal degeneration in MS is incompletely understood and is likely multifaceted (Nave 2010).

### **2.3.1 Programmed axonal degeneration**

The progression of phases of Wallerian degeneration following axonal transection is ordered. Within hours of injury, even as electrical signals are still being propagated in the distal axon, transportation slows and organelles accumulate adjacent to the lesion site, causing the axon to swell and stretch the myelin sheath. Within 12-24 hours, the microtubule system becomes disorganized. By 48 hours, calcium begins to enter the

axon, thereby activating a calpain-mediated destruction of neurofilaments. With the organelles dissolving and the axonal cytoskeleton collapsing, granular disintegration of the axon occurs within the largely intact myelin sheath. Around this time, the myelin begins to degrade, and macrophages are recruited to phagocytose the debris. At this point in the peripheral nervous system, Schwann cells step in to help the neuronal regenerative sprouts find their target, but CNS oligodendrocytes are not able to create a regenerative microenvironment (Carroll 2009).

Strong evidence for a controlled program of Wallerian degeneration has come from work done with the spontaneous mutant Wallerian Degeneration slow mice (*Wld<sup>s</sup>*). In these mice, axons remain viable for transmitting action potentials for up to 3 weeks after transection or toxic injury (Carroll 2009). Possible mechanisms by which *Wld<sup>s</sup>* prevents axonal dysfunction and Wallerian degeneration include: 1) altering the mitochondria fusion/fission equilibrium; 2) blocking mitochondrial depolarization and the cascade of ROS, ATP depletions and eventual cell death; and 3) preventing tagging of small, depolarized mitochondria for mitophagy (Burke & O'Malley 2013). Importantly, *Wld<sup>s</sup>* has been shown to prevent axonal degeneration in a number of animal models of disease, such as Parkinson's disease.

Dying-back axonopathy – degeneration that progresses in a retrograde fashion from axon terminals – is also under review. For instance, it has been shown that loss of the elongation factor EF1A2 instigates dying-axonopathy in lower motor neurons while inhibiting Wallerian degeneration (L. M. Murray et al. 2008). The concept of "dysferopathies" – diseases in which alterations in axonal transmission represents a critical component in pathogenesis, usually due to dying-back axonal degeneration – has been put forth to provide a framework to study axonal degeneration in diseases such as Parkinson's (PD), Alzheimer's (AD) and Huntington's (HD) (Morfini et al. 2009).

Pathophysiological studies of the autosomal dominant genetic forms of PD (alpha-synuclein, LRRK2) demonstrate the predominate site of pathology at onset to be in axons (Burke & O'Malley 2013). In AD, abnormalities in fast axonal transport lead to synaptic dysfunction and problems with axonal connectivity. When a threshold of dysfunction is reached, dying-back axonal degeneration occurs (Kanaan et al. 2013). In HD, dysfunction in axonal transport (due to misfolded huntingtin protein blocking microtubules) leads to synaptic dysfunction and eventual dying-back axonopathy (Li & Conforti 2013). In a viral animal model of MS, Theiler's murine encephalomyelitis virus, impaired neurofilament transport initiated axonopathy leads to an axonal self-destruction process (Kreutzer et al. 2012).

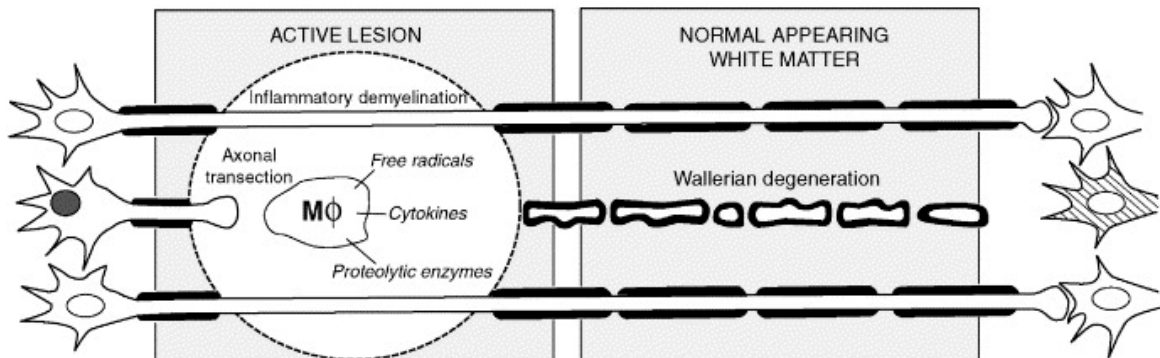


Figure 2.1. Axonal injury related to an inflammatory demyelinating lesion in MS. Reprinted from "Axonal loss in the pathology of MS: consequences for understanding the progressive phase of the disease" by C. Bjartmar et al., 2003, *Journal of Neurological Sciences*, 206, page 166.

Copyright 2003 by Elsevier. Reprinted with permission.

### **2.3.2 Axonal degeneration in MS**

Neuro-axonal degeneration is a major contributor to clinical disability in MS (Miller & Leary 2007; Bjartmar et al. 2000; Hauser & Oksenberg 2006; Trapp et al. 1998; Tallantyre et al. 2010; Tallantyre et al. 2009; Stadelmann et al. 2011; Trapp & Nave 2008; Dutta & Trapp 2011). Inflammation and demyelination have been established as the triggers of acute and usually reversible relapses in the early phase, but it is now accepted that neuro-axonal pathology is an important player in the progressive disability associated with chronic MS. Ferguson et al. (Ferguson et al. 1997) demonstrated, using amyloid precursor protein (APP) accumulation as a marker of early axonal damage, that areas of acute inflammation and demyelination in MS lesions are associated with greater axonal damage. While studies of axonal degeneration in EAE have shown that some axons exhibiting signs of focal degeneration can recover (Nikić et al. 2011), axonal loss occurs focally within MS lesions during de- and remyelination (Trapp & Nave 2008; Trapp et al. 1998; Bitsch et al. 2000) as well as more diffusely in normal appearing white matter (NAWM) (Figure 2.1) (Miller & Leary 2007; Dutta et al. 2006; Kutzelnigg et al. 2005).

Axonopathy in chronic lesions could result from loss of trophic support from myelin and oligodendrocytes (Rovaris et al. 2005; Nave 2010; Filippi et al. 2003; Narayana et al. 2004; Lucchinetti & Brück 2004; Kutzelnigg et al. 2005), from vulnerability to the inflammatory milieu (Kutzelnigg et al. 2005; Trapp & Nave 2008) or from a specific immunological attack on axons (Kutzelnigg et al. 2005; Trapp & Stys 2009; Leech et al. 2007). Diffuse axonal loss could be due to Wallerian degeneration and dying-back axonopathy originating from axonal transection in lesions (Dziedzic et al. 2010; Seewann et al. 2009) or an underlying primary axonopathy independent of inflammatory demyelination (DeLuca et al. 2006; De Stefano et al. 2002).

Axonal degeneration in progressive MS may be due, in large part, to a metabolic mismatch in chronically demyelinated axons – an imbalance between increased energy demands and limited supply (Trapp & Nave 2008). Without adequate myelination, axons require more voltage-gated  $\text{Na}^+$  channels to be equally spaced along the length of the axon, instead of being concentrated at nodes of Ranvier. The resultant increase in  $\text{Na}^+$  influx during axolemma repolarization must be countered by augmented activity of the  $\text{Na}^+/\text{K}^+$  ATPase. Mitochondria in these axons may be decreased in number or may function suboptimally due to oxidative damage and reduced respiratory chain complex activity (Mahad et al. 2009; Campbell & Mahad 2011; Dutta et al. 2006). If ATP production in the axon cannot keep up with demand, the intracellular  $\text{Na}^+$  concentration increases and the  $\text{Na}^+/\text{Ca}^{2+}$  antiporter begins to bring  $\text{Ca}^{2+}$  into the axon in exchange for  $\text{Na}^+$ .  $\text{Ca}^{2+}$  accumulation is associated with a number of deleterious effects in the axon and eventual entry into a cell death pathway.

Disorganized axoskeleton and problems with axonal transport could also contribute to axonal degeneration in chronic MS. Axonal neurofilament stoichiometry and phosphorylation state are highly regulated to direct axonal transport and maintain structural integrity. At the same time, certain stoichiometry and phosphorylation environments are related to various neurodegenerative processes (Kim et al. 2011). In MS samples, unusual patterns of neurofilament phosphorylation and packing compared to normal tissue suggest a less organized axoskeleton and/or problems with axonal transport (Petzold et al. 2008). These alterations have been detected in vivo in normal appearing white matter suggesting that these changes may precede lesion formation or be associated with extra-lesional axonopathy (Petzold et al. 2011).



### **2.3.3 Axonal degeneration in animal models of MS**

Experimental autoimmune encephalomyelitis (EAE) and cuprizone-mediated demyelination are animal models of MS that emphasize, respectively, the inflammatory and demyelinating aspects of MS. Recently, these models have been extended beyond the acute phase of the disease to encompass some chronic aspects of MS. EAE in rodents and marmosets is induced by injecting white matter antigens with inflammatory adjuvants, causing widespread demyelination and motor performance decline ('t Hart et al. 2011). Hampton et al. utilized auto-immune tolerization in mice with EAE to arrest clinical relapses at early (29 days after EAE induction) and late (58 days) time points (Hampton et al. 2013). They then examined histological indicators of inflammation, myelination, and neurodegeneration very late in the disease (105 days after EAE induction) in these animals in comparison to matched non-tolerized EAE controls. They found that inflammation and axonal/neurodegeneration became uncoupled in this model; while the CD4 driven, myelin-targeted immune response was suppressed and remyelination was promoted with tolerization, neuro-/axonopathy progressed. Of note, in this model, where tolerization is likened to the use of disease modifying therapies (DMTs) in MS, early tolerization was more protective than late. Additionally, there was no change in the number of chronically activated microglia with either early or late tolerization.

Cuprizone is a copper-chelating agent that induces relatively non-inflammatory demyelination and decreased locomotor performance in rodents when it is administered chronically in the diet for 5-6 weeks (Benetti et al. 2010; Schmidt et al. 2012). If cuprizone is discontinued after 5-6 weeks, animals will remyelinate and regain much of their function in the short-term. Manrique-Hoyos et al. set out to examine the long-term effects of cuprizone demyelination after cessation of drug administration (Manrique-

Hoyos et al. 2012). For this, they induced 1 or 2 rounds of cuprizone demyelination in rodents and examined motor ability and CNS histology up to 28 weeks after cuprizone removal from the diet. They found that motor function recovered with remyelination up to 20 weeks after demyelination and then declined approximately 6 months after demyelination. In conjunction with these late-onset deficits, histological analysis revealed axonal loss in the face of extensive remyelination. These animal models mimic some of the aspects of chronic progressive MS: relapsing, remitting course of demyelination with motor deficits; and late neuro-axonal loss despite terminating demyelinating events and allowing remyelination.

## **2.4 Conclusions**

Multiple sclerosis is a complicated, heterogeneous disease about which we have learned a great deal but understand little. While disease modifying therapies have started to make real impacts on the inflammatory aspects of the disease, so far, they have not been shown to stop the progression of permanent neurological disability (Dutta & Trapp 2011). In chronic lesions and progressive MS, the process of axonal degeneration is slow and steady. There is mounting evidence that, in order to prevent or slow irreversible neuronal and axonal loss in MS, research efforts will have to focus on regenerative and neuroprotective strategies (Franklin et al. 2012). However, currently there are no specific measures of neurodegeneration or neuroaxonal metabolism with which to study such strategies in vivo. The next chapter will discuss the use of nuclear magnetic resonance techniques to measure and study multiple sclerosis.

### 3 MS & NUCLEAR MAGNETIC RESONANCE

As discussed in chapter 2, multiple sclerosis is an ancient disease that has been described by physicians and neuropathologists since the mid nineteenth-century. Yet, it is only recently, in the last 30 years, that disease-modifying therapies have been developed. In this same time period, one technological achievement has hugely advanced our understanding of MS in vivo – magnetic resonance imaging (T. J. Murray 2009). In 1981, Ian Young published the first study of nuclear magnetic resonance scans in MS (Young et al. 1981). For the first time it was possible to visualize disease activity in the living brain. Ten patients with MS were compared to 10 healthy controls by x-ray computed tomography (CT) and NMR  $T_1$ -weighted inversion recovery scans (Figure 3.1). While none of the healthy controls demonstrated any abnormalities on CT or MRI, all 10 of the MS patients had focal hypointensities on MRI scans that were consistent with the distribution of lesions usually seen at necropsy. Finally, the observed hypointensity within lesions was interpreted as increased relaxation time due to loss of lipids within plaques.

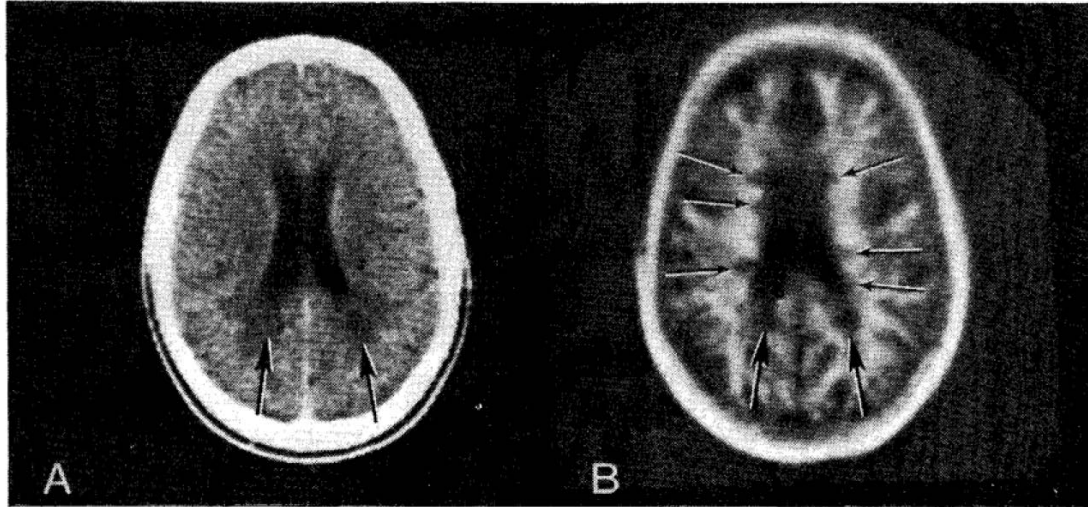


**Fig. 1—Comparable CT (A) and NMR (B) scans in patient 10 at mid-ventricular level.**

The two posterior periventricular lesions seen on the CT scan are also seen on the NMR scan (large arrows). In addition 6 smaller lesions are seen on the NMR scan at the lateral margin of the lateral ventricles (small arrows). The sharply defined area on the medial margin of the left posterior horn is a circular artefact.

*Figure 3.1. First published MR images of multiple sclerosis.* Reprinted from “Nuclear Magnetic Resonance Imaging of the Brain in Multiple Sclerosis” by I.R. Young et al., 1981, *The Lancet*, 318(8255), page 1064. Copyright 1981 by Elsevier. Reprinted with permission.

Since these first MR images of MS brains were published, the field of MRI devoted to MS has exploded. The ability to visualize the disease in vivo allows the study of the disease process over time. T<sub>1</sub>- and T<sub>2</sub>-weighted image contrasts have been optimized and analyzed in hundreds of ways. The use of contrast enhancement as a marker of blood brain barrier breakdown and inflammation has become a clinical mainstay. The effort to derive quantifiable measures of disease burden and progression in MS has generated an unquantifiable mass of research devoted to understanding nuclear magnetic resonance alterations in MS, including magnetization transfer imaging, diffusion tensor imaging, T<sub>2</sub> and T<sub>2</sub>\* decay curve analysis and magnetic resonance spectroscopy. Importantly, some of these methods have been cleverly used to further our understanding of the pathophysiology of lesions and normal appearing brain tissue. Physicians heavily rely on MRI to make the diagnosis of MS, and some techniques have

become important outcomes in various phases of drug trials.

Using these radiological techniques in collaboration with neurologists, pathologists and immunologists, students of multiple sclerosis have come to understand that inflammation and neurodegeneration are connected in MS and are heterogeneous processes that can differ between people, tissues, and disease phases. There is discussion of a “clinico-radiological paradox” in multiple sclerosis due to the seeming disconnect between clinical progression and radiological findings in the disease: many CNS lesions cannot be associated with a clinical relapse, and for many patients the progressive phase of the disease is unrelated to lesional activity (McFarland 2010). This seeming “paradox” most likely highlights the need for investigators to dig deeper into the pathophysiological mechanisms of multiple sclerosis. With greater understanding of the disease process, many of the quantifiable, yet paradoxical, results we have encountered may fit into the big picture of MS.

Cortical lesions have emerged as a dominating issue in the field of MS. The expanding research on cortical lesions suggests that gray matter (GM) pathology may play a central role in disease pathogenesis and that it almost certainly contributes to disability and disease progression in MS. A full discussion of cortical lesions is beyond the scope of this dissertation and is complementary to understanding measurement of neurodegeneration in white matter (WM). We can be certain that a fuller understanding of cortical and meningeal pathology will be important for interpreting the range and heterogeneity of pathology seen in multiple sclerosis. For example, based on histological comparisons, it is estimated that we are missing as much as 72% of cortical lesions in MS with our best dedicated MR imaging techniques (Seewann et al. 2012; Geurts et al. 2005; Sethi et al. 2013). Interestingly, cortical thinning has one of the strongest correlations with disability and disease progression as any quantitative brain measure

established (Fisher et al. 2008).

### **3.1 *What can NMR tell us about MS?***

#### **3.1.1 A brief and hand-wavy (non-mathematical) introduction to nuclear magnetic resonance imaging principles**

“The water is the only place I can completely relax.”

- Aquaman

Before we can discuss the various NMR techniques that have been applied to multiple sclerosis, we should define some terms and concepts. Nuclear magnetic resonance imaging (MRI; the N was dropped partly to signal that MRI does not use ionizing radiation and mostly because “Nuclear” scares people) takes advantage of the inherent properties and behavior of atomic nuclei in external magnetic fields. As hydrogen atoms are an important part of water molecules, and as hydrogen is one of the most abundant atoms in living organisms, most nuclear magnetic resonance imaging has focused on hydrogen nuclei, also known as protons. Therefore, “proton” and “nucleus” will be used interchangeably here.

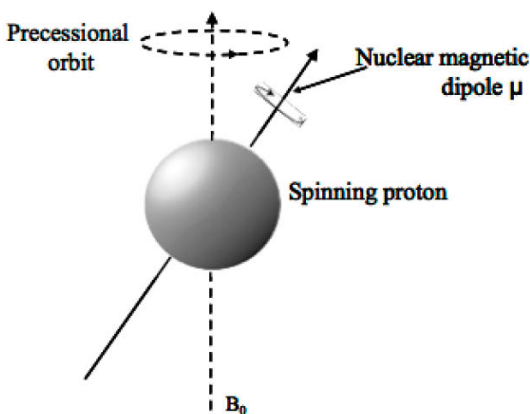


Figure 3.2. Spin and precession of a proton in an external magnetic field ( $B_0$ ). The solid arrow represents the magnetic moment or pole around which the proton spins (movement shown as a light gray spin circle). The dotted-line straight arrow represents the direction of  $B_0$  around which the nuclear magnetic moment precesses (movement shown as dotted-line spin circle) Reprinted from *Basic Concepts in NMR Spectroscopy* (page 4) by K.V.R Chary et al., 2008, Dordrecht, The Netherlands: Springer. Copyright 2008 by Springer. Reprinted with permission.

All nuclei are spinning and precessing (Figure 3.2). Nuclei precess at a rate proportional to the strength of the applied external magnetic field ( $B_0$ ). This rate proportionality is known for most nuclei and is called the gyromagnetic ratio – protons precess at a rate of  $267.513 \times 10^6$  radians per second per tesla. In an external magnetic field, the axes of spinning protons will self-orient to be either parallel or anti-parallel to the magnetic field. The parallel spins are in a lower energy state than the anti-parallel spins and the magnitude of the energy difference between the two states is proportional to the strength of the magnetic field. Due to this energy differences, there will be slightly more spins oriented parallel to the magnetic gradient resulting in a “net” magnetic moment that we can measure. (In Figure 3.3, the external magnetic field is oriented along Z. In Figure 3.3.A, the net magnetic moment vector is in its equilibrium position). If

a certain amount of radiofrequency energy is added at the rate of the gyromagnetic ratio to a system of protons spinning in an external magnetic field, those spins are excited to flip (or nutate) away from the longitudinal equilibrium (In Figure 3.3.B,  $H_1$  represents the applied radiofrequency pulse and the net magnetic moment vector is shown to be tipping away from the Z axis) and will precess in phase coherence (pointing the same direction at the same time) on a plane transverse to the longitudinal axis (Figure 3.3.C). Once the radiofrequency pulse is stopped, the precessing nuclei will begin relaxing back toward their longitudinal equilibrium position and the spins will lose phase coherence (Figure 3.3.D illustrates the loss of phase coherence as individual spins precessing at slightly different frequencies will spread out according to the rotating frame of reference).

Each of the spinning protons is also a tiny magnet or magnetic dipole. Just as any moving magnet can induce current in a loop of wire, the transverse component of these spinning protons can induce a sinusoidal current in nearby receiving coils of wire. We refer to this induced current as “signal.” Therefore, during the process of excitation and relaxation described earlier, we can measure the signal from the protons in the

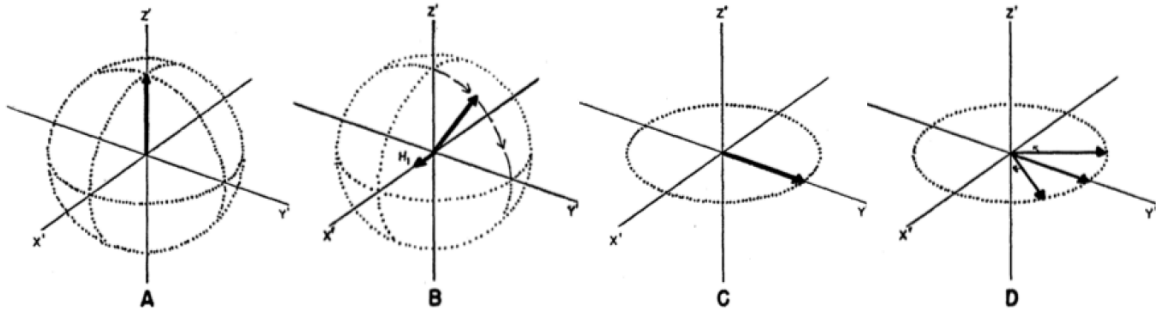


Figure 3.3 Nutation of a spin net magnetic moment vector (bold arrow) onto the transverse (XY) plane with application of radiofrequency field  $H_1$ . Adapted from Carr & Purcell, *Physical Review* 94:3, 1954, Figure 3. A,B,C,D. Adapted from “Effects of Diffusion on Free Precession in Nuclear Magnetic Resonance Experiments” by H.Y. Carr and E.M. Purcell, 1954, *Physical Review*, 94(3), page 632. Copyright 1954 by American Physical Society. Adapted with permission.



system we are studying. The detected signal is called the “free-induction decay” (FID) and is measured as a function of time. With magnetic field gradients, we can spatially vary the magnetic field experienced by protons so that the received signal comes with location information. Finally, a mathematical concept called the “Fourier transform” allows us to easily transform signals between the time or spatial domain and the frequency domain. Used together, these principles make it possible to “see” tissues inside the human body without a single scalpel.

In radiological research, we seek imaging techniques that can show us the location of and relationship between certain molecules and/or tissues in the body. Toward this aim, in nuclear magnetic resonance, we exploit the properties and behaviors of nuclei to find those features that differ between tissue types and disease states, thereby creating contrast. If we can highlight the contrast between adjacent tissues, we will be able to “see” those tissues as separate. As opposed to other medical imaging techniques that rely on a single property, NMR can utilize many different parameters to obtain contrast, including: proton density, relaxation times ( $T_1$ ,  $T_2$  and  $T_2^*$ ), chemical shift, magnetic susceptibility, flow, diffusion, perfusion, and magnetization transfer (MT) (Chary & Govil 2008). Of these,  $T_1$  and  $T_2$  relaxation times have formed the basis of clinical imaging and have played a major role in diagnosis and monitoring of MS. Among other experimental techniques, magnetization transfer,  $T_2^*$  relaxation, and susceptibility-weighted imaging have provided great insight into disease mechanisms in MS and will be discussed briefly. Chemical shift or magnetic resonance spectroscopy and diffusion weighted imaging have also been used with success to study MS and are the basis for diffusion weighted spectroscopy.

### 3.1.2 T<sub>1</sub>-weighted imaging

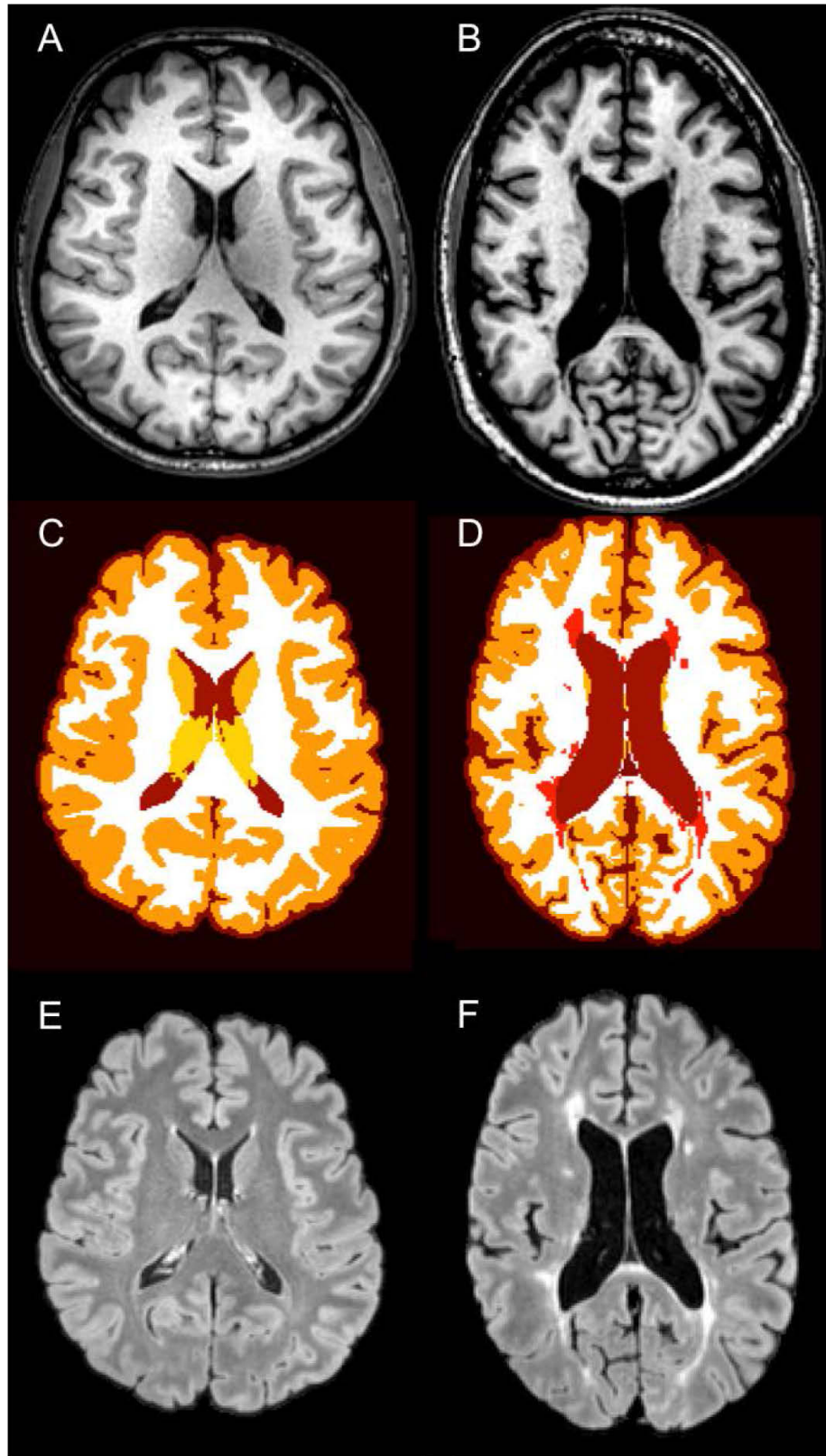
As mentioned above, in an external magnetic field, the low energy or equilibrium state for protons is to be aligned with the field. If we add energy to tip the spins away from this longitudinal equilibrium, as soon as we stop adding energy the spins will begin to relax back toward the equilibrium state. This happens because the protons share or exchange energy with the surrounding molecular lattice until equilibrium is reached. Therefore this process is referred to as “spin-lattice” or “longitudinal relaxation” and is described by the T<sub>1</sub> relaxation time constant. After being tipped onto a transverse plane 90 degrees from the equilibrium state, the spins will recover 63% of their equilibrium value in one time constant T<sub>1</sub>. As we can only measure signal from spins that have a transverse component, the measureable signal will decrease due to T<sub>1</sub> relaxation.

The T<sub>1</sub> relaxation time is useful because different tissues have different lattice environments, which have different T<sub>1</sub> relaxation times. We can take advantage of this by collecting the NMR signal at a time that maximizes the difference in the relaxation state between the tissues of interest. Tissues with shorter T<sub>1</sub> time constants appear brighter on T<sub>1</sub>-weighted images. For neuroimaging, T<sub>1</sub>-weighted sequences have been developed to maximize the contrast between gray matter, white matter, and cerebrospinal fluid (CSF) for optimal assessment of brain anatomy. In these images, tissues rich in lipids, such as myelin-containing white matter, are bright while watery CSF is dark and gray matter is somewhere in-between (Figure 3.4, A & B).

In the very first MR images of MS brains, it was noted that lesions were darker or hypointense when compared to the surrounding white matter in T<sub>1</sub>-weighted images (Figure 3.1). Lesions of this type are sometimes called “black holes” by researchers and clinicians. Histopathological studies in conjunction with post-mortem MRI have demonstrated severe tissue destruction in T<sub>1</sub>-hypointense lesions. In particular, all T<sub>1</sub>-

hypointense lesions were seen to have less myelin, decreased cellularity and reactive astrocytes. Furthermore, the degree of hypointensity was correlated with greater loss of axons and higher disability (van Walderveen et al. 1998; van Waesberghe et al. 1999). Research into the persistence of black hole lesions suggests that those lesions with greater duration of initial contrast enhancement (2 months) are more likely to persist as black holes (30% persisted at least 4 years) and may have more tissue damage (Bagnato et al. 2003). Interestingly, overall measurements of  $T_1$  hypointensities have not been shown to be either very sensitive or specific measures of tissue destruction in MS.

*Figure 3.4. (next page) Axial MRI slices of a healthy subject (A, C & E) and a multiple sclerosis patient (B, D & F). (A & B)  $T_1$ -weighted magnetization prepared rapid gradient echo images (MPRAGE). (C & D) Tissue segmentation maps from the TOADS algorithm – white = white matter, orange = cortical gray matter, maroon = CSF, red = lesion, light orange & yellow = deep gray matter structures. (E & F)  $T_2$ -weighted fluid attenuated inversion recovery (FLAIR) images.*



Major advances in MRI pulse sequence development have rapidly improved  $T_1$ -weighted image acquisition time and quality over the last two decades. The first clinical MR  $T_1$ -weighted images were acquired with spin-echo sequences, which are characterized by a 180-degree refocusing radiofrequency pulse. In classic spin echo experiments, images must be acquired one slice at a time (2D), and scan times are long due to the direct dependence on sequence repetition time (TR). Alternatively, gradient echo sequences can have variable flip angles (smaller than 90 degrees) without refocusing pulses. Gradient echo sequences allow for shorter repetition times, 3D acquisitions and less radiofrequency energy deposition.  $T_1$ -weighted magnetization prepared rapid gradient echo (MPRAGE) is a largely  $T_1$ -weighted 3D sequence that allows the acquisition of 3D data sets in a reasonable time frame (e.g. whole brain, 1 mm x 1 mm x 1 mm resolution in 5 minutes), while providing excellent GM-WM contrast (Mugler & Brookeman 1990). 3D acquisition affords fast high-resolution isotropic imaging (equal resolution for all 3 dimensions) with easy multiplanar reformatting – viewing of axial, sagittal, and coronal orientations.

With the improvements in pulse sequence and high field strengths (3T and 7T), gradient echo  $T_1$ -weighted images can now be used to detect many lesions in MS (Sinnecker, Mittelstaedt, et al. 2012b; Wetzel et al. 2002). In particular, a study that compared MPRAGE, T2-weighted FLASH, and double inversion recovery (DIR; designed to study lesions in gray matter) sequences at 7T demonstrated that every lesion found with the T2 and DIR sequences was visible on the MPRAGE images (Sinnecker, Mittelstaedt, et al. 2012b). Therefore, MPRAGE images are very sensitive to tissue changes associated with MS lesions. At the same time, studies such as this one call into question the specificity of  $T_1$ -weighted lesions and black holes for a particular pathology such as axon degeneration. The fast progression of  $T_1$ -weighted imaging

highlights the need for all MRI findings to be evaluated in the context of the strengths and weaknesses of the technique being utilized.

### **3.1.3 T<sub>2</sub>-weighted/FLAIR imaging**

When protons are tipped away from the axis parallel to the external magnetic field using radiofrequency energy pulses, the spins will also align in the transverse plane and begin to precess in phase. The fact that the nuclei are spinning in phase is what makes it possible to get a measureable signal induced in nearby receiver coils. As soon as the radiofrequency pulse is turned off, each spin takes up a very slightly different precession rate due to the influence of nearby spins. Due to these slightly different precession rates, the spins dephase and the measureable signal declines. This effect is called “spin-spin” or “transverse relaxation” and is described by the T<sub>2</sub> time constant. While longitudinal and transverse relaxation are occurring simultaneously, the interacting forces causing these phenomena are separate and can be teased apart with the use of clever radiofrequency and gradient pulse sequences.

Just as we saw with T<sub>1</sub>-relaxation, the dephasing behavior of nuclei is useful because the T<sub>2</sub> time constant differs between different tissues. On T<sub>2</sub>-weighted images, tissues with more water are more intense – making cerebrospinal fluid by far the brightest compartment – and fatty, hydrophobic white matter is dark on brain scans. In this imaging contrast, MS white matter lesions are easily visible as ovoid hyperintensities on a dark white matter background (Miller et al. 1998). While MS lesions are found throughout the white matter, they have a predilection for periventricular white matter and juxta- or subcortical locations. Lesions in these non-deep white matter locations are more specific for MS. On conventional T<sub>2</sub>-weighted images, it can be difficult to assess bright lesions next to bright CSF compartments. For this reason, FLuid Attenuated

Inversion Recovery (FLAIR) scans have become the preferred clinical sequence for assessing lesion load. FLAIR sequences utilize an inversion pulse that is timed to minimize or null the signal from CSF at the time of signal acquisition (long inversion time) (Figure 3.4.E). It was found that  $T_2$ -weighted FLAIR images increase lesion detection, lesion conspicuity and lesion contrast with CSF compartments compared to conventional  $T_2$ -weighted spin echo images (Rydberg et al. 1994; De Coene et al. 1992).

To date, neither  $T_2$ -lesions nor and contrast-enhancing lesions (CEs) have demonstrated a predictive value for future disability in MS, hence the “clinic-radiological paradox” mentioned previously (McFarland et al. 2002). There are probably multiple reasons for this discrepancy, which explain the paradox. First, and maybe foremost, the actual locations of lesions matters – as all neurologists know, location is everything. Therefore, it is not surprising that more  $T_2$  lesions in the motor and associated tracts is predictive of shorter time to need of bilateral support (Bodini et al. 2011). Secondly, MS lesions are extremely heterogeneous in terms of pathology, extent, amount of inflammation, tissue destruction, etc. So, any measure that lumps all lesions together, such as number of CEs or total amount of lesioned tissue on  $T_2$ , will be losing important information (McFarland 2010).

#### **3.1.4 Tissue segmentation and brain atrophy**

$T_1$ -weighted imaging is a fundamental contrast for automatic tissue segmentation methods. Indeed,  $T_1$ -weighted images demonstrate a robust and substantial contrast between white matter and gray matter, making them ideal for intensity-based tissue classification. Additionally, these images can be acquired at relatively high isotropic resolution with minimal anatomical distortion in reasonable acquisition times – around 5 minutes.  $T_1$ -weighted images are used in a variety of automatic segmentation

techniques, which have been applied to cross-sectional and longitudinal studies of multiple sclerosis brains, including Structural Image Evaluation, using Normalization, of Atrophy (SIENA and SIENAX) (Smith et al. 2002; Smith et al. 2001), Statistical Parametric Mapping (SPM) (Ashburner & Friston 1997; Ashburner & Friston 2000; Ashburner & Friston 2005; Chard et al. 2002), the integrated modeling approach of Fischl et al. (Fischl et al. 2002; Fischl et al. 2004), Subtraction-Based Logistic Inference for Modeling and Estimation (SuBLIME) (Sweeney, Shinohara, Shea, et al. 2013a), and Automated Statistical Inference for Segmentation (OASIS) (Sweeney, Shinohara, Shiee, et al. 2013b). TOpology- preserving Anatomical Segmentation (TOADS) and Lesion-TOADS (Shiee et al. 2010; Ozturk et al. 2010; Shiee et al. 2012; Bazin & Pham 2008) were developed at the Johns Hopkins University. Lesion-TOADS utilizes multichannel image information, preferably  $T_1$ -weighted and  $T_2$ -weighted/FLAIR images, in combination with topological and statistical atlases to create brain segmentations with separate classifications for major brain structures (e.g. thalamus, caudate, cortical gray matter, etc.) and white matter lesions (Figure 3.5, C & D). Importantly, Lesion-TOADS creates robust, topologically constrained segmentations that are suitable for simultaneous measurement of lesion volume, cortical and sub-cortical atrophy, and cortical thickness.

Brain atrophy is a terminal measure of neurodegeneration and has been proposed as a surrogate disease marker for use as an outcome in clinical trials in MS (Jones et al. 2013; Barkhof et al. 2009; Borges et al. 2013). While most healthy people the general population are slowly losing brain volume from their early 20's onward at a rate of 0.1-0.4% per annum (Enzinger et al. 2005; N. C. Fox et al. 1999), the rate of loss is greater in patients with MS compared to age-matched healthy controls – around 0.5% per annum (Klawiter 2013; De Stefano et al. 2010; Fisher et al. 2008). Even in patients



with relatively low disability, brain atrophy can be quite profound (Simon et al. 1999). While MS is traditionally considered to be a WM disease, GM atrophy is present and may be a better indicator of disability (Shiee et al. 2012; Rudick et al. 2009; Fisniku et al. 2008; Fisher et al. 2008).

### **3.1.5 Contrast enhancing lesions (CELs)**

In MRI, exogenous solutions with advantageous relaxation parameters can be introduced into the body to create greater contrast for tissues or processes of interest. Solutions containing paramagnetic ions with unpaired electrons such as gadolinium ( $Gd^{3+}$ ) act as potent MRI contrast agents since they decrease the  $T_1$  and  $T_2$  relaxation times of nearby water protons. For example, tissues associated with local deposits of gadolinium ions appear hyperintense on  $T_1$ -weighted images due to the  $T_1$  shortening effect. Importantly, gadolinium-based contrast agents (where gadolinium is chelated) are relatively safe in patients with adequate renal function. When injected intravenously, gadolinium-chelates will circulate throughout the cardiovascular system and are unable to pass an intact blood brain barrier (BBB). Therefore, MRI of a healthy brain after gadolinium injection will demonstrate contrast enhancement of vessels, but not of parenchyma. In the case of BBB opening or breakdown, especially due to an inflammatory process, gadolinium-based contrast will leak out of the blood vessel at the site of opening, along with other large molecules that are normally restricted from passing the BBB. As a consequence, the tissue where leakage occurs will appear very bright, especially when compared to non-contrast enhanced  $T_1$ -weighted images (Figure 3.5).

In multiple sclerosis, gadolinium-based contrast agents are used to detect acute inflammatory activity (McFarland 2010). Early in the application of MRI to MS, it was discovered that contrast enhancement was a precursor or early sign of lesion formation (Harris et al. 1991; Miller et al. 1988). At that point, the MS community was largely

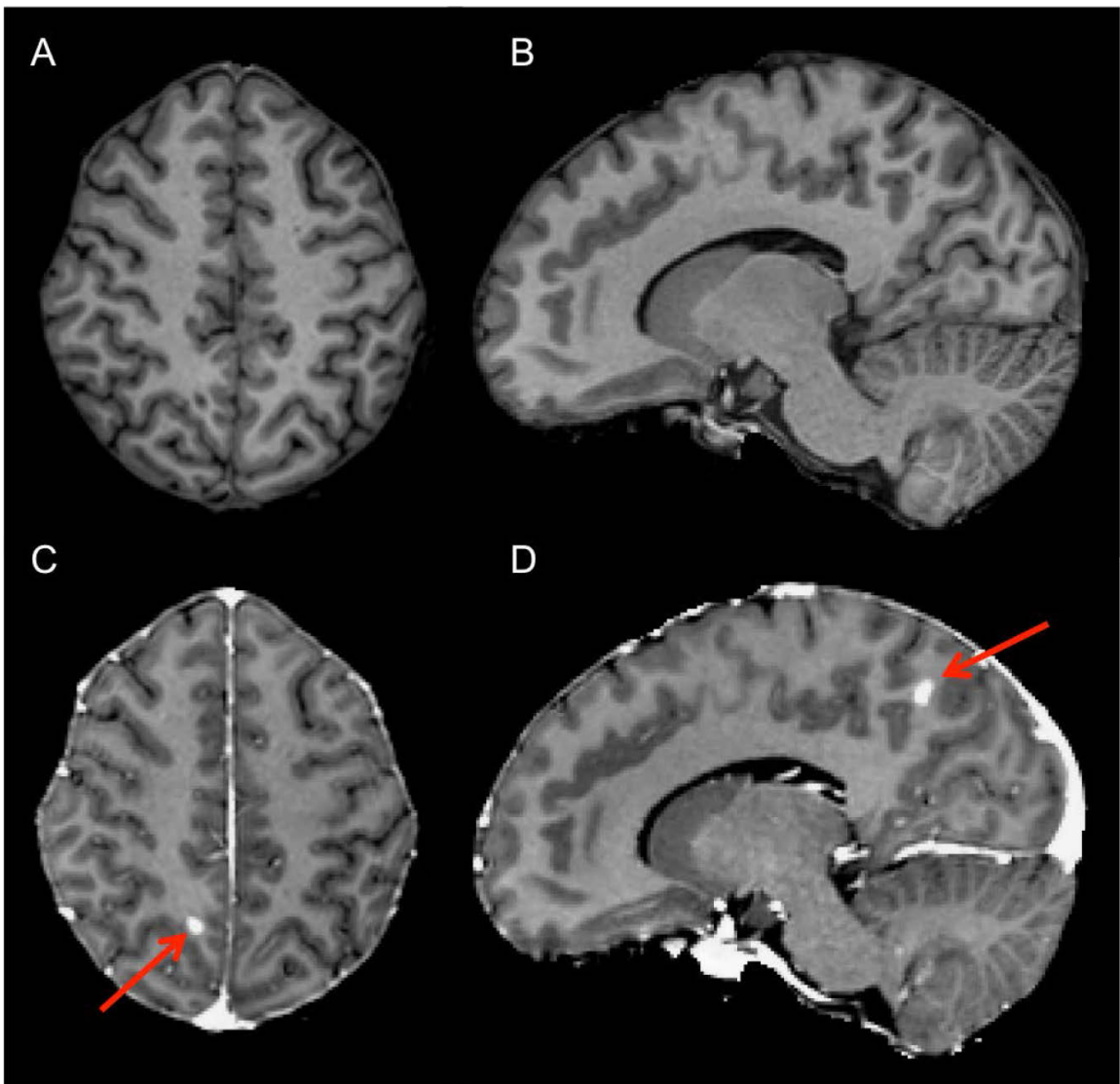


*Figure 3.5. Skull-stripped T1-weighted images before (A & B) and after (C & D) injection of gadolinium contrast agent. 28-year-old female patient with multiple sclerosis. Contrast enhancing lesion (red arrows). Axial (A & C) and sagittal (B & D) images.*

undecided on the issue of whether inflammation is a cause of or response to neurodegeneration in MS. The jury is still out on the precise relationship between inflammation and neurodegeneration in all tissues during all stages of MS. Nonetheless, some key studies of CELs in white matter led to the understanding that inflammation is an important step in white matter lesion formation. In 1993, the McFarland lab at the National Institutes of Health was able to study the brain at autopsy of a patient with chronic progressive MS, who experienced acute neurological worsening leading to death (Katz et al. 1993). In the weeks before death, this patient underwent MR imaging with gadolinium contrast injection, and Katz et al. were able to identify acute lesions on histopathology that corresponded with the areas of contrast enhancement on MRI. Lending specificity to the finding, lesions identified as chronic by histopathology were seen on T<sub>2</sub>-weighted images but did not demonstrate contrast enhancement. Since the early days of CEL research, it has become generally accepted that most, if not all, white matter lesions originate with inflammatory activity, and this activity is visible with contrast enhancement for 1-2 months (Miller et al. 1998).

The use of CELs, or any MRI measure, as a surrogate biomarker in MS is under investigation. Petkau et al. used a meta-analysis-type approach to create a multi-phase study of the concurrent and predictive relationship between CELs and MS relapse rate (Petkau et al. 2008). This study did not proceed beyond the feasibility phase because, given the relatively short time span investigated (6-months) and the small number of subjects in their dataset, they were unable to demonstrate strong enough correlations between CELs and MS relapses. More recently, in a meta-analysis of randomized treatment trials, Sormani et al. have shown that treatment effects on MRI lesions can reliably predict treatment effects on relapses (Sormani & Bruzzi 2013). And, the effects of treatment on CELs and on brain atrophy are independently predictive of the treatment

effect on disability progression (Sormani et al. 2014). These studies suggest that CELs should be considered as primary endpoints in some clinical trials of treatments in MS.

It has been established that contrast enhancement is associated with active inflammation and increased permeability of the BBB. Recently, the pattern of enhancement of CELs on dynamic contrast-enhanced (DCE) MRI sequences has been linked with the developmental stage of the lesion (Gaitán et al. 2011). In DCE-MRI, T<sub>1</sub>-weighted images are acquired rapidly before, during, and for some time after injection of the gadolinium contrast agent. This allows for study of hemodynamic patterns and the spatio-temporal dynamics of lesion enhancement. Based on the time series analysis of DCE images, Gaitán et al. found that some lesions enhance centrifugally (from the center to the periphery) and others centripetally (from the periphery to the center). With both cross-sectional evidence of lesions of different sizes and longitudinal evidence from patients at several time points during the 1-2 months window of lesion contrast enhancement, it was determined that young and small lesions are more likely to enhance centrifugally whereas more mature and larger lesions tend to enhance centripetally. These studies and others have also identified central veins in most MS white matter lesions. Therefore, this spatio-temporal pattern of contrast enhancement suggests that MS lesions initially form around a central vein. Next, inflammation, demyelination and tissue damage extend out in a radial pattern from the central vein until nearby vessels are affected. At some point, anti-inflammatory mediators may overcome the initial inflammation at the central vein, thereby closing the BBB at that site. In the meantime, inflammatory mediators that have spread to the peripheral vessels have opened the BBB at those sites. Perhaps due to edema and tissue damage, gadolinium enhancement at these later stages is stronger within the lesioned tissue than the surrounding area, resulting in the centripetal pattern of enhancement seen in more

mature lesions. Importantly, these in vivo studies of lesion formation are consistent with and shed light on pathological findings, which by their nature cannot provide temporal information about lesion development (Gaitán et al. 2011; Gaitán et al. 2013).

### ***3.2 Diffusion Weighted Imaging***

While diffusion magnetic resonance imaging has been heralded as the latest and greatest technique for the last two decades, the concept of measuring diffusion is not new. In fact, the first iteration of the spin-echo NMR technique was made in 1950 by Hahn, who described how random molecular diffusion obscures the accurate measurement of relaxation times (Hahn 1950). When Carr and Purcell proposed their multiple echo enhancement of the Hahn spin echo technique, they intended to minimize the effects of molecular diffusion on the measurement of T2 relaxation. In so doing, they realized that they could apply their “free precession technique” in a complementary way to directly measure molecular self-diffusion (Carr & Purcell 1954). Finally, in 1965, Stejskal and Tanner introduced the pulsed gradient spin echo (PGSE), which allowed the precise timing of diffusion measurements, thus paving the way for NMR diffusion techniques to measure restricted diffusion (Stejskal & Tanner 1965).

The basis of diffusion imaging is that water molecules in restricted environments such as ordered tissue move anisotropically. As a method for analyzing tissue microstructure, diffusion weighted imaging (DWI) is particularly useful for examining very anisotropic tissues such as white matter. Research into DWI took off with the application by Basser et al. of a formal description of restricted diffusion, the diffusion tensor (P. J. Basser et al. 1994; P. Basser 1995; P. Basser & Pierpaoli 1996), and then expanded further with the development of fiber tracking by Mori et al. (Mori et al. 1999; Mori & P.

van Zijl 2002). These techniques provided an accessible yet rigorous language for discussing and studying in vivo diffusion phenomenon.

### 3.2.1 Brownian Motion

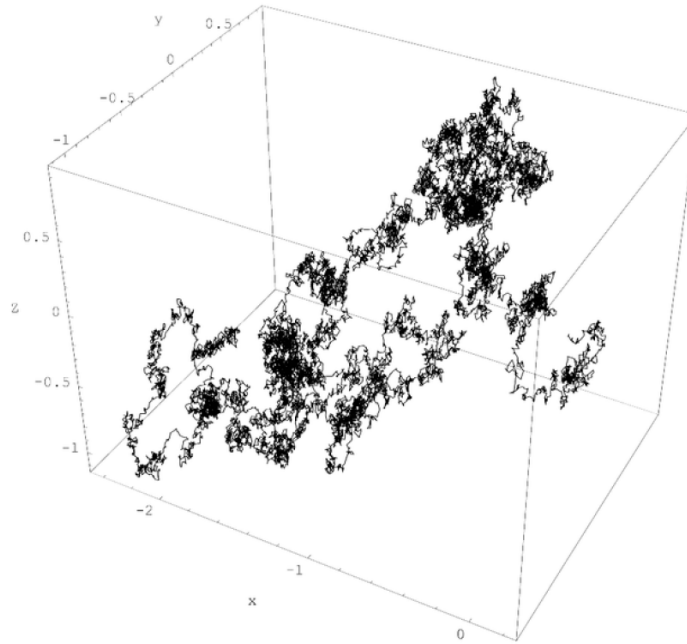


Figure 3.6. Brownian motion in 3D. Adapted from “Brownian Motion” by T.J. Sullivan, *Wikipedia*, 2007. Retrieved from [http://commons.wikimedia.org/wiki/File:Wiener\\_process\\_3d.png](http://commons.wikimedia.org/wiki/File:Wiener_process_3d.png).

The thermally driven random motions of molecules in a solution, Brownian motion, can be described by a physical constant called the “diffusion coefficient” ( $D$ , units of area/time).  $D$  is affected by the size of the molecule of interest and the viscosity and temperature of the solution. The nature of this relationship was first described by the Stokes-Einstein equation (Equation 3-1) (Einstein 1956):

$$D = \frac{k_B T}{6\pi\eta r}$$

$k_B$  = Boltzman Constant  
 $T$  = temperature  
 $\eta$  = viscosity of the medium  
 $r$  = radius of molecule

Equation 3-1

Of note, this equation tells us that larger molecules move more slowly than smaller ones.

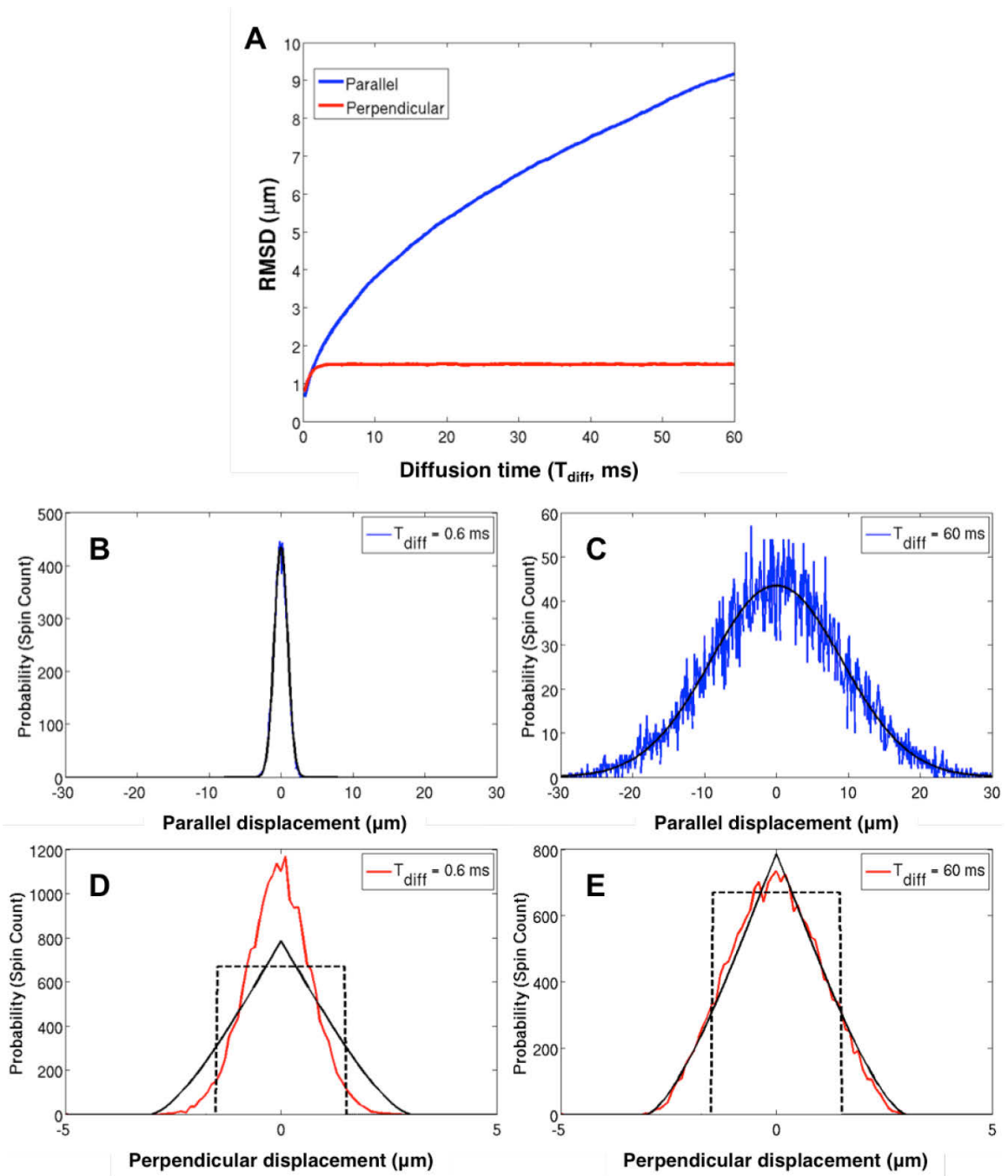
The root mean square displacement (*RMSD*) is a measure of the magnitude of displacement of a diffusing molecule – the distance between the starting and ending points, not the path as shown in Figure 3.6. If *D* is known, the *RMSD* for diffusion in 3 dimensions is:

$$RMSD = \sqrt{6Dt} \quad \begin{array}{l} D = \text{diffusion coefficient} \\ t = \text{diffusion time} \end{array} \quad \text{Equation 3-2}$$

A plot of *RMSD* versus *t* ( $T_{diff}$ ) is shown in Figure 3.7.A (blue) for free diffusion.

*Figure 3.7 (next page) Ensemble average of a simulation of 10,000 particles in a 3 dimensional random walk in impermeable cylinders. A. The root mean square displacement (RMSD) for diffusion parallel (blue) and perpendicular (red) to the long axis of the cylinders versus diffusion time ( $T_{diff}$ ). Panels B-E show histograms of the particle displacement for  $T_{diff} = 0.6$  ms (B & D) and  $T_{diff} = 60$  ms (C & E). In B & C, both the simulated parallel displacement (blue) and the calculated free diffusion (black) are shown. D & E demonstrate the simulated perpendicular displacement (red), the confining geometry (diameter of the cylinder) (black dotted), and the autocorrelation function*

*Simulation parameters: cylinder radius = 1.5  $\mu\text{m}$ ,  $T_{diff} = 200$  increments from 0.03-60  $\mu\text{m}$ , diffusion constant (*D*) = 0.7  $\mu\text{m}^2/\text{ms}$ , time-steps of  $t = 1$  ms, and 10000 particles.*





### 3.2.2 Restricted Diffusion

Magnetic resonance diffusion imaging takes advantage of the physical process of Brownian motion by applying diffusion-sensitizing gradients that attenuate the signal received from excited spins in a logarithmic relationship to the diffusion of those spins (Beaulieu 2002; Hagmann et al. 2006). When the spins of interest are freely diffusing – there are no external barriers to their Brownian motion – NMR can measure the  $D$  of those molecules (Stejskal & Tanner 1965).

$$S(b) = S_0 e^{-bD} \qquad b = \gamma^2 G^2 \delta^2 (\Delta - \delta/3) \qquad \text{Equation 3-3}$$

In DW imaging,  $b$  is known as the b-value and is thought of as the amount of diffusion sensitization. For realistic diffusion experiments, stronger gradients ( $G$ ) and longer gradient pulses ( $\delta$ ) as well as a longer time between pulses, diffusion time ( $\Delta$ ), generally increase the amount of diffusion weighting (Melhem et al. 2002). Of note, this magnetic resonance technique is sensitive to the translational, but not rotational, diffusion of molecules – it does not differentiate molecules based on their spatial orientation.

However, in biological systems, cellular membranes, structural fibers, and a whole host of macromolecules and other structures act as barriers to restrict the free diffusion of molecules. The diffusion time used in a typical in vivo diffusion weighted MRI experiment, for example 50 msec, is long enough for water molecules in brain tissue to move, on average, around 10-20 $\mu$ m (Le Bihan et al. 2001). During this trip, the molecules probe the tissue microstructure by interacting with or bouncing off of cellular structures (see Figure 3.8.A, red arrows). Therefore, the diffusion coefficient that is measured with diffusion MRI in vivo is called the “apparent diffusion coefficient” (ADC) to signify that it is not a measure of intrinsic or unrestricted diffusion (Beaulieu 2002).

Important to our study of tissue microstructure, the ensemble average of molecular diffusion in 3 dimensions can be described by a probability density function. The probability density function is directly related to the autocorrelation function of the confining geometry. The autocorrelation function is like a histogram of the final displacement of the particles once they have had enough time to interact with (bounce off) the walls of the restricting geometry. This is demonstrated in Figure 3.7: in B & C, the ensemble average displacement parallel (blue) to the long axis of an endless cylinder follows the PDF of free diffusion (the sum of 3 Gaussian curves for each of the 3 dimensions) at both short (B) and long (C) diffusion times; the ensemble average displacement perpendicular (red) to the cylinder axis follows the autocorrelation function (black) when  $T_{diff}$  is long enough for the molecules to sample the container (dotted line) (E); but, at short  $T_{diff}$  the perpendicular displacement looks like free diffusion (D). Therefore, when given enough time to sample the environment, measurement of the average displacement of the molecules in a compartment can provide information about the shape of the restricting geometry (J. A. Farrell 2009).

A note on nomenclature: many students of diffusion in biological systems use the terms “hindered” diffusion and “restricted” diffusion to refer to distinct aspects of molecular diffusion in complex biological systems. In particular, hindered diffusion is that random molecular motion which is decreased due to aspects of the solution. From the Stokes-Einstein equation (Equation 3-1), we know that decreased temperature, increased viscosity, or an alteration (e.g. pH) that would increase the diameter of the molecules would decrease the diffusion coefficient. This change in diffusivity would be called “hindered.” On the other hand, “restricted” diffusion is the decreased displacement of randomly moving molecules due to (micro)structural barriers.

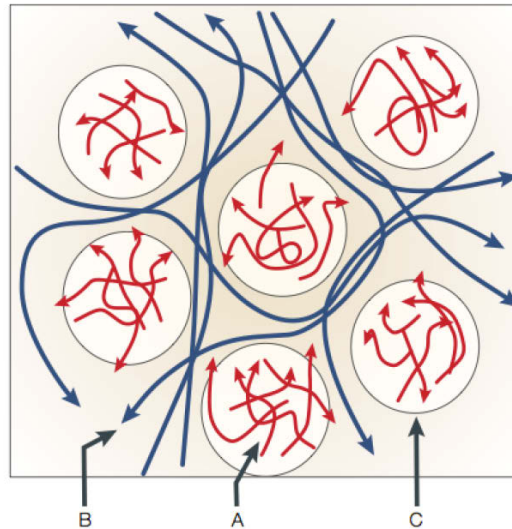


Figure 3.8. Molecular diffusion in restricting environments. Shown is a simplified rendering of a cross-section of axons - looking down the end of the cylinders. A is pointing to restricted diffusion within axons where the molecules are largely confined by the cell membranes. B shows the somewhat obstructed diffusion of molecules moving through the extracellular space. C shows the path of molecules diffusing across membranes - a much slower process. Reprinted from "Looking into the functional architecture of the brain with diffusion MRI" by D. Le Bihan, 2003, *Nature Reviews Neuroscience*, 4(6), page 470. Copyright 2003 by Nature Publishing Group. Reprinted with permission.

The distinction between hindered and restricted diffusion can be important when evaluating the parameters of an MR diffusion weighting technique or when comparing diffusion in different environments such as in vivo versus ex vivo. For instance, diffusion weighting measurements that rely on large gradient amplitudes and use short diffusion times may not allow enough time for the molecules of interest to explore the restricting structures. Therefore, such diffusion measurements will not be able to report on microstructure but may be able to provide information about the solution. For ex vivo experiments, in addition to other changes that take place in dying tissue, ex vivo tissue is

typically colder than its in vivo counterpart. Therefore, all molecular diffusion will be hindered to some extent, and longer diffusion times are required to allow molecules to adequately explore and report on the restricting microstructure (Nair et al. 2005). On the other hand, the distinction between hindered and restricted diffusion can become blurred when the tissue microstructure does not strictly confine the molecules of interest and may hinder the diffusion more than restrict it. This is illustrated in Figure 3.8 by the dark blue lines (arrow B) demonstrating molecules moving around the axons in the extracellular space and by the cell membranes (arrow C), which are semi-permeable.

### 3.2.3 The Diffusion Tensor & Tractography

As presented by Basser, Mattiello and Le Bihan in the 1990s (P. J. Basser et al. 1994), modeling molecular diffusion with an ellipsoid and tensor provides a rigorous and widely adaptable set of methods to study and describe the nature and orientation of anisotropic diffusion in biological tissue. The diffusion tensor (DT) was developed in order to improve the sensitivity and specificity of DW images by providing diffusion information independent of imaging orientation. By acquiring DW images along at least 6 independent directions, we can generalize the Stejskal-Tanner equation as a tensor model where the signal attenuation for each direction is given as a vector and the b-value is written as a vector of orientations:

$$\ln\left(\frac{\vec{S}}{\vec{S}_0}\right) = -\vec{b}\overline{\overline{D}} \quad \overline{\overline{D}} = \begin{bmatrix} D_{xx} & D_{xy} & D_{xz} \\ D_{yx} & D_{yy} & D_{yz} \\ D_{zx} & D_{zy} & D_{zz} \end{bmatrix} \quad \text{Equation 3-4}$$

With this formalization, the direction and degree of anisotropic movement of molecules in a voxel can be modeled as an ellipsoid where the directions and length of the three orthogonal axes are described by eigenvectors ( $v_1, v_2, v_3$ ) and eigenvalues ( $\lambda_1, \lambda_2, \lambda_3$ ) such that  $\lambda_1 v_1$  has the greatest magnitude and  $\lambda_3 v_3$  has the least magnitude (Figure 3.9). In this way, the eigenvectors provide information about the orientation of diffusion within a voxel, and the eigenvalues represent the magnitude of diffusivity of molecules along those directions (Pierpaoli et al. 1996).

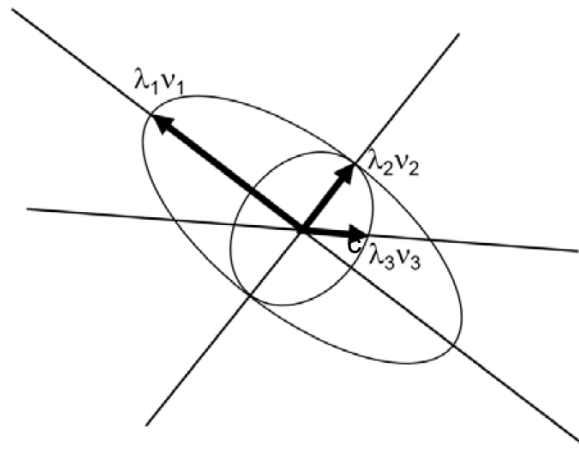


Figure 3.9. An ellipsoid where axis directions or orientations are described by eigenvectors ( $v_1, v_2, v_3$ ) and the magnitude or length of each axis is described by the eigenvalues ( $\lambda_1, \lambda_2, \lambda_3$ ).

Two commonly used quantitative measures of diffusion properties are mean diffusivity (MD) and fractional anisotropy (FA). MD serves to describe the size of the tensor in a volume of interest (VOI) and, therefore, is directly related to the amount of diffusion (diffusion constant) of that volume. ADC or mean diffusivity (MD) is an average of the eigenvalues; for *in vivo* white matter MD values are typically around  $1 \mu\text{m}^2/\text{ms}$ .

$$MD = \frac{\lambda_1 + \lambda_2 + \lambda_3}{3} \quad \text{Equation 3-5}$$

Other quantities typically analyzed in white matter are the diffusivity along the

primary axis of a fiber tract ( $\lambda_{\parallel} = \lambda_1$ , also known as parallel, axial, or longitudinal diffusivity), the diffusivity transverse to the fiber axis ( $\lambda_{\perp} = (\lambda_2 + \lambda_3)/2$ , also known as perpendicular, radial, or transverse diffusivity), and fractional anisotropy (FA). FA can take values between [0,1] where 0 is isotropic diffusion (a spherical ellipsoid) and 1 is highly anisotropic diffusion (an ellipsoid approximating a cylinder or cigar).

$$FA = \sqrt{\frac{(\lambda_1 - \lambda_2)^2 + (\lambda_1 - \lambda_3)^2 + (\lambda_2 - \lambda_3)^2}{2(\lambda_1^2 + \lambda_2^2 + \lambda_3^2)}} \quad \text{Equation 3-6}$$

In tissue, cellular membranes and other structures act as barriers to restrict the diffusion of molecules more in certain directions than other directions. For instance, in an axon bundle, water molecules can move more freely along the direction parallel to the length of the axons than they can perpendicular to the axon axis due to cell membranes and other tissue structures (Beaulieu 2002). Through measurement of the apparent diffusion coefficient of molecules along various trajectories, a model of the direction and degree of anisotropic movement of those molecules can be constructed (Losseff et al. 1996; Pierpaoli et al. 1996; Ge et al. 2000). In diffusion tensor imaging (DTI), diffusion weighting is applied along many directions (15-45 directions commonly) so that molecular movement can be modeled as a tensor.

Fiber tracking or diffusion tractography algorithms developed for neuroimaging attempt to find potential biologically relevant white matter tracts that may correspond to the neuronal tracts connecting functionally important brain centers. At basis, this is done by connecting nearby voxels based on the degree and orientation of anisotropy. Fiber assignment by continuous tracking (FACT) was the first tractography algorithm to be widely employed and continues to be useful today. FACT applies a line-propagation approach to connect nearby voxels in a deterministic manner (Figure 3.10)(Mori et al.

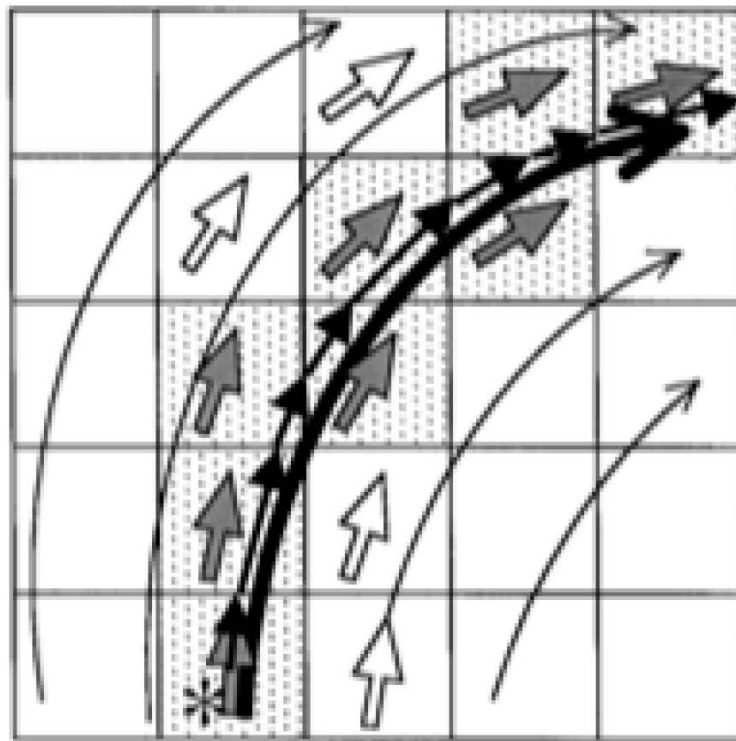


*Figure 3.10 Fiber Assignment by Continuous Tracking (FACT).* Reprinted from “Three-dimensional tracking of axonal projections in the brain by magnetic resonance imaging” by S. Mori et al., 1999, *Annals of Neurology* 45(2), page 266. Copyright 2001 by John Wiley and Sons. Reprinted with permission.

1999). This allows visualization of macroscopic white matter architecture but cannot provide information about cellular connectivity. Additionally, this method has difficulty with regions of crossing fibers. Nonetheless, initial animal studies and many in vivo studies since, have evaluated the usefulness of this method (Mori & P. van Zijl 2002; Mori et al. 2002).

### **3.2.4 DTI in MS**

Diffusion weighted imaging (DWI) has generated considerable research interest in the last 25 years since it has been shown to reflect disease related changes in many pathologies including stroke (Pfeuffer et al. 1998; Warach et al. 1992), and brain tumors (Krabbe et al. 1997), and because it makes for really beautiful colors maps of white matter fiber orientation (Figure 3.11). In an effort to find MRI measures that differentiate axonal degeneration from demyelination and inflammation, DTI of water has been heavily studied in MS and animal models of MS with conflicting results. Most DTI human studies in vivo have demonstrated increased water diffusivity ( $MD$ ,  $\lambda_{||}$ , and  $\lambda_{\perp}$ ) and decreased water FA, in both lesions and NAWM (Evangelou et al. 2000; Werring et al. 1999; Bammer et al. 2000; Roosendaal et al. 2009; Reich et al. 2010). However, the interpretation of pathology-based changes in water diffusivity through measures such as MD and FA is complicated since a single DWI voxel contains information from multiple tissue compartments. This is highlighted by the fact that similar measurement changes have been seen in a number of disease pathologies, suggesting that DTI is highly sensitive but nonspecific for detecting microstructural damage.



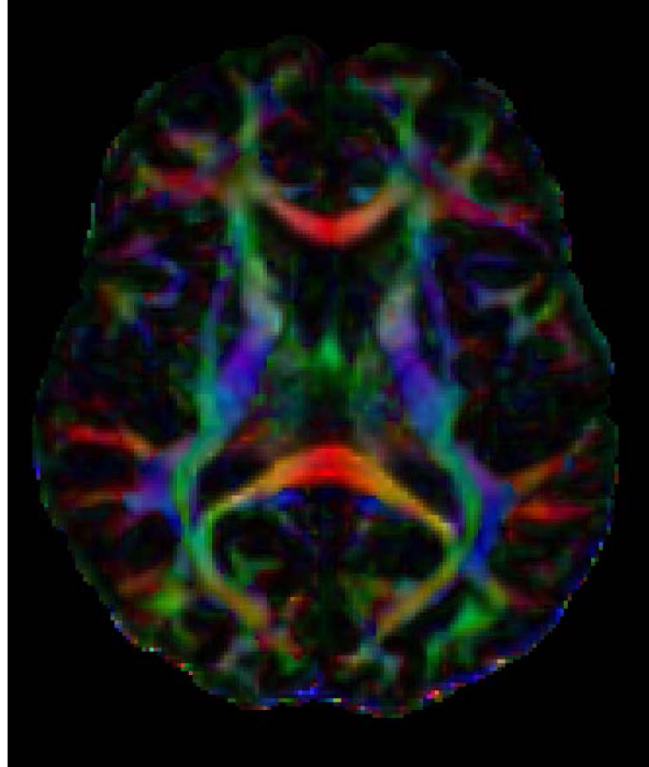


*Figure 3.11. DTI color map of a healthy volunteer. Colors designates primary eigenvector direction – red = right-left; blue = foot-head; green = anterior-posterior. Brightness = FA.*

Nonetheless, DTI continues to be studied in MS both because DTI's ability to predict disability and other disease measures has been promising and because the technique has the physical underpinnings to be able to provide microstructural tissue information. Some of the first results for DTI in MS came from a series of studies conducted by David Miller's group at University College London that examined cross-sectional DTI indices in a range of MS types and disability levels. They found that DTI measures from within lesion tissue and NAWM demonstrate evidence of microstructural alterations in MS compared to healthy controls (Werring et al. 1999). Additionally, decreased FA and increased MD in NAWM was correlated with clinical disability (Ciccarelli et al. 2001). Finally, they found a relationship between higher lesion load in

the cerebrum with decreased FA and increased MD in the corpus callosum, suggesting that DTI can detect Wallerian degeneration (Ciccarelli et al. 2003). Cross-sectional analyses of MS continue to demonstrate that DTI abnormalities are associated with some measures of disability (Ozturk et al. 2010). For example, lower FA in the corpus callosum is associated with worse performance on some neuropsychological tests of attention, memory, and executive function, even after controlling for lesion load in the corpus callosum (Bodini et al. 2013).

In order to develop the possible predictive value of an imaging technique, the same subjects must be studied over time in a longitudinal fashion so that changes in imaging measures and clinical status can be evaluated together. Longitudinal DTI studies of patients with MS and optic neuritis have suggested that DTI may be detecting axonal degeneration. In a longitudinal study of MS patients that focused on changes in DTI measures in regions of interest that were CEL on baseline scans, FA was found to increase, on average, in the year following enhancement (R. J. Fox et al. 2011). On the other hand, in these same patients, FA in the normal appearing brain tissue went down during this period. In a separate study, elevated perpendicular diffusivity and MD, and decreased FA were predictive of transformation to persistent black holes (Naismith et al. 2010). On the other hand, in optic neuritis, lower parallel diffusivity measurements in the optic nerves at presentation were predictive of worse visual acuity at 6 months follow-up (Naismith et al. 2012).

Table 3.1 provides an overview of a representative sample of the many DTI studies of patients with MS and optic neuritis. Of note, the studies in MS span all MS subtypes and tissues, including normal appearing white matter (NAWM), normal appearing brain tissue (NABT), acute and chronic lesions, and deep gray matter. Most of these studies are cross-sectional, but some have evaluated diffusion measures in

subjects longitudinally. Many of these studies attempt to gauge anisotropic diffusion in regions of interest throughout the brain that may not have a strong microstructural basis for anisotropy. Therefore, disease state alterations in FA,  $\lambda_{||}$ , and  $\lambda_{\perp}$  in these areas, such as the thalamus, regions of crossing fibers, or the striatum, should be evaluated with consideration for the expected or underlying tissue structure. Table 3.1 also highlights the difficulty of doing highly controlled experiments in human subjects. While several of these studies attempt to constrain temporal elements of the disease process by examining CELs or subjects with optic neuritis – overall the patients and their disease states are very diverse. This provides motivation for performing diffusion weighted imaging studies in animal models of inflammatory demyelination and axonopathy.

*Table 3.1. A summary of DTI results in a representative subset of DTI studies of multiple sclerosis*

<b>Article</b>	<b>Subjects</b>	<b>Tissue</b>	<b>FA</b>	<b>MD</b>	$\lambda_{  }$	$\lambda_{\perp}$
(Werring et al. 1999)	5 RRMS + 1 SPMS vs. 6 HC	CEL	↓↓↓	↑↑		
		Non-CE Lesions	↓	↑↑		
		NAWM	↓	↑↑		
(Bammer et al. 2000)	14 MS vs. 9 HC	CEL	∅	↑		
		T1-hypo	↓↓	↑↑		
		NAWM	↓	↑		
(Ciccarelli et al. 2001; Ciccarelli et al. 2003)	39 MS vs. 21 HC	NAWM	↓	↑		
(Tovar-Moll et al. 2009)	24 MS (RR & SP) vs. 24 HC	Normal appearing thalamus	↑	↑		

(Naismith et al. 2010)	22 MS advanced	CELs & persistent black holes	↓	↑	∅	↑
(Ozturk et al. 2010)	69 MS vs. 29 HC	NAWM	↓	↑	↑	↑
		Lesions	↓	↑	↓	↑
(Reich et al. 2010)	88 MS vs. 27 HC	WM tract-based measures	↓	↑	↑	↑
(R. J. Fox et al. 2011)	21 MS on natalizumab	CEL at baseline	Δ↑	∅	∅	Δ↓
		NABT	Δ↓	∅	Δ↓	∅
(Naismith et al. 2012)	25 Optic neuritis (Tissue = optic nerves)	Vision recovery status Incomplete	∅	↓	↓	∅
		Complete	↓	∅	∅	↑
(Wheeler-Kingshott et al. 2012)	15 HC vs. 2 MS	Lesions and NAWM			↓↑	↑

[empty] = no data

∅ = no significant change/difference detected

↓ = measure decreased in MS subjects/tissue compared to healthy controls

↑ = measure increased in MS subjects/tissue compared to healthy controls

Δ↓ = Measure decreased in MS subjects over time

Δ↑ = Measure increased in MS subjects over time

### 3.2.5 DTI in animal models of MS

Demyelination in the central nervous system can occur through numerous and varied pathways. MS, in particular, is a highly heterogeneous disease in terms of time course, nervous tissue affected, genetics and pathology. For this reason, a number of animal models have been developed in an attempt to isolate certain aspects of MS

pathophysiology. For example, experimental allergic/autoimmune encephalomyelitis (EAE) is a model that has been studied in rodents and non-human primates. In EAE, an antigen such as purified myelin or myelin basic protein (MBP) in concert with an adjuvant is administered to the animal and produces a T-cell mediated inflammatory demyelinating disease of the CNS. This model has elucidated a number of immunological patterns that can be applied to our pathophysiological understanding of MS (Batoulis et al. 2010). In a focal EAE model in rat spinal cord, Deboy et al. demonstrated that a sustained decrease in FA with a corresponding decrease in  $\lambda_{||}$  was associated with decreased axonal counts, demyelination and loss of neurofilament structure distal to the lesion site (DeBoy et al. 2007). This study suggests that DTI measures are sensitive for different types or stages of inflammatory neurodegeneration. On the other hand, in the EAE model myelin degeneration and regeneration are happening simultaneously with neuronal degeneration. Therefore, it can be difficult to tease apart the contributions from each of these pathophysiological processes to the MRI measurements to discern specific measures.

The cuprizone model of neurotoxic demyelination was developed approximately 40 years ago as a comparatively “clean” (i.e., minimally inflammatory) approach to studying the processes of de- and remyelination, as well as the effects of these processes on axons. Copper is a catalytic and structural cofactor in a number of biochemical processes, and due to its narrow range of optimal concentration, the uptake, transport, storage and release of copper are tightly controlled (Herring & Konradi 2011). The administration of cuprizone, a copper chelator, causes oligodendrocyte demise without primary effects on other cell types or blood-brain barrier opening (Bakker & Ludwin 1987; Matsushima & Morell 2001). The mechanism of action of specific oligodendrocyte death is unknown, but it has been found that cuprizone reduces brain

activity of cytochrome oxidase and monoamine oxidase leading to decreased mitochondrial respiration (Herring & Konradi 2011; Venturini 1973). When added to the chow of certain mouse strains, cuprizone causes oligodendrocyte death and subsequent demyelination over a course of weeks. After 4-5 weeks of continuous cuprizone administration, axons in the corpus callosum (CC) and several other prominent tracts are over 90% demyelinated (Blakemore 1972; Blakemore 1973a; Matsushima & Morell 2001). Following approximately 6 weeks of cuprizone administration, microglia, macrophages and astrocytes are recruited for phagocytosis of myelin. Oligodendrocyte progenitor cells proliferate, up-regulate expression of genes coding for myelin structural components and attempt to remyelinate axons (Jurevics et al. 2002; Stidworthy et al. 2003). If cuprizone is removed from the diet at 6 weeks, remyelination will continue until only 10% of axons in the CC remain without myelin (Blakemore 1973b; Mason et al. 2001). If cuprizone is continued for 12 weeks, the animals lose the ability to remyelinate, neuroaxonal degeneration becomes prominent, and the animals begin to die (Matsushima & Morell 2001).

Morphological studies of axons and myelin have focused on axon counts, axon caliber, and myelin thickness. It has been shown that cuprizone-triggered demyelination is associated with a decrease in mean axon diameter (Mason et al. 2001). As this association was seen despite dramatic decreases in axonal counts, it suggests that there is a functional relationship between myelin and axons. Myelin associated glycoprotein (MAG) is known to signal to axons to influence neurofilament phosphorylation and thereby increase axon diameter (Hsieh et al. 1994; Dashiell et al. 2002). Cuprizone-induced chronic demyelination causes axonal alterations such as reduced axonal conduction, diffuse spread of voltage-gated sodium and potassium channels (Crawford et al. 2009) and neurofilament phosphorylation changes (Lindner et

al. 2009; Xie et al. 2010). These changes are similar those seen in MS autopsy samples that have unusual patterns of neurofilament phosphorylation and packing compared to normal tissue suggesting less organized axoskeleton and/or problems with axonal transport (Petzold et al. 2008).

In an effort to find an MRI measure that differentiates demyelination from axonal degeneration, DTI has been studied in the cuprizone model of neurodegeneration. Song et al. (Song et al. 2003) developed a theory of DTI measures in white matter pathology wherein decreased parallel diffusivity of water (water  $\lambda_{||}$ ) indicates axonal degeneration and increased perpendicular diffusivity (water  $\lambda_{\perp}$ ) is a sign of demyelination. Some of the first evidence in support of this theory came from the analysis of mouse optic nerve diffusion after retinal nerve ischemia, which demonstrated decreased water  $\lambda_{||}$  during the early phase of axonal degeneration and increased water  $\lambda_{\perp}$  later on, when myelin degeneration was most prominent. The Song group undertook a comprehensive analysis of DTI and pathological measures in the cuprizone model throughout the time course from acute demyelination to chronic demyelination and axonal degeneration (Xie et al. 2010). In this study,  $\lambda_{||}$  was decreased early, during the acute demyelinating stage, and was associated with axonal swelling and beading indicating decreased axonal transport, an increase in dephosphorylated neurofilaments (SMI-32+ axons) indicating axonal damage, and microglia and macrophage activation. Perpendicular diffusivity increased in chronically demyelinated regions but did not change during the acute phase of demyelination when there was axonal swelling and inflammatory cell infiltration. These findings have been confirmed and extended in the EAE model where, of the DTI measures, water  $\lambda_{||}$  is best correlated with axonal injury and neurological disability (Budde et al. 2008; Budde et al. 2009).

The dorsal root axotomy or radiculotomy is an experimental procedure for

studying Wallerian degeneration which was described in detail by George and Griffin (George & Griffin 1994a; George & Griffin 1994b). In this model, the cauda equina is exposed by laminectomy, and the dorsal roots of vertebral segments L<sub>2</sub>-L<sub>4</sub> are transected just proximal to the dorsal root ganglion on one side. Therefore, the degeneration of these ascending fibers can be studied through out their course in the spinal cord (rostrally) with comparison to the intact contralateral fibers. Farrell and Zhang studied this system with ex vivo high resolution diffusion weighted MRI analyzed by both conventional DTI methods and *q*-space DWI methods (Zhang et al. 2009; J. Farrell et al. 2008). Their work demonstrated decreased water  $\lambda_{||}$  – with DTI and diffusion kurtosis analysis – at 3 and 30 days post-axotomy. These changes were seen in conjunction with histological evidence of axon injury and degeneration such as neurofilament phosphorylation state and the presence of myelin ovoids. Interestingly, while the decreased water  $\lambda_{||}$  measured with DTI methods remained constant from day 3 to day 30, the high b-value *q*-space measurements of water  $\lambda_{||}$  showed some changes during this time period suggesting that this analysis technique may be more sensitive or specific for ongoing changes in the context of Wallerian degeneration (J. A. D. Farrell et al. 2010).

A potentially important difference between DTI studies in MS and animals models is the timing of imaging in relation to clinical symptoms or inciting events. As described above, animal studies with serial imaging consistently show early decreased water  $\lambda_{||}$  corresponding with histological evidence of axonopathy, followed by normalized or increased water  $\lambda_{||}$ . These studies also describe increased water  $\lambda_{\perp}$  later when inflammation, demyelination, and gliosis become more prevalent. This pattern of DTI changes was borne out in human epilepsy and optic neuritis studies, which benefitted from a known, discrete clinical onset. Specifically, epilepsy patients who underwent



corpus-callosotomy had reduced water  $\lambda_{||}$  in transected portions of the CC (Concha et al. 2006). In patients with optic neuritis, low baseline water  $\lambda_{||}$  was correlated with poor visual acuity and a thinned retinal nerve fiber layer at 6 months (Naismith et al. 2012). However, these studies represent the exception rather than the rule: as axonopathy is ongoing and almost always found in the setting of inflammation and edema in MS, DTI is in most cases unable to reliably identify the presence of axonopathy.

DTI and its brethren, diffusion kurtosis imaging,  $q$ -space imaging, AxCaliber, etc. will continue to be applied to multiple sclerosis because the theory and some of the empirical evidence suggest that it can be made to measure specific microstructural changes in tissue in vivo. In the face of histological evidence that there is neuronal loss in MS (Arnold et al. 1990; Trapp et al. 1998; Fu et al. 1998; Bitsch et al. 2000; Filippi et al. 1995; Dutta et al. 2006; Filippi et al. 1998; Kutzelnigg et al. 2005), DTI must be able to differentiate neurodegenerative changes from inflammation in order to support these assertions. Nonetheless, DTI stands up to its original claims of being a highly quantitative MRI technique with wide-ranging applicability. DTI measures, FA in particular, have been shown to be reproducible – with mean concordance coefficients of 0.90-0.97 across platforms and sites – in multi-center studies (R. J. Fox et al. 2012) and have been used successfully by basic and clinical researchers alike.

### ***3.3 Magnetic Resonance Spectroscopy***

Figure 3.12 depicts a highly simplified version of two axons, running parallel to each other, in a highly anisotropic region of white matter such as the corpus callosum. This illustration highlights the fact that water molecules (blue dots) are everywhere in tissue – in the axoplasm (and its organelles), in and between myelin bilayers, and in the

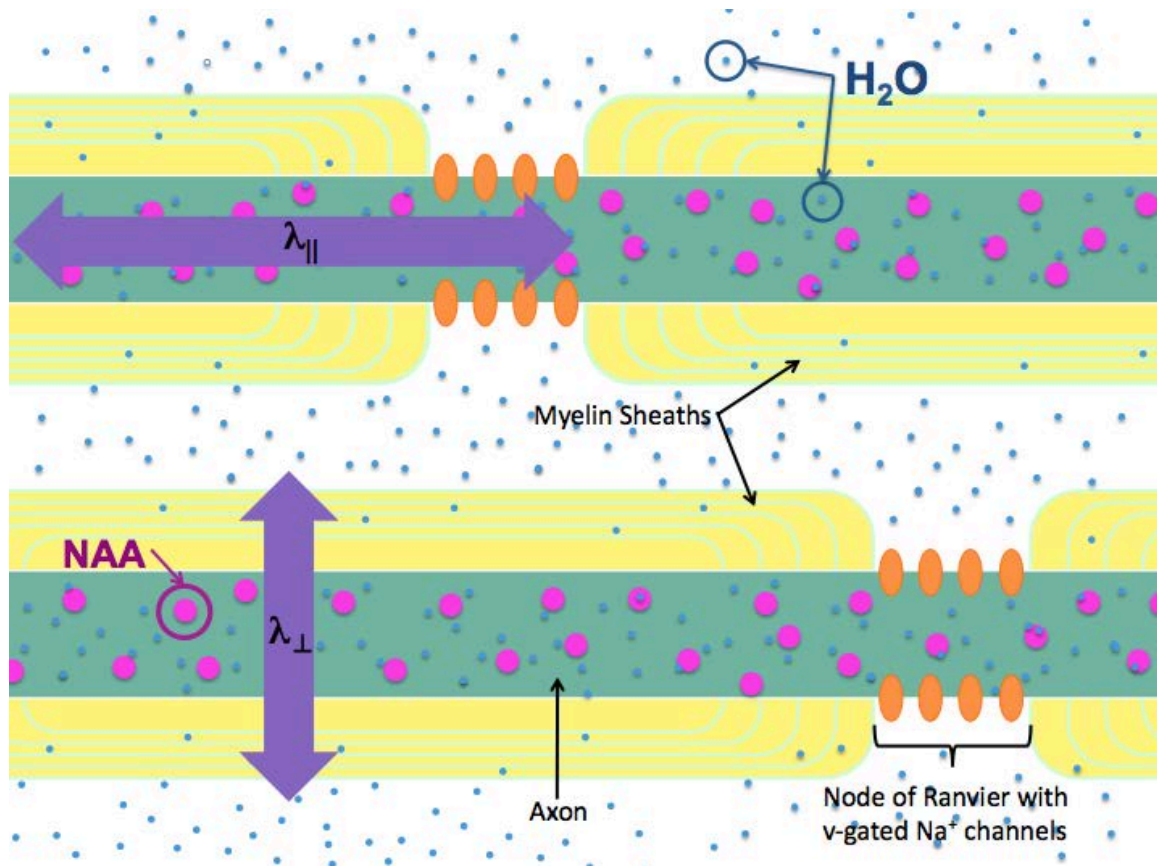


Figure 3.12. Axons in white matter. Green = axons/axoplasm; yellow = myelin bilayers; blue dots = water molecules; magenta dots = N-acetyl aspartate molecules; orange ovals = voltage-gated sodium channels; white = extracellular space; violet arrows demonstrate direction of parallel and perpendicular diffusion with respect to the axon orientation.

extracellular space. Therefore, diffusion weighted imaging, which measures the random movement of water molecules, is inherently non-specific for compartment. On the other hand, other molecules, especially cellular metabolites, are synthesized, degraded and kept in certain tissue compartments by active processes. For example, N-acetyl aspartate (NAA; magenta dots) is found almost exclusively within neurons in the CNS. For this reason, various measurements of metabolites such as NAA may be able to provide specific information related to compartments of interest.

### 3.3.1 MRS Technical overview

Magnetic resonance spectroscopy (MRS) takes advantage of the same inherent properties and behavior of atomic nuclei in external magnetic fields that were discussed previously with reference to imaging. In the case of  $^1\text{H}$ -MRS, we are measuring the spins of protons on many different molecules (including but not limited to water) and deriving contrast from the chemical shift property. Chemical shift is the property of nuclei in slightly different molecular environments to have slightly different resonant frequencies (Barker et al. 2009). The major factor contributing to this effect is the response of the molecule's electron cloud to an applied magnetic field. The external field induces a rotating current in the electrons that generates a very small magnetic field that usually opposes the external field. The case that the induced field opposes the applied magnetic field is called a "diamagnetic effect" and results in the nucleus being somewhat "shielded" from the external field. Therefore, depending on the electron cloud of the nucleus, that nucleus will experience a slightly different resonant frequency from the external field. The difference in resonance is proportional to the external field, and the proportion is called the shielding or screening constant (Chary & Govil 2008). We can measure the resonant frequency of protons and express it as the chemical shift of the nucleus relative to a standard in parts per million (ppm).

MRS can be used to study many different nuclei and can, therefore, be applied to the measurement of a great number of molecules. Unfortunately, in vivo we are limited to studying those molecules that have a great enough concentration for the signal-to-noise ratio to allow us to "see" them. Additionally, the molecules of interest must be relatively small and mobile. Nonetheless, many magnetic resonance spectroscopy imaging (MRSI) methods have been developed which allow multi-voxel measurement of brain metabolites. In brain proton-MRS, the molecules that are most easily detectable

with typical long echo times are cholines (free choline, phosphocholine, and glycerophosphocholine), creatine (creatine and phosphocreatine), and N-acetyl aspartate (NAA). The choline compounds are involved in membrane synthesis and degradation and tend to be elevated in the setting of high membrane turnover. Creatine and phosphocreatine are closely linked to ATP generation through their role in the creatine kinase reaction (Barker et al. 2009). While creatine plays an important role in energy metabolism, the overall level tends to be relatively stable. For this reason, creatine is often used as a comparator for relative concentrations of other molecules.

### **3.3.2 NAA in MS**

N-acetyl aspartate is an enigmatic molecule that is detectable in  $^1\text{H}$  magnetic resonance spectroscopy (MRS) due to its exceptionally high concentration in the brain (Hauser & Oksenberg 2006; Moffett et al. 2007; Noseworthy 2003). Early on in the study of *in vivo* nuclear MRS, it was discovered that NAA is present almost exclusively in the CNS, and within the CNS approximately 95% of NAA is within neurons (Urenjak et al. 1993; Bárány et al. 1987; Simmons et al. 1991). NAA was henceforward hailed as a specific neuroaxonal marker. Therefore, when the first studies of NAA in neurodegenerative diseases found decreased NAA in patients compared to healthy controls, the finding was interpreted as evidence for neuronal loss. Subsequently, *in vivo* studies in patients with MS demonstrated that, in some lesions, the NAA concentration dropped dramatically during the acute stage of the lesion and then rose to subnormal levels in follow-up scans (Arnold et al. 1990; Davie et al. 1994; Bates et al. 1996). These MRS studies led to somewhat increased interest in the physiological role of NAA. It was already known that NAA was made in mitochondria (Patel & Clark 1979). In 1995, it was demonstrated that acute axonal injury of an upstream neuron could cause a transient

decrease in NAA (Rango et al. 1995). Bates et al. (Bates et al. 1996) demonstrated with respiratory chain inhibitors in isolated mitochondrial preparations that ATP and NAA synthesis are directly correlated with oxygen consumption.

While the metabolic and neurochemical roles of NAA remain controversial, some important neurochemical information about NAA has been accrued over the years, and a theory for its role has developed. Canavan's disease is a genetic leukodystrophy caused by a deficiency in the enzyme aspartoacylase (ASPA) and has the unique brain MRS signature of increased NAA concentration (Moffett et al. 2007; Kaul et al. 1994; Kaul et al. 1991). ASPA is the enzyme that catalyzes the deacetylation of NAA. It is almost exclusively found in oligodendrocytes (Baslow et al. 1999). In 2003, Madhavarao et al.

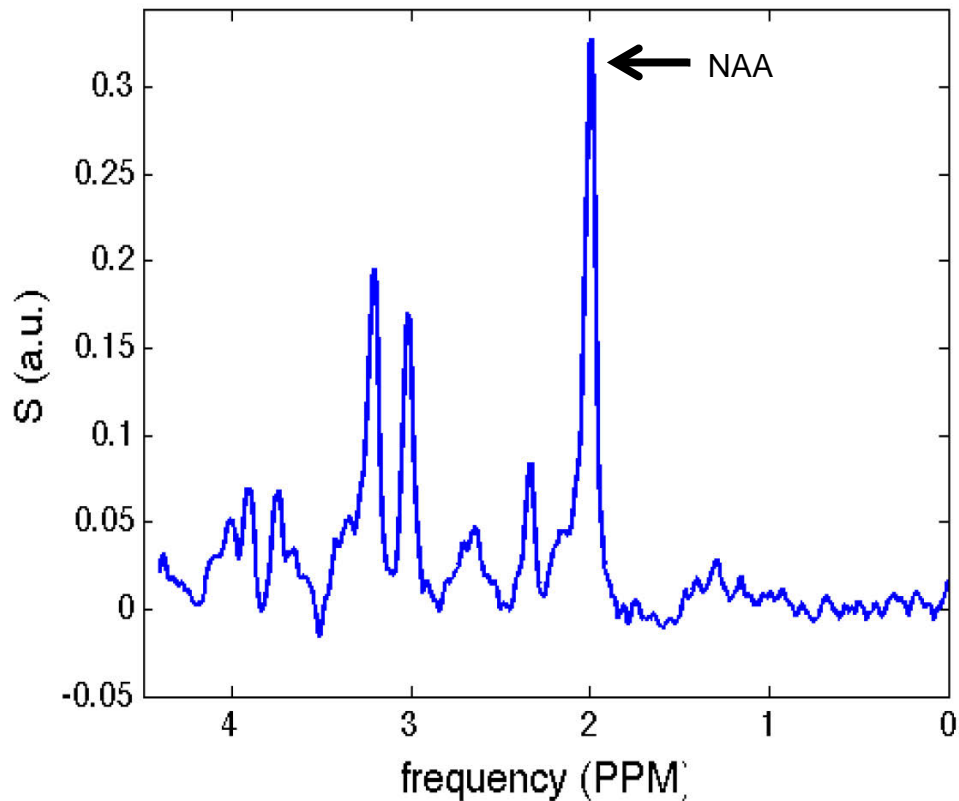


Figure 3.13. An *in vivo* proton magnetic resonance spectroscopy spectrum from the brain of a healthy volunteer at 7T. NAA is the largest peak in the spectrum at 2 ppm.

characterized aspartate N-acetyltransferase (Asp-NAT), the biosynthetic enzyme of NAA (Madhavarao et al. 2003). Asp-NAT is localized primarily in neuronal mitochondria and to some degree in the neuronal cytosol (Ariyannur et al. 2008; Arun et al. 2009; Madhavarao & Namboodiri 2006). Madhavarao and colleagues have proposed a two part model whereby NAA facilitates neuronal mitochondrial metabolism and acts as a source for fatty acid and steroid synthesis in oligodendrocytes (Moffett et al. 2007). In this model, Asp-NAT acts to remove excess aspartate from the mitochondrial matrix, thereby preventing product inhibition of aspartate aminotransferase and facilitating energy metabolism via the TCA cycle. Putative NAA transporters then export NAA to the cytoplasm and on to oligodendrocytes to provide acetate units for fatty acid and steroid production for the myelin bilayers that are critical for neuronal function (Madhavarao et al. 2005). Thus, by nature of its localization within neurons NAA is a neuronal marker, and through its role in energy metabolism NAA provides information about mitochondrial and neuronal health. Interestingly, in the context of MS where demyelination and neurodegeneration occur with concomitant attempts at remyelination, NAA points to a pathway for neuronal injury to impact myelin integrity.

Cross-sectional <sup>1</sup>H-MRS studies in MS have demonstrated low levels of [NAA] within lesions, NAWM, and the whole brain, suggesting axonal loss (Gonen et al. 2000; Pelletier et al. 2003; Kirov et al. 2009; Oh et al. 2004; Leary et al. 1999; Davie et al. 1997; Ciccarelli et al. 2007; Tiberio et al. 2006; Narayana et al. 2004; Inglese et al. 2003; Suhy et al. 2000; Rovaris et al. 2005; Ge et al. 2004; Filippi et al. 2003). However, longitudinal studies in NAWM have not detected declining [NAA] in patients with MS over a 2-3 year span (Tiberio et al. 2006; Sajja et al. 2008; Kirov et al. 2012). Interestingly, [NAA] can drop dramatically within acute lesions, only to rise to near-normal levels in follow-up scans; this suggests that some decreases in [NAA] can be attributed to

reversible metabolic insults (Davie et al. 1994) or perhaps to dilutional effects related to edema. A recent study found that [NAA] is decreased in subjects with radiologically isolated syndrome (Stromillo et al. 2013) providing evidence for metabolic abnormalities and axonal dysfunction in those who have not yet presented with clinical symptoms related to MS.

The Arnold group at the Montreal Neurological Institute has shown that while T2 lesion load may be more sensitive on a short time scale for disease activity in MS, decreases in [NAA] are more specifically related to neurodegeneration (De Stefano et al. 1998; Arnold et al. 1994; Matthews et al. 1996; Fu et al. 1998). In one study, MRSI was used to examine the contralateral hemisphere of 3 patients with large demyelinating lesions (De Stefano et al. 1999). That study found that NAA:Cr decreased from baseline in both the lesions and in normal appearing homologous regions of interest in the contralateral hemisphere at 1-month. At 6-months, the contralateral normal appearing white matter had normalized by MRSI. This provided evidence for Wallerian degeneration or, at least, effects of axon dysfunction over projection pathways.

Potentially, MRS measures of NAA could give us information about both neuronal integrity and function if we can accurately attribute the signal of these separate contributions. Cader et al. (Cader et al. 2007) and Ciccarelli et al. (Ciccarelli et al. 2010) attempted to do this by correlating simultaneously acquired anatomical MRI, DTI and MRS measures in patients with MS. Cader et al. found no associations in the CC between NAA concentration and atrophy (measured by CC cross-sectional area), mean connectivity (probabilistic tractography) or fractional anisotropy (tract-based spatial statistics). Their interpretation of this finding was that most of the reduction in NAA was due to potentially reversible metabolic dysfunction. In the cervical spine, Ciccarelli et al. used linear regression to model the variance in NAA concentration (resNAA) associated

with mitochondrial metabolism by accounting for axonal degeneration (parallel diffusivity) and atrophy (cord cross-sectional area). ResNAA was correlated with clinical impairment even though NAA concentration was not associated with the structural MR measures in the spinal cord. This finding was considered supportive of a role for mitochondrial impairment in neurological dysfunction in MS.

### ***3.4 MRI for diagnosis, prognosis and drug development in MS***

MS can now be diagnosed on the basis of one MRI scan with simplified MAGNIMS criteria for dissemination in space (Katz Sand & Lublin 2013). Dissemination in space is established by 1 or more lesions in at least 2 of the following 4 locations: periventricular, juxtacortical, infratentorial, and spinal cord. Under the McDonald 2010 criteria, it is possible to make the diagnosis of RRMS with a high degree of sensitivity and specificity with a single clinic visit and MRI scan (Klawiter 2013; Polman et al. 2011). While the exact modality or contrast mechanism used to detect MS lesions is not specified in any of the diagnosis criteria, white matter lesions characteristic of MS are most easily seen on FLAIR sequences. Contrast enhancement is used clinically to detect current or recent inflammation and can be the basis for initiating corticosteroid therapy, particularly if clinical symptoms are present. Multiple studies have now demonstrated that the presence of a small vein or venule within a lesion is highly suggestive of MS (Sinnecker, Dorr, et al. 2012a; Sati et al. 2012; Gaitán et al. 2011; Tallantyre et al. 2011). In fact, the periventricular distribution of MS lesions may be due, largely, to their association with venules (Klawiter 2013).

MRI has been central to the development of disease-modifying therapies in MS. Imaging measures of inflammation and BBB opening have proven to be critical in the



development of immunomodulatory therapies for MS (McFarland 2011; Petkau et al. 2008). Acute inflammatory and demyelinating activity can be visualized directly on conventional magnetic resonance images (MRI) – gadolinium contrast enhancement on T<sub>1</sub>-weighted images is associated with blood-brain barrier (BBB) opening, and T<sub>2</sub>-weighted hyperintensity is indicative of inflammation and edema as well as demyelination. Where clinical measures of disability have low sensitivity and reliability, conventional MRI measures are highly sensitive for disease activity, substantially more reproducible, and more or less objective. MRI measures have allowed therapy trials to be shorter and require fewer subjects than previous studies without imaging measures. This has accelerated the pace of approval of disease-modifying therapies in MS. Immunomodulatory therapies have been developed that reduce clinical relapses and the associated MRI indices of disease activity.

While we can detect the consequence of neurodegeneration, we cannot measure the process of degenerating axons in real-time. The long-term effects of neurodegeneration can be detected in the form of tissue loss – brain atrophy can be measured on the time scale of years by structural magnetic resonance imaging (MRI) (Losseff et al. 1996; Ge et al. 2000). Many MRI studies, including proton spectroscopy (<sup>1</sup>H-MRS), diffusion tensor imaging (DTI), and magnetization transfer (Arnold et al. 1990; Fu et al. 1998; Filippi et al. 1995; Filippi et al. 1998), have demonstrated that NAWM – areas of white matter outside focal lesions that appear qualitatively normal on conventional MRI sequences – is in fact abnormal. In post-mortem studies, Evangelou et al. (Evangelou et al. 2000) found decreased axonal density in MS brain tissue in the absence of macroscopic lesions. DTI studies have shown diffuse increases in mean diffusivity and decreases in fractional anisotropy in NAWM suggestive of microstructural damage, specifically disorganization of the fiber bundles that comprise white matter (Ge

et al. 2004; Werring et al. 1999; Bammer et al. 2000; Hasan et al. 2005). <sup>1</sup>H-MRS studies have demonstrated reduced concentrations of a neuronal marker in NAWM, suggesting axonal loss and/or neuronal metabolic dysfunction in areas without massive inflammation (Pelletier et al. 2003; Kirov et al. 2009; Oh et al. 2004; Leary et al. 1999; Davie et al. 1997; Ciccarelli et al. 2007; Tiberio et al. 2006; Narayana et al. 2004; Inglese et al. 2003; Suhy et al. 2000; Rovaris et al. 2005; Ge et al. 2004; Filippi et al. 2003).

Currently, there are no neuroprotective therapies to prevent axonal degeneration in MS (McFarland et al. 2002; Hauser & Oksenberg 2006; Petkau et al. 2008; Noseworthy 2003). For the most part, disease-modifying therapies used in MS treatment, which are primarily anti-inflammatory, are not effective in the progressive phase of the disease due to a lower overall degree of inflammation. In order to accelerate the development of therapies to treat neurodegeneration in MS, better markers of *degenerating* or sick neurons and axons are required. Irreversible neuronal death as measured by brain atrophy and long-term reductions in NAA concentration is inadequate for assessment of therapeutic efficacy. These gaps in knowledge provide the motivation for the work described in this thesis.

## **4 DIFFUSION WEIGHTED SPECTROSCOPY: THEORY & MODELS**

Diffusion weighted spectroscopy (DWS) combines aspects of two widely used MR methods to gain microstructural information about tissue. DWS (Upadhyay et al. 2007; Kan et al. 2012; Kroenke et al. 2004; Ellegood et al. 2006; van Zijl et al. 1994) blends features of both diffusion weighted imaging (DWI) and magnetic resonance spectroscopy (MRS), allowing measurement of the diffusion properties of intracellular metabolites. DWI is a sensitive technique that provides information about microscopic structural features of anisotropic tissues such as white matter (WM) tracts. However, the pathologic specificity of DWI is limited because the measured signal is derived from water protons, which are found in all tissue compartments (including inflammatory cells, myelin, neurons, and glia). By contrast, MRS is neurochemically and compartmentally specific but provides no microstructural information. However, localized MRS can deliver tissue-specific structural information when combined with diffusion sensitization for compartment-specific metabolites such as N-acetyl aspartate (NAA). DWS-based measurements of NAA should thus provide specific information about axonal microstructure and might consequently serve as useful markers of axonal integrity in the complex setting of demyelination, inflammation, edema, and gliosis seen in MS.

### ***4.1 Measuring molecular diffusion in cells***

#### **4.1.1 Molecular diffusion in solution**

With the advent of a rigorous and robust technique to describe water diffusion that led to breakthroughs in anatomy visualization, diffusion tensor imaging stole the spotlight from nuclear magnetic resonance diffusion and became the focus of much

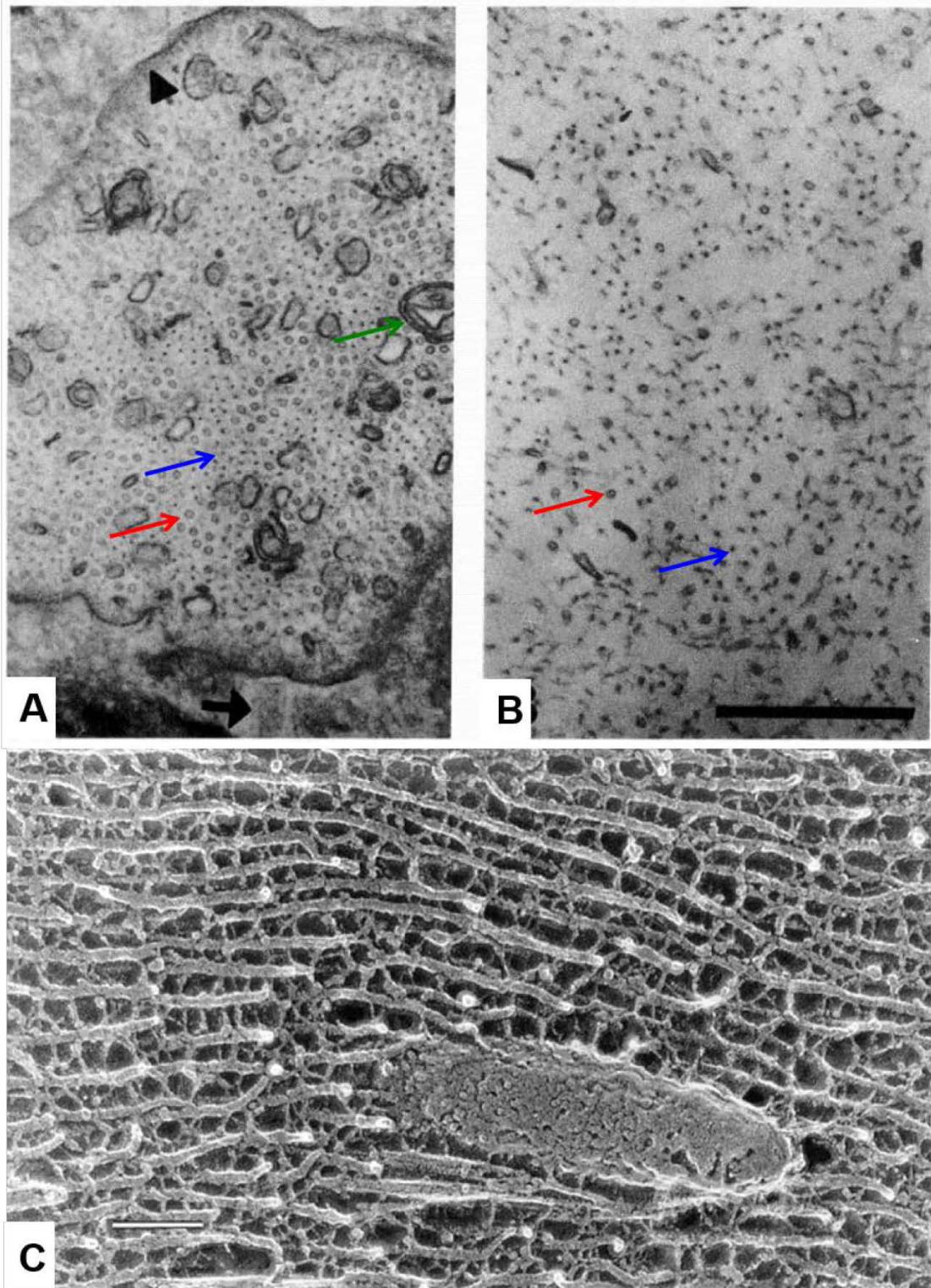
research. Originally, NMR studies of molecular diffusion focused on molecules (other than water) in various solutions and tissue models. For instance, in their first paper on the pulsed gradient spin echo experiment, Stejskal and Tanner tested their technique on aqueous copper sulfate and glycerol at room temperature (Stejskal & Tanner 1965). Indeed, ex vivo pulsed field gradient nuclear magnetic resonance (PFGNMR) experiments afford the means for well planned, tightly controlled studies of biological molecules that can provide detailed information (Callaghan 1984). Isotropic self-diffusion of macromolecules can elucidate information about molecules such as molecular hydrodynamic radius and how the hydrodynamic radius changes in different solutions. By studying a range of solvent dilutions, the viscosity and friction parameters of solutions can be measured. PFGNMR methods can be used in anisotropic mediums such as liquid crystals to detect the thermotropic phase and orientation of the crystal structure. Per Callaghan, the “organizational domain” or scale of common PFGNMR experiments allows for detection of molecular self-displacement on the order of tenths to tens of micrometers (Callaghan 1984). Fortunately, this domain includes the realm of interesting biological microstructure such as axons in the human corpus callosum, which range from 0.1-5  $\mu\text{m}$  in diameter (Aboitiz et al. 1992).

#### **4.1.2 Molecular crowding in cells**

At this point, it could be useful to step back and imagine what intra-neuronal and intra-axonal spaces are like. The cell is sometimes visualized as a lipid bi-layer sack filled with water and some organelles. It turns out that, in the case of most eukaryotic cells, this view is not only overly simplified but highly misleading when it comes to understanding self-diffusion and enzyme kinetics (Ovádi & Saks 2004). The cytoplasm is packed full of soluble macromolecules including enzymes, nucleic acids, structural

proteins, and membranes. It is estimated that macromolecules occupy 20-30% of the volume of a cell – media of this nature is called “crowded,” not “concentrated,” because no single macromolecule has a particularly high concentration (Ellis 2001). In axons, the macromolecular make-up includes highly oriented structures such as microtubules and neurofilaments.

*Figure 4.1. (next page) (A&B) Cross-section of axons and modeled neurofilaments ( electron micrographs, scale bar = 0.5  $\mu$ m). (A) Node of Ranvier as evidenced by lack of myelin and dense cytoskeletal undercoating (arrow head). Microtubules are the small circular structures (red arrows). Neurofilaments appear as dense spots (blue arrows). Vesicular organelles, such as mitochondria (green arrow), are throughout. (B) Myelinated internode with denser neurofilaments and fewer microtubules and organelles than the nearby node of Ranvier. (C) The neurofilament network can be visualized as interconnecting cross bridges connecting to each other and other organelles, such as the mitochondria shown here (quick-freeze deep-etch axon). A&B are reprinted from “Regional modulation of neurofilament organization by myelination in normal axons” by S.T. Hsieh et al., 1994, *Journal of Neuroscience* 14(11), page 6395. Copyright 1994 by the Society for Neuroscience. Reprinted with permission. C is reprinted form “Gene Targeting Studies Begin to Reveal the Function of Neurofilament Proteins” by N. Hirokawa and S. Takeda, 1998, *The Journal of Cell Biology*, 143(1), page 1. Copyright 1998 by the Rockefeller University Press. Reused with permission (non-commercial).*



Neurofilaments (Nfs) are one of the most abundant constituents of the axonal cytoskeleton. Nfs are composed of three related proteins, which are named by their apparent molecular weights (light Nf-L, medium Nf-M and heavy Nf-H) – which share a central rod domain and have different C-terminal regions (Hsieh et al. 1994). In Figure 4.1.A & B, cross-sections through axons demonstrate that the neurofilaments are spread almost uniformly throughout the axoplasm, with somewhat different compositions between nodes of Ranvier and myelinated internodes. Models of neurofilament cross-sections in Figure 4.1.C & D demonstrate that Nfs that appear as electron-dense dots on the micrographs have side arms that extend out from the central backbone (Kim et al. 2011). The phosphorylation state of each of the Nf side-chains is known to regulate axonal transport by altering the ability of the Nfs to participate in Kinesin-based motility or be associated with the stationary axon phase (Shea & Lee 2011). Importantly, a variety of stoichiometric and phosphorylation states of the three Nf proteins are related to various neurodegenerative processes. For example, high levels of hyperphosphorylated Nf-H are found in MS lesions and are associated with disorganized axoskeleton and impaired axonal transport (Petzold et al. 2008; Kim et al. 2011). Also of importance, different phosphorylation states of Nfs will interact differently with water, ions and small molecules in the cytoplasm (Shea & Lee 2011; Petzold et al. 2011).

The precise consequences of molecular crowding within cells remain somewhat controversial. Nonetheless, it is agreed that crowded cytoplasm will influence molecular self-diffusion and molecular interactions. Verkman discusses 3 primary barriers to cytoplasmic diffusion that can be applied to most molecules (each has an associated traffic flow metaphor counterpart): fluid-viscosity (speed), binding (time spent at stop lights), and molecular crowding (route) (Verkman 2002). In a series of studies that utilized probes with fluorescence recovery after photobleaching methods, diffusion of

their probe was around 4 times slower in cytoplasm than in saline. They determined that this was primarily due to probe collisions and secondarily to probe binding while fluid-phase viscosity was low and contributed little to the slower diffusion rate (Verkman 2002). In other words, the diffusion of their probe was most hindered by molecular crowding – it did not have very many direct routes to take.

Brangwynne et al. have used exogenous low molecular weight probes to study the contribution of molecular motor proteins (such as myosin) and filament dynamics (such as microtubule movements) to cytoplasmic motion. Their evidence suggests that the visco-elastic structure of cell scaffolding results in molecular motion that is less than that of pure thermal diffusion. But, mechanical and molecular motors, such as the microtubule system, produce active motion that increases the measured molecule movement back to that predicted by pure thermal diffusion (Brangwynne et al. 2008). They surmise that based on the hydrodynamic coupling of cytoplasm to the cytoskeletal elements, the active movements of microtubules and filaments may drag along the fluid and cause “vigorous stirring and fast transport within the cytoplasm” (Brangwynne et al. 2009).

The concepts of molecular crowding and active or motor-driven flow could have varying, or even contradictory effects, on molecular self-diffusion depending on the size of the molecules and the cell processes and machinery with which the molecules interact. For instance, in Figure 4.2 the large black dots (macromolecules) within each box (cell) take up 30% of the cell area (Ellis 2001). In panel (A), the small molecule can explore the remaining 70% of the area by self-diffusion. In panel (B), we see that a molecule of similar size to the macromolecules would not be able to sample much, if any, of the cell because it would not be able to get through the relatively narrow spaces left by the macromolecules. On the other hand, organized crowding could facilitate



“metabolite channeling,” whereby intermediates are transferred directly from one enzyme to the adjacent enzyme without passing through the free aqueous phase (Ovádi & Saks 2004). Indeed, many studies have demonstrated that macromolecular crowding or confinement enhances the reaction rate of macromolecular interactions and suggest that cells are composed of micro-compartments based on the concentration of various metabolic enzyme complexes (Minton 2001; Rohwer et al. 1998).

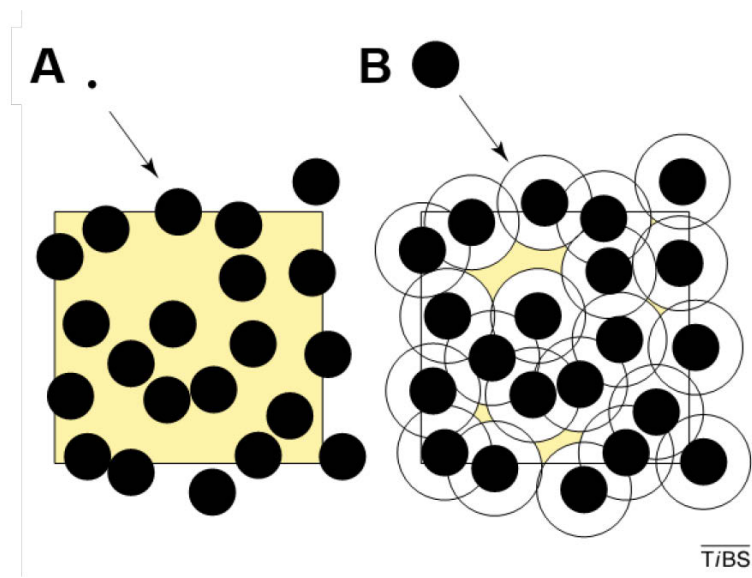


*Figure 4.2 Molecular crowding and volume exclusion. The yellow boxes represent cells filled with macromolecules (black dots). In (A), the small molecule will have many collisions with macromolecules, but it can sample the remaining 70% of the cytosol that is not occupied by macromolecules. In (B), the macromolecules have been marked with an open circle, which represents the radius of the molecule of interest. This molecule will not be able to pass between closely spaced macromolecules and, therefore, will not be able to sample the cytoplasm. Adapted from “The Influence of Macromolecular Crowding and Macromolecular Confinement on Biochemical Reactions in Physiological Media” by A.P. Minton, 2001, *The Journal of Biological Chemistry*, 276(14), page 10578. Copyright 2001 by the American Society of Biochemistry and Molecular Biology. Adapted with permission.*

### 4.1.3 Molecular crowding and NMR methods

The issues of molecular crowding and confinement may be important to our understanding of and approach to NMR-based diffusion methods. For instance, an early study of ionic mobility in muscle cells showed the diffusion constant of a number of metabolites, including phosphorous-containing compounds (such as ATP), to be 2 times slower in myocytes compared to free water (Kushmerick & Podolsky 1969). This study measured labeled radioactive isotope concentrations along the length of single muscle fibers at various times after point application (both at 20° C). From this work, it was concluded that fluid-phase viscosity is the primary determinant of hindered self-diffusion in vivo since most of the metabolites were affected to a similar degree. In contrast, some of the first NMR studies of metabolite diffusion in vivo calculated the unbound diffusivity of phosphocreatine and ATP in muscle cells to be around 90% of the in vitro free diffusion measurements at 37° C (van Gelderen et al. 1994; de Graaf et al. 2000). These measurements were made with <sup>31</sup>P diffusion weighted spectroscopy with pulsed-gradient stimulated echo sequences and demonstrated a very high self-diffusional mobility of phosphorous-containing compounds. The seeming contradiction between these accounts of phosphorous compound diffusion in muscle fibers could be explained, in large part, by the heterogeneous micro-compartmentation or confinement of these molecules in intact cells (Ovádi & Saks 2004). In certain “compartments” (segregation not based on membranes or other lipid bi-layers), ATP is interacting with crowded enzymes and has both a very small apparent diffusivity and a very short T2 due to these molecular interactions. Outside of these “compartments” the macromolecular density is quite low and molecules such as ATP may exhibit self-diffusion similar to that in free water. In this situation, NMR diffusion techniques would measure the apparent diffusion coefficient of ATP to be similar to that in free water. On the other hand, in the isotope

labeling method the muscle fibers were extracted from the animal and measured in solution at room temperature. It is possible that, under these conditions, the micro-compartmentation dissolves and the macromolecules fill the cell homogeneously and dramatically increase the fluid-phase viscosity. In this situation, the macroscopic diffusion measurements by isotope labeling would portray diffusivity measurements that are slower than the in vivo case.

#### **4.1.4 Compartmentation – intra- vs. extra-cellular**

The ability of diffusion measurements to report on the geometry of restricting environment depends a great deal on the location of molecules of interest and the permeability of the restrictive barriers. Van Zijl et al. reported on the ability of diffusion weighted methods to distinguish between extracellular and intracellular environments based on the bi-exponential diffusion behavior of water and metabolites in a medium containing cells compared to the medium alone (van Zijl et al. 1991). Water and metabolites in the less restricted extra-cellular compartment diffuse more quickly, and their signal is virtually lost with higher diffusion weighting. Conversely, the intracellular, restricted component is smaller and is unmasked at higher b-values. Multi-exponential behavior such as this is only possible with a relatively impermeable barrier to diffusion separating the extra and intracellular compartments. Otherwise, for fast exchange between the compartments, the separate diffusion rates would be indistinguishable (van Zijl et al. 1994).

## 4.2 Diffusion of N-acetyl aspartate in vivo (humans and animals)

### 4.2.1 Measurements of NAA diffusivity in vivo

Table 4.1. Summary of NMR studies of in vivo N-acetyl aspartate diffusion. (Diffusivity:  $\mu\text{m}^2/\text{ms}$ )

<b>Manuscript</b>	<b>Tissue</b>	<b>NAA ADC/ MD</b>	<b>NAA <math>\lambda_{\parallel}</math></b>	<b>NAA <math>\lambda_{\perp}</math></b>	<b>NAA FA</b>	<b>VOI (<math>\text{cm}^3</math>)</b>	<b># dirs</b>	<b>T</b>
<i>(Posse et al. 1993)</i>	SWM	0.18				18.0	1	1.5
<i>(van der Toorn et al. 1996)</i>	Rat, SWM, ischemia	0.16				0.45	1	4.7
<i>(Dijkhuizen et al. 1999)</i>	Rat, SWM, cytotoxic edema	~0.18				0.98	1	4.7
<i>(de Graaf et al. 2001)</i>	Rat, SWM	0.15				2.4	3	4.7
<i>(Harada et al. 2002)</i>	SWM	0.18				8.0	1	1.5
<i>(Kroenke et al. 2004)</i>	CC	0.22	0.32	0.12		4.8	2	1.5
<i>(Ellegood et al. 2005)</i>	SWM	0.14				15.6	3	3
	OGM	0.12						
<i>(Ellegood et al. 2006)</i>	Body CC	0.16	0.28	0.13	0.61	10.2	6	3
	Genu CC	0.19	0.30	0.10	0.55	12.0		
	CST	0.18	0.31	0.11	0.59	10.6		
	OGM	0.14	0.21	0.10	0.51	10.6		

Table 4.1. cont.

<b>Manuscript</b>	<b>Tissue</b>		<b>NAA ADC/ MD</b>	<b>NAA <math>\lambda_{  }</math></b>	<b>NAA <math>\lambda_{\perp}</math></b>	<b>NAA FA</b>	<b>VOI (cm<sup>3</sup>)</b>	<b># dirs</b>	<b>T</b>
<i>(Upadhyay et al. 2007)</i>	Body CC		0.17	0.25	0.12	0.52	5.0	6	3
	Genu CC		0.16	0.32	0.08	0.72			
<i>(Upadhyay et al. 2008)</i>	Arcuate Fas- ciculus	Left	0.17	0.27	0.12	0.53	4.0	6	3
		Right	0.17	0.25	0.14	0.43			
<i>(Ellegood et al. 2010)</i>	Body CC		0.21	0.34	0.13	0.56	15.3	6	3
	SWM		0.21	0.33	0.15	0.47	15.6		
	OGM		0.18	0.23	0.16	0.25			
<i>(Kan et al. 2012)</i>	SWM		0.26				6.0	3	7
	OGM		0.15						

\*Some values are estimated or calculated from data provided in tables in manuscripts (e.g. where  $\lambda_2$  &  $\lambda_3$  are given, the  $\lambda_{\perp}$  can be calculated.)

# dirs. = number of diffusion weighted directions measured; T = strength of magnet (Tesla)  
SWM = Subcortical White Matter (frontoparietal); OGM = Occipital Gray Matter; CC = Corpus Callosum; CST = Corticospinal Tract

In the last two decades, a handful of laboratories have researched NMR diffusion weighted spectroscopy techniques in animals and humans. Here, I will focus on the results pertaining to N-acetyl aspartate diffusion.

Table 4.1 summarizes the NAA diffusivity measurements from a substantial proportion of the in vivo diffusion weighted proton spectroscopy studies of brain performed in the last 20 years. For all studies listed, the apparent diffusion coefficient (ADC) or mean diffusivity (MD) was reported. For later studies, diffusion weighting was applied in more directions and other diffusivity values were reported. Initially, ADC

values were measured with diffusion weighting in one direction and multiple  $b$ -values ranging from 0-2,200 s/mm<sup>2</sup> in humans (Posse et al. 1993; Harada et al. 2002) and 0-4,400 s/mm<sup>2</sup> in rats (van der Toorn et al. 1996; Dijkhuizen et al. 1999). Using these parameters, the ADC of NAA in large voxels containing primarily subcortical white matter (SWM) and some cortical gray matter was found to be around 0.16  $\mu\text{m}^2/\text{ms}$ . Additionally, the ADC values of both water and NAA were seen to decrease in the states of ischemia and excitotoxic injury (van der Toorn et al. 1996; Dijkhuizen et al. 1999; Harada et al. 2002). With measurements along 2 or 3 diffusion weighting directions, this ADC value was confirmed (Kroenke et al. 2004; de Graaf et al. 2001). Kroenke et al. collected NAA diffusion data in humans in the splenium of the corpus callosum (CC) along 2 diffusion weighting directions oriented to be primarily parallel and perpendicular to the axon bundles of interest. This resulted in diffusivity measurements of 0.32  $\mu\text{m}^2/\text{ms}$  parallel and 0.12  $\mu\text{m}^2/\text{ms}$  perpendicular (Kroenke et al. 2004).

Diffusion tensor spectroscopy was born when Ellegood et al. implemented 6 orthogonal diffusion weighting directions and calculations of fractional anisotropy (FA), mean diffusivity (MD), parallel diffusivity ( $\lambda_{||}$ ), and perpendicular diffusivity ( $\lambda_{\perp}$ ) into a diffusion weighted spectroscopy scheme (Ellegood et al. 2006). In this study, white matter voxels were located in highly anisotropic structures such as the CC and the corticospinal tract (CST) and exhibited MD values slightly higher than the previously measured ADC values in SWM. The NAA FA values reported are very close to the water FA values calculated from DTI data in the CC and CST. A later study by Ellegood et al. demonstrated that metabolite FA values in gray matter are erroneously high when the maximum  $b$ -values used for diffusion weighting are too low, while white matter measurements were found to be less sensitive to maximum  $b$ -value. In particular, maximum  $b$ -values around 1800 s/mm<sup>2</sup> produced FA values in gray matter of 0.60,

which is a high degree of anisotropy for largely isotropic tissue. With a maximum  $b$ -value of  $5000 \text{ s/mm}^2$ , FA becomes  $\sim 0.30$  - a more likely value. While it is somewhat counterintuitive, this  $b$ -value dependence of FA may be related to the low signal to noise ratio (SNR) of magnetic resonance spectroscopy, causing an erroneous spread of the diffusion tensor eigenvalues with lower maximum  $b$ -values and an artifactual increase in the FA. In other words, in more isotropic tissue, poor SNR spectra will demonstrate more accurate directional differences when  $b$ -values are high enough to separate the contributions from each direction. Additionally, using a bootstrap-like analysis of a different data set, Ellegood showed that the intrasubject variability of FA measurements ranged from 17–37% while MD measurements were around 10% (Ellegood et al. 2006). Taken together, the higher intrasubject variability and  $b$ -value dependence of FA measurements suggests that this diffusion measurement for metabolites should always be interpreted within the parameters of the given experiment.

In Figure 4.3 the NAA diffusivity values for white matter from Table 4.1 are plotted by year of publication. From this plot, we see that single or averaged NAA diffusion measurements, which do not account for the diffusion direction of NAA in anisotropic tissue, provide apparent diffusion coefficients of around  $0.18 \mu\text{m}^2/\text{ms}$ . Alternatively, NAA diffusion measurements made with attention to fiber orientation as in Kroenke et al. (Kroenke et al. 2004) or with enough directional resolution to diagonalize the diffusion tensor, as in Ellegood et al. and Upadhyay et al. (Ellegood et al. 2010; Ellegood et al. 2006; Upadhyay et al. 2007; Upadhyay et al. 2008), provide parallel diffusivity measurements much closer to the free diffusion values measured for NAA in aqueous solution. Kan et al. (Kan et al. 2012) studied metabolite diffusivity in white and gray matter with diffusion weighted spectroscopy methods at 7 tesla. While their measurements used only 3 diffusion weighting directions, greater field strength afforded

them the ability to get adequate spectra SNR from smaller voxels. This way they could acquire spectra from a small white matter voxel with very little partial volume effects from other tissue types. With this technique, they found the ADC of NAA in white matter and gray matter to be 0.24 and 0.17  $\mu\text{m}^2/\text{ms}$ , respectively (Kan et al. 2012). This relationship of lower ADC of NAA in gray matter has been seen previously and may explain why their smaller white matter voxel with less gray matter partial volume averaging exhibited higher ADC values.

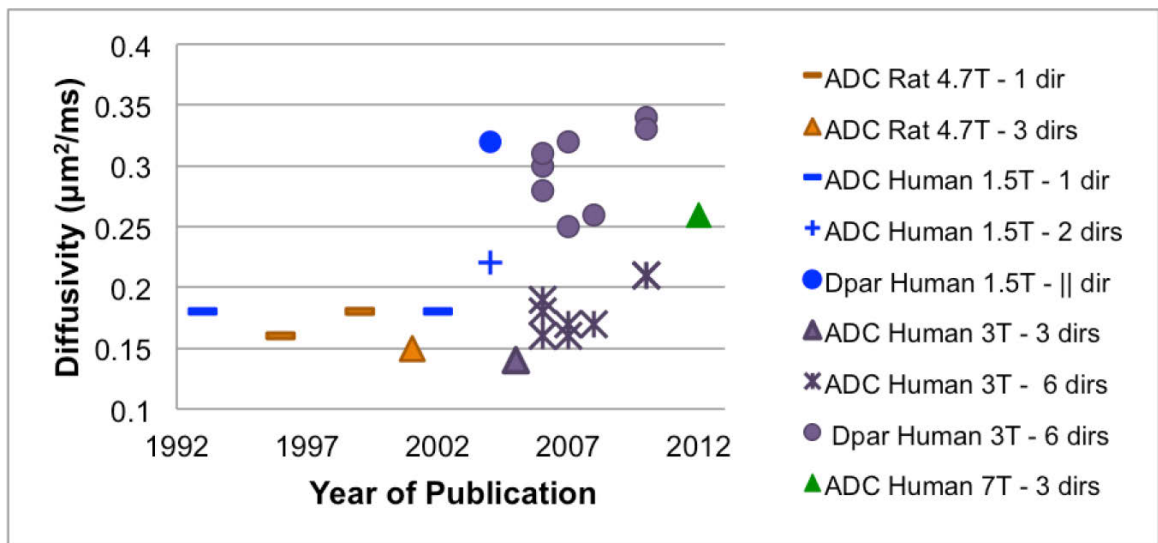


Figure 4.3 ADC and  $\lambda_{||}$  (when available) for the studies listed in Table 4.1.

#### 4.2.2 Using NAA diffusion to study microstructure

Diffusivity measurements of intracellular metabolites can shed light on issues of cytosolic viscosity and crowding. Furthermore, studying the restricted diffusion of metabolites such as NAA can tell us about the microstructure in which these molecules reside. Upadhyay et al. measured NAA diffusivity with 6 diffusion weighting directions across 2 adjacent segments of the CC – the genu and body. Of note, NAA FA values were different between these two segments mainly due to larger  $\lambda_{\perp}$  and a corresponding smaller FA in the body of the CC. Previous histological studies of axon diameter



distributions in the CC have shown that the axons of the body of the CC are on average, larger than those in the genu (Aboitiz et al. 1992). These diffusion weighted spectroscopy measurements could be detecting these axon diameter distribution differences. Similar differences in  $\lambda_{\perp}$  and FA were seen in a separate study of right versus left arcuate fasciculus suggesting axon diameter lateralization of these white matter bundles (Upadhyay et al. 2008).

These microstructural measurements of axon diameter have been extended further to examine the microscopic angular dispersion of axons in white matter. Ronen et al. have developed a model of NAA diffusion in highly coherent white matter bundles that uses diffusion measurements along 2 directions acquired to be mostly parallel and perpendicular to the bundle of interest. The diffusion weighted signal values attained are then fit to a model of diffusion in cylinders which accounts for the nearly Gaussian (free) diffusion of metabolites parallel to the long axis of fibers while diffusion perpendicular to the fibers is expected to be highly restricted by cell membranes and other microstructural barriers. This model utilizes DTI data to correct for the effect of macromolecular curvature within the spectroscopy voxel of interest on the metabolite diffusion measurements (Ronen et al. 2013). This model was compared to independent histological studies in which white matter tissue anisotropy and microscopic orientation dispersion were measured in whole brain slices (Budde & Frank 2012; Annese 2012). While the histological methods are only able to establish fiber orientation distributions in 2 dimensions, comparisons of these data with DTI modeled diffusion weighted spectroscopy of NAA gave very similar values for microscopic angular dispersion in the anterior CC – the standard deviation of fiber angles was 18 degrees (Ronen et al. 2014). These data demonstrate that carefully planned diffusion weighted spectroscopy studies can be utilized to gain specific information about NAA diffusivity and mean axonal

diameter in a very small region of the CC.

Diffusion weighted metabolite measurements have also been combined with neuronal functional activation studies. Branzoli et al. studied metabolite diffusion in the occipital cortex while subjects looked at a flickering checkerboard visual stimulus (Branzoli et al. 2012). They detected an increase in the apparent diffusion coefficient of metabolites, including NAA. This change could be due to cell swelling with activation that could lead to decreased cytoplasmic viscosity. Also, there could be activity depended changes in cytoplasmic streaming that are measured as an overall increased in the diffusivity of intracellular metabolites. In any case, the ability of diffusion weighted spectroscopy to detect microstructural changes with activation suggests that this technique may be sensitive to a variety of changes associated with pathology.

#### **4.2.3 Diffusion weighted NMR with ultra-short diffusion times**

In diffusion weighted NMR, oscillating gradients can be used to assess the diffusion time and frequency dependence of molecular diffusion. These sequences allow for the measurement of diffusion with very short diffusion times. Does et al. demonstrated that oscillating gradient diffusion experiments with diffusion times as short as 375  $\mu\text{s}$  can detect the apparent diffusion coefficient (ADC) value of water in vivo to be as much as 24% higher than experiments using the conventional diffusion times of pulsed gradient spin echo sequences (Does & Gore 2000; Does et al. 2003). The ADC measurements made with very short diffusion times are much closer to those predicted for free diffusion in an aqueous environment. Marchadour et al. applied a similar oscillating gradient technique to diffusion weighted spectroscopy measurements and saw analogous increases in the ADC of endogenous intracellular metabolites (Marchadour et al. 2012). By modeling in vivo brain diffusion as a series of isotropically

oriented cylinders, which they called the neurite model, Marchadour et al. found the diffusivity of the intracellular metabolite N-acetylaspartate (NAA) to be  $0.59 \mu\text{m}^2/\text{ms}$  in cylinders of approximately  $1.7 \mu\text{m}$  diameter. This diffusivity value is about 25% smaller than the unrestricted, free diffusivity of NAA measured in water. This work suggests that cytoplasmic streaming or other active processes are not main contributors to the movement of endogenous metabolites and supports the validity of thermal (Brownian) diffusion models of in vivo metabolite diffusion. Importantly, the data of Does et al. and Marchadour et al. support the notion of measuring the self-diffusion of small molecules, such as water and NAA, with NMR methods to assess cell microstructure.

### ***4.3 Modeling diffusion in impermeable cylinders***

As NAA is found primarily within axons in WM, measures of NAA diffusivity should provide information about axonal structure without contributions from extra-axonal compartments. The intra-axonal location of NAA, together with findings that intact cell membranes are relatively impermeable to NAA and that neuronal export is controlled by a transporter (Urenjak et al. 1993; Moffett et al. 2007; Madhavarao et al. 2003) leads to the prediction that under normal physiological circumstances, NAA should preferentially diffuse parallel to the long axis of axons with a similar anisotropy to intra-axonal water.

In order to predict how pathological changes in axons could influence NMR measurements of NAA diffusion, a series of axon models were tested using the Random Walk Simulator Software (RWS) made available by Landman et al. (Landman et al. 2010). RWS provides a three dimensional framework for simulating restricted diffusion in multiple compartments. In particular, RWS accounts for the interactions between moving, non-interacting particles and the restricting compartment that contains them.

To simulate coherent white matter bundles, the diffusion of NAA and water molecules was modeled in cylinders oriented parallel to each other in a lattice block. The diffusion coefficient of NAA molecules was set at  $D = 0.7 \mu\text{m}^2/\text{ms}$  – an approximate value for the unrestricted diffusivity of NAA in an aqueous solution at 37° C (Kan et al. 2012). For water,  $D = 2.0 \mu\text{m}^2/\text{ms}$ . Diffusion experiments were simulated at 3T with a transverse relaxation time constant for NAA of 250 ms (NAA  $T_2 = 250$  ms) (Kirov et al. 2008; Kirov et al. 2010) and for water of 100 ms ( $\text{H}_2\text{O } T_2 = 100$  ms) (Lu et al. 2005). The maximum diffusion time was 60 ms, and gradient values ranged from 0-60 gauss/cm making for b-values ranging from 0-14,000  $\text{s}/\text{mm}^2$ . To simulate diffusion, the number of spins used in each model was  $10^5$  and the simulator executed time-steps of  $t = 1$  ms giving step lengths of  $l = \sqrt{6D\Delta t} = 2.05 \mu\text{m}$ . To account for the intracellular localization of NAA, only an intracellular compartment with non-permeable boundaries was modeled. Therefore, when an NAA spin encountered a boundary, it was always specularly reflected. For water, spins were initialized both inside and outside of the compartments and the boundary permeability was set at  $10^{-8}$  cm/s. Therefore, when a water spin encountered a boundary it was either specularly reflected or transmitted depending on the boundary permeability and a parameter set to assure no net flux across the boundary.







	Healthy	Bulge	Crimp	Broken	Sphere
Cylinder diameter	1.5 $\mu\text{m}$	1.5 $\mu\text{m}$	1.5 $\mu\text{m}$	1.5 $\mu\text{m}$	na
Structure alteration		4 $\mu\text{m}$ sphere	Diameter reduced to 60%	5 $\mu\text{m}$ gap	4 $\mu\text{m}$ sphere
					
Lattice Dimension = 20 ( $\parallel$ ) $\times$ 10 $\times$ 10 $\mu\text{m}$ Structure alteration repeated every 10 $\mu\text{m}$ (on center)					

Figure 4.4 Geometric models of axonopathy used for simulations.

Four models of axon geometry, and a sphere for comparison, were studied in a  $20 \times 10 \times 10 \mu\text{m}$  lattice. As shown in Figure 4.4, the models were: (1) healthy axons that consisted of a single infinite cylinder 1.5  $\mu\text{m}$  in diameter; (2) bulging axons that consisted of a 1.5  $\mu\text{m}$  diameter cylinder studded by spherical bulges of 4  $\mu\text{m}$  diameter repeated every 10  $\mu\text{m}$  on center; (3) crimped axons that consisted of a 1.5  $\mu\text{m}$  diameter cylinder being squeezed by two 4  $\mu\text{m}$  spheres every 10  $\mu\text{m}$  so that the cylinder was reduced to a minimum diameter of 0.9  $\mu\text{m}$  at those crimps; (4) broken axons consisting of 15  $\mu\text{m}$  segments of 1.5  $\mu\text{m}$  diameter cylinders separated by 5  $\mu\text{m}$  gaps; and (5) spheres with a diameter of 4  $\mu\text{m}$ .

For each of the axons models shown in Figure 4.4, the average motion-probability propagator, the probability density function (PDF, see Chapter 3), for the restricting geometry can be calculated. This was accomplished with simulations of diffusion weighted attenuation due to molecular motion – in this case initialized with

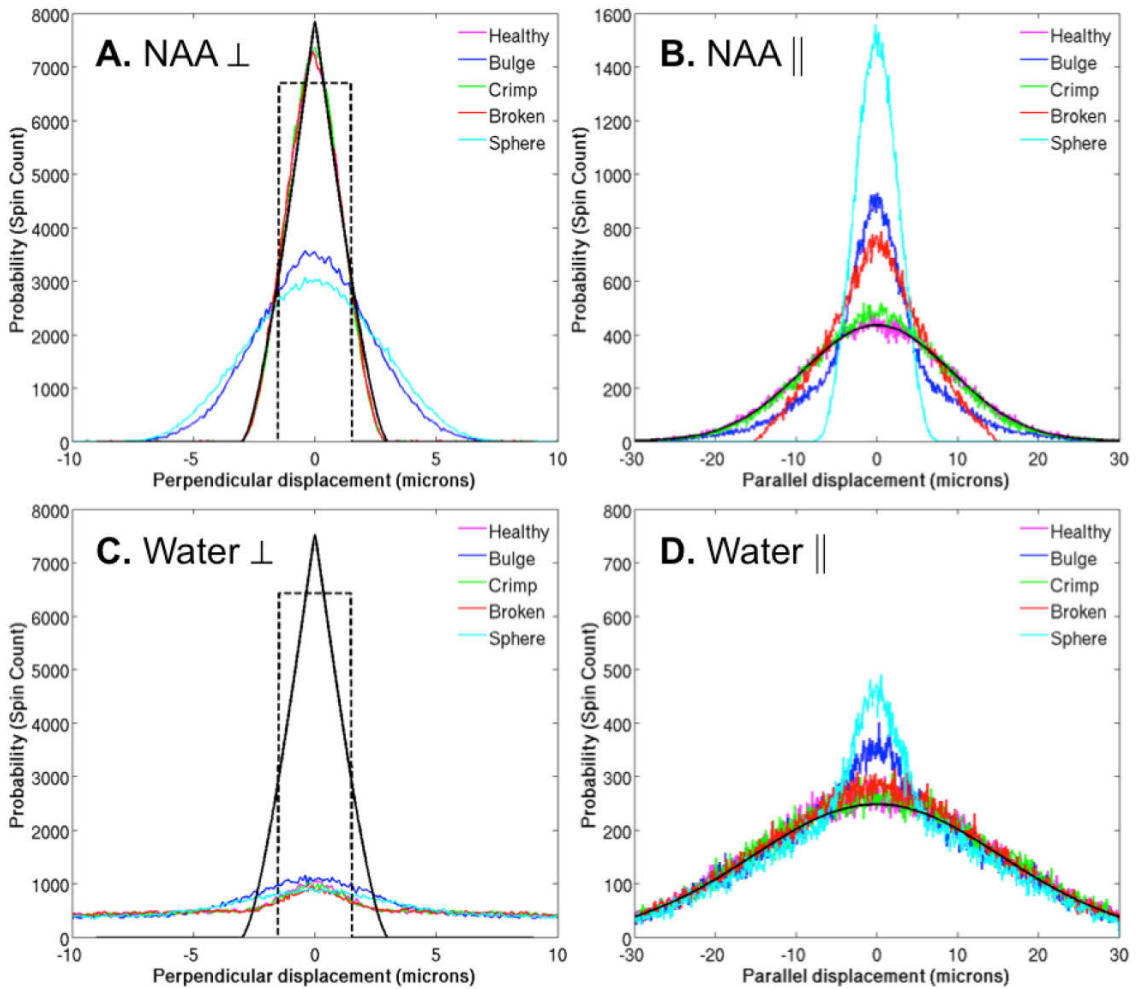


Figure 4.5 NAA (A & B) and water (C & D) motion-probability propagators for each of the axon geometry models shown in Figure 4.4. (A & C) Plot of number of spins versus displacement perpendicular to the axis of the axon cylinders. The dotted line box represents the cylinder diameter. (B & D) Plot of spin counts versus displacement parallel to the axon length. The black curve shows free Gaussian diffusion.

100,000 spins. The motion-probability propagators for NAA and water are plotted in Figure 4.5 separately for displacement perpendicular and parallel to the long axis of the cylinders.

For NAA, the displacement perpendicular to the cylinders/axons appears to be mostly determined by the maximum diameter along the cylinder (Figure 4.5.A). The healthy, crimp, and broken models closely follow each other and the motion-probability propagator that can be found analytically for cylinder cross-section (represented by the black triangle). The bulge and sphere models display a much wider distribution due to the wider 4  $\mu\text{m}$  diameter swellings. The parallel displacement plot demonstrates a more diverse group of distributions (Figure 4.5.B). The healthy and crimp models remain close to the Gaussian diffusion that would be expected along the length of the cylinder if diffusion remains unrestricted. The sphere strays far from Gaussian diffusion since it is limited by 4  $\mu\text{m}$  in all dimensions. The bulge and broken models demonstrate intermediate behaviors between the Gaussian distribution and the isotropically restricted sphere distribution.

For water, where the spins are located both inside and outside the modeled compartments, the perpendicular simulated motion probability propagators do a poor job of approximating the calculated motion probability propagator (Figure 4.5.C, solid black triangle) that would be expected for a cylinder cross-section (dashed line). Only the bulged model differs from the others. Likewise, only the bulged and sphere models demonstrated non-Gaussian diffusion for the parallel motion probability propagator (Figure 4.5.D).

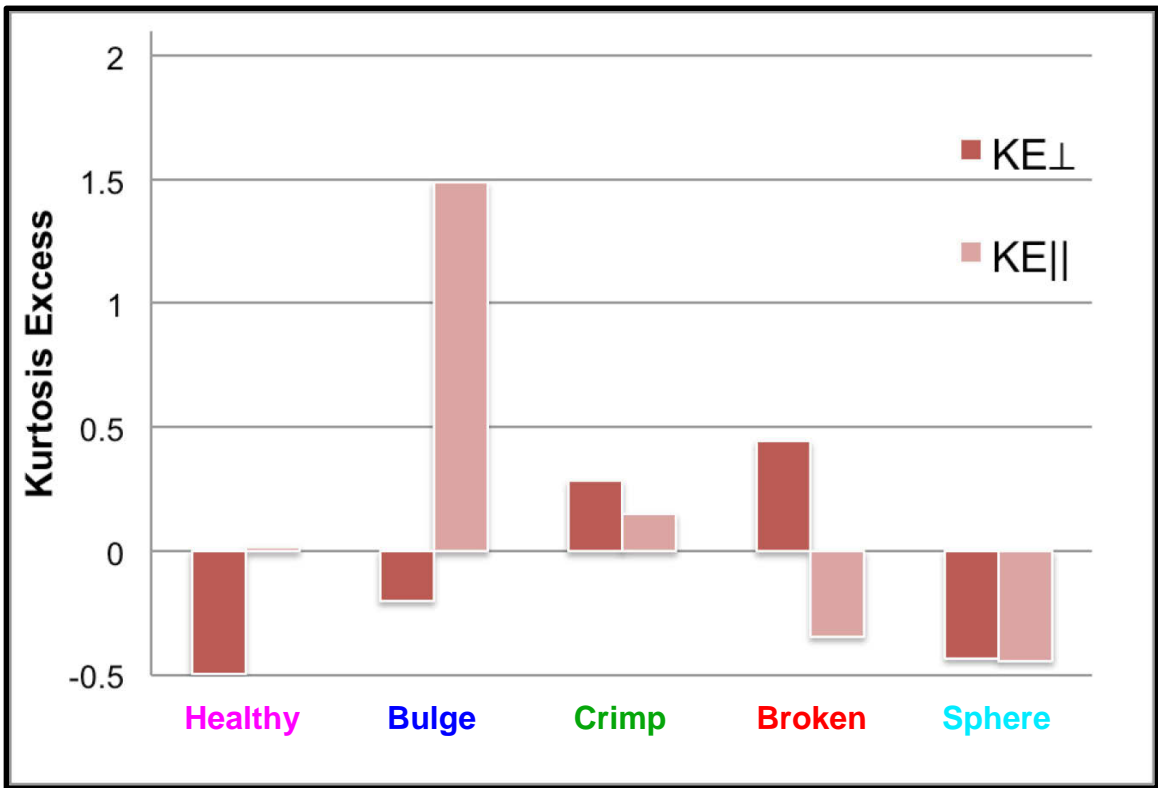


Figure 4.6 NAA kurtosis excess (KE) values for the perpendicular and parallel motion-probability propagator distributions.

The difference between a given probability density function and a Gaussian distribution can be quantified with a measure called Kurtosis Excess (KE), which compares the kurtosis of the probability density function to the kurtosis of the Gaussian distribution of equal variance. Positive values of KE describe distributions with taller peaks and wider tails. Likewise, distributions with shorter broader peaks and thin tails will have negative values of KE. For the simulations shown in Figure 4.5, the KEs and diffusivity measurements (mean, parallel and perpendicular diffusivity) were calculated and are shown for NAA in Figure 4.6 and Figure 4.7 and for water in Figure 4.8 and Figure 4.9. Of note, the diffusivity values of NAA shown in Figure 4.7 are quite different from the measured values reported in Table 4.1. There are several, compatible



explanations for this discrepancy. In the model, all of the cylinders are exactly parallel and uniform in diameter. In contrast, we know that, even in the most coherent white matter, such as the corpus callosum, axons have a range of diameters and microscopic orientations. Furthermore, in vivo DWS measurements require large voxels to have adequate SNR, but this contributes to vast differences in macroscopic curvature across a voxel. Therefore, in vivo diffusion measurements intended to be perpendicular to a group of axons of interest will likely overestimate the perpendicular diffusivity and underestimate parallel diffusivity since diffusion weighting will take place at an oblique angle to many fibers. Additionally, larger diameter fibers may contribute to a larger value for perpendicular diffusivity.

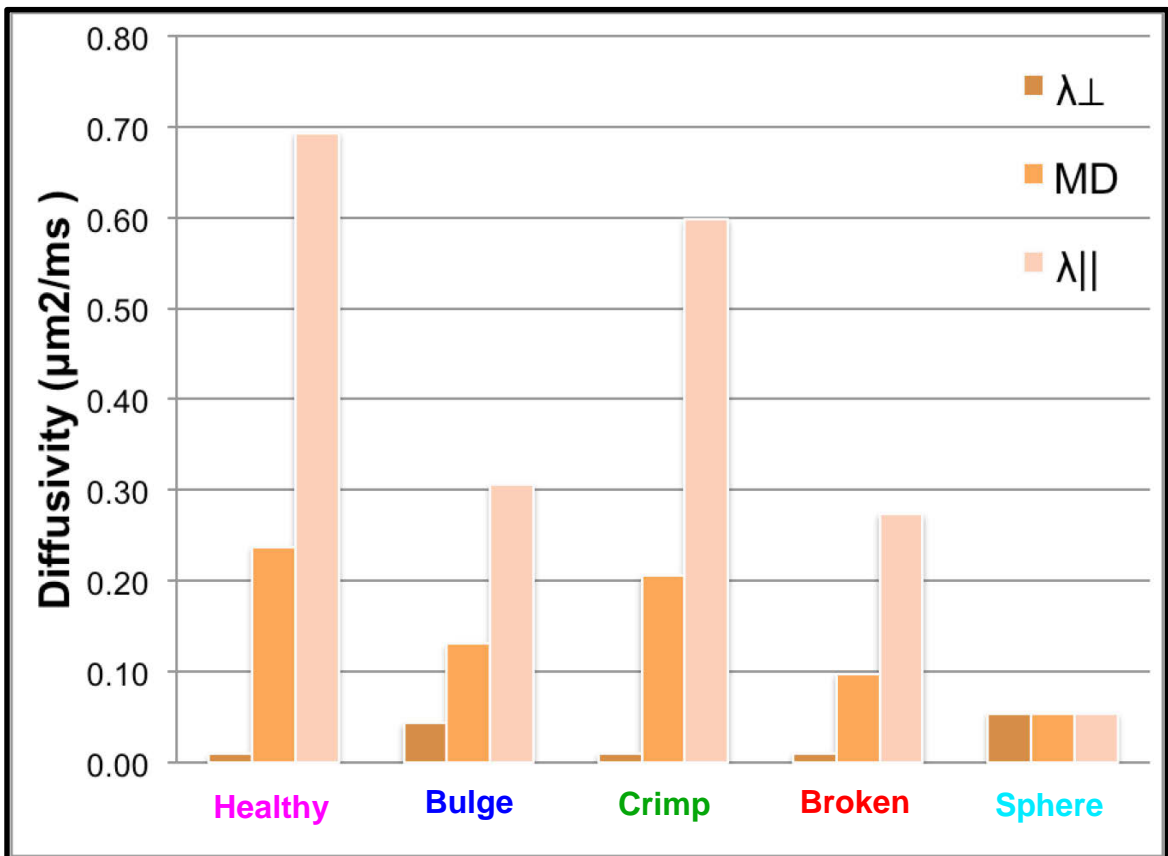


Figure 4.7. NAA diffusivity values of modeled diffusion in a variety of geometries.

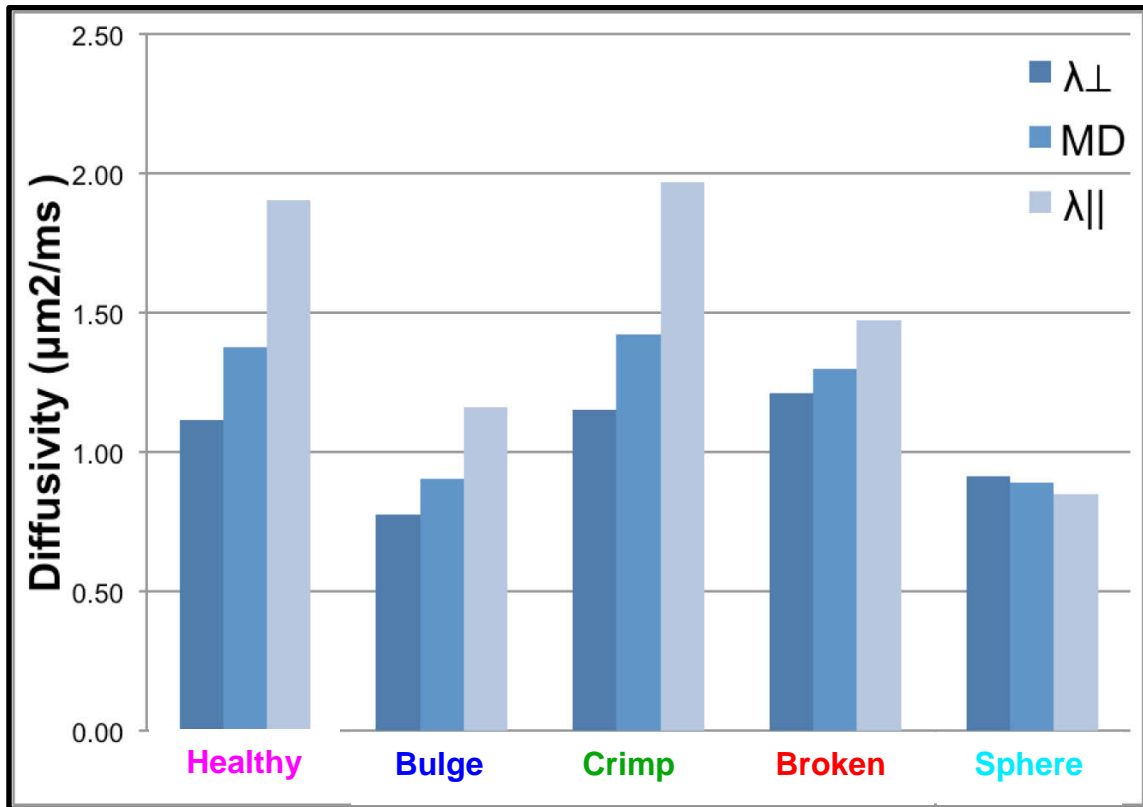


Figure 4.8. Water kurtosis measures.

The patterns of mean, parallel, and perpendicular NAA diffusivity measurements seen for the various axon models suggest that these measurements may be useful for interpreting NAA diffusion changes in tissue. The diffusion measurements of NAA show that a crimped axon would be very difficult to distinguish from healthy axons based on these metrics where parallel and mean diffusivity only decreased to 86% and 87% of the healthy condition values. Both the bulge and broken axons exhibit decreased parallel diffusivity at 44% and 40% of healthy axon parallel diffusivity. The distinguishing factor between the bulge and broken models is a dramatic increase in perpendicular diffusivity for the bulge compartmentation, a 460% increase.

On the other hand, the water diffusivity measures show that broken axons would be associated with a drop in parallel diffusivity to 77% and an increase in perpendicular

diffusivity to 109% of healthy. Bulging would be associated with both parallel and perpendicular diffusivity drops to 61% and 70% of the healthy axon values. Kurtosis excess would show mild elevations for perpendicular measures in the bulge state. Overall, the diffusion measurement changes for water are modest compared to those for NAA based almost solely on the compartmentation of the molecules.

Simulations of NAA diffusion in different models of damaged axons using the RWS framework could be tested in vivo with MS patients, since histological characterizations of diffuse WM injury in MS provide a picture of axonal degeneration similar to animal models and other human pathologies, e.g., axonal swellings and end bulbs,  $\beta$ -amyloid precursor protein accumulation, and neurofilament alterations (Mahad et al. 2009).

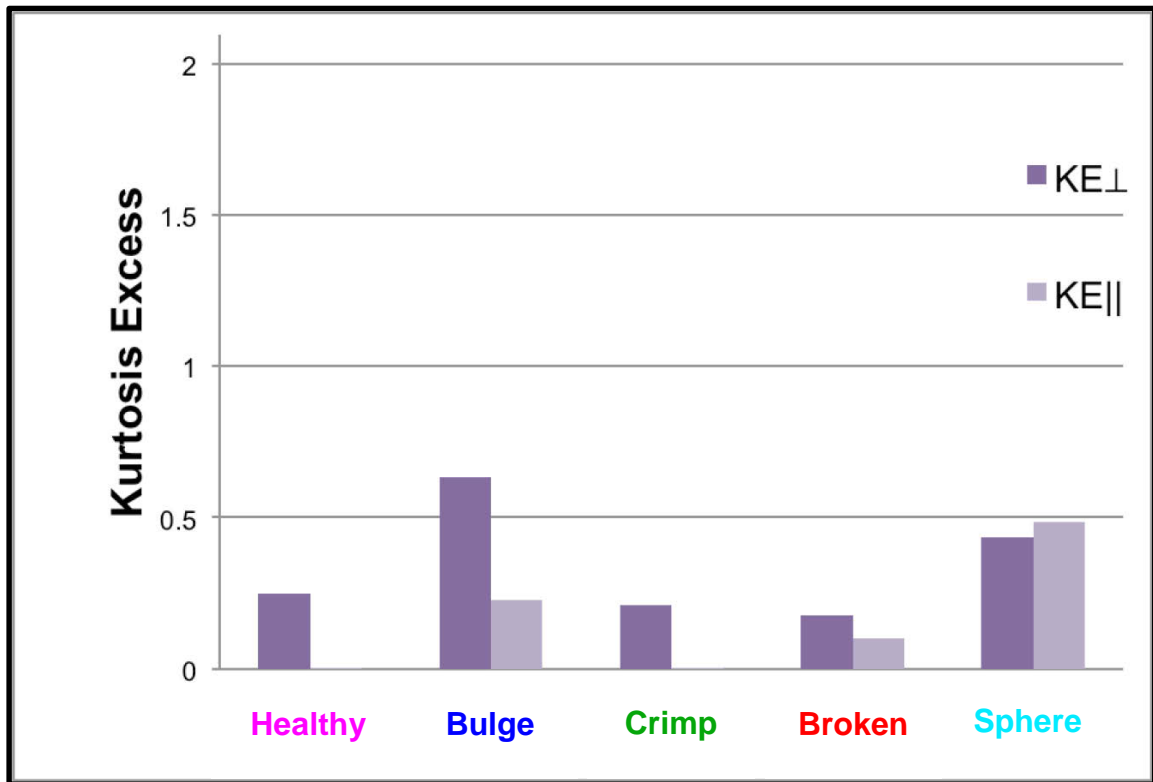


Figure 4.9. Water diffusivity measures of modeled diffusion in a variety of geometries.

## **4.4 Conclusions**

NMR diffusion weighted spectroscopy methods provide a non-invasive means for studying the aqueous phase and restricting geometry of various biological tissue compartments in vivo. Therefore, diffusion weighted spectroscopy can fill knowledge gaps that are unavailable to any other technique. For instance, studies of the diffusion coefficient of NAA in vivo have demonstrated that the intracellular aqueous compartment is packed full of macromolecules and yet there is enough open-space for NAA molecules to sample their environment and report back on the viscosity of the cytoplasm and the shape of the restricting environment. On the other hand, with current systems, the limitations, in terms of SNR and resolution, of diffusion weighted spectroscopy make the technique challenging, especially for use in the clinic. In the next chapters, I will describe the particular diffusion weighted spectroscopy methods that I have utilized and discuss their clinical feasibility and what they might be able to tell us about neurodegeneration in multiple sclerosis.

## **5 DIFFUSION WEIGHTED SPECTROSCOPY METHODS**

As discussed in Chapter 4, diffusion weighted spectroscopy is a technique that has been in research and development for some time. In this chapter, I will lay down the precise methods utilized for these experiments. In Chapter 6, some parameters for obtaining reproducible and reliable results in future experiments will be established.

### **5.1 Hardware**

All magnetic resonance imaging (MRI) and spectroscopy (MRS) data were obtained with Philips Achieva scanners (Philips Medical Systems, Cleveland, Ohio) and multi-channel receive head coils (Nova Medical, Inc., Wilmington, MA). Data were collected on the Philips 7 tesla scanner at the F.M. Kirby Research Center for Functional Brain Imaging at the Kennedy Krieger Institute (associated with the Johns Hopkins Medical Institutions) in Baltimore, Maryland, USA by myself (ETW); on the Philips 7 tesla scanner at the C.J. Gorter Center for High Field MRI Research at the Leiden University Medical Center in Leiden, The Netherlands by Ece Ercan; and on the Philips 3 tesla scanners at the Department of Radiology and Imaging Sciences, at the National Institutes of Health Clinical Center in Bethesda, Maryland, USA by myself (ETW).

All patient and healthy volunteer data was acquired with consent of the subjects under approved Internal Review Board protocols of the respective institutions.

Table 5.1. Scanner parameters

<b>Parameter</b>	<b>NIH</b>	<b>Leiden</b>	<b>Hopkins</b>
<i>Scanner Make/Model</i>	Philips Achieva	Philips Achieva	Philips Achieva
<i>Field strength</i>	3 T	7 T	7 T
<i>Max gradients</i>	60 mT/m	40 mT/m	40 mT/m
<i>Transmit coil</i>	Quadrature volume	Quadrature volume	Quadrature volume
<i>Receive coil</i>	8-channel head	32-channel head	32-channel head

## **5.2 Magnetic resonance image acquisition and processing**

Magnetic resonance spectroscopy cannot, at this juncture, provide detailed anatomical information at a resolution approaching that of water-focused magnetic resonance imaging. For this reason, structural images were acquired for positioning the spectroscopy volume (sVOI) of interest during scanning and for tissue segmentation and assessment of lesions during post-processing. Likewise, diffusion tensor images were obtained for comparison of water diffusivity to NAA diffusivity measures as well as for modeling of tissue microstructure within the large sVOI.

### **5.2.1 T<sub>1</sub>-weighted Images**

T<sub>1</sub>-weighted images were acquired with a 3D-MPRAGE (Magnetization-Prepared Rapid Acquisition GRE) pulse sequence (see Table 5.2 for parameters).

Table 5.2.  $T_1$ -weighted image parameters

Parameter	NIH	Leiden	Hopkins
Pulse sequence	MPRAGE	MPRAGE	MPRAGE
Flip angle ( $^{\circ}$ )	7.0	7.0	7.0
TR (ms)	7.0	5.0	4.1
TE (ms)	3.15	2.2	1.85
FOV (mm <sup>2</sup> )	224x224	246x246	224x224
Resolution (mm)	1 × 1 × 1	0.85 × 0.85 × 1	1 × 1 × 1
Slices	180 sagittal	174 sagittal	180 sagittal
SENSE	2(AP) × 3(RL)	2(AP) × 2.5(RL)	2(AP) × 3(RL)
Scan time (min)	5.3	1.6	1.5

$T_1$ -weighted and DTI volumes were processed in MIPAV (Medical Image Processing, Analysis and Visualization) (McAuliffe et al. 2001) and JIST (Java Image Science Toolbox) (Lucas et al. 2010). The  $T_1$ -weighted image was rigidly registered to the Montreal Neurological Institute (MNI) brain with the Optimized Automatic Registration (OAR) algorithm (Jenkinson & Smith 2001), inhomogeneity corrected using N3 (Sled et al. 1998), skull-stripped with the Simple Paradigm for Extra-Cerebral Tissue REmoval (SPECTRE) (Carass et al. 2011) and segmented into white matter (WM), gray matter (GM) structures, and cerebrospinal fluid (CSF) using the TOpology-preserving Anatomy-Driven Segmentation (TOADS) (Bazin & Pham 2008; Shiee et al. 2010) (see Figure 5.1). The first analysis of the Hopkins 7T cross-sectional data was segmented with the Fuzzy And Noise Tolerant Adaptive Segmentation Method (FANTASM) (Pham

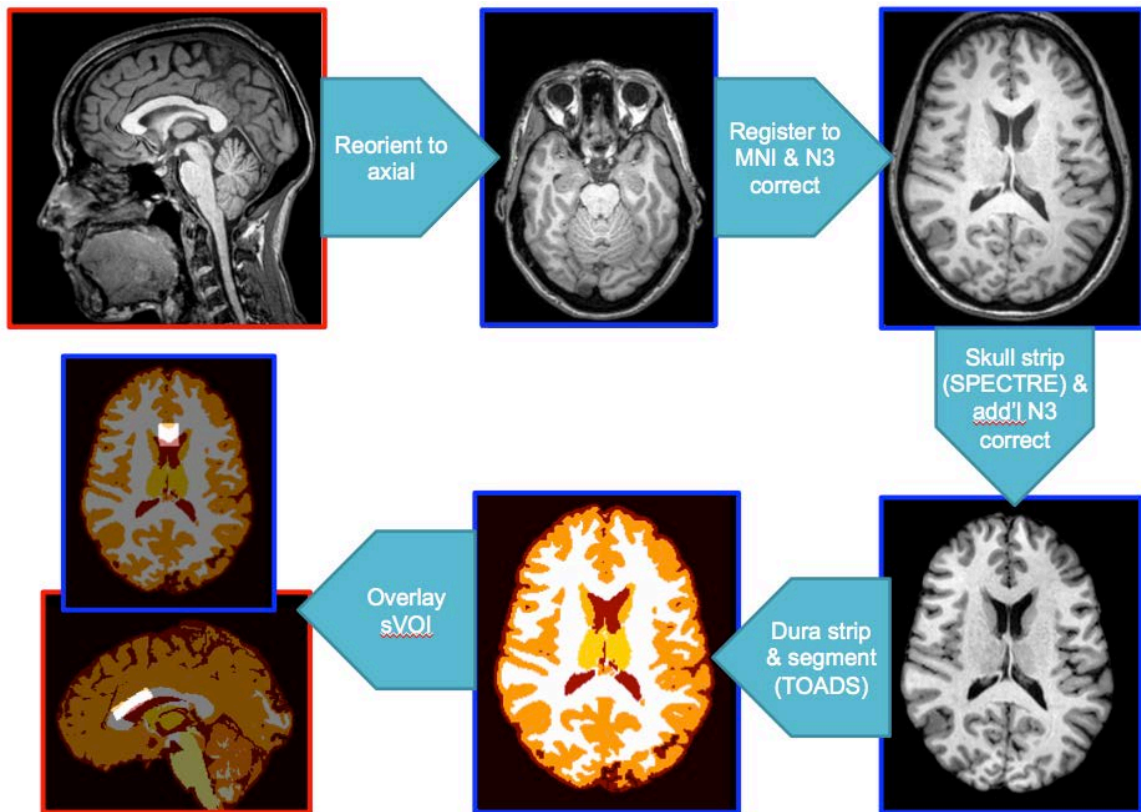


Figure 5.1. Image processing pipeline implemented in MIPAV/JIST

& Prince 1999). A mask of the sVOI was applied to the segmented volume to make a white matter VOI mask (wmVOI).

Corpus callosum (CC) cross-sectional area was measured in MIPAV by drawing regions of interest on the 3 midline, sagittal,  $T_1$ -weighted slices and averaging the area of these regions.



## 5.2.2 FLAIR images

For all patients and some healthy subjects, fluid attenuated inversion recovery (FLAIR) images were acquired (see Table 5.3 for parameters). At 7T, these images were acquired with the magnetization prepared FLAIR sequence developed by Visser et al. (Visser et al. 2010).

Table 5.3. FLAIR image parameters

Parameter	NIH 3T	Hopkins 7T
Pulse sequence	3D-FLAIR-VISTA	MP-FLAIR
TR (ms)	4800	8000
TI (ms)	1600	2175
TE (ms)	365	292
FOV (mm <sup>2</sup> )	224 × 224	224 × 224
Resolution (mm)	1 × 1 × 1	1 × 1 × 1
Slices	180 sagittal	180 sagittal
SENSE	2.6(AP) × 2(RL)	2(AP) × 3(RL)
Scan time (min)	6	8

For patients, FLAIR images were qualitatively examined for lesion detection. When available and demonstrating adequate homogeneity, FLAIR images were also registered to the MNI brain, inhomogeneity corrected, and used as a second channel in the Lesion-TOADS tissue segmentation algorithm (Shiee et al. 2010). Since many of the FLAIR images acquired during the first phase of the Hopkins 7T project suffered from poor sulcal CSF suppression and extreme B0 and B1 magnetic field inhomogeneity, which are known problems at 7T that are difficult to overcome, they were not used for quantitative analysis or segmentation.

### 5.2.3 DTI Images

Whole brain DTI images were acquired in all acquisition sessions for comparison with DWS data (see Table 5.4 for parameters)

Table 5.4. DTI Parameters

Parameter	NIH	Leiden	Hopkins
Pulse sequence	Single-shot SE-EPI	Single-shot SE-EPI	Single-shot SE-EPI
b-value (s/mm <sup>2</sup> )	800	1000	800
# of directions	33	16	30
TR (ms)	7487	7209	12643
TE (ms)	85.2	67	82
FOV (mm <sup>2</sup> )	224 × 224	224 × 224	220 × 220
Resolution (mm)	2 × 2 × 2	2 × 2 × 2	2 × 2 × 2
Slices	60 axial	60 axial	55 axial
SENSE	3(AP)	3(AP)	3(AP)
Scan time (min)	5.5	2.4	7

For the DTI images, the individual diffusion weighted volumes were rigidly registered to the b=0 image, which was registered (affine) to the T<sub>1</sub>-weighted volume in MNI space. From this, the diffusion tensor was estimated and diagonalized for each voxel to yield maps of the primary eigenvector ( $E_1$ ), fractional anisotropy (FA), mean diffusivity (MD), parallel diffusivity ( $\lambda_{||}=\lambda_1$ ) and perpendicular diffusivity ( $\lambda_{\perp}=(\lambda_2+\lambda_3)/2$ ). The white matter mask attained from segmentation of the T<sub>1</sub>-weighted volume could then be applied to these images to obtain eigenvectors and diffusion values corresponding to the acquired DWS VOI.

For the Hopkins 7T cross-sectional analysis, the diffusion weighted data were

analyzed in a second way, at sVOI resolution (svDTI). For svDTI, the DWS VOI mask was applied to each diffusion weighted volume to extract an average diffusion weighted value for each direction to use for tensor fitting. The svDTI analysis served as a control to detect the macrostructural effects of CC curvature on diffusion values in place of the DTS-derived water spectra, which suffered from the partial volume effects of CSF.

### ***5.3 Diffusion weighted spectroscopy acquisition and processing***

#### **5.3.1 Acquisition**

For all experiments described here, diffusion weighted spectra were acquired from a rectangular prism shaped spectroscopy voxel of interest (VOI) located in the midline anterior CC (see Figure 5.2). The VOI was longest along the anterior-posterior dimension (25-30 mm) and positioned and angled on T<sub>1</sub>-weighted images to include portions of the genu and anterior body of the CC while maximizing CC volume and minimizing partial volume effects of gray matter. CSF was preferred over gray matter as the NAA concentration in CSF is very low and freely diffusing and is, therefore, unlikely to make a significant contribution to the measured NAA diffusion.

The corpus callosum was chosen as the volume of interest for these studies for several reasons. From a neuroanatomic point of view, the CC is a good structure for DWS because it is relatively homogeneous and contains fiber bundles that are predominantly oriented in the same direction (see Figure 5.2.B and Figure 5.5 tractography). This makes it possible to measure directional diffusion in large VOIs that are required for spectroscopy. In a brain region with many crossing fibers or little directionally organized microstructure, the diffusion measured from a large VOI would essentially cancel in most directions, resulting in a seemingly isotropic diffusivity. From a

technical point of view, the CC is large enough to harbor a spectroscopy voxel, and the anterior CC has a central position within the head coils, which results in relatively good shimming and magnetic field homogeneity. Finally, in terms of multiple sclerosis, CC damage has been found to be frequent and tightly linked with clinical disability (Roosendaal et al. 2009; Ozturk et al. 2010).

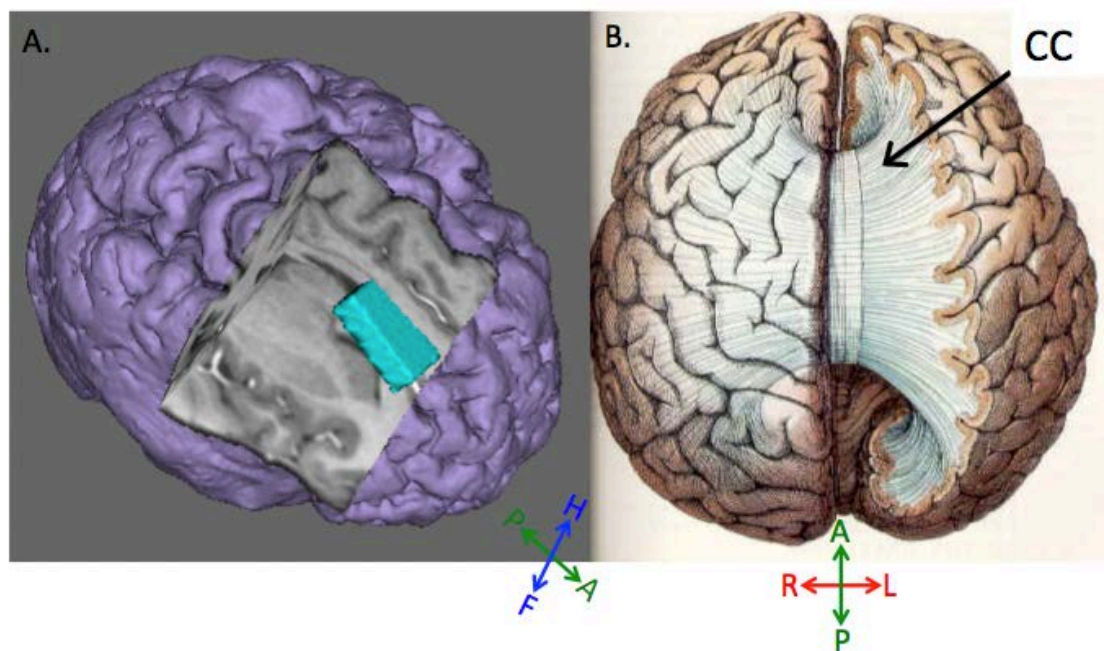


Figure 5.2. A. 3D reconstruction of brain viewed from above right showing placement of teal sVOI in anterior corpus callosum (healthy volunteer). B. Anatomical drawing of brain viewed from above with gray matter cut away on the right side to illustrate the right-left course of corpus callosum fibers. Black arrow points to approximate location of VOI in the anterior CC. (Adapted from *Eye, Brain and Vision*, by D. Hubel, 1988, retrieved from <http://hubel.med.harvard.edu/book/b34.htm>.)

The MR pulse sequence used for these experiments was designed, pulse-programmed and first implemented by Aranee Techawiboonwong and Itamar Ronen. In order to use this sequence, an additional software “patch” was installed on the scanner before each use. NAA diffusion measurements were obtained by incorporating bipolar diffusion gradients within a point-resolved spectroscopic sequence (PRESS) (Bottomley 1987) (see Figure 5.3). Depending on the experiment, this sequence was implemented with 2 to 6 gradient directions and 2 to 7 gradient strengths. Within an experiment, the diffusion times ( $\Delta$  &  $\delta$ ) were kept constant, and only the gradient amplitude was adjusted to vary the b-value. Depending on the experiment, 40-96 spectra were acquired for each b-value/gradient combination. The highest level of the sequence loop was spectra averages, such that 1 iteration included the entire series of b-value/gradient combinations. This guaranteed that conditions were spread out over the course of the scan.

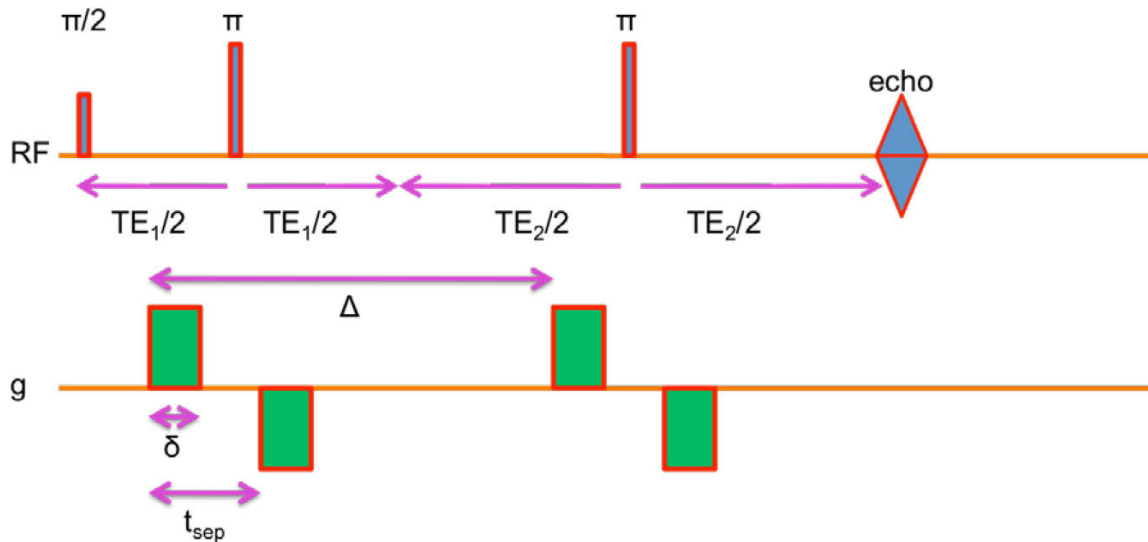
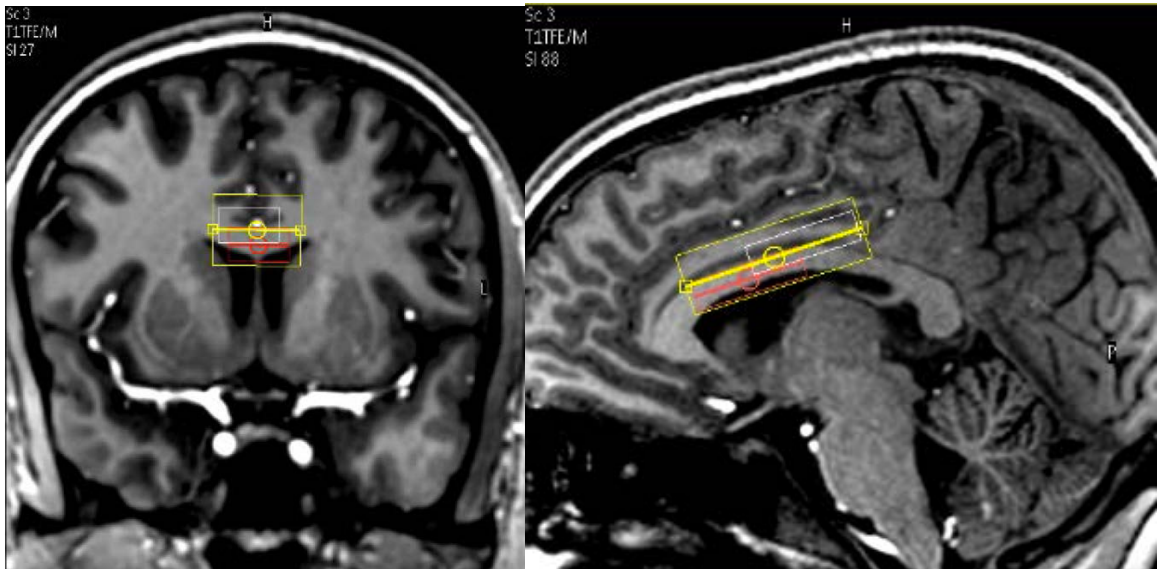


Figure 5.3. PRESS localization sequence with diffusion weighting

For the metabolite spectra, the center frequency was set to the primary NAA peak at 2.0 ppm. The built-in Philips pencil-beam shimming algorithm, up to second order, was used to maximize field homogeneity. The shim volume was localized to the anterior CC and was made just large enough to include both the DWS VOI centered on NAA and the corresponding chemical shift to water (Figure 5.4). Water suppression was achieved with an excitation-selective RF pulse centered at the water resonant frequency followed by a dephasing gradient. First, the built-in Philips Achieva module automatically optimized the water suppression RF pulse for minimal water signal. Then the RF pulse amplitude was manually adjusted to allow reliable NAA quantification while retaining enough residual water signal for post-processing zero-order phase correction prior to spectral averaging.



*Figure 5.4. Coronal and sagittal views of DWS VOI placement and angulation from the scanner console at 7T. Red box = VOI, white box = location of water measured in spectrum due to chemical shift displacement from NAA, yellow box = shim volume*

For a PRESS sequence at 7T, the chemical shift displacement between NAA and water resulted in nearly non-overlapping voxels (see Figure 5.4). Therefore, for each DWS VOI, a second experiment was performed with the same transmitter and receiver gain, shimming, and diffusion parameters as the metabolite spectrum but without water suppression, with the center frequency set to water, and fewer averages. This acquisition was used in post-processing to find and correct for phase and frequency shifts due to eddy currents.

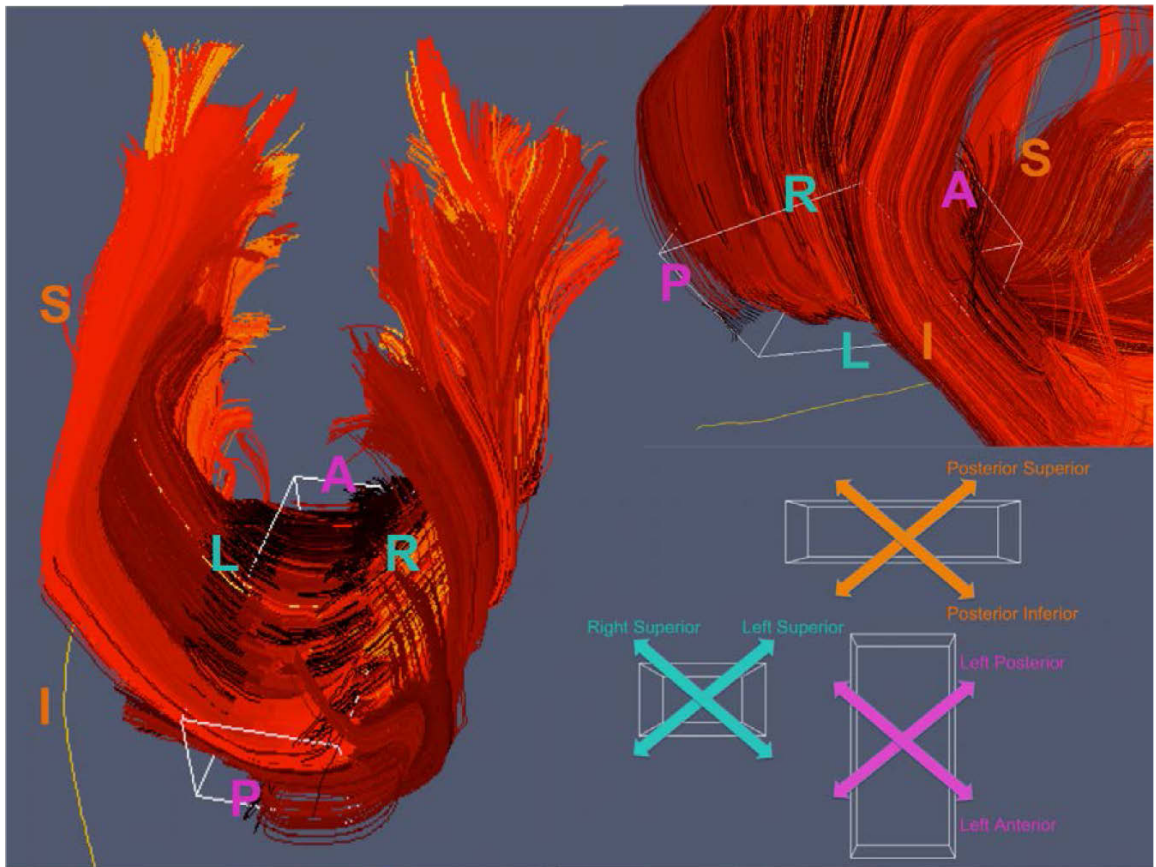


Figure 5.5. DWS gradient directions for 7T Hopkins data. The DWS VOI is represented by white cuboid outline and the 6 orthogonal gradient directions are shown in the right bottom on various VOI views. Red-orange lines represent DTI tractography tracts seeded within the VOI.

The Hopkins 7T data was acquired with diffusion weighting in 6 non-coplanar directions at 2 b-values in addition to a b=0 spectra (13 conditions per averaging loop). Directions were oriented with respect to the VOI as demonstrated in Figure 5.5. For all of these scans the lower b-value was 440 s/mm<sup>2</sup>. 11 scans used a highest b-value of 2250 s/mm<sup>2</sup> and 22 used a highest b-value of 3600 s/mm<sup>2</sup>.

For data collected at the NIH and LUMC, two directions were chosen for all scans: (1) a pure right-left direction in the VOI frame, which is mostly parallel to the direction of the callosal fibers (Figure 5.6, left); (2) a direction perpendicular to the callosal fibers, forming a 45° angle between the anterior-posterior axis and the inferior-superior axis of the VOI (Figure 5.6, right). These gradient directions can be denoted in the VOI coordinates as [1,0,0] for parallel and [0,-1,1] for perpendicular.

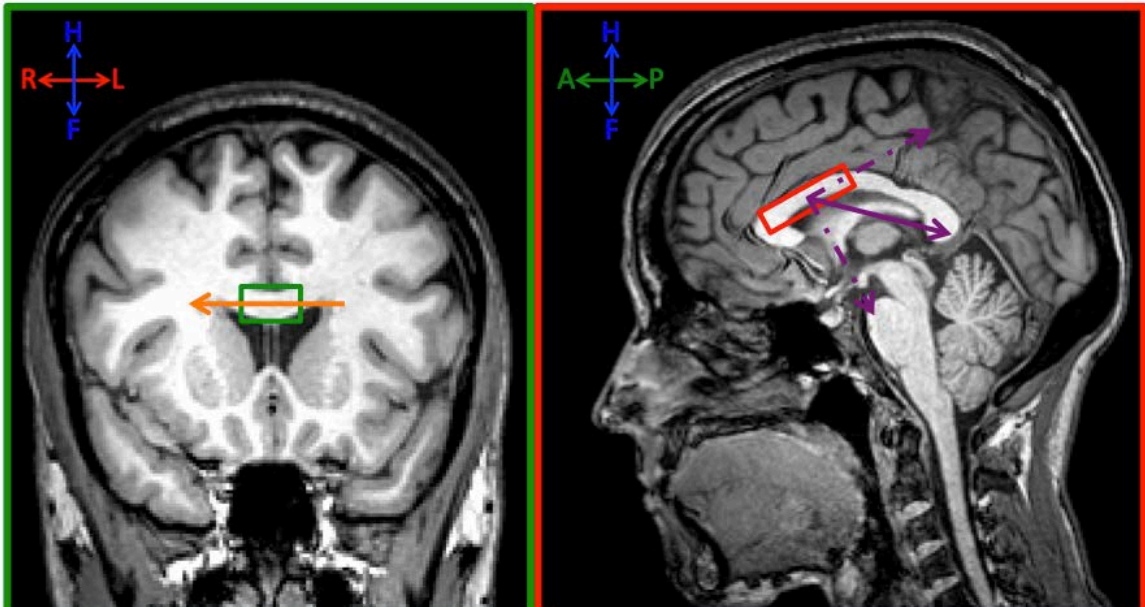


Figure 5.6. Parallel ([1,0,0]) and perpendicular ([0,-1,1]) gradient directions with respect to VOI for 2-direction acquisitions.

The decision regarding how many diffusion weighting directions and b-values to



acquire was based on minimizing total number of spectra acquired, which is directly related to scan time, while having enough signal-to-noise ratio to answer the questions being posed. The Hopkins 7T data experiment was, to my knowledge, the first diffusion weighted spectroscopy investigation of patients and was designed to test the hypothesis that DWS measurements may be able to detect white matter alterations associated with a neurodegenerative process. Collection of 6 orthogonal directions, enough for a tensor calculation, allowed measurement of metabolite diffusion changes along any orientation. With this experiment, we established that we could measure metabolite diffusivity in patients and that alterations in parallel diffusivity may be associated with neurodegeneration. Based on these results, the subsequent NIH 3T study focused on measuring parallel diffusion by acquiring one direction parallel and one direction perpendicular to the fibers of interest. This allowed scan time to be spent acquiring more and higher b-values along each of the two directions. The advantage of acquiring diffusion along 2 directions only is that fewer overall spectra can be acquired to achieve adequate signal-to-noise for each direction. Also, as we will see in Chapter 6, higher b-value spectra, while having lower SNR overall, may have higher yield in terms of accuracy and reproducibility for diffusivity measures.

The brain undergoes pulsatile motion due to arterial expansion associated with systole. This cardiac-cycle-driven brain movement is nonlinear, such that different parts of the brain experience different amounts and velocities of motion over the course of the cycle (Greitz et al. 1992). Measurements of this movement have demonstrated that the greatest velocities occur in inferior and medial brain regions, including the corpus callosum. As diffusion weighted images are designed to be sensitive to molecular movement, they are also extremely sensitive to bulk tissue movement (Nunes et al. 2005). Likewise, the consistency of metabolite diffusion measurements is diminished by

pulsatile motion, becoming more severe with greater diffusion weighting (Upadhyay et al. 2007). In order to compensate for this effect, cardiac gating was applied to metabolite measurements collected at the NIH and LUMC. For this, a peripheral pulse unit was placed on the subjects' index finger, which reports on the oxygen saturation level of the blood and is directly related to the cardiac cycle. The NIH spectroscopy measurements were triggered on every second cycle at 200 msec after the initial phase of the oxygenation curve (trigger delay). As subjects had heart rates ranging from 50-75 beats per minute, the relaxation time ranged from 1600-2400 msec.

*Table 5.5 DWS sequence parameters by experiment*

<b>Parameter</b>		<b>NIH</b>		<b>Leiden</b>	<b>Hopkins</b>
Subject group		MS & HV	Repro (HV)	Repro (HV)	MS & HV
VOI dimensions (APxRLxFH mm)		30 x 15 x 8		25 x 15 x 8	30 x 15 x 8
VOI volume		3600 mm <sup>3</sup>		3000 mm <sup>3</sup>	3600 mm <sup>3</sup>
TE		110 ms		121 ms	120 ms
TR		2 cardiac cycles (1500-2500 ms)		3 cardiac cycles (2400-3600 ms)	2000 ms
Trigger delay		200 ms		300 ms	N/A
MRS Parameters	<i>Localization Sequence</i>	PRESS		PRESS	PRESS
	<i>Spectral Width</i>	1500 Hz		3000 Hz	3000 Hz
	<i>Points Sampled</i>	1024		1024	2048
	<i># spectra per condition</i>	48	72	40	32

Table 5.5 DWS sequence parameters continued

<b>Parameter</b>		<b>NIH</b>				<b>Leiden</b>		<b>Hopkins</b>
<b>Diffusion Parameters</b>	$\Delta$	55 ms				60.5 ms		47 ms
	$\delta$	22 ms				37 ms		28 ms
	<i>bipolar gap</i>	20 ms				16 ms		14 ms
	<i>Number of directions</i>	2 ( $\parallel$ and $\perp$ )				2 ( $\parallel$ and $\perp$ )		6 (orthogonal)
	<i>Collected b=0</i>	No				No		Yes
	<i>Number of b-values</i>	4 $\parallel$	4 $\perp$	7 $\parallel$	7 $\perp$	7 $\parallel$	7 $\perp$	2 & b=0
	<i>b-values (s/mm<sup>2</sup>)</i>	332 888 1730 2889	633 1748 3423 5659	213 469 826 1285 1847 2511 3277	410 917 1629 2544 3665 4989 6518	63 317 664 1278 1912 2885 3808	134 656 1361 2602 3883 5844 7700	440  2250 or 3600

### 5.3.2 DWS Post-Processing

Individual and averaged spectra were phase and frequency drift corrected in MATLAB (The Mathworks, Inc., Natick, MA). The individual spectra were eddy-current corrected (Reese et al. 2002) using the unsuppressed water acquisition and zero-order frequency corrected according to the residual water peak (that which remained due to de-optimization of the water suppression RF pulse). At this point, spectra were averaged within condition except for those individual spectra that did not meet a water peak-to-SNR threshold. This threshold ranged from 100:1 to 10:1 depending on the diffusion weighting value. For noisier, high b-value spectra, the threshold was reduced to be able to retain enough spectra for proper analysis. For the averaged spectrum from each

condition, the remaining water peak was removed with a Hankel singular value decomposition (HSVD) method followed by first-order phase-correction based on the NAA peak.

The water-removed, averaged spectrum for each diffusion direction and  $b$ -value combination was quantified with LCModel (Provencher 1993). Due to low SNR at the highest  $b$ -values, NAA and N-acetylaspartylglutamate (NAAG) were not well separated, so the NAA+NAAG values (Cramér–Rao lower bounds <15%) were used for diffusion analysis.

For the Hopkins 6-direction 7T data, the diffusion tensor was estimated and diagonalized to yield fractional anisotropy (FA), mean diffusivity (MD), parallel diffusivity ( $\lambda_{\parallel} = \lambda_1$ ) and perpendicular diffusivity ( $\lambda_{\perp} = \frac{\lambda_2 + \lambda_3}{2}$ ). [NAA] was estimated from the ratio of NAA+NAAG to creatine + phosphocreatine from the  $b=0$  spectrum.

For the 2-direction data, the parallel ([1,0,0]) and perpendicular ([0,-1,1]) direction data were separately fit with a mono-exponential diffusion equation (Equation 5-1) to yield  $\mathbf{D}_{\text{par}}$  and  $\mathbf{D}_{\text{perp}}$ , respectively. This calculation incorporated  $n$   $b$ -values in a linear least squares fit (Equation 5-2) to derive separate (apparent) diffusivity measurements parallel and perpendicular to the CC fibers.

$$ADC = \frac{1}{-b} \ln\left(\frac{S}{S_0}\right) \quad \text{Equation 5-1}$$

$$\sum = \sum_{i=1}^n \quad ADC = \frac{n \sum b_i \ln\left(\frac{S_i}{S_0}\right) - \sum b_i \sum \ln\left(\frac{S_i}{S_0}\right)}{n \sum b_i^2 - (\sum b_i)^2} \quad \text{Equation 5-2}$$

$\mathbf{D}_{\text{par}}$  and  $\mathbf{D}_{\text{perp}}$  were averaged to calculate  $\mathbf{D}_{\text{avg}}$  – the empirical ADC of NAA.

### 5.3.3 Modeled analysis of DWS data

For the datasets acquired with 2 directions parallel and perpendicular to the corpus callosum fibers, the LCMoDel output was also used as an input to a modeling routine that calculates the *intra-axonal*, or *cytosolic*, diffusivity of NAA. This model was developed by Itamar Ronen (Ronen et al. 2013; Ronen et al. 2014). The procedure is assumed to minimize the variability in the DWS measurements introduced by macroscopic factors such as the position of the VOI within the white matter tract, the main direction of the tract with respect to the DW gradients, and the macroscopic curvature of the tract within the VOI. As seen in Figure 5.7 (left), even in a structure where most fibers are oriented along the same general direction, there is still a great

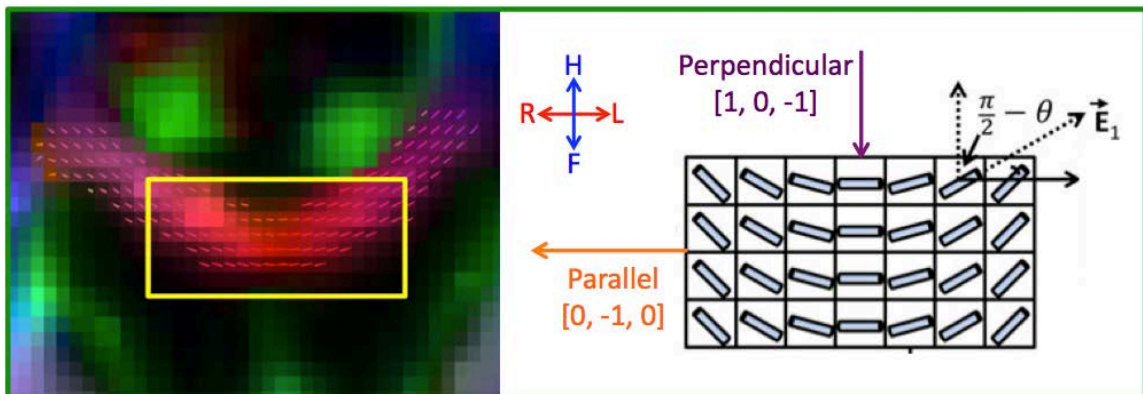


Figure 5.7. (Left) a coronal slice of a DTI color map where brightness represents FA; colors show primary orientation of fibers (red: LR, blue: FH, green: AP); primary eigenvectors ( $\vec{E}_1$ ) are displayed for voxels in the CC. (Right) Illustration of angles between the  $\vec{E}_1$ s and the diffusion weighting directions used for metabolite diffusion. (Adapted from “Axonal and glial microstructural information obtained with diffusion weighted magnetic resonance spectroscopy at 7T” by I. Ronen et al., *Frontiers in Integrative Neuroscience*, 7(13). Open access article distributed under the terms of the Creative Commons Attribution License.)

deal of divergence within a voxel of the size required for DWS measurements. In particular, fibers of the anterior CC are curving through out the midline section to connect corresponding portions of the anterior and superior cortex across the hemispheres. By modeling how we would expect diffusion measurements to be altered given these variations in curvature, we can better approximate the actual diffusion coefficient of NAA in this tissue. Fortunately, as demonstrated in Figure 5.7 (modified from (Ronen et al. 2014)), DTI can provide information about the curvature.

In this model, the CC within the VOI is viewed as a curved cluster of cylinders with distributions of diameters and angular dispersions of individual axons at the microscopic level. This model is based on several important assumptions: 1) diffusion times are long compared to the gradient pulses (van Gelderen et al. 1994); 2) in WM, NAA is primarily in the axonal cytoplasm, and neuronal cell bodies are sparse; 3) diffusion in cylinders can be decomposed into the components of molecular displacement parallel □ (Avram et al. 2008) □ and perpendicular to the axonal diameters in the anterior CC are distributed similarly across people as described by Aboitiz et al. (Aboitiz et al. 1992); and 5) the macroscopic curvature of the CC through the VOI can be described by DTI-derived  $\vec{E}_1$  from within the VOI. For each diffusion weighting direction, the acquired signal is assumed to contain all of the individual components of molecular diffusion parallel and perpendicular to the cylindrical fiber orientation. As was explored in Chapter 4 with simulations in cylinders (Figure 4.5), diffusion parallel to the fiber direction is assumed to have a Gaussian displacement probability distribution, which can be described by a simple mono-exponential diffusion equation as in Equation 5-1. Perpendicular diffusion, on the other hand, is restricted and therefore depends on the diameter of the cylindrical fibers and the particular components that make up the b-value, namely the diffusion time, the gradient strength, and the

gradient duration (Ronen et al. 2013). As molecules are given more time to diffuse and experience their surrounds, especially if they are in a small diameter tube, they will bump up against the walls more frequently. This phenomenon will make the decrease the apparent diffusion coefficient, especially along the perpendicular direction – the diffusion weighting direction that passes through the most diffusion barriers (Figure 5.8, red line).

The angles between the fibers and the gradients can be determined by extracting the vectors for each DTI primary eigenvector ( $\vec{E}_1$ ) within the sVOI and finding the angle between these and the applied gradients using Equation 5-3.

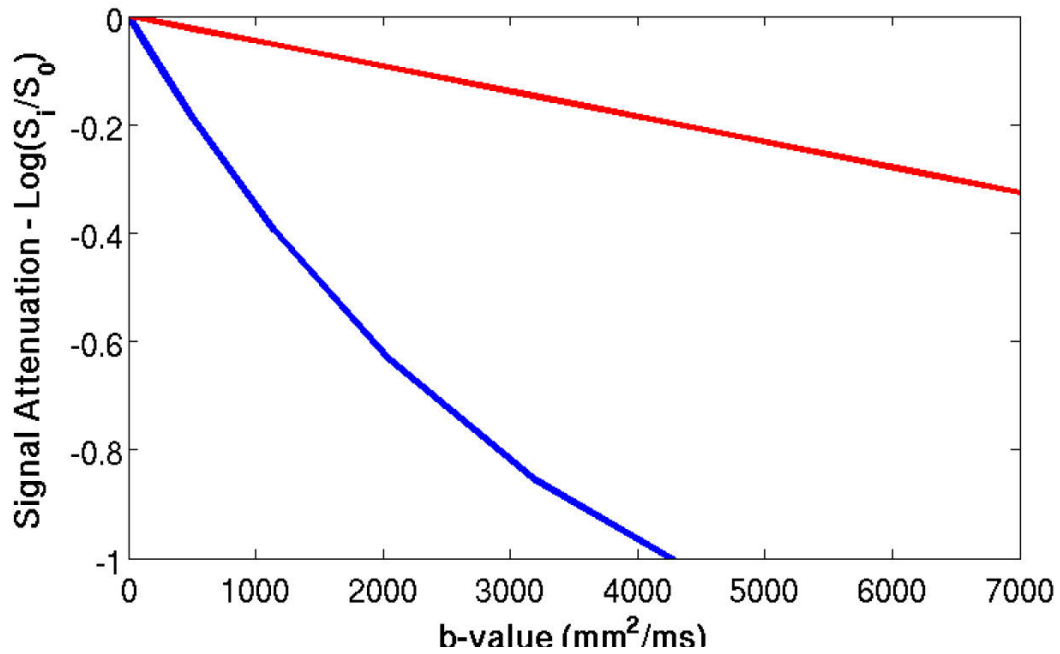


Figure 5.8 Modeled diffusion using the Random Walk Simulator (Landman et al. 2010) with 10,000 molecules intracellular,  $D = 0.7 \mu\text{m}^2/\text{s}$ , cylinder lattice with radius=7 $\mu\text{m}$ . Diffusion parallel = blue, diffusion perpendicular = red. Diffusion perpendicular to the cylinders has a smaller apparent diffusion constant (slope) than the parallel diffusion.

$$\theta_{par} = \cos^{-1} \left( \frac{\vec{g}_{par} \bullet \vec{E}_1}{\|\vec{g}_{par}\| \|\vec{E}_1\|} \right) \quad \theta_{perp} = \cos^{-1} \left( \frac{\vec{g}_{perp} \bullet \vec{E}_1}{\|\vec{g}_{perp}\| \|\vec{E}_1\|} \right) \quad \text{Equation 5-3}$$

This generates a set of angles that can be displayed as a histogram, as in Figure 5.9. These figures are an extension of what is illustrated in Figure 5.7 where we see that there are actually very few DTI voxels with primary eigenvectors perfectly aligned (90° azimuthal angle) with the parallel [0,-1,0] gradient – most are within 45° to 135° and can be skewed due to head/voxel positioning and orientation. The same is true for the perpendicular gradient direction, with the exception that the primary eigenvectors are centered on 0° azimuthal angle and it is more difficult to illustrate this with the 2D view given in Figure 5.7.



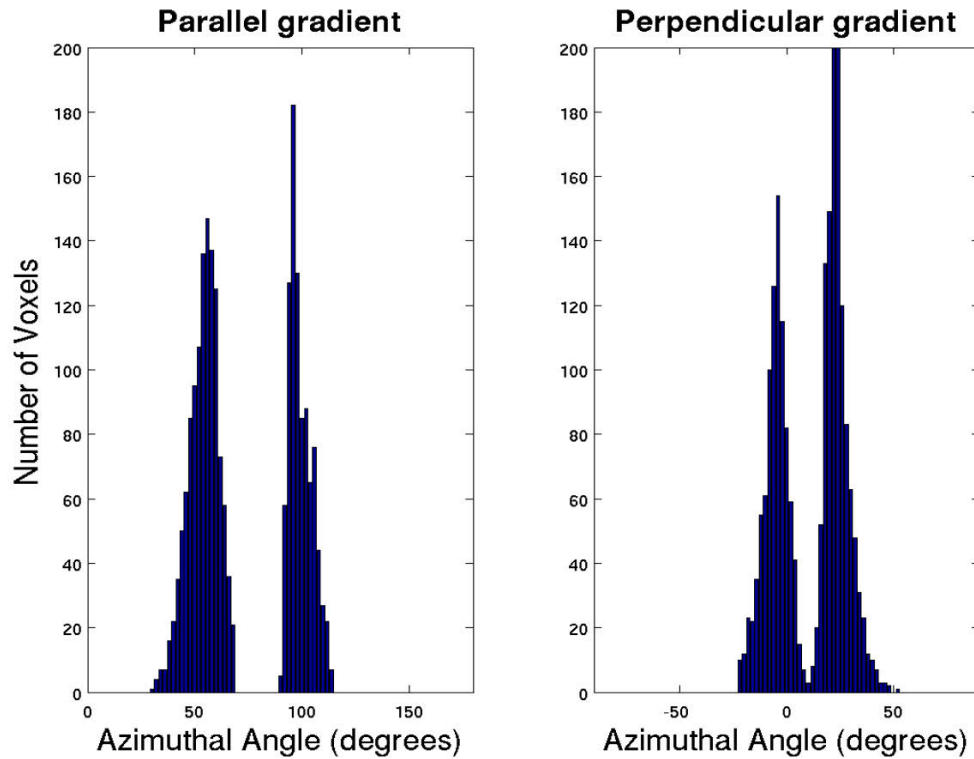


Figure 5.9. Histogram of angles between the parallel gradient  $[0, -1, 0]$  and the  $\vec{E}_1$ s (left) and the perpendicular gradient  $[1, 0, -1]$  and the  $\vec{E}_1$ s (right). By convention angles are with respect to the azimuthal, zero degrees is with respect to a plane orthogonal to the primary fiber direction. From a healthy volunteer, 3T data.

Finally, this model assumes a residual, microscopic angular displacement ( $\varphi$ ) or misalignment of fibers that cannot be modeled by DTI and that would be distributed normally with standard deviation  $\sigma_\varphi$ . Putting the model together, we are able to make robust measurements of the cytosolic diffusion coefficient of NAA ( $\mathbf{D}_{\text{model}}$ ) in the corpus callosum, which should be more robust to the precise curvature of the fibers within the voxel, and which may provide information about the microscopic misalignment – a potential disease marker in and of itself.

This procedure is designed to minimize the variability in the DWS measurements introduced by macroscopic factors such as the position of the VOI within the white matter tract, the main direction of the tract with respect to the DW gradients and the macroscopic curvature of the tract within the VOI. It is important to note that  $D_{\text{model}}$  is independent of the tract geometry within the VOI and thus mostly reflects the effects of the cytosolic medium, e.g. viscosity and molecular crowding, on the diffusion of NAA inside the axons.

## 5.4 Conclusions

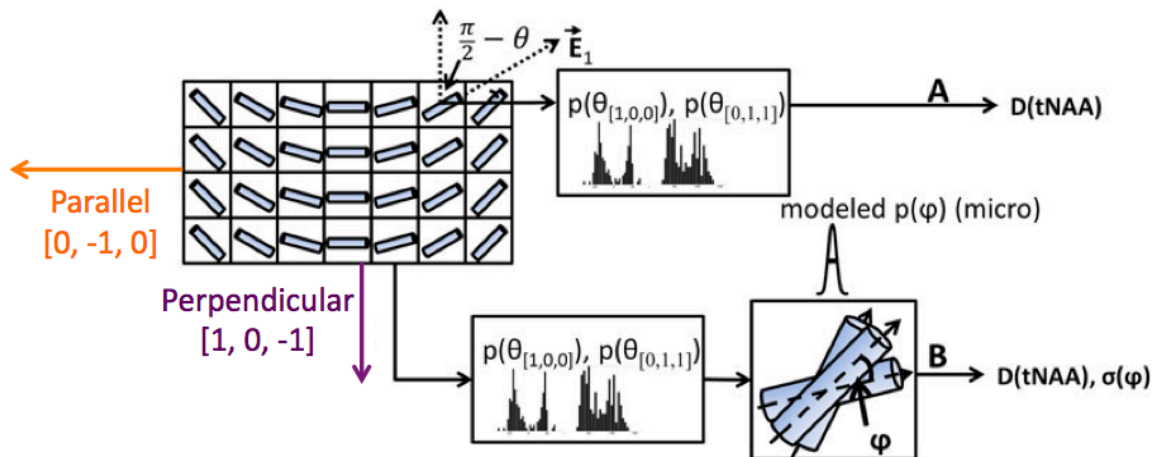


Figure 5.10 Modeled analysis of DWS data. The primary eigenvector information is taken from the DTI image to produce histograms of the eigenvector angles with respect to the diffusion weighted spectroscopy gradients. The histograms can be combined with the signal attenuation data for each direction and (A) fit them to find the diffusion of total NAA or (B) fit these data with a micro dispersion parameter. (Adapted from “Axonal and glial microstructural information obtained with diffusion weighted magnetic resonance spectroscopy at 7T” by I. Ronen et al., *Frontiers in Integrative Neuroscience*, 7(13). Open access article distributed under the terms of the Creative Commons Attribution License.)

Diffusion weighted spectroscopy is a magnetic resonance technique that has

existed for decades. Until this work, DWS had not been studied in patients in vivo. The availability of ultra-high-field clinical magnetic resonance scanners opened the door to attempting DWS in patients. However, with our current systems, the concentration of NAA in the brain still requires the use of fairly large VOIs. Therefore, in order to extract information about microstructure from these VOIs, we have to rely on averaging from large data sets and incorporating information from other techniques. Here we developed and optimized the DWS technique for use in patients with MS. The methods for collecting, processing and analyzing DWS data were detailed in this chapter. In chapter 6, the reliability of these methods is explored and quantitated. In chapters 7 and 8, the results of a pilot cross-sectional study and a longitudinal study, respectively, in patients with MS are presented.

## **6 REPRODUCIBILITY AND OPTIMIZATION OF IN VIVO DIFFUSION WEIGHTED SPECTROSCOPY OF THE HUMAN CORPUS CALLOSUM AT 3T AND 7T**

### ***6.1 Introduction***

Diffusion weighted spectroscopy (DWS) allows for the assessment of diffusion properties of intracellular metabolites, which give intrinsic information about the microstructural properties of the compartments where they reside. Biological limitations on location of these metabolites, as well as their slow exchange characteristics on the time scale of a diffusion experiment, allow compartment-specific measurements. In particular, the diffusion properties of N-acetyl aspartate (NAA), typically co-measured with N-acetylaspartyl glutamate (NAAG) ( $\text{NAA} + \text{NAAG} = \text{tNAA}$ ), have been shown to be sensitive to intraneuronal/axonal damage in a variety of pathologies, such as stroke and multiple sclerosis. Thus, the interpretation of metabolite diffusion measurements in disease may be pathologically specific.

Performing in-vivo DWS measurements on a clinical scanner and deriving meaningful information from these experiments remains challenging, and the robustness and reproducibility of the technique still need to be established. The low concentrations of metabolites compared to that of water, coupled with the long echo times (TE) required to accommodate the diffusion-weighting gradients, dictate a relatively low signal-to-noise ratio (SNR). This, in turn, necessitates long measurement times and/or large volumes of interest, both detrimental to clinical applications. Other effects, such as strong eddy currents, and inter-shot phase and amplitude fluctuations, may further affect the accuracy and reproducibility of the measurements. Additionally, other divergent properties of metabolites may require different optimization parameters from water

diffusion techniques. For instance, as metabolites diffuse more slowly than water, higher b-values are required to achieve sufficient diffusion weighting for calculating the apparent diffusion coefficient. Previous work, for example, emphasized the importance of b-value choice for an accurate estimate of fractional anisotropy (FA) of brain metabolites from DWS experiments (Ellegood et al. 2010).

It is therefore essential to measure the inter/intra-subject variability across the acquisition parameter space, in particular the number of b-values and averages, and thereby to ascertain the optimal parameters for a reliable experiment. Moreover, beyond this relatively straightforward parameter optimization, it is important to assess the robustness of the DWS technique with respect to its potential use in the clinical context.

In order to assess the viability of DWS as a meaningful diagnostic tool, it is therefore essential to ascertain (a) the *inter*- and *intra*-subject variability of metabolite diffusion properties across the acquisition parameter space, e.g. the number and range of different b-values used and the number of spectral averages per single diffusion-weighting condition; (b) the optimal parameters for a reliable DWS experiment within a given experimental time limit that is also suitable for clinical and clinical research purposes. Toward these aims, we established a “maximum” data set based on our experience with the technique, the gradient strengths of the system, and scan time limitations (based primarily on the stamina of our healthy volunteers).

In the first part, reproducibility of NAA DWS measurements parallel and perpendicular to the callosal fiber main direction is assessed on two clinical scanners, operating at different magnetic fields of 3T and 7T, using an almost identical protocol. The reproducibility of derived quantities, such as diffusion coefficients of NAA parallel and perpendicular to the callosal fibers, is estimated across repeated measurements within subjects as well as across subjects. We also test the reproducibility of modeled

quantities with potential clinical relevance, such as the cytosolic diffusion coefficient of NAA within the callosal fibers and the orientation dispersion of axons within the volume of interest (VOI). These quantities are calculated based on a model that accounts for the subject- and position-specific macroscopic curvature of the fibers within the VOI (Ronen et al. 2014). Once the impact of macroscopic curvature is removed, the cytosolic diffusion coefficient is more directly influenced by the hindrances to diffusion within the intracellular space and is thus expected to be more sensitive to alterations in intracellular microstructure caused, for example, by disease processes such as breakdown of microtubules and neurofilaments. The second part of the study reports the dependence of the statistical properties of the diffusion properties of NAA obtained from the direct fit and the modeling as a function of scan parameters, such as the number and range of b-values used for each diffusion-weighting direction, as well as the number of spectral averages.

*Table 6.1. Important abbreviations*

<b>Abbreviation</b>	<b>Meaning</b>
VOI	Volume of interest
$D_{par}$	Apparent diffusivity calculated from mono-exponential fit to diffusion weighted data acquired with parallel gradients ([0 -1 0])
$D_{perp}$	Apparent diffusivity calculated from mono-exponential fit to diffusion weighted data acquired with perpendicular gradients ([1 0 -1])
$D_{avg}$	$(D_{par} + D_{perp})/2$
$D_{model}$	Modeled apparent diffusivity calculated with macrostructural curvature from DTI and fitting the microstructural orientation dispersion ( $\sigma_{\phi}$ ) parameter
CC	Corpus callosum

## 6.2 Methods

### 6.2.1 Subjects

Table 6.2. Subject Demographics

<b>Subject</b>	<b>Sex</b>	<b>Age (years)</b>
<i>3T Subject 1</i>	Male	39
<i>3T Subject 2</i>	Male	41
<i>3T Subject 3</i>	Female	47
<i>7T Subject 1</i>	Male	30
<i>7T Subject 2</i>	Female	23
<i>7T Subject 3</i>	Female	29

Six healthy volunteers (three men, three women, ages:  $34 \pm 8$  years) (Table 6.2), without known neurological abnormalities, participated in this study. Each subject was scanned in 5 separate sessions. The study adhered to local Institutional Review Board guidelines, and informed consent was obtained from all subjects prior to the study.

### 6.2.2 Data acquisition

MRI and MRS data were obtained with 3T and 7T Philips Achieva scanners (Philips Medical Systems, Cleveland, Ohio) (see Table 6.3 for hardware parameters). T<sub>1</sub>-weighted images were acquired for spectroscopy volume of interest (VOI) positioning and tissue segmentation. A DTI volume was acquired for comparison with DWS and modeling of DWS data. Image processing is described in detail in Chapter 5. In short, all images were registered to the Montreal Neurological Institute (MNI) brain atlas. The full brain was segmented into white matter, gray matter, cerebrospinal fluid (CSF), and lesions using the TOology-preserving Anatomy-Driven Segmentation (TOADS) (Shiee

et al. 2010; Bazin & Pham 2008). From the diffusion weighted volumes, the diffusion tensor for each voxel was estimated and diagonalized to yield maps of the primary eigenvector ( $\vec{E}_1$ ) and the fractional anisotropy (FA), which are later used in the modeling. The mask of the spectroscopy VOI was used to obtain segmentation and water diffusion data from the VOI.

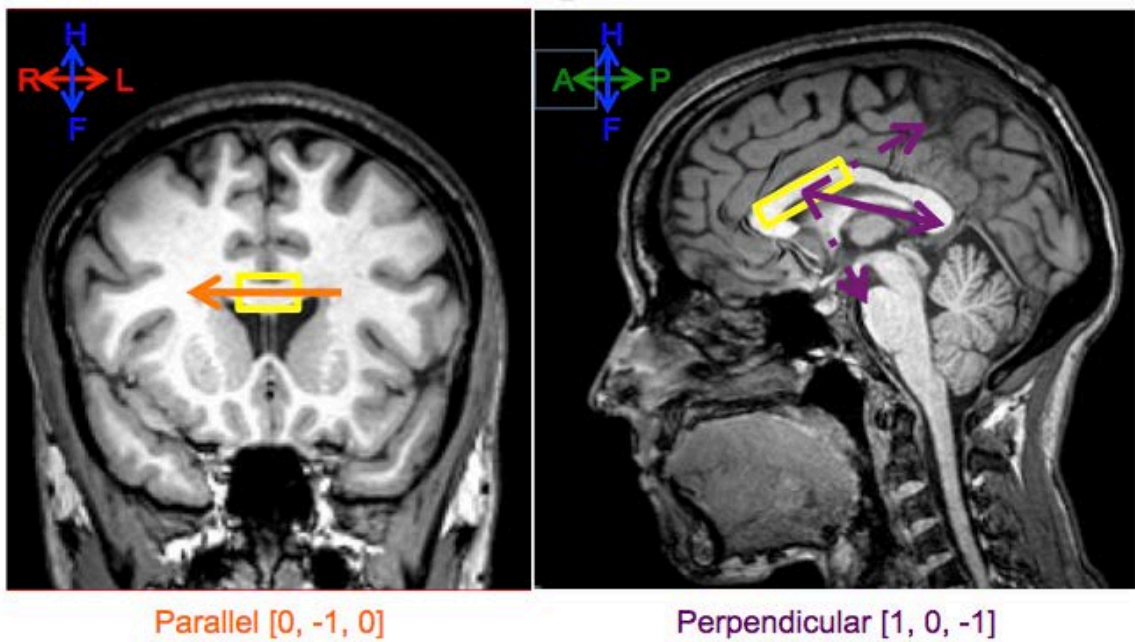


Figure 6.1 Placement of sVOI (yellow box) on coronal (left) and sagittal (right) T1-weighted slices. Directions of parallel and perpendicular gradients for DWS are illustrated as the orange and purple solid lines, respectively.



Table 6.3. Scanner and structural image acquisition parameters.

<b>Magnet</b>		<b>3T</b>	<b>7T</b>
<i>Scanner Make/Model</i>		Philips Achieva	Philips Achieva
<i>Max gradients</i>		60 mT/m	40 mT/m
<i>Slew Rate</i>		100 T/m/s	200 T/m/s
<i>Transmit coil</i>		Quadrature volume	Quadrature volume
<i>Receive coil</i>		8-channel head phased array	32-channel head phased array
<b>T<sub>1</sub>-weighted image parameters</b>	Sequence	MPRAGE	MPRAGE
	Flip angle	7.0°	7.0°
	TR/TE	7.0/3.15 ms	5.0/2.2 ms
	FOV	240 × 240 mm <sup>2</sup>	246 × 246 mm <sup>2</sup>
	Resolution	1.0 mm iso	0.85x0.85x1 mm <sup>3</sup>
	Slices	180 sagittal	174 sagittal
	SENSE	2(AP) × 3(RL)	2(AP) × 2.5(RL)
	Scan time	5.3 min	1.59 min
<b>Diffusion tensor image parameters</b>	Sequence	Single-shot SE-EPI	Single-shot SE-EPI
	b-value	800 s/mm <sup>2</sup>	1000 s/mm <sup>2</sup>
	# of directions	33	16
	TR/TE	7487/85.2 ms	7209/67 ms
	FOV	224x224 mm <sup>2</sup>	224 × 224 mm <sup>2</sup>
	Resolution	2 mm isotropic	2 mm isotropic
	Slices	60 axial	60 axial
	SENSE	3(AP)	3(AP)
	Scan time	5.5 min	2.41 min

Diffusion weighted spectra were collected from a VOI placed in the anterior corpus callosum (CC) of each subject (3600 mm<sup>3</sup> for 3T, 3000 mm<sup>3</sup> for 7T) (Figure 6.1). Each subject was scanned in 5 separate sessions, during which 72 spectra were collected for the 3T scans and 40 spectra for all 7T scans for each of 14 conditions (2 directions, 7 b-values). Total DWS scan time ranged from 30-60 minutes. See Table 6.4 and Chapter 5 for parameters.

Table 6.4 DWS acquisition parameters

<b>Magnet</b>	<b>3T</b>	<b>7T</b>
<i>Spectroscopy VOI dim (AP x RL x FH)</i>	30 x 15 x 8 mm	25 x 15 x 8 mm
<i>VOI volume</i>	3600 mm <sup>3</sup>	3000 mm <sup>3</sup>
<i>Localization Sequence</i>	PRESS	PRESS
<i>Shim</i>	Pencil-beam to 2 <sup>nd</sup> order	Pencil-beam to 2 <sup>nd</sup> order
<i>TE</i>	110 ms	121 ms
<i>TR</i>	2 cardiac cycles (1500-2500 ms)	3 cardiac cycles (2400-3600 ms)
<i>Points Sampled</i>	1024	1024
<i>Spectral Width</i>	1500 Hz	3000 Hz
<i>Number of directions</i>	2	2
<i>Number of b-values</i>	7 [1,0,0] & 7 [0,-1,1]	7 [1,0,0] & 7 [0,-1,1]
<i>b-values (s/mm<sup>2</sup>) range</i>	Perpendicular: 381 – 6101 Parallel: 191 – 3050	Perpendicular: 160 – 7811 Parallel: 80 – 3901
<i>gradient duration (<math>\delta</math>)</i>	22 ms	37 ms
<i>bipolar gap</i>	20 ms	16 ms
<i>diffusion time (<math>\Delta</math>)</i>	55 ms	60.5 ms
<i># spectra per condition</i>	72	40

Table 6.5. Diffusion weighting parameters (*b*-values) used for each scanner strength and direction. (Perpendicular *b*-values are twice those of parallel.)

<b><i>b</i>-values (s/mm<sup>2</sup>)</b>	<b>3T</b>		<b>7T</b>	
	Parallel	Perpendicular	Parallel	Perpendicular
<i>b</i> <sub>1</sub>	213	410	63	134
<i>b</i> <sub>2</sub>	469	917	317	656
<i>b</i> <sub>3</sub>	826	1629	664	1361
<i>b</i> <sub>4</sub>	1285	2544	1278	2602
<i>b</i> <sub>5</sub>	1847	3665	1912	3883
<i>b</i> <sub>6</sub>	2511	4989	2885	5844
<i>b</i> <sub>7</sub>	3277	6518	3808	7700

### 6.2.3 Spectra processing

The full processing scheme is described in Chapter 5. Briefly, following DWS data acquisition, the spectra were eddy-current corrected using the unsuppressed water acquisition and zero-order frequency corrected according to the remaining water peak. Spectra were averaged within condition and then the remaining water peak was removed using a Hankel Singular Value Decomposition (HSVD) method followed by a first-order phase-correction based on the NAA peak. The spectrum from each condition was then analyzed with LCModel (Provencher 1993) to generate metabolite peak integrals.

#### 6.2.4 Derivation of NAA diffusion measures

Based on the LCModel data for tNAA, the following empirical quantities were calculated:  $D_{\text{par}}$ , diffusivity along the [1,0,0] direction (roughly parallel to the callosal fibers);  $D_{\text{perp}}$ , diffusivity along the [0,-1,1] direction (roughly perpendicular to the callosal fibers); and  $D_{\text{avg}}$ , the average of the two diffusivities described above (representing the empirical apparent diffusion coefficient of tNAA in the VOI). Diffusivities were calculated assuming monoexponential decay of the signal as a function of b-value in each direction:

$$\ln\left(\frac{s_{b,i}}{s_{b_1,i}}\right) = -b_i \cdot D_i \quad b = \gamma^2 G^2 \delta^2 (\Delta - \delta/3) \quad \text{Equation 6-1}$$

where  $s_{b,i}$  is the measured signal in direction  $i$ ,  $s_{b_1,i}$  is the signal at the lowest b-value for the same direction,  $b_i$  is the b-value in the direction  $i$ , and  $D_i$  is the calculated diffusion coefficient for direction  $i$ .

The LCModel output was also used as an input to a modeling routine that calculates the *intra-axonal*, or *cytosolic*, diffusivity of NAA. This procedure is assumed to minimize the variability in the DWS measurements introduced by macroscopic factors such as the position of the VOI within the white matter tract, the main direction of the tract with respect to the DW gradients, and the macroscopic curvature of the tract within the VOI. The model, thoroughly described in (Ronen et al. 2014), uses the angles between the main eigenvectors of the DTI data within the DWS VOI and the diffusion weighting gradient directions. The data are fitted to the model using two fitting variables:  $D_{\text{model}}$ , the cytosolic diffusion coefficient of NAA, and  $\sigma_\phi$ , the standard deviation of the axonal angular dispersion. It is important to note that  $D_{\text{model}}$  is independent of the tract geometry within the VOI and thus mostly reflects the effects of the cytosolic medium, e.g. viscosity and molecular crowding, on the diffusion of NAA inside the axons.

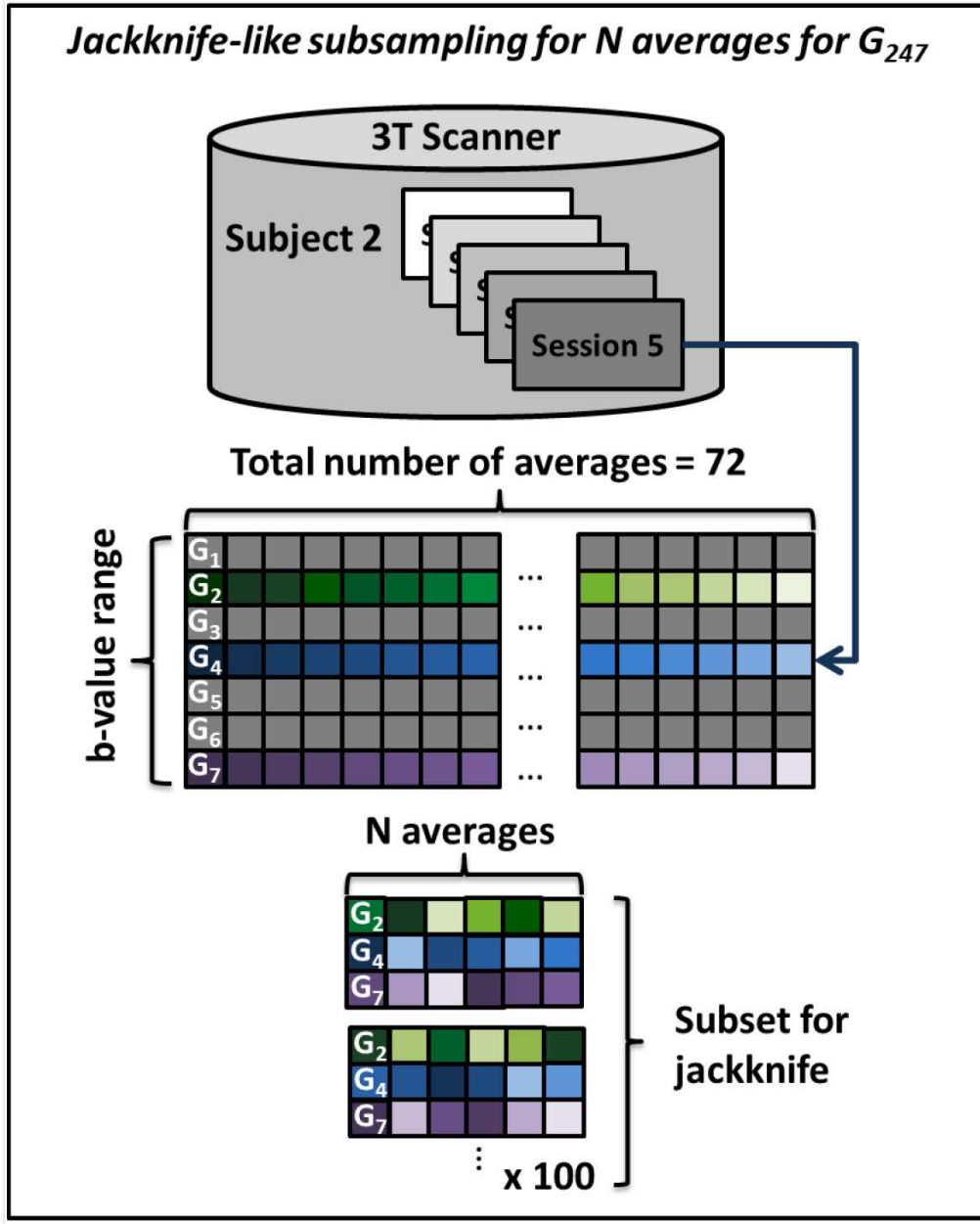


Figure 6.2 Schematic description of the method in which data subsets are randomly selected from the full data set of a single session of a specific subject.

### 6.2.5 Inter-subject variability analysis

For inter-subject variability analysis, the entire data set from each session was used. All spectra belonging to a single diffusion condition were averaged per session.  $D_{\text{par}}$ ,  $D_{\text{perp}}$ ,  $D_{\text{avg}}$ , and  $D_{\text{model}}$  were calculated for each session for all subjects.

### 6.2.6 Intra-subject variability analysis

For the variability analysis within subject, a jackknife-like subsampling procedure was performed (Tu & Shao 1995; Efron & Tibshirani 1994). This procedure used all session data sets from two subjects, one from each scanner, and within-session subsets of these data sets were randomly resampled without replacement prior to averaging. For the 3T case, each subset consisted of 30, 36, 42, 48, 54, and 60 spectra per diffusion weighting condition (the full number of spectra per condition was 72). For the 7T case, 16, 20, 24, 28, and 32 spectra were used out of the 40 spectra available per condition. For each randomly selected subset, an average spectrum was obtained. These spectra for all diffusion-weighting conditions were then used to calculate  $D_{\text{par}}$ ,  $D_{\text{perp}}$ ,  $D_{\text{avg}}$ ,  $D_{\text{model}}$ , and  $\sigma_{\phi}$ . This procedure was then repeated 100 times for each subset size to obtain the jackknife averages and standard deviations of these quantities. A diagram of an example of the jackknife-like procedure is shown in Figure 6.2, where data from 1 session is used to generate 100 subsampled data sets, each with 3 b-values (out of the 7 available) and 6 averages (out of the 72 available). The same procedure was applied to all five sessions, resulting in 5 sets of diffusion properties and their standard deviations for each jackknife subsampling. These averages and standard deviations are used to generate the *across-session* averages and standard deviations of the *intra-session* averages and standard deviations.

### 6.2.7 Statistical analyses

All between group (3T versus 7T) analyses were performed with GraphPad Prism version 6.0b for Mac OS X (GraphPad Software, San Diego, California, USA). Between and within subject analyses were accomplished with STATA release 11 (StataCorp, College Station, Texas, USA). A one-way random-effects ANOVA model was used to estimate the between and within subject variance of the DWS measurements. Between subject variance was used for inter-subject variability analyses whereas within subject variance was used for repeatability coefficient and power/sample size calculations.

The repeatability coefficient ( $C_R$ ) is defined as:

$$C_R = 1.96 \times \sqrt{2} \times \sigma \quad \sigma = \text{standard deviation} \quad \text{Equation 6-2}$$

If data are normally distributed, we expect 95% of differences between two measurements made on the same subject to be less than the  $C_R$  (Bartlett & Frost 2008; Vaz et al. 2013; Beckerman et al. 2001; Myles & Cui 2007).

Additionally, the coefficient of variation:

$$C_V = 100 \times \frac{\sigma}{\mu} \quad \mu = \text{mean} \quad \text{Equation 6-3}$$

where  $\mu$  is the mean and  $\sigma$  is the standard deviation of the resampling results, is reported to compare between diffusivity measures with different mean values.

Power calculations were done to estimate the sample size that would be required to detect a difference ( $\Delta$ ) in DWS measurements between two groups based on the variance ( $\sigma^2$ ) of our measurements. For this, it was assumed that the means were normally distributed and the variance was the same for both groups ( $\sigma_1^2 = \sigma_2^2$ ). For all

calculations, we used a two-sided test with significance level  $\alpha = 0.05$ , ( $z_{1-\alpha/2} = 1.96$ ) and a power of 80% ( $1-\beta = 0.80$ ,  $z_{1-\beta} = 0.84$ ).

The sample size ( $n$ ) required for each group was estimated as (Rosner 2006):

$$n = \frac{(\sigma_1^2 + \sigma_2^2)(z_{1-\alpha/2} + z_{1-\beta})^2}{\Delta^2} \quad \text{Equation 6-4}$$

## 6.3 Results

### 6.3.1 Diffusion weighted spectra and model fit

In Figure 6.3, representative diffusion weighted spectra are shown for 3T and 7T scans. For all directions and field strengths, the NAA signal (tallest peak, located at ~2ppm) decreases with increasing  $b$ -value. The NAA signal loss due to diffusion is greater along the direction parallel to the fiber direction than along the perpendicular direction. Note that the perpendicular  $b$ -values are twice that of the parallel.

Cramér–Rao lower bounds for the tNAA peak from all spectra were between 6% and 20% at 3T and between 3% and 14% at 7T. SNR and spectral resolution at 7T were higher than those at 3T. The highest CRLB values were typically obtained at the highest  $b$ -value in the  $[-1, 0, 0]$  diffusion-weighting direction.

In Figure 6.4, the logarithm of the diffusion weighted tNAA data are plotted as a function of  $b$ -value for the two diffusion gradient directions. The data were obtained from a single session of one subject scanned at 3T (panels A and B) and one subject scanned at 7T (panels C and D). In panels A and C, the data acquired with the 2 gradient directions were separately fitted to 2 independent monoexponential decay functions (equation 2) to give parallel ( $\mathbf{D}_{\text{par}}$ ) and perpendicular ( $\mathbf{D}_{\text{perp}}$ ) diffusivity measures. Panels B and D show the modeled fit and the resulting parameters  $\mathbf{D}_{\text{model}}$  and



$\sigma_\phi$  for these particular data sets. For both 3T (panel B) and 7T (panel D) data sets, the  $\sigma_\phi$  fits of 26.7 and 22.7 degrees are higher than the histology-derived  $\sigma_\phi$  of 18 degrees (Ronen et al. 2013).

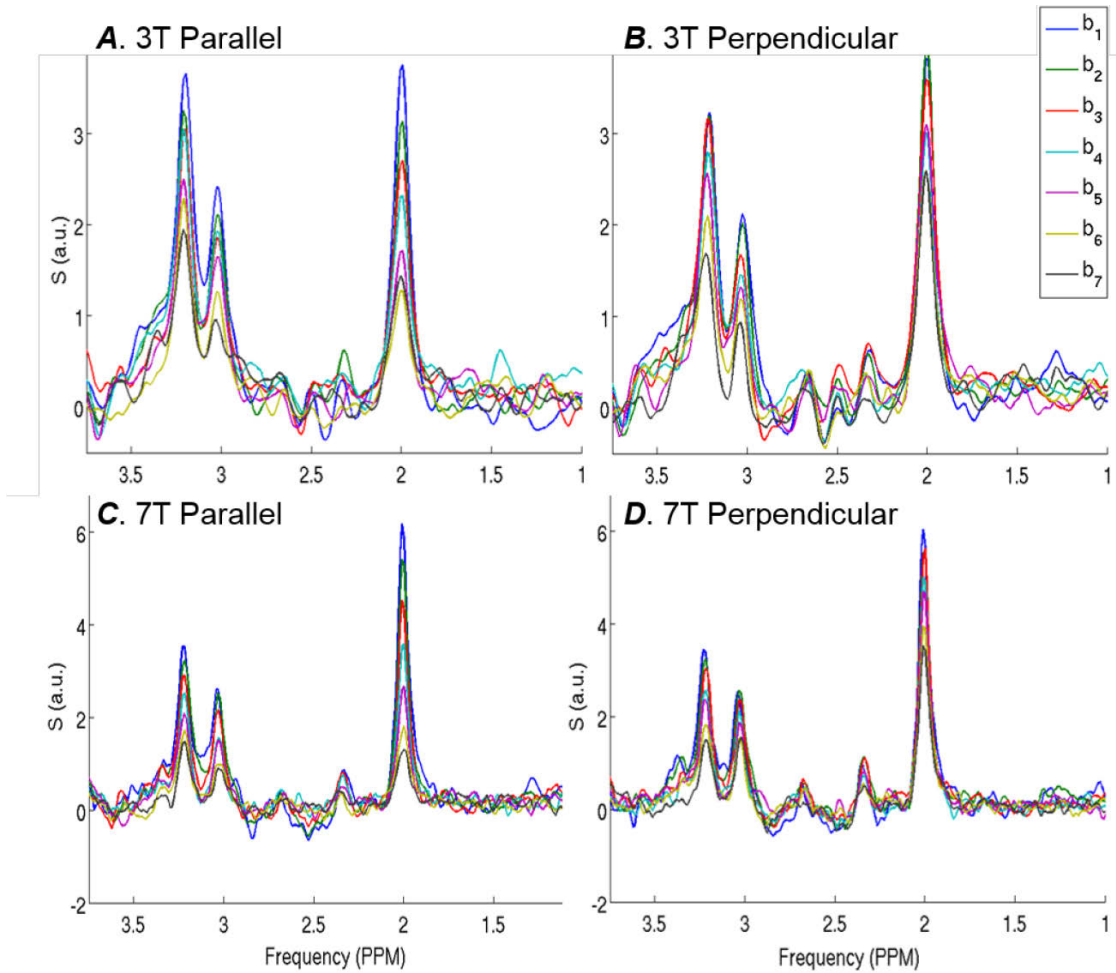


Figure 6.3 Typical spectra acquired at 3T with diffusion-weighting in the parallel ( $g_{[-1,0,0]}$ ) and perpendicular ( $g_{[0,-1,1]}$ ) directions are shown in panels A and C, respectively. Spectra acquired at 7T with the same gradient directions are shown in panels B and D. Line broadening of 5 Hz was applied to all of the spectra for display purposes.

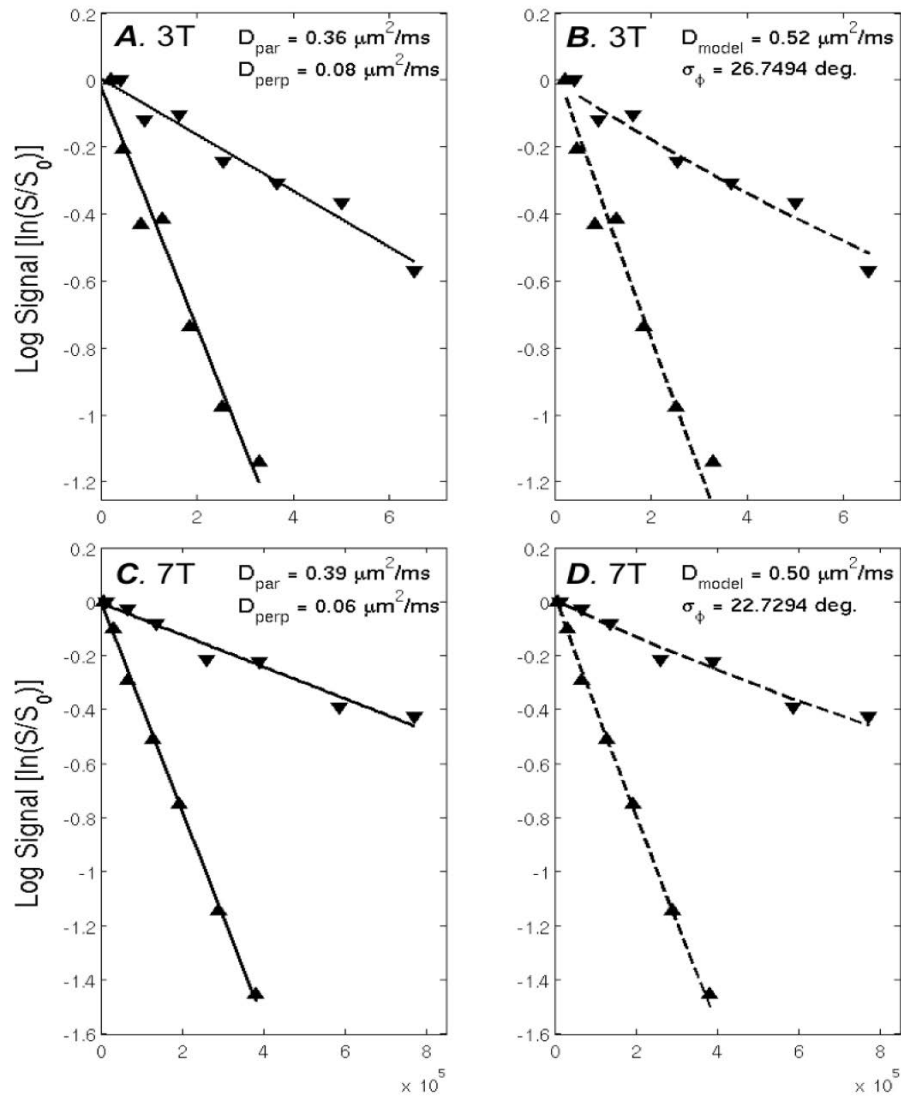


Figure 6.4 Logarithm of the diffusion weighted signal measured with the diffusion weighting applied along the  $[0,-1,1]$  and  $[-1,0,0]$  directions as a function of b-value (measured in s/mm<sup>2</sup>). Panels A and C show the monoexponential fits used to calculate the parallel ( $D_{par}$ ) and perpendicular ( $D_{perp}$ ) diffusivity values from one data set acquired at 3T (A) and one acquired at 7T (C). Panels B and D show the same data fitted to the model described in the text, which yields the cytosolic diffusivity  $D_{model}$  and the standard deviation of the axonal angular dispersion  $\sigma_{\phi}$ .

Table 6.6 Average, standard deviation and coefficient of variation for  $D_{model}$ ,  $D_{par}$ ,  $D_{avg}$ ,  $D_{perp}$ , and  $\sigma_{\phi}$  values calculated based on complete datasets acquired from subjects at 3T and 7T.

		3T Sub1	3T Sub2	3T Sub3	7T Sub1	7T Sub2	7T Sub3
$D_{model}$ ( $\mu\text{m}^2/\text{ms}$ )	Mean (SD)	0.52 (0.05)	0.51 (0.03)	0.48 (0.07)	0.50 (0.06)	0.51 (0.01)	0.50 (0.02)
	$C_V$ (%)	10	5	15	12	2	5
$\sigma_{\phi}$ (degrees)	Mean (SD)	26.78 (12.96)	22.57 (4.68)	36.41 (15.37)	23.81 (1.79)	22.02 (1.66)	29.05 (3.59)
	$C_V$ (%)	48	21	42	8	8	12
$D_{avg}$ ( $\mu\text{m}^2/\text{ms}$ )	Mean (SD)	0.22 (0.01)	0.22 (0.01)	0.21 (0.02)	0.21 (0.02)	0.22 (0.01)	0.22 (0.01)
	$C_V$ (%)	5	3	11	12	2	3
$D_{par}$ ( $\mu\text{m}^2/\text{ms}$ )	Mean (SD)	0.36 (0.03)	0.38 (0.02)	0.34 (0.05)	0.35 (0.04)	0.38 (0.01)	0.36 (0.02)
	$C_V$ (%)	7	5	14	13	2	5
$D_{perp}$ ( $\mu\text{m}^2/\text{ms}$ )	Mean (SD)	0.08 (0.02)	0.07 (0.02)	0.08 (0.00)	0.07 (0.00)	0.06 (0.00)	0.07 (0.01)
	$C_V$ (%)	29	22	2	6	7	11

### 6.3.2 Inter-subject variability

The tNAA diffusivity measures  $D_{par}$ ,  $D_{perp}$ ,  $D_{avg}$ , and  $D_{model}$  were first derived from the full data sets, i.e. all acquired spectra at all b-values with no subsampling. Figure 6.5 shows the distribution of these measures across sessions for each subject. The left panel shows the data from the 3T scanner, and the 7T data are shown on the right. The data are displayed as a box-and-whisker plot to show the variability across the sessions

per subject. Table 6.6 shows the averages, standard deviations, and coefficients of variation of these measures across subjects and sessions. Mean coefficients of variation ranged between 2% and 13% for both scanners, with the exception of that of  $D_{\text{perp}}$  at 3T, which was 29% across subjects and 22% across sessions. No significant differences in  $D_{\text{par}}$ ,  $D_{\text{perp}}$ ,  $D_{\text{avg}}$ , or  $D_{\text{model}}$  were observed between subjects (one-way ANOVA). In Figure 6.6, all measures calculated based on the full data sets from all subjects were grouped. Diffusivity measures obtained from the data acquired at 3T and 7T were not statistically different (Figure 6.6).  $D_{\text{model}}$  values had a smaller (not significant) standard deviation (SD) at 7T compared to 3T: mean (SD) values were  $D_{\text{model}} = 0.501 (0.052)$  at 3T and  $D_{\text{model}} = 0.506 (0.035) \mu\text{m}^2/\text{ms}$  at 7T. For  $D_{\text{avg}}$ , the mean and SD were the same at 3T and 7T: mean (SD) values were  $D_{\text{avg}} = 0.217 (0.015)$  at 3T and  $D_{\text{avg}} = 0.216 (0.015) \mu\text{m}^2/\text{ms}$  at 7T. The standard deviation of  $\sigma_{\varphi}$  was significantly different between scanners (SD 3T v SD 7T  $p < 0.0001$ ).

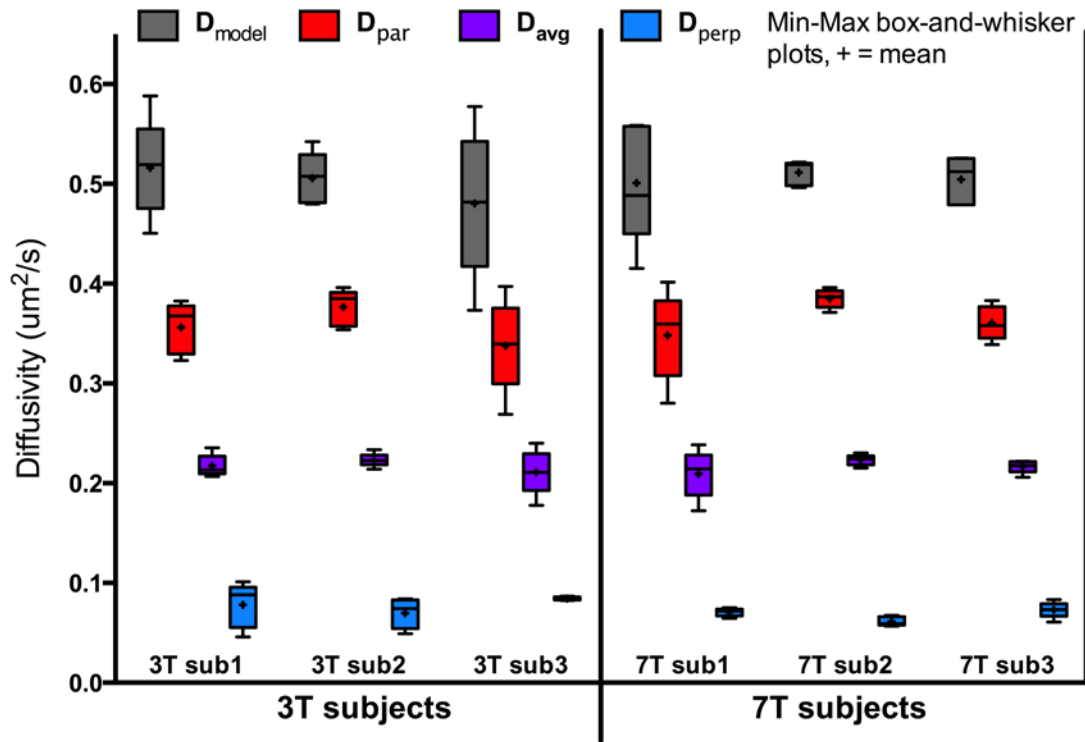


Figure 6.5 Inter-subject and inter-session variability of all diffusivity values ( $D_{par}$ ,  $D_{perp}$ ,  $D_{avg}$  and  $D_{model}$ ), calculated based on complete datasets acquired from 3 subjects at 3T (left panel) and three subjects at 7T (right panel). Box-and-whisker plots show the inter-session variability of diffusivity measures for each subject.

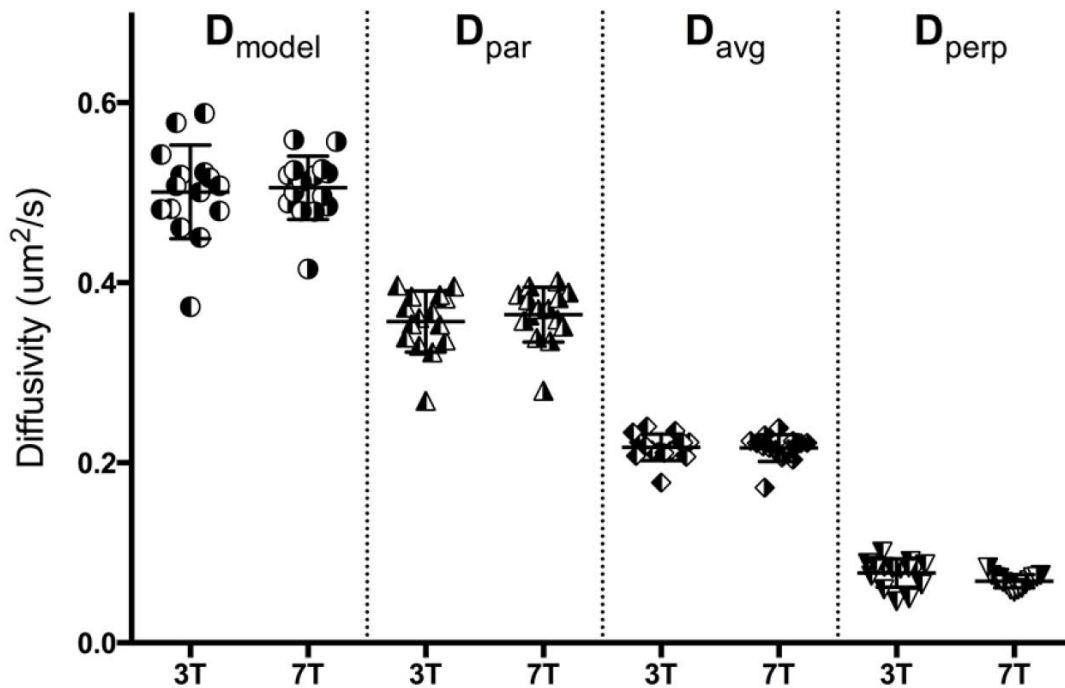


Figure 6.6 Diffusivity measures from all subjects and all sessions obtained from the experiments performed at 3T and 7T.

### 6.3.3 Intra-Subject Variability

#### 6.3.3.1 Effect of spectral averaging

To investigate the effect of number of spectral averages on the tNAA diffusivity measures and their variability, we used the jackknife-like resampling approach described in the methods section. Figure 6.7 show the resulting  $D_{\text{par}}$ ,  $D_{\text{perp}}$ ,  $D_{\text{avg}}$ , and  $D_{\text{model}}$  values obtained using the data from all 5 sessions of a 3T subject and a 7T subject. Here, data acquired at all 7 b-values were used. The mean across sessions ( $\pm$  standard deviation across sessions) of the jackknife estimate of the mean for these diffusivity measures are

shown for each subset size (panels A-D and I-L) expressed in total number of acquired spectra (proportional to the acquisition time). The mean across sessions ( $\pm$  standard deviation across sessions) of the jackknife-like estimate of the standard deviation for these diffusivity measures is shown for each subset size (panels E-H and M-O). As expected, the jackknife-like estimate standard deviations of all measures decrease with increasing number of spectral averages. For all diffusion measures at 3T, the standard deviation decreased by 44-53% with a doubling of spectral averages from 420 to 840. Similarly, at 7T, the standard deviations decreased by 52%-59% with a doubling of spectral averages from 224 to 448. The standard deviations were observed to be lower at 7T than at 3T for all diffusion measures.

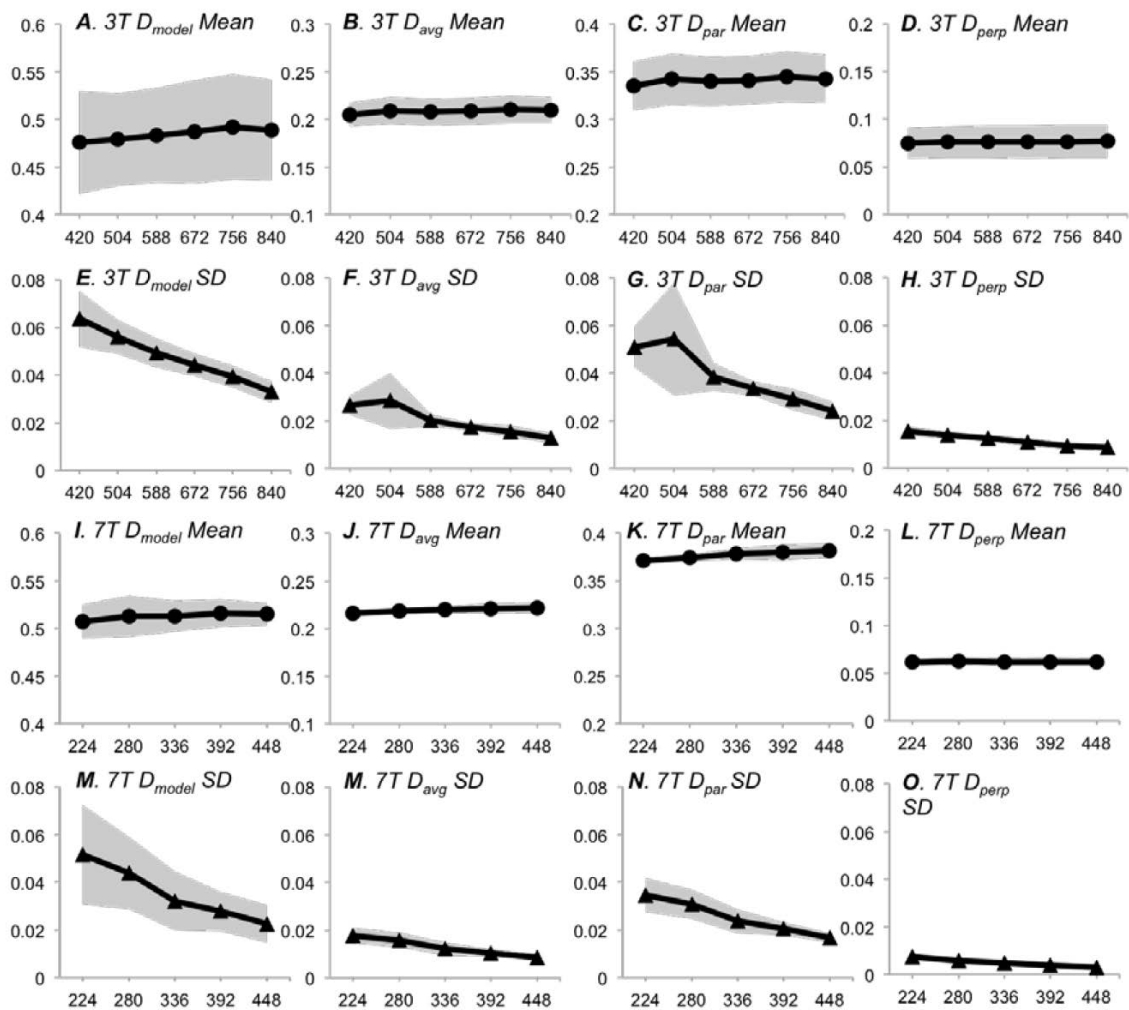


Figure 6.7 Mean diffusivity values and standard deviations obtained from the jackknife-like resampling procedure applied to the data acquired from one subject at 3T (A-H) and one subject at 7T (I-O). The solid symbols in panels A-D and I-L show the diffusivity measures obtained for a given number of acquisitions, averaged first over 100 jackknife evaluations and then over the 5 sessions. The shaded areas show the standard deviations of the means across the 5 sessions. Panels E-H and M-O show the standard deviations of the diffusivity measures shown in the upper panels, similarly obtained first by evaluating the standard deviations of the jackknife results from a single session, and then averaging them across sessions. The shaded areas show the standard deviation of the standard deviations across the 5 sessions.



### **6.3.3.2 Effect of b-value range**

To assess the effect of higher b-value data on the NAA diffusivity measures, we calculated these measures for different ranges of b-values. For this purpose, we focused on data obtained from one subject per scanner and calculated the various diffusivity measures based on ranges of 3, 4, 5, 6, and 7 b-values, always starting from the lowest b-value.

In Figure 6.8, the mean  $D_{\text{par}}$ ,  $D_{\text{perp}}$ ,  $D_{\text{avg}}$ , and  $D_{\text{model}}$  calculated for all sessions, and the standard deviations across sessions, are shown for one subject at 3T and one at 7T. The data are shown as a function of the maximum b-value used. The estimated total scan time was kept constant by using different number of spectral averages for each b-value scheme. Table 6.7. specifies the number of spectral averages ( $x$ ) used for each separate b-value combination. The 3T data show a decrease of 20 to 25% for  $D_{\text{par}}$ ,  $D_{\text{avg}}$ , and  $D_{\text{model}}$  (25%, 20%, and 17%, respectively) across the range of maximum b-value used, whereas the  $D_{\text{perp}}$  values remain constant throughout the range. The standard deviations also noticeably decreased for all diffusivity measures as higher b-values were used. The 7T data show somewhat steeper decreases in  $D_{\text{par}}$ ,  $D_{\text{avg}}$  and  $D_{\text{model}}$  (30%, 25%, and 17%, respectively) across the range of maximum b-value used, and no changes were observed across the values of  $D_{\text{perp}}$ . The standard deviations at 7T were lower than those observed at 3T at all b-value ranges and converged to noticeably smaller values as higher b-value ranges were used.

Table 6.7 List of b-value schemes with the number of spectral averages used for equivalent acquisition time comparisons in Figure 6.8.

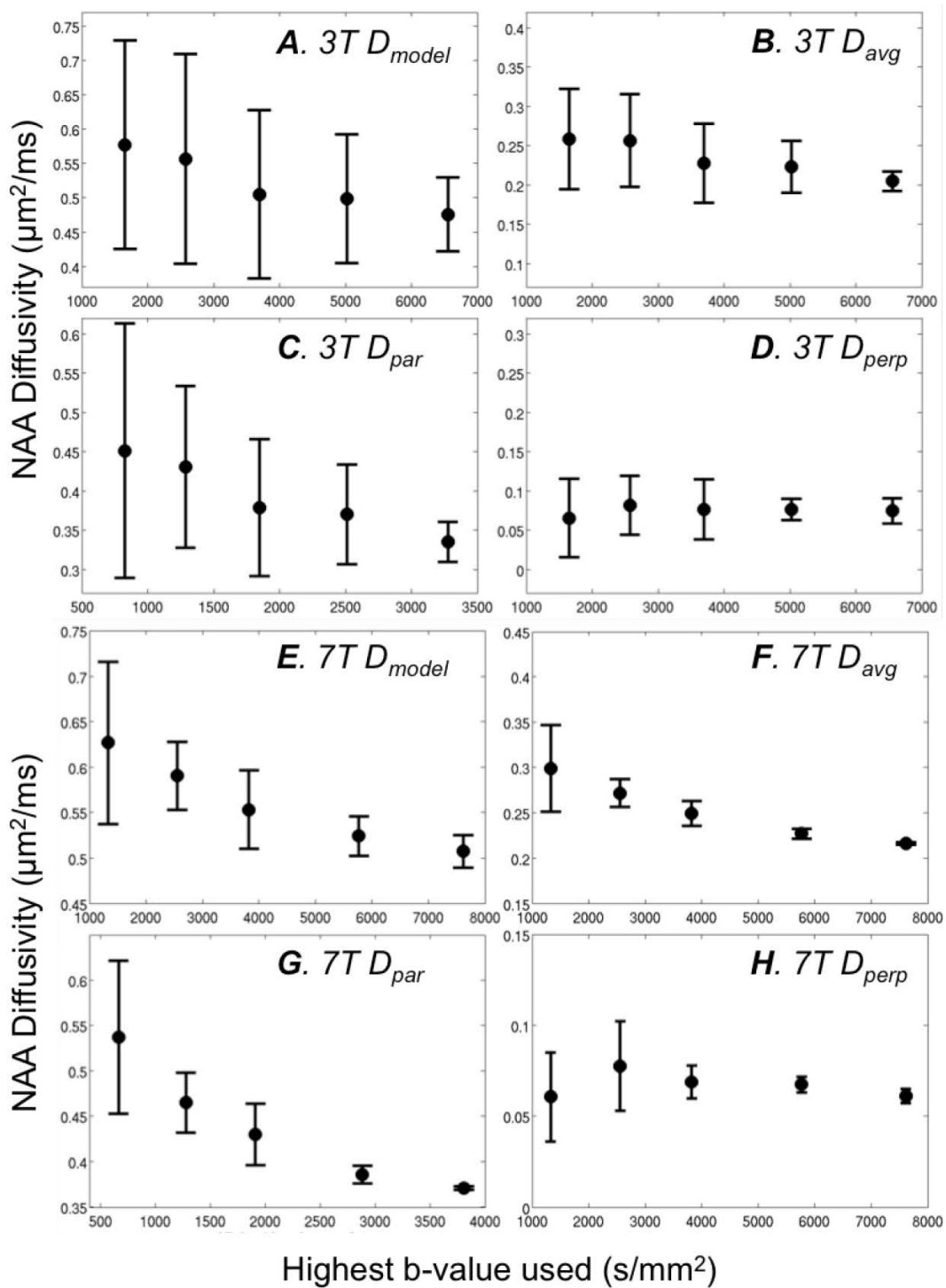
Scheme	b-values used	# b-vals	Equivalent acquisition times*	
			7T	3T
$g_{1-3}$	$b_1, b_2, b_3$	3	9.6 min ( $x = 32$ )	12 min ( $x = 60$ )
$g_{246}$	$b_2, b_4, b_6$	3	9.6 min ( $x = 32$ )	12 min ( $x = 60$ )
$g_{247}$	$b_2, b_4, b_7$	3	9.6 min ( $x = 32$ )	12 min ( $x = 60$ )
$g_{1-4}$	$b_1, b_2, b_3, b_4$	4	9.6 min ( $x = 24$ )	12.8 min ( $x = 48$ )
$g_{1357}$	$b_1, b_3, b_5, b_7$	4	9.6 min ( $x = 24$ )	12.8 min ( $x = 48$ )
$g_{1-5}$	$b_1, b_2, b_3, b_4, b_5$	5	10 min ( $x = 20$ )	12 min ( $x = 36$ )
$g_{1-6}$	$b_1, b_2, b_3, b_4, b_5, b_6$	6	9.6 min ( $x = 16$ )	12 min ( $x = 30$ )
$g_{1-7}$	$b_1, b_2, b_3, b_4, b_5, b_6, b_7$	7	11.2 min ( $x = 16$ )	14 min ( $x = 30$ )

\*Equivalent acquisition time comparisons were made to assess the effect of b-value scheme using approximately the same number of spectra and, therefore, similar scan times.

$x$  = number of spectra per condition, TR = 2 heart beats  $\approx$  2 sec for 3T and TR = 3 heart beats  $\approx$  3 sec for 7T (assuming a heart rate of 60 beats per minute)

Acquisition time = # b-values  $\times$  2 directions  $\times$   $x$  spectra  $\times$  TR

Figure 6.8 (next page) Mean diffusivity values obtained from all 5 sessions are shown as a function of the highest b-value used. Error bars correspond to the inter-session standard deviation. Panels A-D are one subject scanned at 3T. Panels E-H are one subject scanned at 7T.



### 6.3.3.3 Effect of b-value scheme

In order to reach an optimal combination of b-values and number of spectral averages within a preselected experimental time, we investigated the coefficient of variation ( $C_V = 100 \times \frac{\sigma}{\mu}$ ) of empirical ( $D_{avg}$ ) and cytosolic ( $D_{model}$ ) diffusion coefficients of tNAA, for a variety of b-value selections and an increasing number of spectral averages. For example, diffusivity measures resulting from a selection of b-values represented as  $g_{247}$  indicates that these measures were obtained using the 2<sup>nd</sup>, 4<sup>th</sup>, and 7<sup>th</sup> b-values for each direction, starting from the lowest b-value. Figure 6.9 shows the coefficient of variation as a function of number of spectral averages for all of the b-value combinations listed in Table 6.7. The relative error is observed to depend much more strongly on the highest b-value used than on the number of b-values.

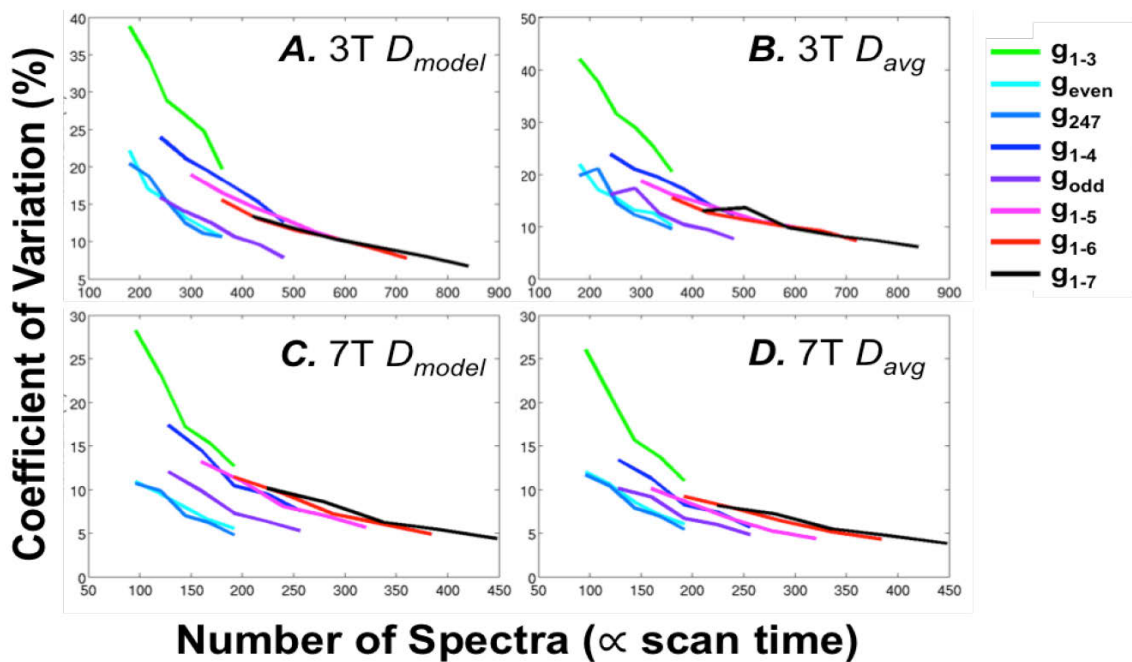


Figure 6.9 The coefficients of variation for  $D_{model}$  (panels A & C) and  $D_{avg}$  (panels B & D) obtained from a single session subject acquired at 3T (panels A & B) and 7T (panels C & D), shown as a function of number of total spectra acquired for different b-value schemes Table 6.7.

### 6.3.4 Inter-subject variability with optimized b-value scheme

In the previous sections, it was determined that the  $g_{247}$  b-value scheme demonstrates excellent intra-subject reproducibility with a much shorter scan time than the maximum set ( $g_{1-7}$ ). Therefore, the inter-subject variability of the  $g_{247}$  b-value combination was analyzed and summarized in Figure 6.10 (comparable to Figure 6.5). Again, there were no differences in  $D_{\text{model}}$ ,  $D_{\text{avg}}$ ,  $D_{\text{par}}$  and  $D_{\text{perp}}$  between subjects (one-way ANOVA). Of note, the scan time for the  $g_{247}$  scheme would be less than half that of the scan time for the  $g_{1-7}$  scheme.

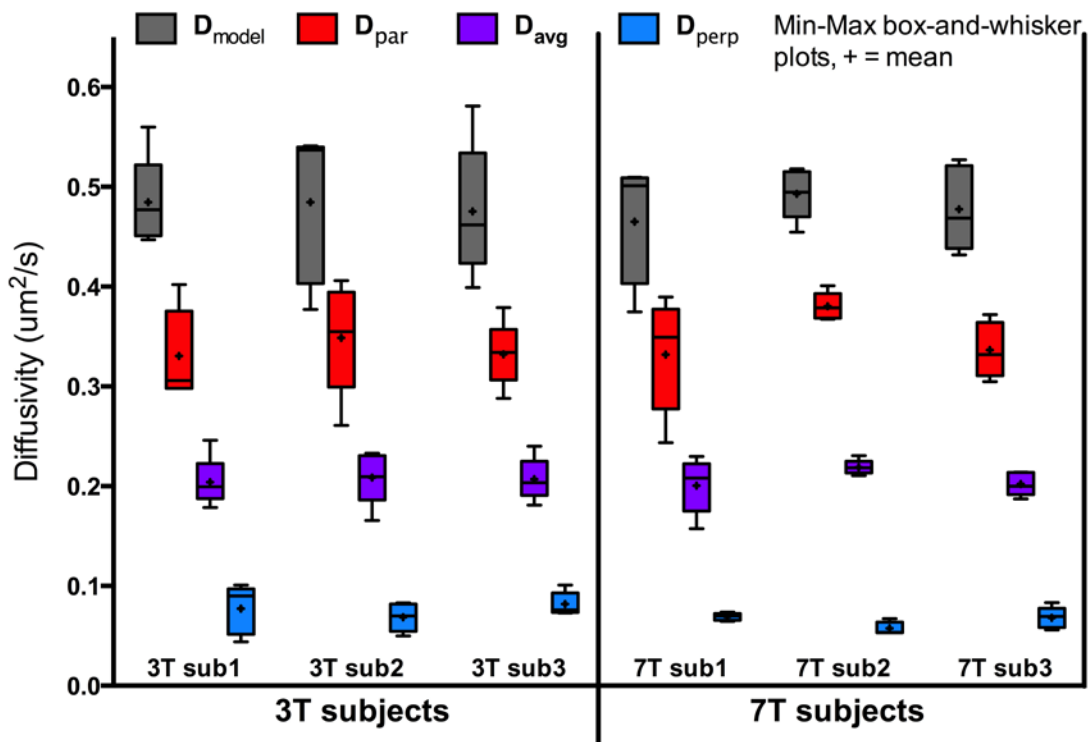


Figure 6.10 Inter-subject and inter-session variability of all diffusivity values ( $D_{\text{par}}$ ,  $D_{\text{perp}}$ ,  $D_{\text{avg}}$ , and  $D_{\text{model}}$ ) calculated for the  $g_{247}$  b-value scheme, a subset of b-values from the maximum datasets, acquired from 3 subjects at 3T (left panel) and three subjects at 7T (right panel). Box-and-whisker plots show the inter-session variability of diffusivity measures for each subject.

### 6.3.5 Reproducibility and sample size analysis

Reproducibility was quantitated with an extension of the Bland-Altman method for analyzing agreement between repeated measures (Bartlett & Frost 2008; Vaz et al. 2013; Beckerman et al. 2001; Myles & Cui 2007). Plots of difference between repeated measures versus mean of repeated measures and plots of within subject variance versus subject mean were assessed for relationships of variability with mean (Figure 6.11) (Bland & Altman 1986). As no positive relationships were detected, log transformations were not required. Repeatability coefficients ( $C_R$ ) were calculated (as described in methods) and are shown in Table 6.8 for both scanners and for measures  $D_{\text{model}}$  and  $D_{\text{avg}}$ . Smaller values of  $C_R$  demonstrate greater reproducibility. As expected, the measurements from data acquired at 7T using all spectra have the lowest  $C_R$  s of 21%. Nonetheless, the 7T  $g_{247}$  scheme measurements, which utilize fewer than half of the spectra of  $g_{1-7}$ , remain low with  $C_R$  s of 25%.

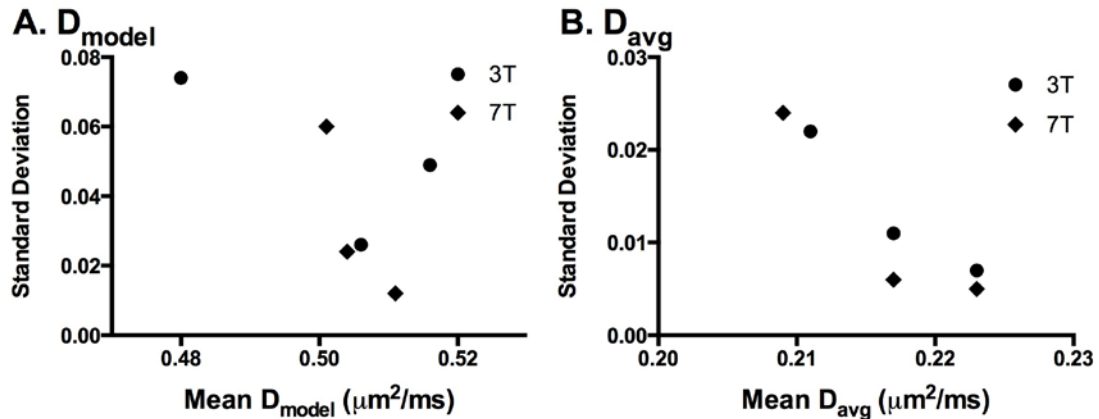


Figure 6.11 Plots of standard deviation versus mean for the  $D_{\text{model}}$  (A) and  $D_{\text{avg}}$  (B) diffusivity measures at 3T and 7T.

Table 6.8 Repeatability and sample size values for b-value scheme  $g_{247}$

Scanner	Measure	$\sigma^{2*}$ (variance)	$n$ (sample size#)	$C_R^*$ (% mean)	Scan Time ( # spectral averages)
3T $g_{1-7}$	$D_{model}$	0.00287	18	0.15 (30%)	33.6 min ( $x=72$ )
	$D_{avg}$	0.00022	9	0.04 (21%)	
7T $g_{1-7}$	$D_{model}$	0.00142	9	0.10 (21%)	28 min ( $x=40$ )
	$D_{avg}$	0.00022	9	0.04 (21%)	
3T $g_{1357}$	$D_{model}$	0.00330	21	0.16 (32%)	19.2 min ( $x=72$ )
	$D_{avg}$	0.00029	11	0.05 (24%)	
7T $g_{247}$	$D_{model}$	0.00201	13	0.12 (25%)	12 min ( $x=40$ )
	$D_{avg}$	0.00032	12	0.05 (25%)	

\* $\mu m^2/ms$

# significance level ( $\alpha$ ) = 0.05, power ( $1-\beta$ ) = 0.80, detectable difference ( $\Delta$ ) = 10%

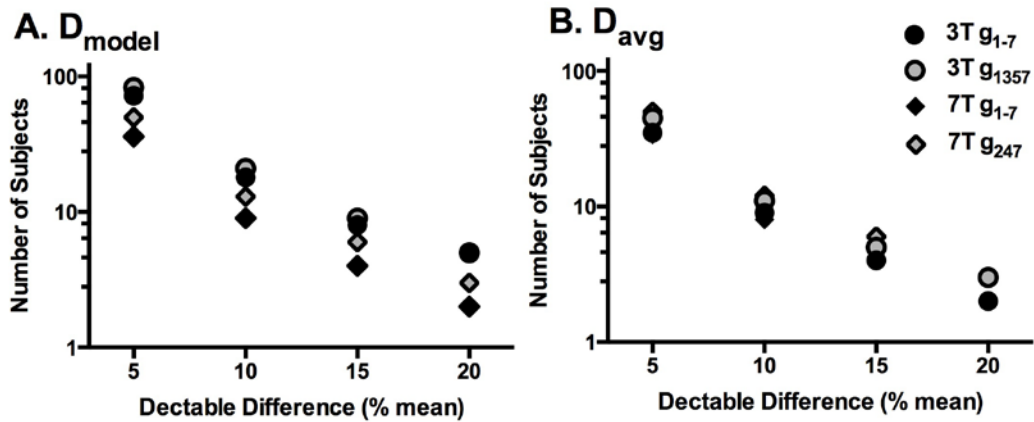


Figure 6.12 Number of subjects required to detect difference (in percent of mean) with significance level of  $\alpha = 0.05$  and power of  $1-\beta = 0.80$  using the  $g_{1357}$  b-value scheme for 3T and  $g_{247}$  b-value scheme for 7T.

Sample size calculations were done to determine the number of subjects per group that would be required to detect a difference between 2 groups with power of 80% and significance level of 5%. Sample size (n) values to detect a 10% difference in both  $D_{\text{model}}$  and  $D_{\text{avg}}$  are shown in *Table 6.8* and the trend in sample size values for 5, 10, 15, and 20% detectable differences are depicted in *Figure 6.12*.

## **6.4 Discussion**

There is a growing interest in using compartment-specific diffusion metrics derived from DWS to investigate disease-related changes. Prior work has shown differences in the metabolite diffusion coefficients of the patients compared to controls in diseases such as multiple sclerosis (Wood et al. 2012), acute cerebral ischemia (Zheng et al. 2011; Harada et al. 2002), brain tumors (Colvin et al. 2008) and psychiatric disorders (Du et al. 2013). To date however, no study has been done for evaluating inter- and intra-subject reproducibility of the DWS method. It is important to assess the variability of calculated and modeled metabolite diffusion coefficients across subjects and between different sessions from the same subject in order to validate the DWS method for the case-control studies.

In this project, we investigated the inter- and intra-subject variability of diffusivity measures of tNAA, both empirical and modeled, derived from DWS experiments performed on the human aCC with 3T and 7T scanners. We also studied the effect of scan parameters, such as number and range of b-values for each diffusion direction and number of spectral averages, in order to suggest optimal scan parameters to perform DWS experiments within a given experimental time limit. To our knowledge, this is the first study to investigate the reproducibility of DWS scans from human brain and to



suggest optimal scan parameters to perform DWS experiments within a given experimental time limit that is suitable for clinical and clinical research purposes.

#### **6.4.1 Intra- and inter-subject variability of DWS Measures**

The coefficients of variation ( $C_V$ ) given in Table 6.6 and the reproducibility coefficients ( $C_R$ ) given in Table 6.8 for  $D_{\text{par}}$ ,  $D_{\text{perp}}$ ,  $D_{\text{avg}}$ , and  $D_{\text{model}}$  indicate reasonable reproducibility of the DWS measurements of tNAA in the corpus callosum. At 7T, all  $C_V$  values were less than 13%, and most were in the range of 2% - 8%. The  $C_V$  values for the diffusion measures evaluated from the data acquired at 3T were higher than those found at 7T, ranging between 3% and 29%. One should keep in mind that the variability measured in these long sessions (typically about 40 minutes in both scanners) also reflects patient motion and scanner-related instabilities, which are expected to be less pronounced in shorter experiments. Past DWS studies that explored the effect of disease reported substantial changes in tNAA diffusion measures, which were hypothesized to be related to neuronal/axonal damage. In one study, an increase in  $\text{ADC}(\text{tNAA})$  of above 50% was reported in malignant brain tumors, and a decrease in  $\text{ADC}(\text{tNAA})$  of about the same magnitude was observed in ischemic stroke (Harada et al. 2002). Zheng et al. (Zheng et al. 2011) reported an age-related drop of 27% in  $\text{ADC}(\text{tNAA})$  values. In our own study on normal appearing white matter changes in MS at 7T, a decrease of about 20% was observed in the  $D_{\text{par}}$  of tNAA in the aCC of a small cohort of multiple sclerosis patients compared to age-matched healthy controls (Wood et al. 2012). Based on our power calculations, a difference between groups of 10% for  $D_{\text{model}}$  or  $D_{\text{avg}}$  could be detected with groups as small as 9-18 subjects each for 3T or 9 subjects each for 7T using the entire dataset. This result is particularly reassuring as it suggests the ability of DWS of NAA to pick up subtle changes in intra-axonal structure in

normal appearing white matter. Such an acquisition would take around 33.6 minutes at 3T and 28 minutes at 7T, necessitating the reduction of acquisition time in order to make the experiments feasible for the clinical studies.

The average inter-subject variability values in  $D_{\text{avg}}$  and in  $D_{\text{model}}$  at 7T were 5.7% and 6.3%, respectively, and thus comparable. At 3T, the variability of  $D_{\text{avg}}$  was  $C_V = 6\%$ , whereas the  $C_V$  of  $D_{\text{model}}$  was higher at 10%.  $D_{\text{avg}}$  is roughly equivalent to the ADC of tNAA within the VOI, i.e. it includes the effect of restrictions on the diffusion of tNAA imposed by axonal membranes. Since the typical DWS measurement is performed on a large volume, these geometric factors introduce a confound that varies across subjects and VOI locations. The model presented in (Ronen et al. 2014) provides a way to remove the impact of macroscopic curvature of white matter tracts within the volume and yields a diffusion measure,  $D_{\text{model}}$ , which represents the cytosolic diffusion coefficient and thus includes the impact of tortuous diffusion within the axonal medium. The stability of the resulting  $D_{\text{model}}$  depends greatly on the SNR of the single DWS measurements that generate the data set needed for the fitting procedure. It can be appreciated that at 7T, where the Cramér–Rao Lower Bound (CRLB) values for the individual measurements were relatively low, the variability in  $D_{\text{model}}$  was comparable to that of  $D_{\text{avg}}$ . At 3T, where the CRLB were higher, in particular at the high b-value range,  $D_{\text{model}}$  was found to be less stable.

#### **6.4.2 Effect of number of spectral averages**

The results of the jackknife-like procedure (Figure 6.7) showed a steep decrease in the standard deviations of  $D_{\text{model}}$  (panel b),  $D_{\text{avg}}$  (panel d),  $D_{\text{par}}$  (panel f), and  $D_{\text{perp}}$  (panel h) with increasing number of averages. The means of all diffusion measures remained constant across the range of spectral averages at both field strengths. This is

particularly reassuring in the case of  $D_{\text{model}}$ , which is derived from a two-parameter nonlinear fitting procedure. Here, the standard deviation of  $D_{\text{model}}$  behaves similarly to that of the empirical  $D_{\text{avg}}$ , and no biases are observed in the mean value of  $D_{\text{model}}$  when the number of averages is low. In all empirical measures, the stability of the means together with the monotonically decreasing standard deviation is expected, leaving the experimenter to decide whether to use longer scan times or to increase the sample size in order to reach a desired variance. The lower SNR of the individual measurements at 3T resulted in higher standard deviations for all measures obtained at 3T compared to those obtained at 7T.

#### **6.4.3 Effect of b-value range**

A general decreasing trend was observed in mean  $D_{\text{par}}$ ,  $D_{\text{avg}}$ , and  $D_{\text{model}}$  when the spectra from higher b-values were included in the calculation of these diffusivity measures at both field strengths, while keeping the acquisition time constant (Figure 6.8). This probably stems from the non-monoexponential decay of the diffusion weighted tNAA signal, caused by non-Gaussian diffusion behavior brought on by geometric restrictions shown in several studies of diffusion properties of metabolites at high diffusion weighting values (Assaf & Cohen 1998a; Assaf & Cohen 1998b). Concomitantly, the standard deviation of all tNAA diffusion measures from the same subject decrease with increasing b-value range. This is expected, given the typical ADC of tNAA in white matter, which is reported to be between  $1 \times 10^{-4}$  and  $2.5 \times 10^{-4}$   $\text{mm}^2/\text{s}$  (Marchadour et al. 2012). Such ADC values require a b-value of about 5000  $\text{s}/\text{mm}^2$  in order to minimize the effect of error propagation on the calculation of the ADC (Ellegood et al. 2010), suggesting that including higher b-values is essential for obtaining robust DWS measures. Interestingly,  $D_{\text{perp}}$  remained constant across the range of maximum b-

value used, both at 3T as well as at 7T. This result is likely due to the fact that the deviation from monoexponentiality becomes apparent at much higher b-values in the case where the gradient direction is mostly perpendicular to the axonal propagation direction.

#### **6.4.4 Effect of b-value scheme on intra-subject variability**

Figure 6.9 can serve as a guideline for choosing a combination of b-values and number of averages in order to reach a desired variability in both  $D_{\text{model}}$  and  $D_{\text{avg}}$ . It is clearly seen that sampling the upper range of b-values is critical for obtaining low variability, e.g. schemes  $g_{247}$ ,  $g_{1357}$ , and  $g_{1-7}$ , which all include a balanced sampling of the entire b-value range with 3, 4, and 7 b-values, respectively, quickly converge to low variability values. On the other hand, the scheme  $g_{123}$  has twice the variability of  $g_{247}$  for the same number of acquisitions. There is a substantial difference between 3T and 7T in the number of averages needed to reach the same variability, stemming from the intrinsically higher SNR of spectroscopic measurements at 7T. For example, for the scheme  $g_{247}$  about 200 acquisitions are needed to reach 5% variability in both diffusion measures at 7T, whereas a similar number of acquisitions at 3T will result in  $C_V = 20\%$ . An acquisition protocol that will consist of 3 b-values applied in 2 gradient directions and 32 averages per diffusion weighting condition (total number of acquisitions = 192) will result in an acquisition time of 9.6 minutes at 7T, when a TR of 3 heart beats is used, and assuming a heart rate of 60 beats per minute. A similar variability ( $\sim 7\%$ ) can be reached at 3T when the scheme  $g_{1357}$  is used with 384 acquisitions (4 b-values applied in 2 gradient directions with 48 averages), with a resulting acquisition time of 12.8 minutes when a TR of 2 heart beats is used. Power calculations based on these schemes suggest that a minimum of 11-13 subjects per group could suffice to detect a subtle

difference of 10% in  $D_{\text{model}}$  (at 7T) and  $D_{\text{avg}}$  (both at 3T and 7T) in case-control studies within a maximum acquisition time of 12 (at 7T) to 19 minutes (at 3T).  $D_{\text{model}}$  at 3T will necessitate a minimum of 21 subjects per group in order to detect the same effect.

The differences in the coefficient of variation of  $D_{\text{model}}$  and  $D_{\text{avg}}$  are rather minor and can only be seen when the variability is high, especially at 7T. We consider this to be an important finding, as it confirms the stability of the modeling process and its robust error-propagation properties. Since  $D_{\text{model}}$  successfully accounts for the macroscopic and microscopic distributions of axonal directions within the VOI, we believe that  $D_{\text{model}}$  is a clinically relevant measure for the cytosolic diffusion coefficient of tNAA.

#### **6.4.5 Limitations of the study**

Our study was subject to several challenges and limitations. The small number of subjects used in our study limits the evaluation of across-subject variability. The choice of different subjects for the 3T and 7T measurements, which were performed on different continents, prevents us from performing a more complete comparison of DWS quantities of tNAA across these 2 field strengths. Subject motion and scanner instabilities across sessions, as well as small differences in the positioning of the VOI in different sessions, can also affect the variability observed in the study. Finally, we restricted this study to focus on the diffusion properties of tNAA in a specific white matter pathway, the corpus callosum. This choice was guided by the apparent simplicity of the fiber structure in the corpus callosum, its easy identification, and the simplicity of repositioning the DWS VOI in subsequent sessions. The corpus callosum also allows a relatively straightforward implementation of our model for extracting  $D_{\text{model}}$  from the two gradient directions. Future work should provide a more general model that will allow an arbitrary choice of DWS VOI with a variety of fiber orientations within the VOI.

#### **6.4.6 Conclusion**

In this study, we evaluated the reproducibility of empirical and modeled diffusion properties of tNAA in the corpus callosum on two MRI scanners operating at 3T and 7T. Statistical assessment of the intra-subject variability shows that DWS experiments can be performed at both field strengths within clinically relevant scan times of about 10-13 minutes while retaining low variance (~5%) for the estimated diffusion properties of tNAA. These measurements provide ample power to detect group mean differences with groups of 10 or fewer subjects.

#### **6.5 Other contributors to this work**

Ayşe Ece Ercan<sup>1</sup>, Francesca Branzoli<sup>2,3</sup>, Andrew Webb<sup>1</sup>, Pascal Sati<sup>4</sup>, Daniel S. Reich<sup>4</sup> and Itamar Ronen<sup>1</sup>

##### **6.5.1 Affiliations**

<sup>1</sup> C.J. Gorter Center for High Field MRI, Dept of Radiology, Leiden University Medical Center, Leiden, Netherlands

<sup>2</sup> Institut du Cerveau et de la Moelle épinière - ICM, Centre for Neuroimaging Research – CENIR, Paris, France

<sup>3</sup> Sorbonne Universités, UPMC Paris 06, Inserm UMR S 1127, CNRS UMR 7225, F-75013, Paris, France

<sup>4</sup> Translational Neuroradiology Unit (NINDS), National Institutes of Health, Bethesda, Maryland, USA

## **7 INVESTIGATING AXONAL DAMAGE IN MULTIPLE SCLEROSIS BY DIFFUSION TENSOR SPECTROSCOPY**

As axonal damage is an important factor of clinical status in multiple sclerosis (MS), sensitive and specific in vivo measures of axonal damage might greatly benefit prognostication and therapy assessment. Diffusion tensor spectroscopy (DTS) combines features of diffusion tensor imaging and magnetic resonance spectroscopy, allowing measurement of the diffusion properties of intracellular, cell-type-specific metabolites. As such, it may be sensitive to disruption of tissue microstructure within neurons. In this cross-sectional pilot study, diffusion of the neuronal metabolite N-acetyl aspartate (NAA) was measured in the normal appearing corpus callosum on a 7 tesla MRI scanner, comparing 15 MS patients and 14 healthy controls. We found that NAA parallel diffusivity is lower in MS ( $p=0.030$ ) and inversely correlated with both water parallel diffusivity ( $p=0.020$ ) and clinical severity ( $p=0.015$ ). In the context of previous experiments, our findings provide preliminary evidence that DTS can distinguish axonopathy from other processes such as inflammation, edema, demyelination and gliosis. By detecting reduced diffusion of NAA parallel to axons in white matter, DTS may thus be capable of distinguishing axonal disruption in MS in the setting of increased parallel diffusion of water, which is commonly observed in MS but pathologically nonspecific.

### ***7.1 Introduction***

Multiple sclerosis (MS) is an immune-mediated demyelinating disease of the central nervous system. While inflammation and demyelination may be the major cause of acute and usually reversible relapses in the early phase of MS, neuroaxonal

pathology is responsible for much of the progressive disability associated with chronic MS (Trapp et al. 1998; Tallantyre et al. 2010). The long-term effects of neurodegeneration can be detected in the form of tissue loss (atrophy), whereas ongoing neurodegeneration, manifested as neurons that are damaged but still intact, is exceedingly difficult to measure in vivo.

N-acetyl aspartate (NAA) is detectable in proton magnetic resonance spectroscopy (<sup>1</sup>H-MRS) due to its exceptionally high concentration in the CNS. It has been hailed as a specific neuroaxonal marker because brain NAA is almost exclusively localized within neurons (Moffett et al. 1991; Simmons et al. 1991). The metabolic role of NAA is believed to be twofold: (1) NAA is synthesized in neurons, where it facilitates mitochondrial metabolism by preventing product inhibition of the tricarboxylic acid cycle; and (2) NAA is exported to oligodendrocytes for rapid breakdown into precursors of fatty acid and steroid synthesis that are critical for myelin formation (Moffett et al. 2007; Madhavarao & Namboodiri 2006). Consequently, decreased NAA concentration in neurodegenerative diseases has been interpreted both as neuronal loss and neuronal dysfunction.

Diffusion tensor spectroscopy (DTS) (Upadhyay et al. 2008; Kan et al. 2012; Kroenke et al. 2004; Ellegood et al. 2006; Upadhyay et al. 2007; van Zijl et al. 1994) combines features of both diffusion tensor imaging (DTI) and MRS, allowing measurement of the diffusion properties of intracellular metabolites. DTI is a sensitive technique that provides information about microscopic structural features of anisotropic tissues such as white matter (WM) tracts. However, the pathologic specificity of DTI is limited because the measured signal is derived from water protons, which are found in all tissue compartments (including inflammatory cells, myelin, neurons, and glia). By contrast, MRS is neurochemically and compartmentally specific but provides no



microstructural information. However, localized MRS can deliver tissue-specific structural information when combined with diffusion sensitization for compartment-specific metabolites such as NAA. As described in previous chapters, DTS measurements of NAA should thus provide specific information about axonal microstructure and might consequently serve as a useful marker of axonal integrity in the complex setting of demyelination, inflammation, edema, and gliosis seen in MS.

In this study, we compare the diffusion properties of NAA and water in the corpus callosum (CC) between MS patients and healthy controls (HC) at 7T. CC damage is frequent and tightly linked with clinical disability in MS (Roosendaal et al. 2009; Ozturk et al. 2010). From a neuroanatomic point of view, the CC is a good structure in which to apply DTS because it is relatively homogeneous, contains fiber bundles that are predominantly oriented in the same direction and is large enough to harbor a spectroscopy voxel. Acquisition at 7T makes it possible to achieve adequate signal-to-noise ratio in less time.

## **7.2 *Materials & Methods***

### **7.2.1 *Subjects & hardware***

Study procedures were approved by the Johns Hopkins Medicine Institutional Review Board. 15 MS patients were recruited from the Johns Hopkins MS Clinic and 14 HC from the university community, and informed consent was obtained from each participant. Patients had not experienced clinical relapse within 3 months of enrollment. All patients and 7 HC underwent clinical testing, including measures of motor function (25-Foot Walk, 9-Hole Peg test) and cognitive function (Paced Auditory Serial Addition Test (PASAT)), and patients were assigned Expanded Disability Status Scale (EDSS) scores.

MRI and MRS data were obtained with a 7T Philips Achieva scanner with 40mT/m maximum gradients (Philips Medical Systems, Cleveland, Ohio) and quadrature volume transmit and 16- or 32-channel receive head coils (Nova Medical, Inc., Wilmington, MA).

### 7.2.2 Structural images

T<sub>1</sub>-weighted images were acquired for spectroscopy volume of interest (sVOI) positioning and tissue segmentation: 3D MPRAGE sequence with TR/TE = 4.1 ms/1.85 ms, flip angle = 7.0°, resolution = 1mm isotropic, scan time = 92 sec, SENSE factor = 2 (AP) × 3 (RL). T<sub>1</sub>-weighted volumes were processed in MIPAV (McAuliffe et al. 2001), including inhomogeneity correction (Sled et al. 1998), skull-stripping with SPECTRE (Carass et al. 2011) and segmentation into WM, gray matter (GM), and cerebrospinal fluid (CSF) using the FANTASM (Pham & Prince 1999). A mask of the sVOI was applied to the segmented volume to make a tissue (no CSF) mask (tVOI). CC cross-sectional area (CCarea) was measured in MIPAV by drawing regions of interest on the 3 midsagittal T<sub>1</sub>-weighted slices and averaging the area of these regions. T<sub>2</sub>-weighted FLAIR images were acquired and qualitatively examined for lesion detection: 3D MP-FLAIR sequence (Visser et al. 2010), TR/TI/TE = 8000 ms/2175 ms/292 ms, resolution = 1mm isotropic, scan time = 8 min, SENSE factor = 2 × 3.

A DTI volume was acquired for comparison with DTS: SE ssEPI sequence, TR/TE = 12643 ms/82 ms, *b*-value = 800 s/mm<sup>2</sup>, resolution = 2.0 mm isotropic, number of directions = 30, scan time = 7 min, SENSE factor = 3 (AP). In MIPAV, the individual diffusion weighted volumes were rigidly registered to the *b*=0 image, which was registered (affine) to the T<sub>1</sub>-weighted volume. The diffusion weighted data were then analyzed in two ways: at native resolution with averaging within the tVOI (avgDTI) and at

sVOI resolution (svDTI). For svDTI, the tVOI mask was applied to each diffusion weighted volume to extract an average diffusion weighted value for each direction prior to tensor fitting. The svDTI analysis controls for the macrostructural effects of CC curvature on diffusion values and is used instead of DTS-derived water spectra, which suffered from partial volume averaging with CSF.

### 7.2.3 Diffusion weighted spectroscopy

Diffusion weighted spectra were acquired from a 3.6 cm<sup>3</sup> sVOI (3.0 cm AP × 1.5 cm RL × 0.8 cm FH) positioned and angled on T<sub>1</sub>-weighted images to include portions of the genu and anterior body of the normal appearing CC and to minimize partial volume effects of CSF and GM (Fig. 1 a, c). NAA diffusion measurements were obtained by incorporating bipolar diffusion gradients into a point-resolved spectroscopic sequence (PRESS) (Kan et al. 2012; Upadhyay et al. 2007): TR/TE = 2000 ms/120 ms, bandwidth = 3 kHz, 2048 points, 32-40 averages, scan time = 15 min. Frequency-selective excitation/dephasing water suppression was optimized to allow reliable NAA quantification while retaining enough residual water signal for zero-order phase correction prior to spectral averaging. A non-water-suppressed spectrum, with the transmitter frequency on water, was acquired from the sVOI for eddy current correction. Diffusion weighting was applied in 6 non-coplanar directions using two *b*-values in addition to *b*=0: 440 s/mm<sup>2</sup> and either 2250 s/mm<sup>2</sup> (11 scans) or 3600 s/mm<sup>2</sup> (22 scans). Individual and averaged spectra were phase- and frequency-drift corrected in MATLAB (The Mathworks, Inc., Natick, MA). The averaged spectrum for each diffusion direction and *b*-value combination was quantified with LCModel (Provencher 1993). Due to low SNR at the highest *b*-values, NAA and N-acetylaspartylglutamate (NAAG) were not well separated, so the NAA+NAAG values (Cramér–Rao lower bounds <15%) were used for

diffusion analysis. The diffusion tensor was estimated and diagonalized to yield fractional anisotropy (FA), mean diffusivity (MD), parallel diffusivity ( $\lambda_{||}=\lambda_1$ ; diffusion parallel to the primary fiber orientation) and perpendicular diffusivity ( $\lambda_{\perp}=(\lambda_2+\lambda_3)/2$ ; diffusion orthogonal to the primary fiber orientation). tNAA/tCr was estimated from the ratio of NAA+NAAG to creatine+phosphocreatine from the  $b=0$  spectrum.

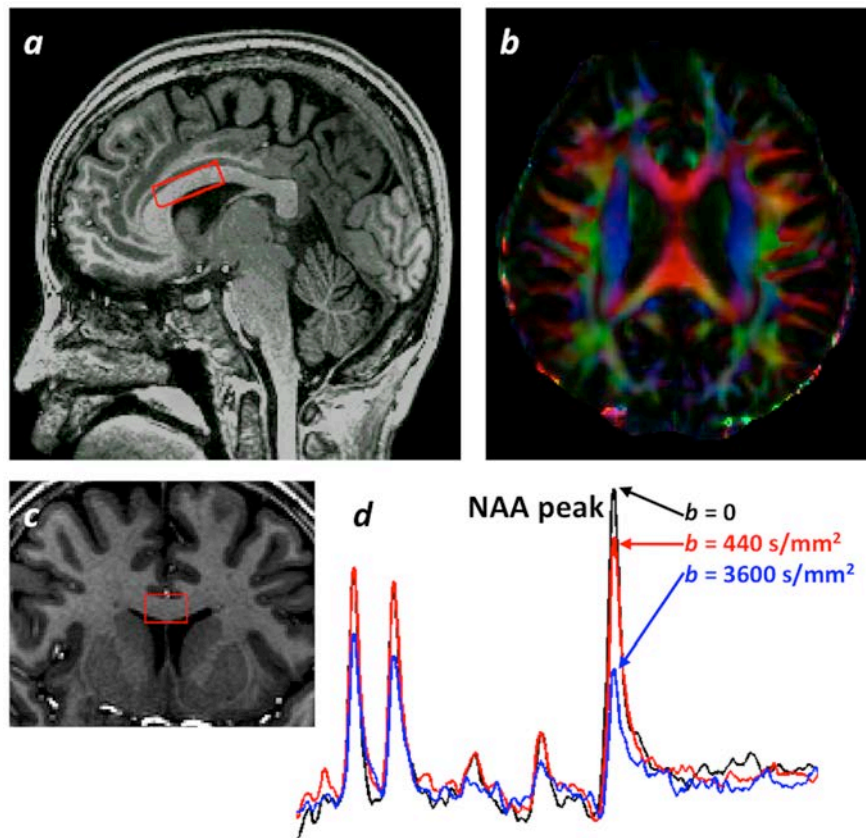


Figure 7.1. Voxel location and spectra. **a**, sagittal and **c**, coronal T1-weighted images demonstrating voxel location in red. **b**, DTI axial color map. **d**, non-diffusion weighted spectrum (black) and diffusion weighted spectra with gradient direction primarily parallel to fiber tract (red & blue).

#### 7.2.4 Statistics

All statistical analyses were done with STATA (StataCorp, College Station, TX).  $p$ -values  $< 0.05$  were considered statistically significant. Group differences in age and sex were assessed with  $t$ -tests. Linear regression was used to characterize associations between age, MRS, DTI, DTS, continuous clinical measures and disease status. For this, a mixed effects model was employed to account for the random effects of repeated scans for 4 HC. When applicable, the regression coefficient (RC), coefficient of determination ( $R^2$ ) and  $p$ -value are reported. Correlations ( $\rho$ ) of measures with EDSS were assessed with the Spearman rank correlation test.

### 7.3 Results

Table 7.1 Subject demographics – no significant differences between patients and controls.

	<b>Patients (n=15)</b>	<b>Controls (n=14)</b>
<i>Mean age (years) (range)</i>	44.2 (28-55)	38.4 (24-56)
<i>Sex (women)</i>	7	6
<i>RRMS</i>	12	
<i>SPMS</i>	1	
<i>PPMS</i>	2	
<i>Mean EDSS (range)</i>	3.2 (1-6.5)	
<i>Mean disease duration (years) (range)</i>	8.1 (1-26)	

The HC group was not significantly different from the MS group with regards to age and sex. 12 patients were on immunomodulatory treatment; none had received steroids within 30 days of scanning. Patients demonstrated smaller CCarea and lower tNAA/tCr (Table 7.1) in accordance with previous studies (Riccitelli et al. 2011; Davie et al. 1994). tNAA/tCr was negatively correlated with age for MS (RC=-0.012/year,  $p=0.007$ ) and HC (RC=-0.011/year,  $p=0.026$ ) (Figure 7.2), as seen previously (Haga et al. 2009). There was no significant difference between groups for use of a higher b-value of 2250 versus 3600 mm/s<sup>2</sup> or between NAA diffusion values measured with different higher b-values.

Table 7.2. Mean imaging and spectroscopy measures for MS patients and healthy controls

<b>Mean values</b>		<b>Patients (n = 15)</b>	<b>Controls (n = 14)</b>	<b>p value</b>
CC Cross-sectional area (mm <sup>2</sup> ) (range)		575 (454-698)	653 (467-830)	0.017
[NAA] (NAA+NAAG:Cr+PCr ratio) (range)		1.47 (1.08-1.76)	1.84 (1.43-2.32)	< 0.001
Fractional Anisotropy (FA)	NAA	0.53	0.56	ns
	Water	0.43	0.49	0.016
Mean Diffusivity (MD) (μm <sup>2</sup> /ms)	NAA	0.15	0.18	ns
	Water	1.48	1.22	<0.001
Parallel Diffusivity (λ <sub>  </sub> ) (μm <sup>2</sup> /ms)	NAA	0.25	0.31	0.030
	Water	2.13	1.86	<0.001
Perpendicular Diff. (λ <sub>⊥</sub> ) (μm <sup>2</sup> /ms)	NAA	0.11	0.12	ns
	Water	1.15	0.90	<0.001

Mean values and regression p-values unless otherwise noted. Water values from avgDTI analysis. ns, not significant. \*Student's t-test.

NAA diffusion data from the DTS acquisition are summarized in Table 7.2. NAA  $\lambda_{||}$  was the only DTS measure significantly different between groups (Figure 7.3). Note that no macroscopic lesions were identified in the sVOI on visual inspection of the T<sub>1</sub>-weighted or FLAIR images. MS and HC had similar proportions of GM in the tVOI (means: MS=0.28, HC=0.26;  $p=0.39$ ). Diffusion weighted spectroscopy has been studied previously in healthy human volunteers at lower field strengths (Posse et al. 1993; Kroenke et al. 2004; Ellegood et al. 2010; Ellegood et al. 2006; Upadhyay et al. 2007) and 7T (Kan et al. 2012), yielding comparable diffusivity findings. Studies that acquired diffusion weighted spectroscopy with enough directions to measure FA report similar values in the anterior CC.

All water diffusion results are derived from the DTI acquisition. svDTI values were correlated with, but lower than, their avgDTI counterparts – e.g., avgDTI FA vs. svDTI FA (RC=0.70,  $p<0.001$ ,  $R^2=0.56$ ), avgDTI MD vs. svDTI MD (RC=0.77,  $p<0.001$ ,  $R^2=0.83$ ) (Figure 7.4) – and svDTI FA (mean = 0.28) was lower than avgDTI FA (mean=0.47) (paired  $t$ -test,  $p<0.0001$ ). This difference was expected due to macroscopic curvature of the CC within the tVOI, since combining diffusion data across a volume with a variety of axonal orientations will decrease FA. The mean avgDTI FA is low compared to previous studies (Reich et al. 2010), probably due to partial volume averaging with GM in the tVOI.

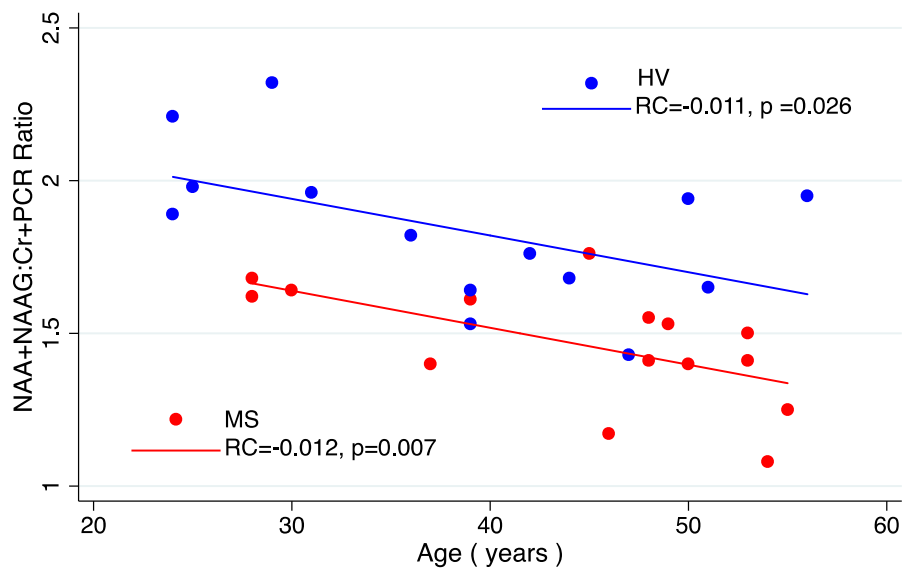


Figure 7.2.  $tNAA/tCr$ , a measure of NAA concentration, was negatively correlated with age for both patients and healthy controls.

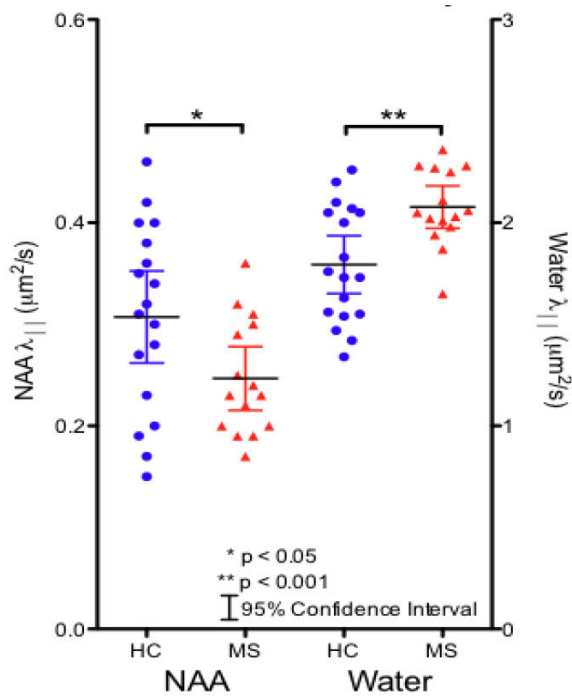


Figure 7.3.  $NAA \lambda_{||}$  and  $avgDTI \text{ water } \lambda_{||}$  for multiple sclerosis patients (MS) and healthy controls (HC) (\* $p < 0.05$ , \*\* $p < 0.001$ , error bars represent 95% confidence intervals).



NAA MD and  $\lambda_{||}$ , as well as avgDTI FA, were positively correlated with tNAA/tCr ( $p < 0.001$ ,  $p = 0.013$ , and  $p = 0.032$ , respectively). On the other hand, avgDTI MD,  $\lambda_{||}$ , and  $\lambda_{\perp}$  were negatively correlated with tNAA/tCr (all  $p < 0.001$ ). There was also a significant negative correlation between NAA  $\lambda_{||}$  and water  $\lambda_{||}$  ( $p = 0.022$ ) (Figure 7.5). A logistic regression of disease status on NAA  $\lambda_{||}$  and water  $\lambda_{||}$  was not significant for either regressor.

Finally, several NAA measures, but no measures of water diffusion, were related to clinical measures of disease severity. Lower tNAA/tCr was associated with longer times to complete the 9-hole peg test ( $p < 0.001$ ) and lower PASAT scores ( $p = 0.042$ ). Lower NAA MD ( $\rho = -0.59$ ,  $p = 0.020$ ), NAA  $\lambda_{||}$  ( $\rho = -0.61$ ,  $p = 0.015$ ) (Figure 7.6), and NAA  $\lambda_{\perp}$  ( $\rho = -0.53$ ,  $p = 0.045$ ) values were related to higher EDSS scores (more clinical disability).

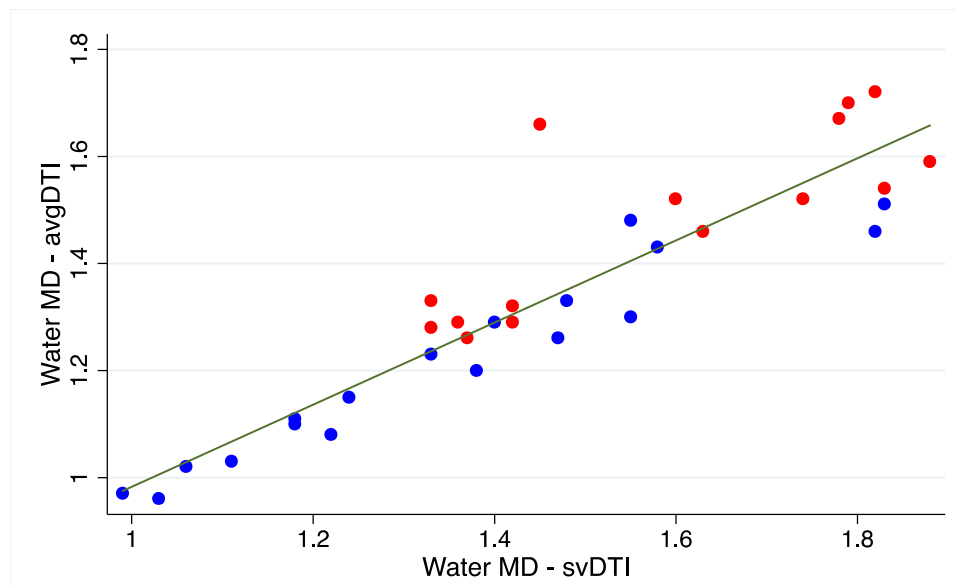


Figure 7.4. Comparison of water mean diffusivity values calculated with the single-voxel DTI analysis scheme versus the conventional averaging of voxels after the tensors have been found.

## 7.4 Discussion

These results demonstrate that DTS is clinically relevant in MS and brings specificity to MRS and DTI measures of neurodegeneration. In MS, neurodegeneration occurs in the setting of multiple pathological processes (including inflammation, edema, demyelination and gliosis) in different tissue compartments. Because NAA is primarily found within axons in WM, NAA diffusion properties should be a more specific marker of WM integrity than water diffusion alone. Consistent with previous studies and discussed further below, we found higher water  $\lambda_{||}$  and  $\lambda_{\perp}$  in MS compared to HC, indicating nonspecific microstructural changes in these patients with low disease burden. By contrast, we found that NAA  $\lambda_{||}$  was lower in MS and inversely correlated with water  $\lambda_{||}$ . Additionally, only DTS measures were correlated with clinical disability as measured by

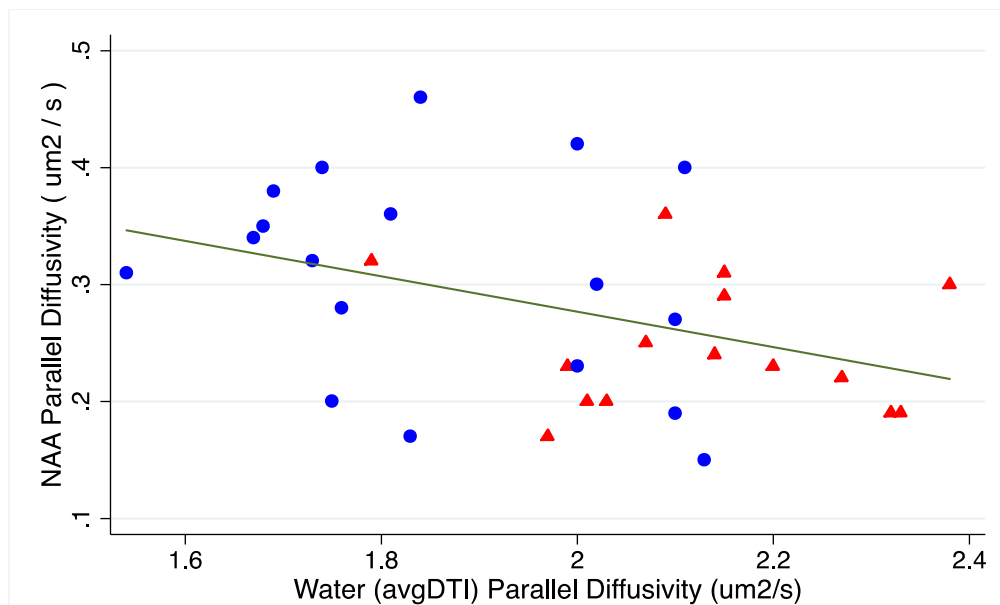
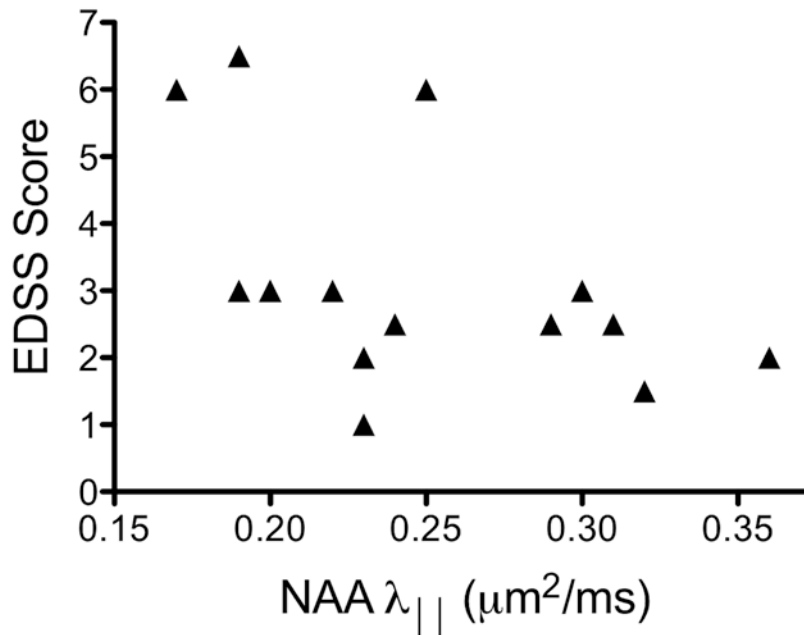


Figure 7.5. Parallel diffusivity ( $\lambda_{||}$ ) of NAA and water. a, NAA  $\lambda_{||}$  was negatively correlated with avgDTI water  $\lambda_{||}$  (all subjects,  $R^2 = 0.16$ ,  $p = 0.02$ ).



EDSS. These results lend support to diffusion measurements of NAA being a more specific marker for previous and ongoing axonopathy in MS than water diffusion alone.

The intra-axonal location of NAA, together with findings that intact cell membranes are relatively impermeable to NAA and neuronal export is controlled by a transporter (Moffett et al. 2007), leads to the prediction that under normal physiological circumstances, NAA should preferentially diffuse parallel to the long axis of axons with a similar anisotropy to intra-axonal water. It has been shown at 3T that NAA FA is more sensitive than water FA to microstructural organization of axons across two segments of the CC (Upadhyay et al. 2007). That result offers support for the notion that NAA diffusion is a more specific probe of intra-axonal physiology than water diffusion and can therefore add additional information.

There is mounting evidence that axonal loss and neurodegeneration are responsible for progressive and irreversible neurological disability in MS (Gonen et al.

2000; Trapp & Nave 2008). However, there are no specific therapies or in vivo measures for neurodegeneration in MS. Axonal degeneration in MS is known to occur in lesions and normal appearing WM (NAWM) (Trapp et al. 1998; Kutzelnigg et al. 2005). Histological characterizations of diffuse WM injury in MS provide a picture of axonal degeneration similar to animal models and other human pathologies, e.g., axonal swellings and end bulbs,  $\beta$ -amyloid precursor protein accumulation, and neurofilament alterations (Mahad et al. 2009). Measurements of [NAA] in CSF are similar between MS and HC, suggesting that neurons do not leak more NAA in MS (Teunissen et al. 2009). Based on simulated diffusion models of axon damage in complex geometries (Landman et al. 2010; Budde & Frank 2010), we expect that the structural disruptions described in axonal degeneration would restrict the diffusion of NAA along the length of axons and would be associated with lower NAA  $\lambda_{||}$ , as seen in our data. Decreased NAA  $\lambda_{||}$  may confirm the presence of axonopathy in the face of overall increased water diffusion due to inflammation, edema, and demyelination in MS. This is highlighted by the correlation between clinical status and NAA  $\lambda_{||}$  (but not water  $\lambda_{||}$ ), since disability may be more closely related to neuroaxonal pathology than to inflammation.

The finding of reduced NAA  $\lambda_{||}$  may explain a paradox in the MS MRI literature. In an effort to find MRI measures that differentiate axonal degeneration from demyelination and inflammation, DTI has been heavily studied in MS patients and animal models with conflicting results. Most MS studies have demonstrated increased water MD,  $\lambda_{||}$ , and  $\lambda_{\perp}$  and decreased water FA, in both lesions and NAWM, suggesting nonspecific microstructural damage (Werring et al. 1999; Bammer et al. 2000; Roosendaal et al. 2009; Reich et al. 2010). By contrast, studies in mouse models of inflammation, such as allergic/autoimmune encephalomyelitis (DeBoy et al. 2007; Budde et al. 2009), and demyelination, such as cuprizone (Xie et al. 2010), have demonstrated decreased water

$\lambda_{||}$  in conjunction with axon injury and degeneration.

A potentially important difference between DTI studies in MS and animal models is the timing of imaging in relation to clinical symptoms or inciting events. As described above, animal studies with serial imaging consistently show early decreased water  $\lambda_{||}$ , corresponding to histological evidence of axonopathy, followed by normalized or increased water  $\lambda_{||}$ . These studies also describe increased water  $\lambda_{\perp}$  later when inflammation, demyelination and gliosis become more prevalent. This pattern of DTI changes was borne out in human epilepsy and optic neuritis studies, which benefitted from a known, discrete clinical onset. Specifically, epilepsy patients who underwent corpus callosotomy had reduced water  $\lambda_{||}$  in transected portions of the CC (Concha et al. 2006). In patients with optic neuritis, low baseline water  $\lambda_{||}$  was correlated with poor visual acuity and a thinned retinal nerve fiber layer at 6 months (Naismith et al. 2012). However, these studies represent the exception rather than the rule: As axonopathy is ongoing and almost always found in the setting of inflammation and edema in MS, DTI is in most cases unable to reliably identify the presence of axonopathy.

Cross-sectional  $^1\text{H-MRS}$  studies in MS, including this one, have demonstrated decreased [NAA] compared to HC in lesions, NAWM and the whole brain, suggesting axonal loss (Gonen et al. 2000; Fu et al. 1998; Leary et al. 1999; Oh et al. 2004). Decreased [NAA] has been found in NAWM and GM in the earliest stages of the disease and in those with relatively little disability (Filippi et al. 2003; Inglese et al. 2004; Wattjes et al. 2007; Rigotti et al. 2011). However, longitudinal studies in NAWM have not been able to detect declining [NAA] in patients with MS over the course of 2-3 years (Tiberio et al. 2006; Sajja et al. 2008). Interestingly,  $^1\text{H-MRS}$  MS studies have seen [NAA] drop dramatically within acute lesions only to rise to near-normal levels in follow-up scans, suggesting that some decreases in [NAA] can be attributed to reversible metabolic

insults (Davie et al. 1994) or perhaps to dilutional effects related to edema. To distinguish [NAA] decreases due to neuron or axon loss from metabolic issues, some studies have used regression modeling to adjust [NAA] for DTI measures of axon integrity (Cader et al. 2007; Ciccarelli et al. 2010). While these studies support a role for mitochondrial impairment in MS, it remains difficult to judge by MRS measures of [NAA] whether axons are damaged or destroyed.

DTS measurements are limited by low concentrations of metabolites compared to water, thereby lowering the signal-to-noise ratio of DTS relative to DTI. In this experiment, the signal-to-noise ratio and measurement variability of DTS could have been improved by acquiring and averaging more spectra, but acquisition time was limited because this pilot project was part of a larger study. Although high magnetic field and strong gradients allowed us to use a relatively small voxel containing primarily coherent WM fibers, our measurements still have partial-volume effects of GM and vasculature. However, when DTS is applied to a specific fiber tract with a known orientation, most of the variability in the DTS measures can be attributed to microstructural properties of the WM tract. The high correlation between svDTI and avgDTI measures suggests that partial-volume and macroscopic curvature effects may not be important limiting factors. Finally, the overlap of NAA  $\lambda_{||}$  between MS and HC (Fig. 2b) indicates that DTS measurements in NAWM are unlikely to be highly sensitive for detecting the presence of diseased tissue in individual cases. Therefore, it is important to interpret the finding of low NAA  $\lambda_{||}$  in one particular brain region in the context of other MRI measures across the brain.

In conclusion, DTS may be a relatively specific marker of neurodegeneration in MS, in contrast to more conventionally acquired MRI measures such as  $T_1$  gadolinium contrast-enhancement (indicating inflammatory blood-brain-barrier opening), focal  $T_2$

hyperintensity (a range of pathologies including inflammation, edema, demyelination, gliosis, and leukomalacia), and magnetization transfer (changes in myelination and water content). In MS, DTS changes may help interpret findings from more sensitive techniques, such as DTI, elucidating their pathophysiological significance. Future studies will further explore the specificity of NAA diffusion by in-depth analysis of the natural history of DTS measures in MS, in animal models of demyelination and neurodegeneration, where histopathological correlates can be examined, and in autopsy tissue.

## **7.5 Other contributors to this work**

Itamar Ronen<sup>1</sup>, Aranee Techawiboonwong<sup>2</sup>, Craig K. Jones<sup>3</sup>, Peter B. Barker<sup>3,4</sup>, Peter Calabresi<sup>5</sup>, Daniel Harrison<sup>5</sup>, Daniel S. Reich<sup>6</sup>

### **7.5.1 Affiliations**

<sup>1</sup> C.J. Gorter Center for High Field MRI, Dept of Radiology, Leiden University Medical Center, Leiden, Netherlands

<sup>2</sup> Dept of Electrical Engineering, Mahidol University, Salaya, Nakhon Pathom, Thailand

<sup>3</sup> F.M. Kirby Research Center for Functional Brain Imaging, Kennedy Krieger Institute, Baltimore, MD, United States

<sup>4</sup> Department of Radiology, Johns Hopkins University School of Medicine, Baltimore, MD, United States

<sup>5</sup> Department of Neurology, Johns Hopkins University School of Medicine, Baltimore, MD, United States

<sup>6</sup> Translational Neuroradiology Unit (NINDS), National Institutes of Health, Bethesda, MD, United States

## **8 FOLLOWING NEURODEGENERATION IN MS WITH DIFFUSION SPECTROSCOPY – LONGITUDINAL ANALYSIS OF MS PATIENTS AT 3T**

Multiple sclerosis (MS) is a complex CNS disease in which inflammation, demyelination and neuroaxonal degeneration are concurrent processes. These processes are etiologically intertwined, but therapies developed to date are directed at the immune-mediated, inflammatory destruction of myelin, whereas axonal degeneration is ongoing and has not been specifically targeted. For this reason, in vivo techniques to measure axonal degeneration could be useful in developing neuroprotective agents. Diffusion weighted spectroscopy is a novel technique that measures the diffusivity of metabolites, such as N-acetyl aspartate (NAA), in vivo, allowing compartment specific assessment of disease-related changes. In this longitudinal study, we demonstrate that NAA diffusivity in the corpus callosum is a specific measure of axonal integrity in MS. In particular, NAA diffusivity decreased by 8.3% ( $p < 0.05$ ) over 6 months in patients who were experiencing clinical or MRI evidence of inflammatory relapse ( $n=16$ ). There was no significant change in NAA diffusivity in stable MS patients. Additionally, water DTI and volumetric measures did not detect changes in active MS changes. As NAA diffusivity measurements reflect specifically on the intra-axonal space, these data suggest that NAA diffusivity is a read-out of axonal health in a background of multiple pathological processes in MS.

### **8.1 Introduction**

Axonal degeneration is relevant in a number of complex neurologic and psychiatric diseases, including Parkinson's disease (Burke & O'Malley 2013), traumatic



brain injury (Johnson et al. 2013), Huntington's disease (J.-Y. Li & Conforti 2013), Alzheimer's disease (Kanaan et al. 2013), and multiple sclerosis (Trapp et al. 1998). In these diseases, axonal degeneration is likely an important direct cause of permanent disability. Therefore, being able to detect and measure axonal degeneration could be useful for early diagnosis and monitoring of disease progression and therapeutic interventions.

MS is an autoimmune, inflammatory, demyelinating disease of the CNS that is characterized in its early stage by relapses where neurological function is associated with inflammatory brain or spinal cord lesions. While most MS patients experience a disease course with periods of remission during which they may return to near baseline function, they also suffer an underlying, gradual progression of neurological deficits in motor, sensory and cognitive function. Even with the advent of disease modifying therapies that decrease the incidence of inflammatory episodes, neurological function declines for most patients (Kappos et al. 2010). Examination of spinal cord tissue obtained at autopsy from MS patients has demonstrated progressive neuroaxonal neurofilament alterations consistent with metabolic abnormalities in chronic lesions with very low microglia/macrophage activity (Schirmer et al. 2011). Additionally, it has been found that neurodegeneration, measured with magnetic resonance spectroscopy, may be taking place in the earliest stages of MS, in a radiologically isolated period, before many patients have any clinical signs of inflammation (Stromillo et al. 2013).

MS patients develop lesions in an inflammatory setting that can be detected by MRI. T<sub>1</sub>-weighted contrast enhancement indicates blood brain barrier breakdown, and T<sub>2</sub>-weighted hyperintensities suggest increased water that may reflect edema or tissue breakdown. In vivo measurement of neurodegeneration in MS has, so far, focused on the end result: fewer neurons. Volumetric studies in MS demonstrate that brain and

spinal cord atrophy can be measured on the time scale of years by structural MRI (Bermel & Bakshi 2006; Jones et al. 2013). These measurements demonstrate that the rate of atrophy is accelerated in patients with MS and that volumetric analyses are correlated with clinical impairment (Gao et al. 2014; Rudick et al. 2009).

N-acetyl aspartate (NAA) is a neurometabolite found almost exclusively within neurons in the CNS (Choi et al. 2007) and is detectable with proton magnetic resonance spectroscopy ( $^1\text{H-MRS}$ ). Therefore, it is used as an *in vivo* neuronal marker. Cross-sectional  $^1\text{H-MRS}$  studies in MS have demonstrated low levels of [NAA] within lesions, normal-appearing white matter (WM), and the whole brain, suggesting axonal loss (Gonen et al. 2000; Pelletier et al. 2003; Kirov et al. 2009; Oh et al. 2004; Leary et al. 1999; Davie et al. 1997; Ciccarelli et al. 2007; Tiberio et al. 2006; Narayana et al. 2004; Inglese et al. 2003; Suhy et al. 2000; Rovaris et al. 2005; Ge et al. 2004; Filippi et al. 2003). However, longitudinal studies in normal-appearing WM have not been able to detect declining [NAA] in patients with MS over a 2-3 year span (Tiberio et al. 2006; Sajja et al. 2008; Kirov et al. 2012).

DTI of water has been heavily studied in MS and animal models of MS with conflicting results. Most DTI studies in humans *in vivo* have demonstrated increased water diffusivity (MD,  $\lambda$ , and  $\lambda$ ), and decreased water FA, in both lesions and normal-appearing WM (Evangelou et al. 2000; Werring et al. 1999; Bammer et al. 2000; Roosendaal et al. 2009; Reich et al. 2010). Fink et al. compared DTI-based tractography and brain volume analysis to distinguish the types of information contributed by these techniques (Fink et al. 2010). Their analysis showed that whereas both volumetry and tractography are loosely associated with composite measures of disease progression such as lesion load and EDSS, they are not specific for the underlying biological process, e.g. inflammation or neurodegeneration (Samann et al. 2012).

The corpus callosum is a good location for studying axonal degeneration from anatomical, functional and technical standpoints. The corpus callosum is centrally located, easily distinguished on conventional MR images and contains axons that connect corresponding cortices of the right and left hemispheres. These fibers are important for midline fusion of sensory information, coordinating interhemispheric processing and attentional control (Banich 1998; Aboitiz & Montiel 2003). At the midline, the corpus callosum has enough quasi-coherently oriented fibers to fit the relatively large voxel that is required to generate adequate signal for diffusion weighted spectroscopy experiments to be performed. The corpus callosum is frequently damaged in MS, and this damage is linked to disability (Ozturk et al. 2010). Alterations in quantitative MRI measures, such as DTI and relaxometry, in the corpus callosum are associated with whole brain measures, such as lesion load, and functional readouts, such as the Expanded Disability Scale Score (EDSS) (Hasan et al. 2012; Reich et al. 2010).

In a previous cross-sectional pilot study, diffusion of NAA was measured in the human normal-appearing corpus callosum on a 7 tesla MRI scanner, comparing 15 MS patients and 14 healthy controls (Wood et al. 2012). We found that NAA *parallel diffusivity*, i.e. diffusivity along the axonal propagation direction, was lower in MS and inversely correlated with both water parallel diffusivity and clinical severity (EDSS). In the context of previous experiments, our findings provided preliminary evidence that diffusion weighted spectroscopy of NAA can distinguish axonopathy from other processes such as inflammation, edema, demyelination, and gliosis. By detecting reduced diffusion of NAA parallel to axons in white matter, DWS may thus be capable of distinguishing axonal disruption in MS in the setting of increased parallel diffusion of water, which is commonly observed in MS but pathologically nonspecific.

Recently, we have shown that by modeling the corpus callosum as a cluster of

cylinders with macroscopic curvature and microscopic angular dispersion distributions, DWS measurements made parallel and perpendicular to the long axis of those cylinders can be combined to yield NAA diffusivity values that more accurately reflect the cytosolic diffusion coefficient of NAA and realistically account for the organization of the many fibers that make up a spectroscopy voxel (Ronen et al. 2013).

In MS, axonal degeneration plays out over time, and as such we set out to explore whether the DWS technique is capable of detecting longitudinal changes in white matter tissue and is feasible in a clinical setting with a 3T scanner.

## **8.2 Methods**

### **8.2.1 Subjects**

All study procedures were approved by the National Institutes of Health Institutional Review Board. All participants gave informed consent. Participants were evaluated neurologically in the Neuroimmunology Clinic, National Institute of Neurological Disorders and Stroke, NIH, Bethesda, Maryland, US.

The MS cohort was recruited from the Neuroimmunology Clinic and consisted of a wide range of patients – from long-term stable with no new lesions for 1-10 years (based on existing prior MRI scans) to patients with high disease activity, who had formed new T<sub>2</sub> lesions in the 6 months before or during the study. For this study, 19 patients were scanned. At recruitment, 9 patients were stable: they had not had a relapse or new T<sub>2</sub> lesion for at least 1 year. Three of these patients had a new T<sub>2</sub> lesion during the study so were moved into the active group. Therefore, at study conclusion, there were 6 stable patients and 13 active patients.

Healthy volunteers (HVs) were recruited from the NIH Clinical Research Volunteer Program. All HVs had neurological exams and clinical MRI scans within normal limits. HVs were compensated for taking part in the study.

Participants were assessed with the Expanded Disability Status Scale (EDSS), Scripps Neurological Rating Scale (SNRS), Symbol Digit Modality Test (SDMT, paper-based), Paced Auditory Symbol Addition Test (PASAT, 3 second version), 9-Hole Peg Test, and 25-Foot Timed Walk. These are standard tests performed for the evaluation of MS patients at the NINDS Neuroimmunology Clinic. Clinical data were obtained within 30 days of MRI acquisition.

During each scan session, structural and diffusion weighted spectroscopy (DWS) scans were acquired for all participants. All scans were acquired on 3T Philips Achieva scanners in the NIH Clinical Center Radiology and Imaging Sciences Department. These scanners have maximum gradients of 60 mT/m, quadrature volume transmit coils, and 8-channel receive head coils. Data were stored, processed and analyzed on servers of the Translational Neuroradiology Unit, Division of Neuroimmunology and Neurovirology, NINDS, NIH.

All MS patients were scanned at baseline (month 0) and month 6. In most cases, active MS patients were also scanned at 3 months in order to more closely follow disease activity. Healthy volunteers were scanned twice with scans separated by 1-39 days. For all repeat scans, volumes of interest were placed to match the original placement as closely as possible.

### **8.2.2 Structural image acquisition and processing**

3D T<sub>1</sub>-weighted gradient echo images were acquired for positioning of the volume of interest (VOI) in the DWS experiments and for tissue segmentation in the

post-processing stage. Imaging parameters for the  $T_1$ -weighted image were: field of view (Anterior-Posterior (AP), Foot-Head (FH), Right-Left (RL)) = 240x240x180 mm<sup>3</sup>, 1.00 mm isotropic resolution, TR/TE = 7.00 ms/3.15 ms and total scan time of 5.30 minutes + delay for scanner preparation.

$T_2$ -weighted Fluid Attenuated Inversion Recovery (FLAIR) images were acquired for all patient scan sessions using a 3D-FLAIR-VISTA sequence with parameters: field of view (AP, FH, RL) = 240x240x180 mm<sup>3</sup>, 1.00 mm isotropic resolution, TR/TE= 4800 ms/365 ms, TI = 1600 ms, and total scan time of 5.30 minutes. FLAIR images were acquired just prior to acquisition of the final contrast-enhanced  $T_1$ -weighted volume. For this reason, gadolinium contrast was administered during the FLAIR scan: a single dose (0.1 mmol/kg) of gadobutrol (Gadavist; Bayer Healthcare, Leverkusen, Germany) was injected by power injector (Medrad, Warrendale, Pa) over a period of 60 seconds. Gadolinium-enhanced  $T_1$ -weighted scans were acquired for all active MS patients and for stable patients at the discretion of the patient's clinician.

$T_1$ -weighted, FLAIR, and DTI volumes were processed in MIPAV (Medical Image Processing, Analysis and Visualization) (McAuliffe et al. 2001) and JIST (Java Image Science Toolbox) (Lucas et al. 2010). The  $T_1$ -weighted and FLAIR images were rigidly registered to the Montreal Neurological Institute (MNI) brain with the Optimized Automatic Registration (OAR) algorithm (Jenkinson & Smith 2001), inhomogeneity-corrected using N3 (Sled et al. 1998), and skull-stripped with the Simple Paradigm for Extra-Cerebral Tissue REmoval (SPECTRE) (Carass et al. 2011). Tissue segmentation into WM, gray matter (GM), deep gray structures, cerebrospinal fluid (CSF), and lesions was performed with Lesion TOpology-preserving Anatomy-Driven Segmentation (L-TOADS) (Bazin & Pham 2008; Shiee et al. 2010). L-TOADS utilizes both the  $T_1$ -weighted and FLAIR image intensities as channels in conjunction with an empirically

derived brain atlas to assign tissue type. L-TOADS was constrained to identify lesions only within WM that were hyper-intense on FLAIR. For healthy volunteers, segmentation was performed with TOADS without a lesion category. Two healthy volunteers did not have FLAIR images. Brain volume values reported here are given as a percentage of intracranial volume (ICV), and lesion load is calculated as a percentage of white matter volume.

Whole brain DTI images were acquired for all scan sessions using single-shot 2D spin-echo echo planar imaging. DTI parameters were: field of view (AP, FH, RL) = 224x224x120 mm<sup>3</sup>, 2x2x2 mm<sup>3</sup> isotropic resolution, TR/TE= 7487 ms/85 ms, 32 diffusion weighting directions with b = 800 s/mm<sup>2</sup>, SENSE = 3(AP), and total scan time of 5.50 minutes. For the DTI, the individual diffusion weighted volumes were registered with 7 degrees of freedom to the b=0 image, which was registered using affine transformation to the T<sub>1</sub>-weighted volume in MNI space (see below). From this, the diffusion tensor was estimated and diagonalized for each voxel to yield maps of the primary eigenvector (E1), fractional anisotropy (FA), mean diffusivity (MD), parallel diffusivity ( $\lambda_{||}=\lambda_1$ ), and perpendicular diffusivity ( $\lambda_{\perp}=(\lambda_2+\lambda_3)/2$ ). The white matter VOI mask attained from segmentation of the T<sub>1</sub>-weighted volume could then be applied to these images to obtain eigenvectors and diffusion values corresponding to the acquired DWS VOI.

### **8.2.3 DWS volume of interest & acquisition**

Two DWS volumes of interest (VOI) were acquired in each session. Both volumes of interest were centered on corpus callosum white matter. For all participants, 1 VOI measured 30 AP x 15 RL x 8 FH mm (3600 mm<sup>3</sup>) and was placed on the genu and anterior body of the corpus callosum (yellow box in Figure 8.1.A). For all participants, a second VOI was placed on either the posterior body (16 MS, 5 HV; same

dimensions as anterior corpus callosum volume) or splenium (2 MS active, 1 MS stable, 1 HV; 12 AP × 15 RL × 18 FH mm (3240mm<sup>3</sup>)) of the corpus callosum (Figure 8.1; green box demonstrates splenium VOI placement). The splenium location was chosen when the posterior body was very thin or curved such that the VOI could not adequately contain it.

The PRESS (Point Resolved Spectroscopy) sequence was chosen as the base spectroscopic sequence for the single volume DWS experiments and was supplemented with a bipolar diffusion-weighting scheme for minimization of eddy currents and of cross-terms with background and imaging gradients. For the diffusion weighting, 2 directions were chosen for all scans: (1) a pure right-left direction in the VOI frame, which is mostly parallel to the direction of the callosal fibers; (2) a direction perpendicular to the callosal fibers, forming a 45° angle between the anterior-posterior axis and the inferior-superior axis of the VOI. These gradient directions can be denoted in the VOI coordinates as [1,0,0] and [0,-1,1]. The position of the gradient directions with respect to the VOI is shown in Figure 8.1.A. In all experiments, the center frequency was set to the NAA singlet peak at 2.0 ppm. Water suppression was achieved using 2 frequency-selective excitation pulses centered at the water resonance frequency, which were followed by dephasing gradients. The water suppression was “de-optimized” for the diffusion-weighting conditions in order to allow sufficient residual water signal for later use in the post-processing stage for zero-order phase correction and frequency drift correction of individual spectra prior to spectral averaging. A wired peripheral pulse unit (PPU) was used for cardiac synchronization of the DWS acquisition in order to minimize signal fluctuations due to cardiac pulsation. Pencil-beam shimming was applied up to second order, resulting in a typical NAA singlet linewidth of 7 Hz. Following each scan, a shorter



scan with identical VOI position and diffusion conditions was performed with the center frequency set at the water resonance frequency and without water suppression. This scan was subsequently used for eddy-current correction.

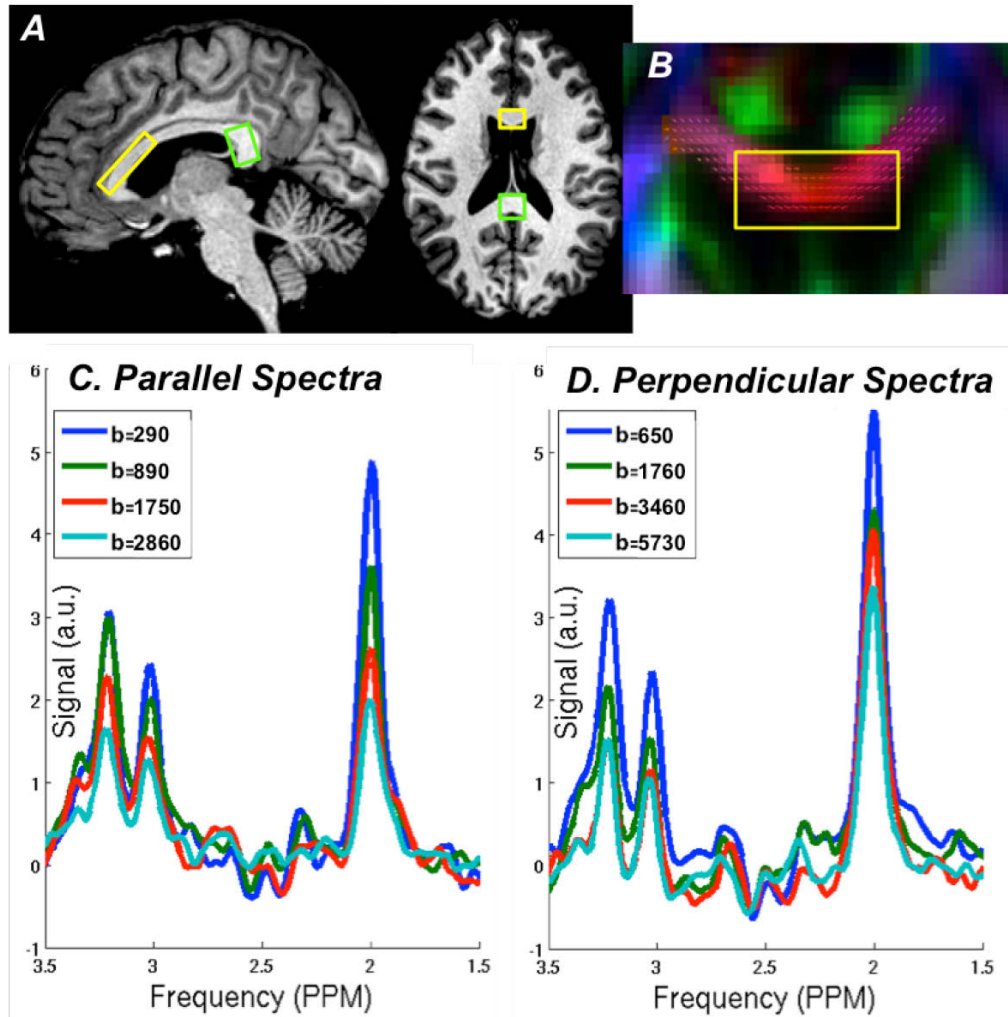


Figure 8.1 A. DWS VOI placement on anterior CC (yellow) and splenium (green). B. Coronal view of anterior CC VOI on DTI color map overlaid with the primary eigenvector (color denote direction of primary eigenvector: red = RL, green = AP, blue = FH). C & D. Diffusion weighted spectra acquired parallel  $[1,0,0]$  and perpendicular  $[0,-1,1]$  to the CC fibers. b-values measured in  $s/mm^2$ .

The DWS parameters were: TE = 110 ms, TR = 2 cardiac cycles (about 2000 ms), trigger delay = 200 ms, number of time-domain points = 1024, spectral width = 1500 Hz, gradient duration ( $\delta$ ) = 22 ms, bipolar gap = 20 ms, diffusion time ( $\Delta$ ) = 55 ms with 4 different gradient amplitudes resulting in b-values of 290, 890, 1750, and 2860 s/mm<sup>2</sup> in the [1,0,0] direction and 650, 1760, 3460, and 5730 s/mm<sup>2</sup> in the [0,-1,1] direction. 48 spectra were collected for each diffusion condition (2 directions, 4 b-values), plus an additional 48 for the highest gradient in each direction. Total DWS scan time ranged from 16-24 minutes, depending upon heart rate.

#### 8.2.4 DWS data processing

Post-processing of the DWS data was performed using custom Matlab® routines (Mathworks, Natick MA). Following DWS data acquisition, the individual spectra were first corrected for zero-order phase jitter and frequency drift according to the remaining water peak and then eddy-current corrected using the unsuppressed water acquisition. Spectra were averaged within condition, and then the remaining water peak was removed using a Hankel Singular Value Decomposition (HSVD) method followed by a first-order phase-correction based on the NAA peak. These spectra were quantified using LCModel (Provencher 1993).

Based on the LCModel data for NAA, diffusivities were calculated assuming monoexponential decay of the signal as a function of b-value in each direction. The following empirical quantities were calculated:  $D_{\text{par}}$ , diffusivity along the [1,0,0] direction, which is roughly parallel to the callosal fibers;  $D_{\text{perp}}$ , diffusivity along the [0,-1,1] direction, which is roughly perpendicular to the callosal fibers;  $D_{\text{avg}}$ , the average of the 2

diffusivities described above and represents the empirical ADC of NAA in the VOI.

The LCModel output was also used as an input to a modeling routine that calculates the *intra-axonal*, or *cytosolic* diffusivity of NAA. This procedure is assumed to minimize the variability in the DWS measurements introduced by macroscopic factors such as the position of the VOI within the white matter tract, the main direction of the tract with respect to the DW gradients and the macroscopic curvature of the tract within the VOI. The model, described in Chapter 4 and (Ronen et al. 2013), assumes that the diffusion weighted NAA signal can be decomposed to the contributions from the diffusion of NAA parallel and perpendicular to the axons, and it uses the angles between the main eigenvectors of the DTI data within the DWS VOI and the diffusion weighting gradient directions. The diffusion weighted data in both directions are fitted simultaneously to the model using two fitting variables:  $D_{\text{model}}$ , the cytosolic diffusion coefficient of NAA, and  $\sigma_{\phi}$ , the standard deviation of the axonal angular dispersion (Figure 8.2.B). Importantly,  $D_{\text{model}}$  is independent of the tract geometry within the VOI and thus mostly reflects the effects of the cytosolic medium, e.g. viscosity and molecular crowding, on the diffusion of NAA inside the axons.

### 8.2.5 Statistics

Cross-sectional analyses were performed by averaging all measurements across time for each volume of interest. Linear regression was used to characterize associations between DWS measures, DTI measures, brain volumetry, age, disease duration and EDSS. When applicable the regression coefficient ( $RC$ ), coefficient of determination ( $R^2$ ), and  $p$  value are reported.

Longitudinal analyses consisted of calculating the difference between measures at 6-months and baseline (a positive difference value represents an increase at 6-

months). For comparison, healthy volunteer differences are shown between the second and first scans. Between-groups analyses – stable versus active or MS versus healthy – of demographic, cross-sectional and longitudinal difference measures were tested with a Student's *t*-test. EDSS and 25-foot Walk Time were evaluated with the Mann-Whitney U test. Statistical analyses were performed with GraphPad Prism version 6.0b for Mac OS X, GraphPad Software, San Diego, California, USA and STATA release 11, StataCorp, College Station, Texas, USA.

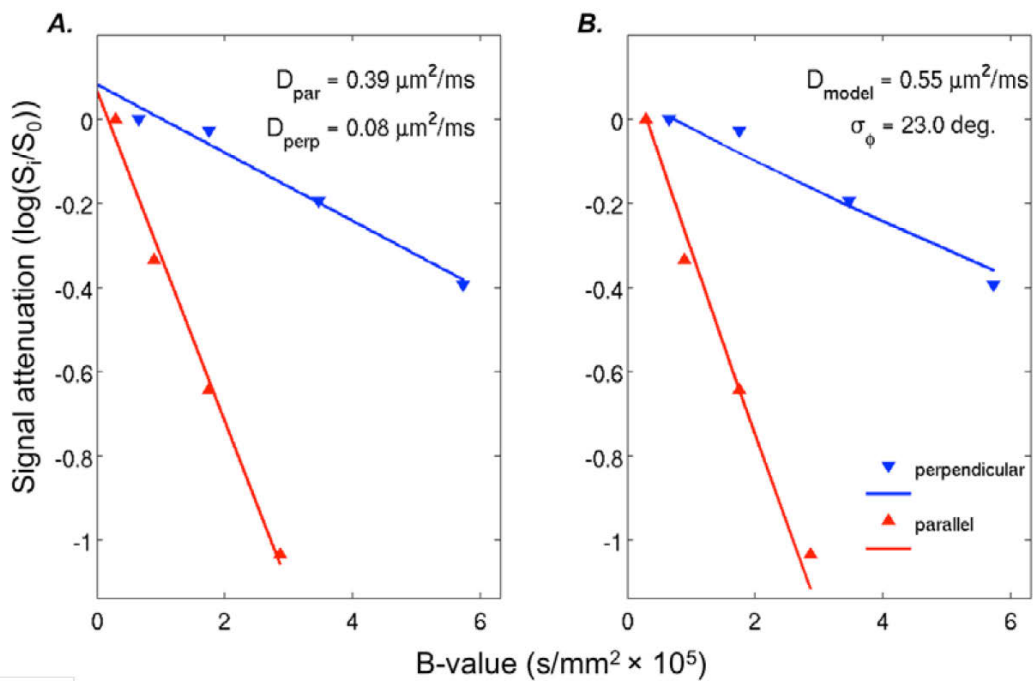


Figure 8.2 Logarithm of the diffusion-weighted signal measured from one active MS patient with the diffusion weighting applied along the parallel ([1,0,0], red triangles) and perpendicular ([0,-1,1], blue triangles) directions as a function of b-value (measured in s/mm<sup>2</sup>). **A**, the monoexponential fits used to calculate the parallel ( $D_{par}$ ) and perpendicular ( $D_{perp}$ ) diffusivity values. **B**, the same data fitted to the model described in the text, which yields the cytosolic diffusivity  $D_{model}$  and the standard deviation of the axonal angular dispersion  $\sigma_{\phi}$ .

## 8.3 Results

### 8.3.1 Demographics and example cases

Table 8.1 Patient Demographics

		Stable MS (n=6)	Active MS (n=13)	Healthy Volunteers (n=6)
<b>Age, years</b>	<i>mean (SD)</i>	48.3 (12.7)	40.9 (12.2)	48.2 (9.3)
	<i>range</i>	30 - 69	20 - 62	40 - 62
<b>Sex</b>	<i>number of women</i>	4	6	1
<b>Disease sub-type</b>	<i>RR, SP, PP</i>	6 RR	12 RR, 1 PP	-
<b>EDSS</b>	<i>median</i>	1.5	1.5	-
	<i>range</i>	0 - 2	0 - 6.5	-
<b>PASAT score</b>	<i>mean (SD)</i>	51.0 (7.5)	50.5 (10.1)	
	<i>range</i>	40 - 60	25.0 - 60.0	
<b>25-foot walk time, seconds</b>	<i>mean (SD)</i>	5.0 (1.1)	4.6 (1.5)	
	<i>range</i>	4.0 - 7.1	3.2 - 8.3 <sup>#</sup>	

<sup>#</sup> One patient uses an assistive device for walking and was excluded from this analysis (25-ft time = 117.8 sec)

Demographics for all participants are shown in Table 8.1 for the stable and active MS groups. There was no significant difference between groups for age, sex, PASAT score or 25-foot walk time.

Spectra were of poor quality for 3 DWS volume acquisitions, and there was no 6-month follow-up for three DWS volumes. Therefore, in total there were 12 HV, 10 stable MS, and 21 active MS DWS volumes with both baseline and 6-month data for

longitudinal analysis. Additionally, as planned for known active patients, there were 11 active MS patients with 3-month scans (2 DWS volumes each). All available time points (baseline, 3-month, and 6-month) were averaged for each DWS volume, resulting in 12 HV, 10 stable MS, and 26 active MS DWS measurements for cross-sectional analyses. All DTI-acquired water diffusivity measures are from the same corpus callosum volumes of interest as the DWS measurements.

### 8.3.2 Cross-sectional analysis

In line with our previous findings of water and NAA diffusivity measures in the corpus callosum in a cross-sectional study, MS patients had higher average water MD (MS mean MD =  $1.23 \mu\text{m}^2/\text{ms}$ , HV mean MD =  $1.12 \mu\text{m}^2/\text{ms}$ ,  $p < 0.01$ ) and lower average NAA  $D_{\text{model}}$  (MS mean  $D_{\text{model}} = 0.48 \mu\text{m}^2/\text{ms}$ , HV mean =  $0.53 \mu\text{m}^2/\text{ms}$ ,  $p < 0.05$ ) compared to healthy volunteers (Figure 8.3) (Wood et al. 2012). In this cohort, NAA diffusivity measures were not significantly correlated with any water diffusivity measures

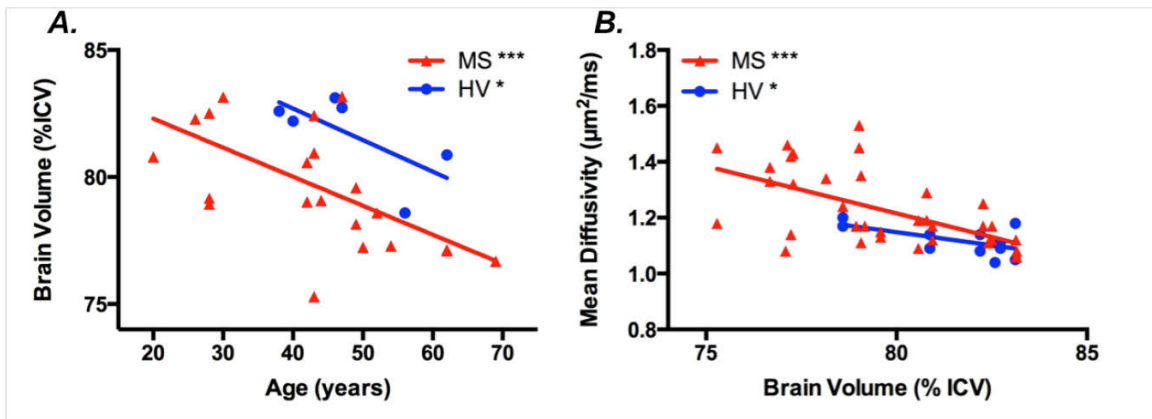


Figure 8.3 **A.** Average brain volume (% intracranial volume) across scans versus age for all subjects, MS=red triangles, HV=blue circles. \*\*\*MS  $R^2 = 0.36$ ,  $p < 0.001$  (red line); \*HV  $R^2 = 0.46$ ,  $p = 0.01$  (blue line). **B.** Average water mean diffusivity ( $\mu\text{m}^2/\text{s}$ ) across scans versus brain volume (%ICV) for all subjects. \*\*\*MS  $R^2 = 0.36$ ,  $p < 0.001$ ; \*HV  $R^2 = 0.36$ ,  $p < 0.05$ .

(Figure 8.3).

Brain volume – estimated as a percentage of total intracranial volume – was negatively correlated with age (Figure 8.4.A) for both MS patients ( $RC = -0.11$  %ICV/year,  $R^2 = 0.36$ ,  $p < 0.001$ ) and HVs ( $RC = -0.12$  %ICV/year,  $R^2 = 0.46$ ,  $p = 0.01$ ). Water MD correlated negatively with brain volume (Figure 8.4.B) for MS patients ( $RC = -0.03$ ,  $R^2 = 0.36$ ,  $p < 0.001$ ) and HVs ( $RC = -0.02$ ,  $R^2 = 0.36$ ,  $p < 0.05$ ).

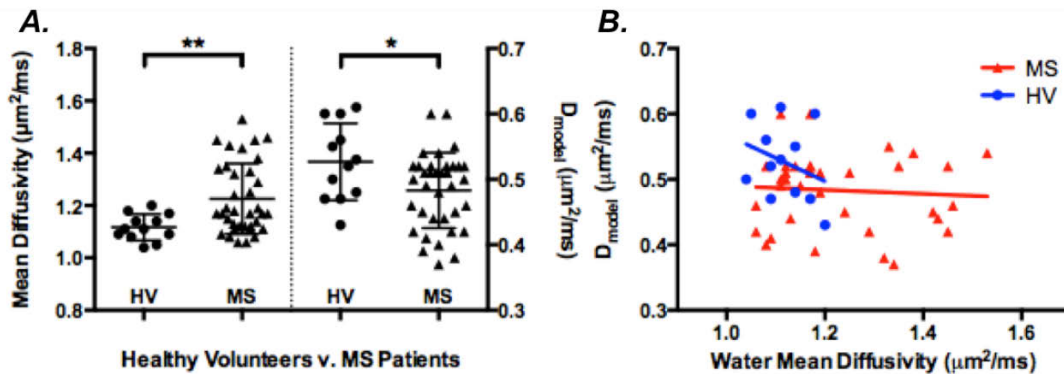


Figure 8.4 A. Water mean diffusivity and NAA  $D_{\text{model}}$  for healthy volunteers and MS patients,  $**p < 0.01$ . B. NAA  $D_{\text{model}}$  versus water mean diffusivity for MS patients and healthy volunteers (ns).

The segmentation method used here, Lesion TOADS, is configured such that lesions are only identified within white matter structures. Measurements of lesion load (reported as % of white matter) demonstrated no differences between active and stable MS groups (Figure 8.5, right). Likewise, there was no difference between the means of stable and active groups for lesion load (actual volume,  $\text{mm}^3$ ) within the volumes of interest (Figure 8.5, left). For MS patients, total white matter lesion load was negatively correlated with NAA  $D_{\text{model}}$  ( $RC = -0.02$ ,  $R^2 = 0.16$ ,  $*p < 0.05$ ) and water fractional anisotropy ( $R^2 = 0.19$ ,  $**p < 0.01$ ) (Figure 8.6.A & B). Total white matter lesion load was positively correlated with water mean diffusivity ( $R^2 = 0.18$ ,  $*p < 0.05$ ), water

perpendicular diffusivity ( $R^2 = 0.19$ ,  $**p < 0.01$ ) (Figure 8.6.C & D), and water parallel diffusivity ( $R^2 = 0.12$ ,  $*p < 0.05$ ).

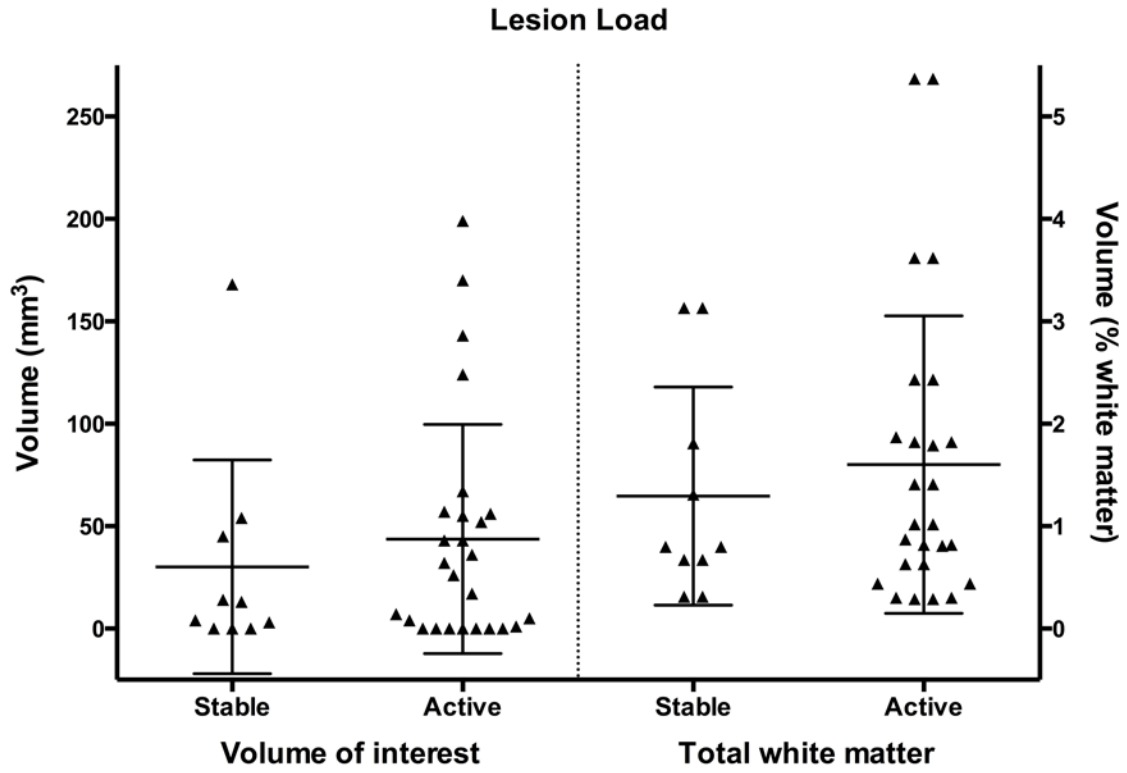


Figure 8.5 Lesion load for stable and active MS patients. Left: volume of lesion segmented in corpus callosum volume of interest. ns. Right: lesion load as percent of total brain white matter, ns.



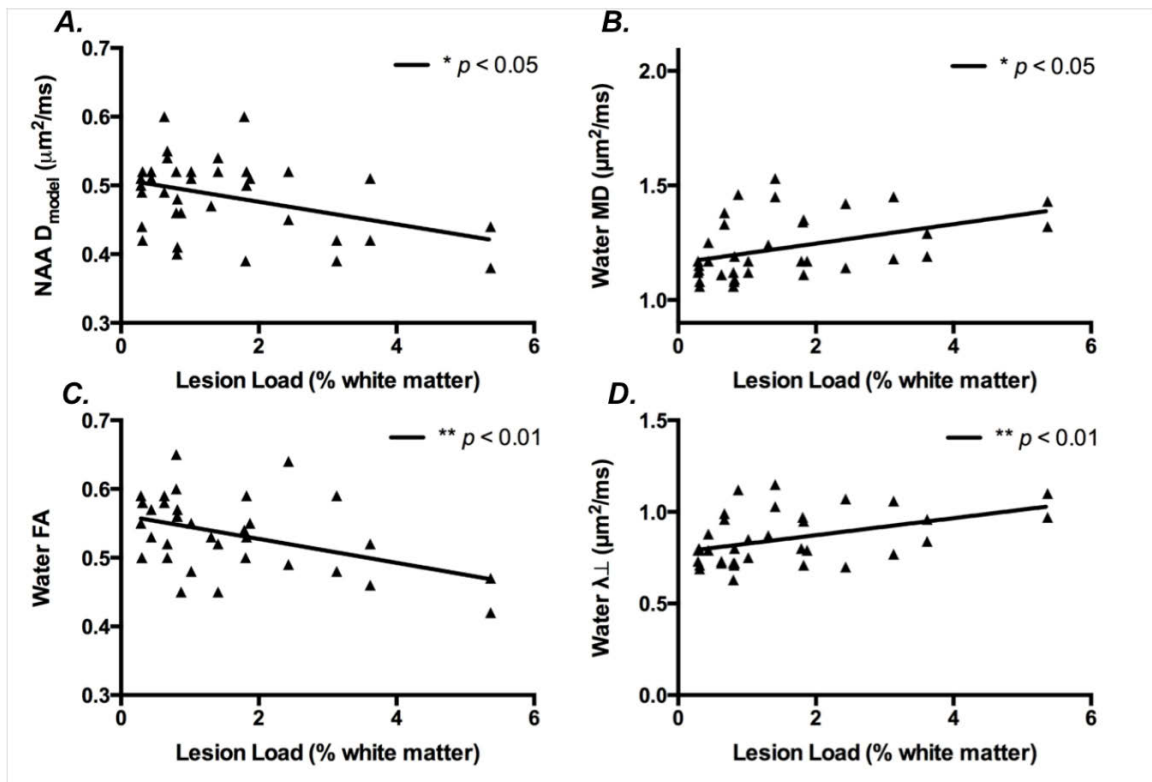


Figure 8.6 **A.** NAA  $D_{model}$  was negatively correlated with lesion load (% white matter),  $R^2 = 0.16$ ,  $*p < 0.05$ . **B.** Water fractional anisotropy was negatively correlated with lesion load (% white matter),  $R^2 = 0.19$ ,  $**p < 0.01$ . **C.** Water mean diffusivity was positively correlated with lesion load (% white matter),  $R^2 = 0.18$ ,  $*p < 0.05$ . **D.** Water perpendicular diffusivity was positively correlated with lesion load (% white matter),  $R^2 = 0.19$ ,  $**p < 0.01$ .

Disease duration, measured as years since first symptoms attributable to MS, was not statistically different between stable and active MS groups although there was a trend toward those with the shortest disease duration being in the active group (Figure 8.7.A). There was also a trend toward a positive correlation between average water MD values and age ( $RC = 0.003 \mu\text{m}^2/\text{ms}/\text{year}$ ;  $R^2 = 0.10$ ,  $p = 0.07$ ) (Figure 8.7.B).

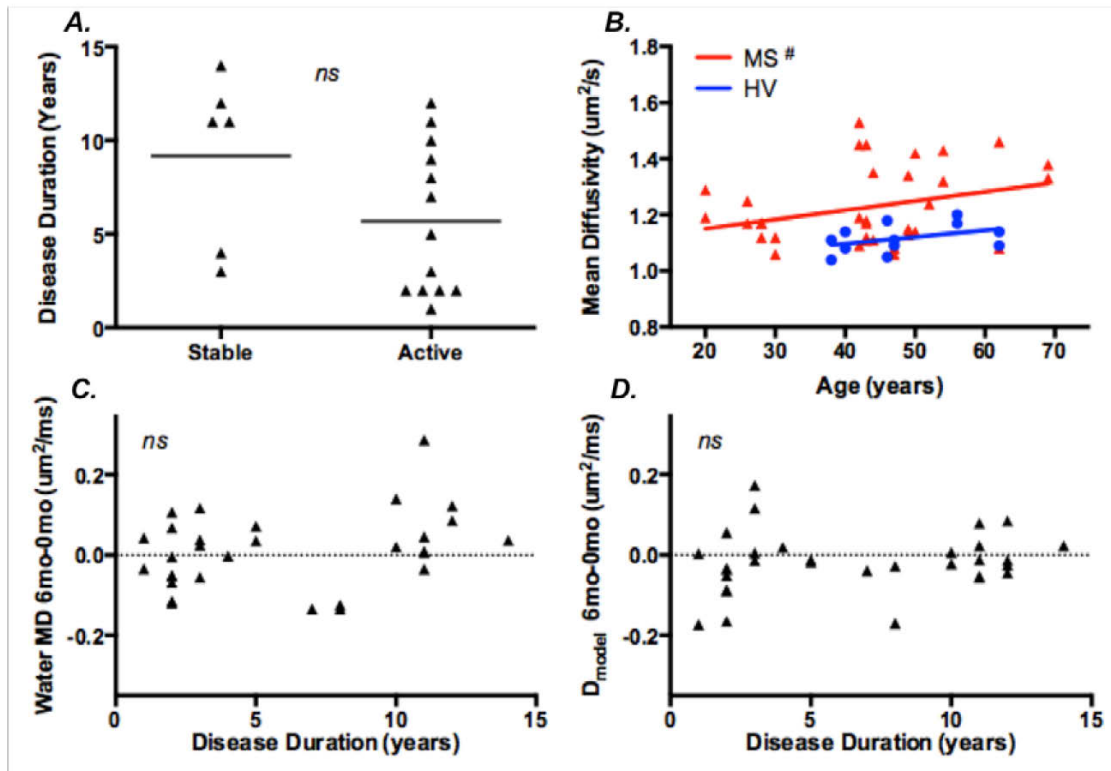


Figure 8.7 MS disease duration. **A.** Disease duration for stable and active MS patients, *ns*. **B.** Mean diffusivity versus age in MS patients, #non-significant trend  $RC = 0.003 \mu\text{m}^2/\text{ms}/\text{year}$ ,  $R^2 = 0.10$ ,  $p = 0.07$ . **C.** Change in water mean diffusivity over 6 months versus disease duration (*ns*,  $p = 0.15$ ). **D.** Change in  $D_{\text{model}}$  over 6 months versus disease duration (*ns*)

### 8.3.3 Longitudinal Analysis

To assess changes in diffusivity values between baseline and 6 months, difference values were calculated ( $\Delta = t_{6\text{mo}} - t_{0\text{mo}}$ ) for each DWS VOI; a positive value expresses an increase in a measurement over 6 months. These difference values were then compared between the stable and active MS groups. Healthy volunteers were

scanned twice within 6 weeks – not at baseline and 6 months – therefore, HV difference values are not directly comparable to MS values and are shown for reference (Figure 8.8). For healthy volunteers the average difference between scans for NAA diffusivity, water diffusivity and brain volumetry measures were not significantly different from zero.

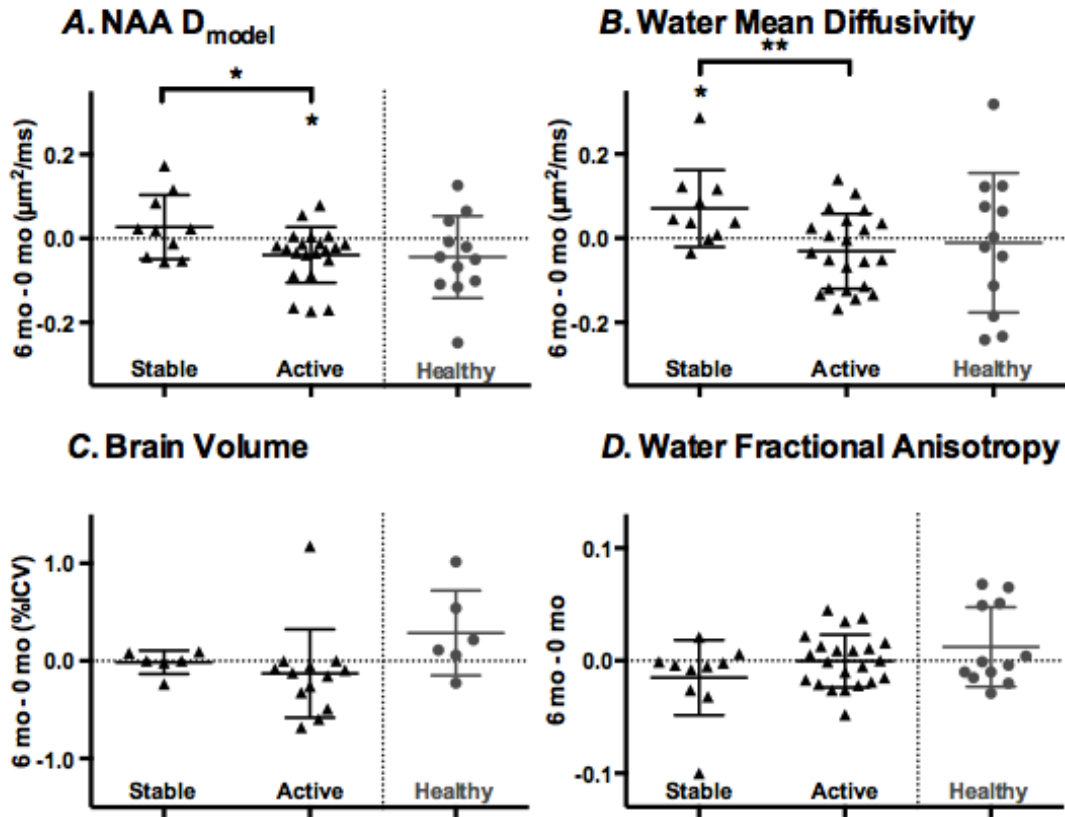


Figure 8.8. Difference in measurement between baseline and 6 months for stable and active MS patients. For healthy controls, scans were 0-1 months apart. **A.** NAA diffusivity (modeled analysis), \* $p < 0.05$  for stable  $\neq$  active, \* $p < 0.05$  for active  $\neq$  0. **B.** Brain volume (%=total brain/total intracranial volume), no significant differences (ns). **C.** Water mean diffusivity (MD), \*\* $p < 0.01$  for stable  $\neq$  active, \* $p < 0.05$  for stable  $\neq$  0. **D.** Water fractional anisotropy, ns.

$\Delta$  NAA  $D_{\text{model}}$  values were different between stable and active MS groups (stable mean  $\Delta D_{\text{model}} = 0.03 \mu\text{m}^2/\text{ms}$ , active mean  $\Delta D_{\text{model}} = -0.04 \mu\text{m}^2/\text{ms}$ ,  $p < 0.05$ ) primarily based on lower MS  $D_{\text{model}}$  values in active patients at 6 months ( $p < 0.05$ ) (Figure 8.8.A).  $\Delta$  Water MD was also different between stable and active groups (stable mean  $\Delta\text{MD} = 0.07 \mu\text{m}^2/\text{ms}$ , active mean  $\Delta\text{MD} = -0.03 \mu\text{m}^2/\text{ms}$ ,  $p < 0.01$ ), driven by an average increase in water MD values at 6 months in stable patients ( $p < 0.05$ ) (Figure 8.8.B). On the other hand, other measurements such as water fractional anisotropy (Figure 8.8.C) and brain volume (all MS mean  $\Delta\% \text{ICV} = -0.09$ , stable MS mean  $\Delta\% \text{ICV} = -0.01$ , active MS mean  $\Delta\% \text{ICV} = -0.13$ ; Figure 8.8.D) did not demonstrate detectable changes over the 6-month study period in either the stable or active MS groups.  $\Delta\text{MD}$  and  $\Delta D_{\text{model}}$  were not statistically significantly correlated with disease duration (Figure 8.7.A & B).

## **8.4 Discussion**

This longitudinal diffusion weighted spectroscopy study, performed on a clinical 3T MRI scanner with standard hardware, supports the hypothesis that diffusivity measurements of the intraneuronal metabolite N-acetyl aspartate may reflect the health of axons in the corpus callosum in MS. The cross-sectional NAA diffusivity data presented here are in agreement with those from a separate DWS study of patients with MS that was performed on a research 7T scanner and utilized different diffusion weighting parameters and a tensor analysis scheme (Wood et al. 2012). In that cross-sectional study, the tensor-derived NAA parallel diffusivity in the CC was lower in MS patients compared to healthy controls – as was seen here as well. Additionally, we measured NAA diffusivity in the corpus callosum of MS patients at baseline and 6 months. We found, that in those patients with known active disease, cytosolic NAA diffusivity in the corpus callosum decreased at month 6 compared to baseline, even

though water mean diffusivity and fractional anisotropy in the same volume of interest and total brain volume (% intracranial volume) did not change in active patients during this same period. These DWS data were collected on 3T clinical scanners in a scan time of 15-20 minutes per volume of interest, that was easily fit into a full clinical scanning session, including T<sub>1</sub>-weighted images without and with contrast enhancement, FLAIR and DTI images.

The modeled NAA diffusivity values measured here are in line with previous reports in healthy volunteers including the experiments described in Chapter 6 and elsewhere (Ronen et al. 2014; Ronen et al. 2013). Additionally, other quantitative MRI measurements made here are consistent with previous studies in MS. For instance, brain volume loss in patients with MS has been estimated at between 0.2-0.5% per year (Fisher et al. 2008; Gao et al. 2014). The percent intracranial volume changes found here were not significant but approached 0.2% per year. Likewise, increased water diffusivity measures in MS patients compared to healthy volunteers has been seen in multiple DTI studies (Bammer et al. 2000; Werring et al. 1999; Reich et al. 2010; Wood et al. 2012). Additionally, water mean diffusivity has been seen to increase over time in MS patients in the corpus callosum at a rate of 0.5% (95%CI=0.0-1.0, not significant (Harrison et al. 2011)).

In a diffusion weighted spectroscopy experiment such as this, the spatial resolution is on the order of centimeters. In order to measure coherent white matter, the volume of interest must be placed in a large structure such as the corpus callosum. In this setting, measurement of NAA diffusivity is determined by the apparent diffusion coefficient of NAA in the intra-axonal space, the degree of microscopic axon alignment, the length of axons and the macroscopic curvature of axons across the large voxel. Here, we were able to utilize the information provided by water DTI to account for

macroscopic curvature of the corpus callosum. Therefore, in comparison to water, the modeled NAA diffusivity values reflect more specifically the intra-axonal environment. With these data, we confirmed that in MS, NAA parallel diffusivity in the corpus callosum is decreased compared to healthy controls. Additionally, we found that in those patients who would be expected to be undergoing more acute axonal pathology due to a more active inflammatory setting, there was a decrease in NAA diffusivity over a 6-month period. This change in NAA diffusivity was not seen those patients without detectable MRI or clinical signs of inflammation.

Interestingly, in this study the annualized rate of change of water MD in the corpus callosum for all MS patients was 0.13% and as much as 11.80% for stable MS patients. This result is somewhat surprising given that the stable patients were not experiencing clinical or radiological relapses. One explanation that is hinted at by these data and others is that water MD is very sensitive to many sources of microstructural change in tissue. While there was no statistical difference between the active and stable MS patients in terms of disease duration and age, the stable group consisted of 4 of 6 patients with disease duration greater than 9 years while the active group had only 3 of 13 patients with disease duration over 9 years (Figure 8.7.A). In addition to the stable group having a larger proportion of chronic patients, those patients with disease duration greater than 9 years were more likely to have positive  $\Delta$ MD (Figure 8.7.C), suggesting that water mean diffusivity is increasing more in patients with chronic MS. Chronic lesions do not demonstrate frank inflammation but still may be associated with ongoing demyelination, remyelination, axonopathy, and neurodegeneration, which is especially pronounced in progressive MS (Frischer et al. 2009; Lassmann 2014). In the chronic phase of MS, oxidative stress mechanisms are ongoing and may be amplified by age-dependent iron accumulation and mitochondrial gene mutations (Lassmann et al. 2012).

In this context, it might be expected that some chronic patients would have increasing water mean diffusivity in a centrally located and well connected brain region, such as the corpus callosum, due to widespread ongoing smoldering damage. Another possibility is that this increased MD is a sign of remyelination and/or other processes that might constrict axons. In models of diffusion in cylinders (Chapter 4) when the molecules of interest are found both inside and outside the cylinders (water in and around axons) and the cylinders become crimped, simulated measures of mean diffusivity increase slightly. Another explanation is that this is a spurious result due to the small size of the stable group. Further assessment in a larger longitudinal cohort could clarify whether this result is generalizable.

In general, magnetic resonance spectroscopy measurements and, especially DWS data, are limited by a low metabolite concentration compared to water. DWS at 3T lives on the edge of adequate SNR. This constraint likely contributes to the fact that while NAA diffusivity measurements are relatively specific and hence more interpretable than their water counterparts, they are often less sensitive. For instance, the  $\Delta$  NAA  $D_{\text{model}}$  values of the stable and active MS patients are greatly overlapping, even though those groups are completely segregated by their presence or absence of new T2 lesions. On the other hand, DTI measures are no better than DWS at determining disease activity. In other words, DWS measurements, as with any neuroimaging study, must be evaluated in the context of other neuroimaging and clinical data.

## **8.5 Conclusion**

Diffusion weighted spectroscopy is a powerful technique that can be applied to MS patients in a clinical setting. By way of its compartmental specificity, DWS of NAA may provide answers to questions that are otherwise difficult to address with more

conventional MRI techniques. In particular, its specificity for axonal pathology helps elucidate the fundamental disconnect between findings of increased parallel diffusivity of water in the setting of known axonopathy.



## 9 CONCLUSIONS

### ***9.1 Multiple sclerosis and neuro-axonal degeneration***

Multiple sclerosis (MS) is a neurodegenerative disease. In MS, active inflammation is associated with clinical relapses, demyelination, blood brain barrier breakdown and axonal damage (Trapp et al. 1998; Kornek et al. 2000). Disease modifying therapies are helping people with multiple sclerosis live longer lives with fewer relapses and less disability (Goodin et al. 2012). Nonetheless, MS is the main cause of death in more than 50% of patients with MS (Scalfari et al. 2013), and MS affects more than 2 million people worldwide. Chronic MS does not typically exhibit high levels of inflammation with blood brain barrier breakdown, but axonal degeneration remains prominent and weighs heavily in the progression of clinical disability (Mahad et al. 2008). Mounting evidence suggests that in order to slow and prevent irreversible neuronal loss in MS, research efforts should focus on strategies aimed at neuroprotection and regeneration (Franklin et al. 2012; Ellwardt & Zipp 2014).

Axonal degeneration in MS is likely multifaceted in etiology (Nave 2010). Due to their tremendous length and large volume, axons face many unique challenges and stresses. These include long distance antero- and retrograde transport, great metabolic demands, signaling between distant organelles, great risk for mechanical damage, and affiliations with glia for myelin and neurotrophic support (Coleman 2013). Recent research has demonstrated that axonal degeneration is usually a programmed autonomous destruction process that is distinct from neuronal cell body apoptosis and necrosis (Yan et al. 2010) and can be incited by inflammation independent of demyelination (Nikić et al. 2011). In MS samples, unusual patterns of neurofilament

phosphorylation and packing compared to normal tissue suggest a less organized axoskeleton and/or problems with axonal transport (Petzold et al. 2008). These alterations have been detected in vivo in normal appearing white matter, suggesting that these changes may precede lesion formation or be associated with extra-lesional axonopathy (Petzold et al. 2011). Another sign of axonal pathology found in chronic MS is accumulation of amyloid precursor protein, which is a marker of fast axonal transport block (Mahad et al. 2009).

## **9.2 *Magnetic resonance and multiple sclerosis***

Nuclear magnetic resonance imaging exploits the behavior of atomic nuclei in external magnetic fields in concert with magnetic gradients to create image contrast of biological tissue based on the local environment of spinning nuclei in the tissue. By manipulating the gradients and radiofrequency pulse sequences employed by the scanners, a growing variety of different contrast modes are available, including T<sub>1</sub>-weighted, T<sub>2</sub>-weighted and diffusion weighted images, as well as magnetic resonance spectroscopy (MRS). Additionally, the administration of intravenous contrast solution concurrent with and/or followed by image acquisition provides supplementary information about vasculature. In MS, these imaging techniques have become central to diagnosis and following disease progression (Klawiter 2013). Moreover, through the study of MR images in MS patients, contributions have been made to our understanding of the pathophysiology of the disease (McFarland 2010; Gaitán et al. 2011; Absinta et al. 2013).

At the tissue level, MS is a heterogeneous disease with multiple pathological processes – including blood brain barrier breakdown, invasion by various immune cells (T-cells, B-cells, macrophages, etc.), demyelination, remyelination, gliosis, axon

transection, and axon degeneration – occurring at any one time in any one lesion. In order to study the interaction and time course of these processes, many researchers have sought in vivo MRI techniques that are specific for one or more processes. Diffusion weighted imaging measures MR signal changes due to the random motion of water molecules. In restricted environments, such as white matter axonal bundles, water molecules move anisotropically: they travel further along the length of an axon than across the cell membranes. For a restrictive microstructure, diffusion tensor imaging (DTI, diffusion weighting in many directions to establish a tensor model of anisotropy) can provide information about the enclosing geometry.

Many studies of DTI have been undertaken in patients with MS and animal models of the disease. In experimental autoimmune encephalomyelitis (EAE), an inflammatory animal model of MS with associated axonal degeneration, decreased water  $\lambda$  has been associated with measures of axonal degeneration such as decreased staining for properly phosphorylated neurofilaments (SMI31) (Budde et al. 2009) and decreased axon counts (DeBoy et al. 2007). Similarly, in models of demyelination (cuprizone (Sun et al. 2006; Xie et al. 2010)) and traumatic injury (Loy et al. 2007), decreased water  $\lambda$  is found during phases of axon injury and degeneration. Likewise, an acute reduction in water  $\lambda$  has been seen in transected portions of the CC in epilepsy patients undergoing corpus callosotomy (Concha et al. 2006). A report of DTI in patients with optic neuritis (ON) found a negative correlation of baseline water  $\lambda$  with 6-month follow-up of visual acuity and retinal nerve fiber layer thickness (Naismith et al. 2012).

In both lesional and normal-appearing white matter, DTI studies of MS most often show increased water mean diffusivity (MD), parallel diffusivity ( $\lambda$ ) and perpendicular diffusivity ( $\lambda$ ) and decreased water fractional anisotropy (Evangelou et al. 2000; Werring et al. 1999; Bammer et al. 2000; Roosendaal et al. 2009; Reich et al. 2010). In DTI

experiments such as these, spatial resolution is typically on the order of a few millimeters, so that in coherent white matter a single voxel would contain many axons with associated oligodendrocytes and glia. In this setting, measurement of water  $\lambda$  is largely determined by the apparent diffusion coefficient of water molecules in the intra- and extracellular space and the degree of microscopic alignment of the axons within the voxel (Ronen et al. 2014) as well as the length of axons, which is assumed to be very large in comparison to the diffusion coefficient. In MS, we know that there are multiple pathologic processes occurring in the extra-neuroaxonal space including inflammatory cell activity, edema, demyelination, and remyelination. Diffusion studies of water continue to detect increases in water diffusivity in MS patients, suggesting that DTI is sensitive to but not specific for all of these pathologies.

DTI studies in MS and animals or optic neuritis differ greatly in the timing of imaging in relation to clinical symptoms or inciting events. Animal studies, where the timing of pathology provocation is precisely known and serial imaging is the norm, consistently show early decreased water  $\lambda_{||}$ , corresponding to histological evidence of axonopathy, followed by normalized or increased water  $\lambda_{||}$  and increased water  $\lambda_{\perp}$  when inflammation, demyelination, and gliosis become more prevalent. This pattern of DTI changes was also borne out in the human epilepsy and ON studies that benefitted from a known time-course due to surgical intervention and discrete clinical onset, respectively. Instead, MS lesions are often silent, and imaging studies are done without knowledge of their onset, so that axonopathy is always found in a mixed setting of inflammation, edema, demyelination, and remyelination.

Magnetic resonance spectroscopy affords in vivo study of molecules other than water. While water is by far the most abundant molecule in brain tissue, there are other molecules with a high enough concentration to be measurable with clinical MR

scanners. Importantly, most of these molecules are relatively specific for either a tissue compartment or a functional process. For example, N-acetyl aspartate (NAA) is found almost exclusively (95%) within neurons/axons in the brain and is therefore considered to be a neuronal marker. A number of studies of MS have demonstrated lower levels of NAA in patients compared to healthy volunteers and in lesions compared to normal appearing white matter (Sajja et al. 2009; Ciccarelli et al. 2007; Gonen et al. 2002), demonstrating the usefulness of this measure to detect neuro-axonal loss. On the other hand, longitudinal studies in normal appearing white matter have not detected declining NAA concentration ([NAA]) in patients with MS over a 2-3 year span (Kirov et al. 2012). Therefore, [NAA] alone is unlikely to provide an adequate read-out of neuro-axonal health in MS.

### ***9.3 Diffusion weighted spectroscopy***

Diffusion weighted spectroscopy (DWS) combines diffusion weighting gradients with a MRS localization sequence in order to detect the diffusion of metabolites. NAA is contained within neurons and axons; therefore diffusion of NAA provides specific information about the neuronal compartment. Of note, the intra-axonal space is far from homogenous. Neurofilaments and microtubules are present throughout the axon to serve as both cytoskeletal support and transportation route. Additionally, axonal micro-compartments maximize efficiency of enzyme processes and localize necessary machinery at Nodes of Ranvier. Studies designed to measure hindered diffusion or cytoplasm viscosity in vivo have shown the intracellular diffusivity of NAA to be about 25% lower than the unrestricted, free diffusivity of NAA in an aqueous solution and validate the use of Brownian motion diffusion models to describe metabolite diffusion (Marchadour et al. 2012). Models of molecular diffusion in impermeable cylinders

((Landman et al. 2010), see chapter 3) predict that molecular diffusivity, particularly parallel to the long axis of axons/cylinders ( $\lambda$ ), will decrease in configurations suggestive of axonal degeneration (e.g. bulging, broken or crimped cylinders).

Two approaches were used to analyze the diffusion weighted spectra acquired for this work. For data acquired with 6 orthogonal diffusion weighting directions, a tensor was estimated and the associated eigenvalues and diffusion measurements were analyzed. The tensor-based experiment demonstrated that diffusion parallel to the axon fibers is sensitive to the axonal degeneration and that signal-to-noise ratio is important. Therefore, for the subsequent studies, fewer diffusion weighting directions were acquired in order to focus on parallel diffusivity and to maximize signal-to-noise ratio by increasing repetitions and averaging.

In order to have adequate signal-to-noise ratio, the spatial resolution of a DWS voxel of interest (VOI) is on the order of centimeters and the VOI must be placed in a large coherent white matter structure such as the corpus callosum. In this setting, measurement of NAA diffusivity is determined by the apparent diffusion coefficient of NAA in the intra-axonal space, the degree of microscopic axon alignment, the length of axons, and the macroscopic curvature of axons across the large voxel. The macroscopic curvature of axons across a large spectroscopy voxel can be determined by analyzing diffusion tensor images of the same region. Therefore, a model was introduced to minimize the variability in the DWS measurements generated by macroscopic factors such as the position of the VOI within the white matter tract, the main direction of the tract with respect to the DW gradients, and the macroscopic curvature of the tract within the VOI. The model, thoroughly described in (Ronen et al. 2013) and in Chapter 5, uses the angles between the main eigenvectors of the DTI data within the DWS VOI and the diffusion-weighting gradient directions. The data are fitted to the model using two fitting

variables:  $D_{\text{model}}$ , the cytosolic diffusion coefficient of NAA, and  $\sigma_{\phi}$ , the standard deviation of the axonal angular dispersion. It is important to note that  $D_{\text{model}}$  is relatively independent of the tract geometry within the VOI and thus, in comparison to water, the modeled NAA diffusivity values reflect more specifically the intra-axonal environment, including viscosity and molecular crowding.

In order to establish parameters for the reproducibility and reliability of this DWS technique, we acquired comprehensive single volume DWS data sets of the human corpus callosum at 3T and 7T and investigated the *inter*- and *intra*-subject variability of empirical and modeled diffusion properties of NAA. Subsequently, we used a jackknife-like resampling approach to explore the variance of these properties in partial data subsets reflecting different total scan durations. The repeatability coefficients of empirical and modeled NAA diffusion measures were found to be 24% and 32% at 3T and 25% and 25% at 7T. Moreover, we found that a careful choice of diffusion weighting conditions at both field strengths allows reliable measurement of NAA diffusion properties in clinically relevant experimental time (under 20 minutes). Power calculations based on  $D_{\text{model}}$  and  $D_{\text{avg}}$  show that a 20% difference between two groups could be detected with small sample size per group as small as of 5 subjects at 3T and 3 subjects at 7T.

#### **9.4 Measuring axonal degeneration in multiple sclerosis with diffusion weighted spectroscopy**

Based on 1) previous work in DTI of MS, 2) pathological studies of axonal degeneration in MS, and 3) known physical underpinnings of diffusion weighted spectroscopy, we hypothesized that NAA diffusivity could be an *in vivo* marker of axonal health. DTI studies in well-controlled animal models of axonopathy demonstrate

decreased water parallel diffusivity during the phases of white matter tract tissue destruction when axonal pathology dominates or is not overshadowed by other pathological processes. DTI measures the diffusion of water molecules, which exist in all tissue both intra- and extracellularly. In DTI studies of patients with MS, water diffusivity is seen to increase in all directions in both lesions and normal appearing white matter. As these experiments are typically scheduled without respect for the precise phase of lesion development, we can expect that DTI is picking up on microstructural tissue changes due to an array of the pathological mechanisms seen in MS, including inflammation, demyelination, remyelination, gliosis and axonopathy. Even so, based on the animal model experiments and computational models of diffusion in cylinders, we expect that axonopathy – which manifests in MS as axonal swelling, neurofilament phosphorylation alterations and breakdown, inadequate axonal transport, fiber transections, end-bulbs, and dying-back features – is decreasing the parallel diffusion of water molecules inside axons. However, due to the complicated lesion milieu and the non-specific nature of water diffusion measurements, the signal from axonal degeneration is lost in the noise.

While DTI is a sensitive but nonspecific measure of white matter microstructural changes, measurements of NAA concentration with magnetic resonance spectroscopy are highly specific for neuronal degeneration but have poor sensitivity. In the central nervous system, NAA is localized almost exclusively to neurons and neuronal processes and there is enough NAA to be able to reliably measure it with <sup>1</sup>H-MRS. Not surprisingly, neuro-axonal loss has been associated with decreases in [NAA] in multiple neurodegenerative diseases including MS. Compared to water, the [NAA] in brain tissue is miniscule, with a water to metabolite ratio of approximately 10<sup>4</sup>-10<sup>5</sup>:1. Consequently, in order to get enough signal-to-noise to reliably detect [NAA], the volume of tissue



sampled must be quite large. Likewise, to detect longitudinal changes in [NAA] in a large VOI in cases of gradual neurodegeneration requires long time intervals to allow enough neurons to die.

Diffusion weighted spectroscopy seeks to capitalize on the strengths of DTI and MRS by combining the features of microstructural and time-course sensitivity and compartmental specificity. NAA molecules are diffusing almost exclusively inside axons in white matter. Even in a background of pathological processes occurring outside of axons, measurements of NAA diffusion should provide a read-out of the axonal compartment.

In the first cross-sectional study of DWS in MS patients (Chapter 7), diffusion of NAA was measured in the normal appearing corpus callosum on a 7 tesla MRI scanner, comparing 15 MS patients and 14 healthy controls. We found that NAA parallel diffusivity was lower in MS and inversely correlated with both water parallel diffusivity and clinical severity as measured by EDSS. This led us believe that, by detecting reduced diffusion of NAA parallel to axons in white matter, DWS may be capable of distinguishing axonal disruption in MS in the setting of increased parallel diffusion of water, which is commonly observed in MS but pathologically nonspecific.

Subsequent DWS experiments have sought to determine the specificity of measurements of NAA diffusivity for ongoing neuro-axonal degeneration by studying MS patients with stable and active disease longitudinally. While we have come to recognize that MS patients have ongoing neurodegeneration despite inflammation-targeted disease-modifying therapies, it is known that MS inflammatory lesions are sites of active axonal degeneration (Trapp et al. 1998). MS patients experiencing more inflammatory relapses have greater neuronal loss and impairment (Paty & D. K. Li 1993; D. K. Li et al. 2001). The Neuroimmunology Clinic at the NIH has cared for and followed a large group

of MS patients for long periods of time; some patients have been followed for decades. From this population, we were able to select two groups of patients: 1 group with patients who had been clinically stable without relapse or MRI evidence of inflammation for at least 1 year and 1 group with patients who had experienced a relapse and/or lesion activity the last 6 months. We then measured the NAA diffusivity in the CC of these patients at baseline and 6 months (Chapter ...). In addition to replicating our previous cross-sectional findings, we found that active MS patients had lower NAA diffusivity at 6 months while stable patients remained constant. Additionally, water mean diffusivity did not change for active patients and increased for stable patients.

These in vivo NAA diffusivity measurements follow the pattern of changes expected for axonal degeneration based on simulated diffusion models of axon damage in complex geometries (Chapter 4). In particular, randomly moving particles localized inside impermeable broken cylinders (transected axons), bulging cylinders (swollen axons) and crimped cylinders (constricted axons) exhibit decreased parallel diffusivity ( $\lambda$ ) compared to intact impermeable cylinders. Conversely, when the particles are both inside and outside the cylindrical compartments and can move between, changes such as bulging or broken cylinders change the mean diffusivity and  $\lambda$  very little, or even increase the mean diffusivity and  $\lambda$  as in the case of the crimped cylinder.

In addition to changes in the restricting geometry, NAA diffusivity measurements may be detecting changes in the cytosol itself. In order to account for the macroscopic curvature of the corpus callosum in the DWS VOI, primary eigenvector information from the DTI acquisitions was incorporated with the NAA signal values in a model that calculates the intra-axonal diffusivity of NAA. This measure is largely reflective of the cytosolic medium. Histopathological study of degenerating axons in MS and otherwise have shown that there are many changes that occur, such as neurofilament

phosphorylation alterations, mitochondrial breakdown with release of reactive oxygen species, and dissolution of intracellular enzymatic microcompartments. All of these changes could decrease the cytosolic diffusivity of NAA due to viscosity and molecular crowding.

## ***9.5 Summation, limitations and possible future directions***

Diffusion weighted spectroscopy is a compelling MR technique that can be employed to measure axonopathy in studies of patients in vivo. Due to its compartmental specificity and microstructural sensitivity, it can provide information about axonal degeneration over a relatively short time period when used in concert with other MRI sequences. Reproducibility analysis and power calculations demonstrated that a difference of 10% in NAA diffusivity could be detected with group sizes as small as 21 patients at 3T with a sequence that runs in under 20 minutes. These qualities make DWS a potential marker of axon health in future therapy trials of neuroprotective drugs in patients with MS or other central nervous system neurodegenerative disease.

In general, magnetic resonance spectroscopy measurements and, especially DWS data, are limited by a low metabolite concentration compared to water. DWS at 3T lives on the edge of adequate SNR, which will limit its applicability to routine clinical care. This constraint likely contributes to the fact that while NAA diffusivity measurements are relatively specific and hence more interpretable than their water counterparts, they are often less sensitive. Therefore, much care must be taken with DWS sequences to optimize parameters and scan time before clinical studies are underway.

Future studies must explore the specificity of NAA diffusivity measures and seek

the biophysical basis of the findings seen here. Ideally, DWS would be tested in animal models of inflammation, demyelination, and neurodegeneration, where histopathological correlates of imaging findings can be examined. This endeavor will be limited by the size of the brains of those animal models of multiple sclerosis that currently exist. Therefore, studies of DWS in other neurodegenerative diseases of humans as well as in longer longitudinal studies may offer important information regarding pathological specificity.

Patients with chronic MS experience disability progression despite the use of the disease-modifying therapies that decrease inflammation and relapses. Evidence suggests that neurodegeneration is ongoing in these patients and that in order to slow and prevent irreversible neuronal loss in MS research efforts should focus on strategies aimed at neuroprotection and regeneration. As a relatively specific measure of axonal degeneration, diffusion weighted spectroscopy could be used in clinical trials of potential MS therapies. For instance, there are a host of drugs, currently FDA-approved for other purposes, that may be neuroprotective in a disease such as MS. Diffusion weighted spectroscopy could be applied to the process of repurposing these drugs in phase 2 and 3 efficacy trials. As diffusion weighted spectroscopy may be able to detect axonal degenerative changes in small groups of patients over a time course as short as 6 months, a large number of drugs could be trialed in a relatively short time. In this way, diffusion weighted spectroscopy could contribute to the treatment options available to patients with MS.

## **10 REFERENCES**

### ***10.1 Permissions***

**ELSEVIER LICENSE  
TERMS AND CONDITIONS**

Mar 09, 2015

---

This is a License Agreement between Emily T Wood ("You") and Elsevier ("Elsevier") provided by Copyright Clearance Center ("CCC"). The license consists of your order details, the terms and conditions provided by Elsevier, and the payment terms and conditions.

**All payments must be made in full to CCC. For payment instructions, please see information listed at the bottom of this form.**

Supplier	Elsevier Limited The Boulevard, Langford Lane Kidlington, Oxford, OX5 1GB, UK
Registered Company Number	1982084
Customer name	Emily T Wood
Customer address	Johns Hopkins University MSTP BALTIMORE, MD 21205
License number	3584781263791
License date	Mar 09, 2015
Licensed content publisher	Elsevier
Licensed content publication	Journal of the Neurological Sciences
Licensed content title	Axonal loss in the pathology of MS: consequences for understanding the progressive phase of the disease
Licensed content author	C Bjartmar, J.R Wujek, B.D Trapp
Licensed content date	15 February 2003
Licensed content volume number	206
Licensed content issue number	2
Number of pages	7
Start Page	165
End Page	171
Type of Use	reuse in a thesis/dissertation
Intended publisher of new work	other
Portion	figures/tables/illustrations
Number of figures/tables /illustrations	1
Format	electronic
Are you the author of this Elsevier article?	No
Will you be translating?	No
Original figure numbers	Figure 1

**ELSEVIER LICENSE  
TERMS AND CONDITIONS**

Mar 04, 2015

---

This is a License Agreement between Emily T Wood ("You") and Elsevier ("Elsevier") provided by Copyright Clearance Center ("CCC"). The license consists of your order details, the terms and conditions provided by Elsevier, and the payment terms and conditions.

**All payments must be made in full to CCC. For payment instructions, please see information listed at the bottom of this form.**

Supplier	Elsevier Limited The Boulevard, Langford Lane Kidlington, Oxford, OX5 1GB, UK
Registered Company Number	1982084
Customer name	Emily T Wood
Customer address	Johns Hopkins University MSTP BALTIMORE, MD 21205
License number	3582221113081
License date	Mar 04, 2015
Licensed content publisher	Elsevier
Licensed content publication	The Lancet
Licensed content title	NUCLEAR MAGNETIC RESONANCE IMAGING OF THE BRAIN IN MULTIPLE SCLEROSIS
Licensed content author	I.R Young, A.S Hall, C.A Pallis, G.M Bydder, N.J Legg, R.E Steiner
Licensed content date	14 November 1981
Licensed content volume number	318
Licensed content issue number	8255
Number of pages	4
Start Page	1063
End Page	1066
Type of Use	reuse in a thesis/dissertation
Portion	figures/tables/illustrations
Number of figures/tables /illustrations	1
Format	electronic
Are you the author of this Elsevier article?	No
Will you be translating?	No
Original figure numbers	Figure 1
Title of your thesis/dissertation	In Vivo Diffusion Weighted Magnetic Resonance Spectroscopy in Multiple Sclerosis
Expected completion date	Apr 2015

**SPRINGER LICENSE  
TERMS AND CONDITIONS**

Mar 04, 2015

---

This is a License Agreement between Emily T Wood ("You") and Springer ("Springer") provided by Copyright Clearance Center ("CCC"). The license consists of your order details, the terms and conditions provided by Springer, and the payment terms and conditions.

**All payments must be made in full to CCC. For payment instructions, please see information listed at the bottom of this form.**

License Number	3582240095040
License date	Mar 04, 2015
Licensed content publisher	Springer
Licensed content publication	Springer eBook
Licensed content title	Basic Concepts In NMR Spectroscopy
Licensed content author	K.V.R. Chary
Licensed content date	Jan 1, 2008
Type of Use	Thesis/Dissertation
Portion	Figures
Author of this Springer article	No
Order reference number	None
Original figure numbers	Figure 1.2
Title of your thesis / dissertation	In Vivo Diffusion Weighted Magnetic Resonance Spectroscopy in Multiple Sclerosis
Expected completion date	Apr 2015
Estimated size(pages)	280
Total	0.00 USD
Terms and Conditions	



**American Physical Society  
License Details**

Mar 04, 2015

This is an Agreement between Emily T Wood ("You") and American Physical Society ("Publisher"). It consists of your order details, the terms and conditions provided by American Physical Society, and the payment instructions.

License Number	3582240742383
License date	Mar 04, 2015
Licensed content publisher	American Physical Society
Licensed content publication	Physical Review (1893-1969)
Licensed content title	Effects of Diffusion on Free Precession in Nuclear Magnetic Resonance Experiments
Licensed copyright line	Copyright © 1954, American Physical Society
Licensed content author	H. Y. Carr and E. M. Purcell
Licensed content date	May 1, 1954
Volume number	94
Type of Use	Thesis/Dissertation
Requestor type	Student
Format	Electronic
Portion	chart/graph/table/figure
Number of charts/graphs /tables/figures	1
Portion description	Figure 3. panels A,B,C,D
Rights for	Main product
Duration of use	Life of current edition
Creation of copies for the disabled	no
With minor editing privileges	no
For distribution to	Worldwide
In the following language(s)	Original language of publication
With incidental promotional use	no
The lifetime unit quantity of new product	0 to 499
The requesting person/organization is:	Emily T Wood, Johns Hopkins University
Order reference number	None
Title of your thesis / dissertation	In Vivo Diffusion Weighted Magnetic Resonance Spectroscopy in Multiple Sclerosis
Expected completion date	Apr 2015
Expected size (number of pages)	280
Total	0.00 USD
Terms and Conditions	

**NATURE PUBLISHING GROUP LICENSE  
TERMS AND CONDITIONS**

Mar 04, 2015

---

This is a License Agreement between Emily T Wood ("You") and Nature Publishing Group ("Nature Publishing Group") provided by Copyright Clearance Center ("CCC"). The license consists of your order details, the terms and conditions provided by Nature Publishing Group, and the payment terms and conditions.

**All payments must be made in full to CCC. For payment instructions, please see information listed at the bottom of this form.**

License Number	3582241088008
License date	Mar 04, 2015
Licensed content publisher	Nature Publishing Group
Licensed content publication	Nature Reviews Neuroscience
Licensed content title	Looking into the functional architecture of the brain with diffusion MRI
Licensed content author	Denis Le Bihan
Licensed content date	Jun 1, 2003
Volume number	4
Issue number	6
Type of Use	reuse in a dissertation / thesis
Requestor type	academic/educational
Format	electronic
Portion	figures/tables/illustrations
Number of figures/tables /illustrations	1
High-res required	no
Figures	Figure 1.b
Author of this NPG article	no
Your reference number	None
Title of your thesis / dissertation	In Vivo Diffusion Weighted Magnetic Resonance Spectroscopy in Multiple Sclerosis
Expected completion date	Apr 2015
Estimated size (number of pages)	280
Total	0.00 USD
Terms and Conditions	



11200 Rockville Pike  
Suite 302  
Rockville, Maryland 20852

August 19, 2011

American Society for Biochemistry and Molecular Biology

---

To whom it may concern,

It is the policy of the American Society for Biochemistry and Molecular Biology to allow reuse of any material published in its journals (the Journal of Biological Chemistry, Molecular & Cellular Proteomics and the Journal of Lipid Research) in a thesis or dissertation at no cost and with no explicit permission needed. Please see our copyright permissions page on the journal site for more information.

Best wishes,

Sarah Crespi

[American Society for Biochemistry and Molecular Biology](#)

11200 Rockville Pike, Rockville, MD

Suite 302

240-283-6616

[JBC](#) | [MCP](#) | [JLR](#)

---

## Permission to reprint in dissertation

---

jn permissions <jnpermissions@sfn.org>  
To: Emily Wood <ewood9@jhmi.edu>

Tue, Mar 10, 2015 at 4:56 PM

Dear Emily Wood,

Thank you for your email. Permission is granted to reproduce the requested material listed below with NO fee in print and electronic format for use in your doctoral thesis/dissertation. Please contact me if you have any questions or if you need another form of permission.

Regards,  
SfN Central Office

### Regional modulation of neurofilament organization by myelination in normal axons

ST Hsieh, GJ Kidd, TO Crawford, Z Xu, WM Lin, BD Trapp, DW Cleveland, and JW Griffin  
The Journal of Neuroscience, 1 November 1994, 14(11):6392-6401

---

**From:** emilytwood@gmail.com [emilytwood@gmail.com] on behalf of Emily Wood [ewood9@jhmi.edu]

**Sent:** Wednesday, March 04, 2015 10:47 PM

**To:** jn permissions

**Subject:** Permission to reprint in dissertation

To whom it may concern:

I am completing a doctoral dissertation at Johns Hopkins University titled "In Vivo Diffusion Weighted Magnetic Resonance Spectroscopy in Multiple Sclerosis." I would like your permission to reprint the following figure in my dissertation:

**Hsieh, S.T. et al., 1994.** Regional modulation of neurofilament organization by myelination in normal axons. *Journal of Neuroscience*, 14(11), pp.6392–6401. Figure 3.

The expected publication date of my dissertation is April 2015. It will be published electronically in PDF format on my institutional repository. If you have questions about the Johns Hopkins University electronic dissertation repository you can contact the coordinator, David Reynolds (etd-support@jhu.edu or (410) 516-7220)

If you grant permission for me to reprint this figure the associated caption would include the article title, authors, date, journal, volume, page, figure, copyright year and copyright holder.

Thank you so much for your time and consideration. I look forward to hearing from you.

Be well,

Emily T. Wood  
MS 4, MSTP, Johns Hopkins University SOM  
410-349-7130

---

**JOHN WILEY AND SONS LICENSE  
TERMS AND CONDITIONS**

Mar 04, 2015

---

This Agreement between Emily T Wood ("You") and John Wiley and Sons ("John Wiley and Sons") consists of your license details and the terms and conditions provided by John Wiley and Sons and Copyright Clearance Center.

License Number	3582250469272
License date	Mar 04, 2015
Licensed Content Publisher	John Wiley and Sons
Licensed Content Publication	Annals of Neurology
Licensed Content Title	Three-dimensional tracking of axonal projections in the brain by magnetic resonance imaging
Licensed Content Author	Susumu Mori, Barbara J. Crain, V. P. Chacko, Peter C. M. Van Zijl
Licensed Content Date	May 31, 2001
Pages	5
Type of use	Dissertation/Thesis
Requestor type	University/Academic
Format	Electronic
Portion	Figure/table
Number of figures/tables	1
Original Wiley figure/table number(s)	Figure 1
Will you be translating?	No
Title of your thesis / dissertation	In Vivo Diffusion Weighted Magnetic Resonance Spectroscopy in Multiple Sclerosis
Expected completion date	Apr 2015
Expected size (number of pages)	280
Requestor Location	Emily T Wood Johns Hopkins University MSTP 1830 E. Monument Street Suite 2-300 BALTIMORE, MD 21205 United States Attn: Emily T Wood
Billing Type	Invoice
Billing Address	Emily T Wood Johns Hopkins University MSTP 1830 E. Monument Street Suite 2-300 BALTIMORE, MD 21205 United States Attn: Emily T Wood
Total	0.00 USD
Terms and Conditions	

## **10.2 Bibliography**

- 't Hart, B.A., Gran, B. & Weissert, R., 2011. EAE: imperfect but useful models of multiple sclerosis. *Trends in molecular medicine*, 17(3), pp.119–125.
- Aboitiz, F. et al., 1992. Fiber composition of the human corpus callosum. *Brain Research*, 598(1-2), pp.143–153.
- Aboitiz, F. & Montiel, J., 2003. One hundred million years of interhemispheric communication: the history of the corpus callosum. *Brazilian journal of medical and biological research*, 36(4), pp.409–420.
- Absinta, M. et al., 2013. Seven-tesla phase imaging of acute multiple sclerosis lesions: A new window into the inflammatory process. *Annals of Neurology*, 74(5), pp.669–678.
- Annese, J., 2012. The importance of combining MRI and large-scale digital histology in neuroimaging studies of brain connectivity and disease. pp.1–6.
- Ariyannur, P.S., Madhavarao, C.N. & Namboodiri, A.M.A., 2008. N-acetyl aspartate synthesis in the brain: mitochondria vs. microsomes. *Brain Research*, 1227, pp.34–41.
- Arnold, D., Riess, G. & Matthews, P., 1994. Use of proton magnetic resonance spectroscopy for monitoring disease progression in multiple sclerosis. *Annals of Neurology*, 36, pp. 76-82.
- Arnold, D.L. et al., 1990. Proton magnetic resonance spectroscopy of human brain in vivo in the evaluation of multiple sclerosis: assessment of the load of disease. *Magnetic resonance in medicine*, 14(1), pp.154–159.

- Arun, P., Moffett, J.R. & Namboodiri, A.M.A., 2009. Evidence for mitochondrial and cytoplasmic N-acetyl aspartate synthesis in SH-SY5Y neuroblastoma cells. *Neurochemistry international*, 55(4), pp.219–225.
- Ascherio, A., Munger, K.L. & Lünemann, J.D., 2012. The initiation and prevention of multiple sclerosis. *Nature Publishing Group*, 8(11), pp.602–612.
- Ashburner, J. & Friston, K., 1997. Multimodal image coregistration and partitioning--a unified framework. *NeuroImage*, 6(3), pp.209–217.
- Ashburner, J. & Friston, K., 2000. Voxel-based morphometry--the methods. *NeuroImage*, 11(6), pp.805–821.
- Ashburner, J. & Friston, K.J., 2005. Unified segmentation. *NeuroImage*, 26(3), pp.839–851.
- Assaf, Y. & Cohen, Y., 1998a. In vivo and in vitro bi-exponential diffusion of N-acetyl aspartate (NAA) in rat brain: a potential structural probe? *NMR in Biomedicine*, 11(2), pp.67–74.
- Assaf, Y. & Cohen, Y., 1998b. Non-Mono-Exponential Attenuation of Water and N-Acetyl Aspartate Signals Due to Diffusion in Brain Tissue. *Journal of Magnetic Resonance*, 131(1), pp.69–85.
- Avram, L. et al., 2008. Three-dimensional water diffusion in impermeable cylindrical tubes: theory versus experiments. *NMR in Biomedicine*, 21(8), pp.888–898.
- Bagnato, F. et al., 2003. Evolution of T1 black holes in patients with multiple sclerosis imaged monthly for 4 years. *Brain*, 126(Pt 8), pp.1782–1789.
- Bakker, D.A. & Ludwin, S.K., 1987. Blood-brain barrier permeability during Cuprizone-

induced demyelination. Implications for the pathogenesis of immune-mediated demyelinating diseases. *Journal of the Neurological Sciences*, 78(2), pp.125–137.

Bammer, R. et al., 2000. Magnetic resonance diffusion tensor imaging for characterizing diffuse and focal white matter abnormalities in multiple sclerosis. *Magnetic resonance in medicine*, 44(4), pp.583–591.

Banich, M.T., 1998. The missing link: the role of interhemispheric interaction in attentional processing. *Brain and cognition*, 36(2), pp.128–157.

Barker, P.B. et al., 2009. *Clinical MR Spectroscopy*, Cambridge University Press.

Barkhof, F. et al., 2009. Imaging outcomes for neuroprotection and repair in multiple sclerosis trials. *Nature Publishing Group*, 5(5), pp.256–266.

Barnett, M.H. & Prineas, J.W., 2004. Relapsing and remitting multiple sclerosis: pathology of the newly forming lesion. *Annals of Neurology*, 55(4), pp.458–468.

Bartlett, J.W. & Frost, C., 2008. Reliability, repeatability and reproducibility: analysis of measurement errors in continuous variables. *Ultrasound in Obstetrics and Gynecology*, 31(4), pp.466–475.

Baslow, M.H. et al., 1999. Expression of aspartoacylase activity in cultured rat macroglial cells is limited to oligodendrocytes. *Journal of Molecular Neuroscience*, 13(1-2), pp.47–53.

Basser, P., 1995. Inferring microstructural features and the physiological state of tissues from diffusion weighted images. *NMR in Biomedicine*, 8(7), pp.333–344.

Basser, P. & Pierpaoli, C., 1996. Microstructural and physiological features of tissues



- elucidated by quantitative-diffusion-tensor MRI. *Journal of Magnetic Resonance Series B*, 111(3), pp.209–219.
- Basser, P.J., Mattiello, J. & Le Bihan, D., 1994. Estimation of the effective self-diffusion tensor from the NMR spin echo. *Journal of Magnetic Resonance Series B*, 103, pp.247–247.
- Bates, T.E. et al., 1996. Inhibition of N-acetyl aspartate production: implications for 1H MRS studies in vivo. *Neuroreport*, 7(8), pp.1397–1400.
- Batoulis, H., Addicks, K. & Kuerten, S., 2010. Emerging concepts in autoimmune encephalomyelitis beyond the CD4/T(H)1 paradigm. *Annals of anatomy*, 192(4), pp.179–193.
- Bazin, P.-L. & Pham, D.L., 2008. Homeomorphic brain image segmentation with topological and statistical atlases. *Medical image analysis*, 12(5), pp.616–625.
- Bárány, M. et al., 1987. High resolution proton magnetic resonance spectroscopy of human brain and liver. *Magnetic resonance imaging*, 5(5), pp.393–398.
- Beaulieu, C., 2002. The basis of anisotropic water diffusion in the nervous system - a technical review. *NMR in Biomedicine*, 15(7-8), pp.435–455.
- Beckerman, H. et al., 2001. Smallest real difference, a link between reproducibility and responsiveness. *Quality of life research*, 10(7), pp.571–578.
- Benetti, F. et al., 2010. Cuprizone neurotoxicity, copper deficiency and neurodegeneration. *Neurotoxicology*, 31(5), pp.509–517.
- Bermel, R.A. & Bakshi, R., 2006. The measurement and clinical relevance of brain atrophy in multiple sclerosis. *Lancet neurology*, 5(2), pp.158–170.

- Bitsch, A. et al., 2000. Acute axonal injury in multiple sclerosis. Correlation with demyelination and inflammation. *Brain*, 123 ( Pt 6), pp.1174–1183.
- Bjartmar, C. & Trapp, B.D., 2001. Axonal and neuronal degeneration in multiple sclerosis: mechanisms and functional consequences. *Current opinion in neurology*, 14(3), pp.271–278.
- Bjartmar, C. et al., 2000. Neurological disability correlates with spinal cord axonal loss and reduced N-acetyl aspartate in chronic multiple sclerosis patients. *Annals of Neurology*, 48(6), pp.893–901.
- Bjartmar, C., Wujek, J.R. & Trapp, B.D., 2003. Axonal loss in the pathology of MS: consequences for understanding the progressive phase of the disease. *Journal of the Neurological Sciences*, 206(2), pp.165–171.
- Blakemore, W.F., 1973a. Demyelination of the superior cerebellar peduncle in the mouse induced by cuprizone. *Journal of the Neurological Sciences*, 20(1), pp.63–72.
- Blakemore, W.F., 1972. Observations on oligodendrocyte degeneration, the resolution of status spongiosus and remyelination in cuprizone intoxication in mice. *Journal of neurocytology*, 1(4), pp.413–426.
- Blakemore, W.F., 1973b. Remyelination of the superior cerebellar peduncle in the mouse following demyelination induced by feeding cuprizone. *Journal of the Neurological Sciences*, 20(1), pp.73–83.
- Bland, J.M. & Altman, D.G., 1986. Statistical methods for assessing agreement between two methods of clinical measurement. *Lancet*, 1(8476), pp.307–310.

- Bodini, B. et al., 2013. Corpus callosum damage predicts disability progression and cognitive dysfunction in primary-progressive MS after five years. *Human Brain Mapping*, 35(5), pp. 1163–1172.
- Bodini, B. et al., 2011. T2 lesion location really matters: a 10 year follow-up study in primary progressive multiple sclerosis. *Journal of Neurology, Neurosurgery & Psychiatry*, 82(1), pp.72–77.
- Borges, I.T. et al., 2013. The effect of daclizumab on brain atrophy in relapsing-remitting multiple sclerosis. *Multiple Sclerosis and Related Disorders*, 2(2), pp.133–140.
- Bottomley, P.A., 1987. Spatial localization in NMR spectroscopy in vivo. *Annals of the New York Academy of Sciences*, 508, pp.333–348.
- Brangwynne, C.P. et al., 2008. Cytoplasmic diffusion: molecular motors mix it up. *The Journal of cell biology*, 183(4), pp.583–587.
- Brangwynne, C.P. et al., 2009. Intracellular transport by active diffusion. *Trends in cell biology*, 19(9), pp.423–427.
- Branzoli, F. et al., 2013. Functional diffusion weighted magnetic resonance spectroscopy of the human primary visual cortex at 7 T. *Magnetic Resonance in Medicine*, 69(2), pp.303–309.
- Brück, W. et al., 1995. Monocyte/macrophage differentiation in early multiple sclerosis lesions. *Annals of Neurology*, 38(5), pp.788–796.
- Budde, M.D. & Frank, J.A., 2010. Neurite beading is sufficient to decrease the apparent diffusion coefficient after ischemic stroke. *Proceedings of the National Academy of Sciences*, 107(32), pp.14472–14477.

- Budde, M.D. et al., 2009. Axial diffusivity is the primary correlate of axonal injury in the experimental autoimmune encephalomyelitis spinal cord: a quantitative pixelwise analysis. *Journal of Neuroscience*, 29(9), pp.2805–2813.
- Budde, M.D. et al., 2008. Axonal injury detected by in vivo diffusion tensor imaging correlates with neurological disability in a mouse model of multiple sclerosis. *NMR in Biomedicine*, 21(6), pp.589–597.
- Budde, M.D. & Frank, J.A., 2012. Examining brain microstructure using structure tensor analysis of histological sections. *NeuroImage*, 63(1), pp.1–10.
- Burke, R.E. & O'Malley, K., 2013. Axon degeneration in Parkinson's disease. *Experimental neurology*, 246(C), pp.72–83.
- Cader, S. et al., 2007. Discordant white matter N-acetylaspartate and diffusion MRI measures suggest that chronic metabolic dysfunction contributes to axonal pathology in multiple sclerosis. *NeuroImage*, 36(1), pp.19–27.
- Callaghan, P.T., 1984. Pulsed field gradient nuclear magnetic resonance as a probe of liquid state molecular organization. *Australian journal of physics*, 37, p.359.
- Campbell, G.R. & Mahad, D.J., 2011. Mitochondrial changes associated with demyelination: Consequences for axonal integrity. *MITOCH*, pp.1–7.
- Carass, A. et al., 2011. Simple paradigm for extra-cerebral tissue removal: Algorithm and analysis. *NeuroImage*, 56(4), pp.1982–1992.
- Carr, H.Y. & Purcell, E.M., 1954. Effects of diffusion on free precession in nuclear magnetic resonance experiments. *Physical Review*, 94(3), p.630.
- Carroll, S.L., 2009. *Wallerian Degeneration* L. R. Squire, ed., Elsevier.

- Charcot, J.-M., 1868. Histologie de la sclérose en plaques M. Bourneville, ed. *Gazette Hôpitaux*, pp.1–32.
- Chard, D.T. et al., 2002. Brain atrophy in clinically early relapsing-remitting multiple sclerosis. *Brain*, 125(Pt 2), pp.327–337.
- Chary, K.V. & Govil, G., 2008. BASIC CONCEPTS IN NMR SPECTROSCOPY. In *NMR in biological systems: from molecules to human*. Dordrecht, The Netherlands: Springer.
- Choi, J.-K., Dedeoglu, A. & Jenkins, B.G., 2007. Application of MRS to mouse models of neurodegenerative illness. *NMR in Biomedicine*, 20(3), pp.216–237.
- Ciccarelli, O. et al., 2003. A study of the mechanisms of normal-appearing white matter damage in multiple sclerosis using diffusion tensor imaging--evidence of Wallerian degeneration. *Journal of Neurology*, 250(3), pp.287–292.
- Ciccarelli, O. et al., 2010. Assessing Neuronal Metabolism In Vivo by Modeling Imaging Measures. *Journal of Neuroscience*, 30(45), pp.15030–15033.
- Ciccarelli, O. et al., 2001. Investigation of MS normal-appearing brain using diffusion tensor MRI with clinical correlations. *Neurology*, 56(7), pp.926–933.
- Ciccarelli, O. et al., 2007. Spinal cord spectroscopy and diffusion-based tractography to assess acute disability in multiple sclerosis. *Brain*, 130(8), p.2220.
- Cohen, J.A. et al., 2010. Oral fingolimod or intramuscular interferon for relapsing multiple sclerosis. *The New England journal of medicine*, 362(5), pp.402–415.
- Coleman, M.P., 2013. The challenges of axon survival: Introduction to the special issue on axonal degeneration. *Experimental neurology*, 246(C), pp.1–5.

- Colvin, Daniel C, Thomas E Yankeelov, Mark D Does, Zoe Yue, Chad Quarles, and John C Gore. 2008. "New Insights Into Tumor Microstructure Using Temporal Diffusion Spectroscopy." *Cancer Research* 68 (14): 5941–47.
- Compston, A. & Coles, A., 2008. Multiple sclerosis. *Lancet*, 372(9648), pp.1502–1517.
- Concha, L. et al., 2006. Diffusion tensor imaging of time-dependent axonal and myelin degradation after corpus callosotomy in epilepsy patients. *NeuroImage*, 32(3), pp.1090–1099.
- Crawford, D.K. et al., 2009. Functional recovery of callosal axons following demyelination: a critical window. *Neuroscience*, 164(4), pp.1407–1421.
- Dashiell, S.M. et al., 2002. Myelin-associated glycoprotein modulates expression and phosphorylation of neuronal cytoskeletal elements and their associated kinases. *Journal of neurochemistry*, 81(6), pp.1263–1272.
- Davie, C.A. et al., 1997. 1H magnetic resonance spectroscopy of chronic cerebral white matter lesions and normal appearing white matter in multiple sclerosis. *Journal of Neurology, Neurosurgery & Psychiatry*, 63(6), pp.736–742.
- Davie, C.A. et al., 1994. Serial proton magnetic resonance spectroscopy in acute multiple sclerosis lesions. *Brain*, 117 ( Pt 1), pp.49–58.
- De Coene, B. et al., 1992. MR of the brain using fluid-attenuated inversion recovery (FLAIR) pulse sequences. *American Journal of Neuroradiology*, 13(6), pp.1555–1564.
- de Graaf, R.A., Braun, K.P. & Nicolay, K., 2001. Single-shot diffusion trace (1)H NMR spectroscopy. *Magnetic resonance in medicine*, 45(5), pp.741–748.

- de Graaf, R.A., van Kranenburg, A. & Nicolay, K., 2000. In vivo (31)P-NMR diffusion spectroscopy of ATP and phosphocreatine in rat skeletal muscle. *Biophysical Journal*, 78(4), pp.1657–1664.
- De Stefano, N. et al., 2010. Assessing brain atrophy rates in a large population of untreated multiple sclerosis subtypes. *Neurology*, 74(23), pp.1868–1876.
- De Stefano, N. et al., 1998. Axonal damage correlates with disability in patients with relapsing-remitting multiple sclerosis. Results of a longitudinal magnetic resonance spectroscopy study. *Brain*, 121 ( Pt 8), pp.1469–1477.
- De Stefano, N. et al., 2002. Diffuse axonal and tissue injury in patients with multiple sclerosis with low cerebral lesion load and no disability. *Archives of neurology*, 59(10), pp.1565–1571.
- De Stefano, N. et al., 1999. In vivo evidence for axonal dysfunction remote from focal cerebral demyelination of the type seen in multiple sclerosis. *Brain*, 122 ( Pt 10), pp.1933–1939.
- DeBoy, C.A. et al., 2007. High resolution diffusion tensor imaging of axonal damage in focal inflammatory and demyelinating lesions in rat spinal cord. *Brain*, 130(Pt 8), pp.2199–2210.
- DeLuca, G.C. et al., 2006. The contribution of demyelination to axonal loss in multiple sclerosis. *Brain*, 129(Pt 6), pp.1507–1516.
- Dijkhuizen, R.M. et al., 1999. Changes in the diffusion of water and intracellular metabolites after excitotoxic injury and global ischemia in neonatal rat brain. *Journal of cerebral blood flow and metabolism*, 19(3), pp.341–349.

- Does, M.D. & Gore, J.C., 2000. Compartmental study of diffusion and relaxation measured in vivo in normal and ischemic rat brain and trigeminal nerve. *Magnetic resonance in medicine*, 43(6), pp.837–844.
- Does, M.D., Parsons, E.C. & Gore, J.C., 2003. Oscillating gradient measurements of water diffusion in normal and globally ischemic rat brain. *Magnetic resonance in medicine*, 49(2), pp.206–215.
- Du, Fei, Alissa J Cooper, Thida Thida, Ann K Shinn, Bruce M Cohen, and Dost Öngür. 2013. “Myelin and Axon Abnormalities in Schizophrenia Measured with Magnetic Resonance Imaging Techniques.” *Biological Psychiatry* 74 (6): 451–57.  
doi:10.1016/j.biopsych.2013.03.003.
- Dutta, R. & Trapp, B.D., 2011. Mechanisms of neuronal dysfunction and degeneration in multiple sclerosis. *Progress in Neurobiology*, 93(1), pp.1–12.
- Dutta, R. et al., 2006. Mitochondrial dysfunction as a cause of axonal degeneration in multiple sclerosis patients. *Annals of Neurology*, 59(3), pp.478–489.
- Dziedzic, T. et al., 2010. Wallerian degeneration: a major component of early axonal pathology in multiple sclerosis. *Brain pathology (Zurich, Switzerland)*, 20(5), pp.976–985.
- Efron, B. & Tibshirani, R.J., 1994. *An Introduction to the Bootstrap*, Boca Raton, Florida, USA: CRC Press.
- Einstein, A., 1956. *Investigations on the Theory of the Brownian Movement* R. Fürth, ed., Dover Publications, Inc.
- Ellegood, J., Hanstock, C.C. & Beaulieu, C., 2010. Considerations for measuring the



- fractional anisotropy of metabolites with diffusion tensor spectroscopy. *NMR in Biomedicine*, 24(3), pp.270–280.
- Ellegood, J., Hanstock, C.C. & Beaulieu, C., 2006. Diffusion tensor spectroscopy (DTS) of human brain. *Magnetic resonance in medicine*, 55(1), pp.1–8.
- Ellegood, J., Hanstock, C.C. & Beaulieu, C., 2005. Trace apparent diffusion coefficients of metabolites in human brain using diffusion weighted magnetic resonance spectroscopy. *Magnetic resonance in medicine*, 53(5), pp.1025–1032.
- Ellis, R.J., 2001. Macromolecular crowding: obvious but underappreciated. *Trends in biochemical sciences*, 26(10), pp.597–604.
- Ellwardt, E. & Zipp, F., 2014. Experimental Neurology. *Experimental neurology*, 262(PA), pp.8–17.
- Enzinger, C. et al., 2005. Risk factors for progression of brain atrophy in aging: Six-year follow-up of normal subjects. *Neurology*, 64(10), pp.1704–1711.
- Evangelou, N. et al., 2000. Quantitative pathological evidence for axonal loss in normal appearing white matter in multiple sclerosis. *Annals of Neurology*, 47(3), pp.391–395.
- Farrell, J. et al., 2008. High b-value q-space diffusion weighted MRI of the human cervical spinal cord in vivo: feasibility and application to multiple sclerosis. *Magnetic Resonance in Medicine*, 59(5), pp.1079–1089.
- Farrell, J.A., 2009. *Q-SPACE DIFFUSION IMAGING OF AXON AND MYELIN DAMAGE IN THE HUMAN AND RAT SPINAL CORD*. Baltimore, MD: Thesis.
- Farrell, J.A.D. et al., 2010. q-space and conventional diffusion imaging of axon and

- myelin damage in the rat spinal cord after axotomy. *Magnetic Resonance in Medicine*, 63(5), pp.1323–1335.
- Ferguson, B. et al., 1997. Axonal damage in acute multiple sclerosis lesions. *Brain*, 120 (Pt 3), pp.393–399.
- Filippi, M. et al., 1995. A magnetization transfer imaging study of normal-appearing white matter in multiple sclerosis. *Neurology*, 45(3), pp. 478-482.
- Filippi, M. et al., 2003. Evidence for widespread axonal damage at the earliest clinical stage of multiple sclerosis. *Brain*, 126(2), p.433.
- Filippi, M. et al., 1998. Magnetization transfer changes in the normal appearing white matter precede the appearance of enhancing lesions in patients with multiple sclerosis. *Annals of Neurology*, 43(6), pp.809–814.
- Filippini, G. et al., 2000. Corticosteroids or ACTH for acute exacerbations in multiple sclerosis. *Cochrane Database Syst Rev*, 4(4).
- Fink, F. et al., 2010. Comparison of diffusion tensor-based tractography and quantified brain atrophy for analyzing demyelination and axonal loss in MS. *Journal of neuroimaging*, 20(4), pp.334–344.
- Fischer, M.T. et al., 2013. Disease-specific molecular events in cortical multiple sclerosis lesions. *Brain*, 136(Pt 6), pp.1799–1815.
- Fischl, B. et al., 2004. Sequence-independent segmentation of magnetic resonance images. *NeuroImage*, 23, pp.S69–S84.
- Fischl, B. et al., 2002. Whole brain segmentation: automated labeling of neuroanatomical structures in the human brain. *Neuron*, 33(3), pp.341–355.

- Fisher, E. et al., 2008. Gray matter atrophy in multiple sclerosis: a longitudinal study. *Annals of Neurology*, 64(3), pp.255–265.
- Fisniku, L.K. et al., 2008. Gray matter atrophy is related to long-term disability in multiple sclerosis. *Annals of Neurology*, 64(3), pp.247–254.
- Fox, N.C. et al., 1999. Correlation between rates of brain atrophy and cognitive decline in AD. *Neurology*, 52(8), pp.1687–1687.
- Fox, R.J. et al., 2012. A Validation Study of Multicenter Diffusion Tensor Imaging: Reliability of Fractional Anisotropy and Diffusivity Values. *American Journal of Neuroradiology*, 33(4), pp.695–700.
- Fox, R.J. et al., 2011. Measuring Myelin Repair and Axonal Loss with Diffusion Tensor Imaging. *American Journal of Neuroradiology*, 32(1), pp. 85-91.
- Franciotta, D. et al., 2008. B cells and multiple sclerosis. *Lancet neurology*, 7(9), pp.852–858.
- Franklin, R.J.M. et al., 2012. Neuroprotection and repair in multiple sclerosis. *Nature Publishing Group*, 8(11), pp.624–634.
- Freedman, M.S., 2013. Present and emerging therapies for multiple sclerosis. *Continuum (Minneapolis, Minn.)*, 19(4 Multiple Sclerosis), pp.968–991.
- Frischer, J.M. et al., 2009. The relation between inflammation and neurodegeneration in multiple sclerosis brains. *Brain*, 132(5), pp.1175–1189.
- Frohman, E.M. et al., 2007. Corticosteroids for multiple sclerosis: I. Application for treating exacerbations. *Neurotherapeutics*, 4(4), pp.618–626.
- Fu, L. et al., 1998. Imaging axonal damage of normal-appearing white matter in multiple

- sclerosis. *Brain*, 121 ( Pt 1), pp.103–113.
- Gaitán, M.I. et al., 2013. Initial investigation of the blood-brain barrier in MS lesions at 7 tesla. *Multiple Sclerosis*, 19(8), pp.1068–1073.
- Gaitán, M.I. et al., 2011. Evolution of the blood-brain barrier in newly forming multiple sclerosis lesions. *Annals of Neurology*, 70(1), pp.22–29.
- Gao, K.C. et al., 2014. Sub-millimeter imaging of brain-free water for rapid volume assessment in atrophic brains. *NeuroImage*, 100C, pp.370–378.
- Ge, Y. et al., 2000. Brain atrophy in relapsing-remitting multiple sclerosis and secondary progressive multiple sclerosis: longitudinal quantitative analysis. *Radiology*, 214(3), pp.665–670.
- Ge, Y. et al., 2004. Neuronal cell injury precedes brain atrophy in multiple sclerosis. *Neurology*, 62(4), pp.624–627.
- George, R. & Griffin, J.W., 1994a. Delayed macrophage responses and myelin clearance during Wallerian degeneration in the central nervous system: the dorsal radiculotomy model. *Experimental neurology*, 129(2), pp.225–236.
- George, R. & Griffin, J.W., 1994b. The proximo-distal spread of axonal degeneration in the dorsal columns of the rat. *Journal of neurocytology*, 23(11), pp.657–667.
- Geurts, J.J.G. et al., 2005. Cortical lesions in multiple sclerosis: combined postmortem MR imaging and histopathology. *AJNR American journal of neuroradiology*, 26(3), pp.572–577.
- Gold, R., Buttgereit, F. & Toyka, K.V., 2001. Mechanism of action of glucocorticosteroid hormones: possible implications for therapy of neuroimmunological disorders.

*Journal of neuroimmunology*, 117(1-2), pp.1–8.

Goldschmidt, T. et al., 2009. Remyelination capacity of the MS brain decreases with disease chronicity. *Neurology*, 72(22), pp.1914–1921.

Gonen, O. et al., 2002. Relapsing-remitting multiple sclerosis and whole-brain N-acetyl aspartate measurement: evidence for different clinical cohorts initial observations. *Radiology*, 225(1), pp.261–268.

Gonen, O. et al., 2000. Total brain N-acetyl aspartate: a new measure of disease load in MS. *Neurology*, 54(1), pp.15–19.

Goodin, D.S. et al., 2012. Cause of death in MS: long-term follow-up of a randomised cohort, 21 years after the start of the pivotal IFN -1b study. *BMJ Open*, 2(6), pp.e001972–e001972.

Greitz, D. et al., 1992. Pulsatile brain movement and associated hydrodynamics studied by magnetic resonance phase imaging. The Monro-Kellie doctrine revisited. *Neuroradiology*, 34(5), pp.370–380.

Haga, K.K. et al., 2009. A systematic review of brain metabolite changes, measured with 1H magnetic resonance spectroscopy, in healthy aging. *Neurobiology of Aging*, 30(3), pp.353–363.

Hagmann, P. et al., 2006. Understanding diffusion MR imaging techniques: from scalar diffusion weighted imaging to diffusion tensor imaging and beyond. *Radiographics*, 26 Suppl 1, pp.S205–23.

Hahn, E.L., 1950. Spin echoes. *Physical Review*, 80(4), p.580.

- Hampton, D.W. et al., 2013. Neurodegeneration progresses despite complete elimination of clinical relapses in a mouse model of multiple sclerosis. *Acta neuropathologica communications*, 1(1), p.84.
- Harada, M. et al., 2002. Diffusion weighted in vivo localized proton MR spectroscopy of human cerebral ischemia and tumor. *NMR in Biomedicine*, 15(1), pp.69–74.
- Harris, J.O. et al., 1991. Serial gadolinium-enhanced magnetic resonance imaging scans in patients with early, relapsing-remitting multiple sclerosis: implications for clinical trials and natural history. *Annals of Neurology*, 29(5), pp.548–555.
- Harrison, D.M. et al., 2011. Longitudinal changes in diffusion tensor-based quantitative MRI in multiple sclerosis. *Neurology*, 76(2), pp.179–186.
- Hasan, K.M. et al., 2005. Diffusion tensor fractional anisotropy of the normal-appearing seven segments of the corpus callosum in healthy adults and relapsing-remitting multiple sclerosis patients. *Journal of magnetic resonance imaging : JMRI*, 21(6), pp.735–743.
- Hasan, K.M. et al., 2012. Human brain atlas-based multimodal MRI analysis of volume-etry, diffusimetry, relaxometry and lesion distribution in multiple sclerosis patients and healthy adult controls: implications for understanding the pathogenesis of multiple sclerosis and consolidation of quantitative MRI results in MS. *Journal of the Neurological Sciences*, 313(1-2), pp.99–109.
- Hauser, S.L. & Oksenberg, J.R., 2006. The neurobiology of multiple sclerosis: genes, inflammation, and neurodegeneration. *Neuron*, 52(1), pp.61–76.
- Herring, N.R. & Konradi, C., 2011. Myelin, copper, and the cuprizone model of

- schizophrenia. *Frontiers in bioscience (Scholar edition)*, 3, pp.23–40.
- Hsieh, S.T. et al., 1994. Regional modulation of neurofilament organization by myelination in normal axons. *Journal of Neuroscience*, 14(11 Pt 1), pp.6392–6401.
- Inglese, M. et al., 2003. Diffusely elevated cerebral choline and creatine in relapsing-remitting multiple sclerosis. *Magnetic resonance in medicine : official journal of the Society of Magnetic Resonance in Medicine / Society of Magnetic Resonance in Medicine*, 50(1), pp.190–195.
- Inglese, M. et al., 2004. Indirect evidence for early widespread gray matter involvement in relapsing-remitting multiple sclerosis. *NeuroImage*, 21(4), pp.1825–1829.
- Jenkinson, M. & Smith, S., 2001. A global optimisation method for robust affine registration of brain images. *Medical image analysis*, 5(2), pp.143–156.
- Johnson, V.E., Stewart, W. & Smith, D.H., 2013. Axonal pathology in traumatic brain injury. *Experimental neurology*, 246(C), pp.35–43.
- Jones, B.C. et al., 2013. Quantification of multiple-sclerosis-related brain atrophy in two heterogeneous MRI datasets using mixed-effects modeling. *NeuroImage. Clinical*, 3, pp.171–179.
- Jurevics, H. et al., 2002. Alterations in metabolism and gene expression in brain regions during cuprizone-induced demyelination and remyelination. *Journal of neurochemistry*, 82(1), pp.126–136.
- Kan, H.E. et al., 2012. Differences in apparent diffusion coefficients of brain metabolites between grey and white matter in the human brain measured at 7 T. *Magnetic*

*Resonance in Medicine*, 67(5), pp.1203–1209.

- Kanaan, N.M. et al., 2013. Axonal degeneration in Alzheimer's disease: When signaling abnormalities meet the axonal transport system. *Experimental neurology*, 246(C), pp.44–53.
- Kappos, L. et al., 2010. A placebo-controlled trial of oral fingolimod in relapsing multiple sclerosis. *The New England journal of medicine*, 362(5), pp.387–401.
- Kappos, L. et al., 2009. Long-term effect of early treatment with interferon beta-1b after a first clinical event suggestive of multiple sclerosis: 5-year active treatment extension of the phase 3 BENEFIT trial. *Lancet neurology*, 8(11), pp.987–997.
- Katz Sand, I.B. & Lublin, F.D., 2013. Diagnosis and differential diagnosis of multiple sclerosis. *Continuum (Minneapolis, Minn.)*, 19(4 Multiple Sclerosis), pp.922–943.
- Katz, D. et al., 1993. Correlation between magnetic resonance imaging findings and lesion development in chronic, active multiple sclerosis. *Annals of Neurology*, 34(5), pp.661–669.
- Kaul, R. et al., 1994. Canavan disease: genomic organization and localization of human ASPA to 17p13-ter and conservation of the ASPA gene during evolution. *Genomics*, 21(2), pp.364–370.
- Kaul, R. et al., 1991. Purification, characterization, and localization of aspartoacylase from bovine brain. *Journal of neurochemistry*, 56(1), pp.129–135.
- Kim, S. et al., 2011. Journal of the Neurological Sciences. *Journal of the Neurological Sciences*, 307(1-2), pp.132–138.
- Kirov, I.I. et al., 2009. MR spectroscopy indicates diffuse multiple sclerosis activity during



- remission. *Journal of Neurology, Neurosurgery & Psychiatry*, 80(12), pp.1330–1336.
- Kirov, I. et al., 2010. Brain Metabolite Proton T2 Mapping at 3.0 T in Relapsing-Remitting Multiple Sclerosis1. *Radiology*, 254(3), pp. 858-866.
- Kirov, I.I. et al., 2008. Age dependence of regional proton metabolites T2 relaxation times in the human brain at 3 T. *Magnetic Resonance in Medicine*, 60(4), pp.790–795.
- Kirov, I.I. et al., 2012. Serial proton MR spectroscopy of gray and white matter in relapsing-remitting MS. *Neurology*, 80(1), pp.39–46.
- Klawiter, E.C., 2013. Current and new directions in MRI in multiple sclerosis. *Continuum (Minneapolis, Minn.)*, 19(4 Multiple Sclerosis), pp.1058–1073.
- Krabbe, K. et al., 1997. MR diffusion imaging of human intracranial tumours. *Neuroradiology*, 39(7), pp.483–489.
- Kornek, B. et al., 2000. Multiple sclerosis and chronic autoimmune encephalomyelitis: a comparative quantitative study of axonal injury in active, inactive, and remyelinated lesions. *The American journal of pathology*, 157(1), pp.267–276.
- Kreutzer, M. et al., 2012. Axonopathy is associated with complex axonal transport defects in a model of multiple sclerosis. *Brain pathology (Zurich, Switzerland)*, 22(4), pp.454–471.
- Kroenke, C.D., Ackerman, J.J.H. & Yablonskiy, D.A., 2004. On the nature of the NAA diffusion attenuated MR signal in the central nervous system. *Magnetic Resonance in Medicine*, 52(5), pp.1052–1059.

- Krumbholz, M. et al., 2012. B cells and antibodies in multiple sclerosis pathogenesis and therapy. *Nature Publishing Group*, 8(11), pp.613–623.
- Kushmerick, M.J. & Podolsky, R.J., 1969. Ionic mobility in muscle cells. *Science*, 166(3910), pp.1297–1298.
- Kutzelnigg, A. & Lassmann, H., 2014. Pathology of multiple sclerosis and related inflammatory demyelinating diseases. *Handbook of clinical neurology*, 122, pp.15–58.
- Kutzelnigg, A. et al., 2005. Cortical demyelination and diffuse white matter injury in multiple sclerosis. *Brain*, 128(Pt 11), pp.2705–2712.
- Landman, B.A. et al., 2010. Complex geometric models of diffusion and relaxation in healthy and damaged white matter. *NMR in Biomedicine*, 23(2), pp.152–162.
- Lassmann, H., 2014. Mechanisms of white matter damage in multiple sclerosis. *Glia*, 62(11), pp. 1816-1830.
- Lassmann, H., 2011. Review: the architecture of inflammatory demyelinating lesions: implications for studies on pathogenesis. *Neuropathology and Applied Neurobiology*, 37(7), pp.698–710.
- Lassmann, H., Van Horssen, J. & Mahad, D., 2012. Progressive multiple sclerosis: pathology and pathogenesis. *Nature Publishing Group*, 8(11), pp.647–656.
- Le Bihan, D., 2003. Looking into the functional architecture of the brain with diffusion MRI. *Nature reviews Neuroscience*, 4(6), pp.469–480.
- Le Bihan, D. et al., 2001. Diffusion tensor imaging: concepts and applications. *Journal of magnetic resonance imaging : JMRI*, 13(4), pp.534–546.

- Leary, S.M. & Thompson, A.J., 2005. Primary progressive multiple sclerosis : current and future treatment options. *CNS drugs*, 19(5), pp.369–376.
- Leary, S.M. et al., 1999. 1H magnetic resonance spectroscopy of normal appearing white matter in primary progressive multiple sclerosis. *Journal of Neurology*, 246(11), pp.1023–1026.
- Leech, S. et al., 2007. Persistent endothelial abnormalities and blood-brain barrier leak in primary and secondary progressive multiple sclerosis. *Neuropathology and Applied Neurobiology*, 33(1), pp.86–98.
- Li, D.K. et al., 2001. Randomized controlled trial of interferon-beta-1a in secondary progressive MS: MRI results. *Neurology*, 56(11), pp.1505–1513.
- Li, J.-Y. & Conforti, L., 2013. Axonopathy in Huntington's disease. *Experimental neurology*, 246(C), pp.62–71.
- Lindner, M. et al., 2009. Chronic toxic demyelination in the central nervous system leads to axonal damage despite remyelination. *Neuroscience letters*, 453(2), pp.120–125.
- Losseff, N.A. et al., 1996. Progressive cerebral atrophy in multiple sclerosis. A serial MRI study. *Brain*, 119 ( Pt 6), pp.2009–2019.
- Loy, D.N. et al., 2007. Diffusion tensor imaging predicts hyperacute spinal cord injury severity. *Journal of neurotrauma*, 24(6), pp.979–990.
- Lu, H. et al., 2005. Routine clinical brain MRI sequences for use at 3.0 Tesla. *Journal of magnetic resonance imaging : JMRI*, 22(1), pp.13–22.
- Lucas, B.C. et al., 2010. The Java Image Science Toolkit (JIST) for rapid prototyping

- and publishing of neuroimaging software. *Neuroinformatics*, 8(1), pp.5–17.
- Lucchinetti, C. & Brück, W., 2004. The pathology of primary progressive multiple sclerosis. *Multiple sclerosis (Houndmills, Basingstoke, England)*, 10 Suppl 1, pp.S23–30.
- Lucchinetti, C. et al., 1999. A quantitative analysis of oligodendrocytes in multiple sclerosis lesions. A study of 113 cases. *Brain*, 122 ( Pt 12), pp.2279–2295.
- Lucchinetti, C. et al., 2000. Heterogeneity of multiple sclerosis lesions: implications for the pathogenesis of demyelination. *Annals of Neurology*, 47(6), pp.707–717.
- Lucchinetti, C.F. et al., 2011. Inflammatory cortical demyelination in early multiple sclerosis. *The New England journal of medicine*, 365(23), pp.2188–2197.
- Madhavarao, C.N. & Namboodiri, A.M.A., 2006. NAA synthesis and functional roles. *Advances in experimental medicine and biology*, 576, pp.49–66; discussion 361–3.
- Madhavarao, C.N. et al., 2003. Characterization of the N-acetyl aspartate biosynthetic enzyme from rat brain. *Journal of neurochemistry*, 86(4), pp.824–835.
- Madhavarao, C.N. et al., 2005. Defective N-acetyl aspartate catabolism reduces brain acetate levels and myelin lipid synthesis in Canavan's disease. *Proceedings of the National Academy of Sciences of the United States of America*, 102(14), pp.5221–5226.
- Maggi, P. et al., 2014. The formation of inflammatory demyelinated lesions in cerebral white matter. *Annals of Neurology*, 76(4), pp. 594-608.
- Magliozzi, R. et al., 2007. Meningeal B-cell follicles in secondary progressive multiple

sclerosis associate with early onset of disease and severe cortical pathology.

*Brain*, 130(Pt 4), pp.1089–1104.

Mahad, D., Lassmann, H. & Turnbull, D., 2008. Review: Mitochondria and disease progression in multiple sclerosis. *Neuropathology and Applied Neurobiology*, 34(6), pp.577–589.

Mahad, D.J. et al., 2009. Mitochondrial changes within axons in multiple sclerosis. *Brain*, 132(Pt 5), pp.1161–1174.

Manrique-Hoyos, N. et al., 2012. Late motor decline after accomplished remyelination: impact for progressive multiple sclerosis. *Annals of Neurology*, 71(2), pp.227–244.

Marchadour, C. et al., 2012. Anomalous diffusion of brain metabolites evidenced by diffusion weighted magnetic resonance spectroscopy in vivo. 32(12), pp.2153–2160.

Mason, J.L. et al., 2001. Episodic demyelination and subsequent remyelination within the murine central nervous system: changes in axonal calibre. *Neuropathology and Applied Neurobiology*, 27(1), pp.50–58.

Matsushima, G.K. & Morell, P., 2001. The neurotoxicant, cuprizone, as a model to study demyelination and remyelination in the central nervous system. *Brain pathology (Zurich, Switzerland)*, 11(1), pp.107–116.

Matthews, P. et al., 1996. Assessment of lesion pathology in multiple sclerosis using quantitative MRI morphometry and magnetic resonance spectroscopy. *Brain*, 119(3), pp. 715-722.

- McAuliffe, M.J. et al., 2001. Medical Image Processing, Analysis & Visualization in Clinical Research. In 14th IEEE Symposium on Computer-Based Medical Systems. IEEE Comput. Soc, pp. 381–386.
- McFarland, H., 2011. The importance of clinical trials in unraveling the mysteries of multiple sclerosis. *Journal of neuroimmunology*, 231(1-2), pp.3–6.
- McFarland, H.F., 2010. Examination of the role of MRI in multiple sclerosis: a problem orientated approach. *Results and problems in cell differentiation*, 51, pp.287–301.
- McFarland, H.F. et al., 2002. The role of MRI as a surrogate outcome measure in multiple sclerosis. *Multiple sclerosis (Houndmills, Basingstoke, England)*, 8(1), pp.40–51.
- Melhem, E. et al., 2002. Diffusion tensor MR imaging of the brain and white matter tractography. *American Journal of Roentgenology*, 178(1), p.3.
- Miller, D.H. & Leary, S.M., 2007. Primary-progressive multiple sclerosis. *Lancet neurology*, 6(10), pp.903–912.
- Miller, D.H. et al., 1988. Serial gadolinium enhanced magnetic resonance imaging in multiple sclerosis. *Brain*, 111 ( Pt 4), pp.927–939.
- Miller, D.H. et al., 1998. The role of magnetic resonance techniques in understanding and managing multiple sclerosis. *Brain*, 121 ( Pt 1), pp.3–24.
- Minton, A.P., 2001. The Influence of Macromolecular Crowding and Macromolecular Confinement on Biochemical Reactions in Physiological Media. *Journal of Biological Chemistry*, 276(14), pp.10577–10580.

- Moffett, J.R. et al., 1991. Immunohistochemical localization of N-acetyl aspartate in rat brain. *Neuroreport*, 2(3), pp.131–134.
- Moffett, J.R. et al., 2007. N-acetyl aspartate in the CNS: from neurodiagnostics to neurobiology. *Progress in Neurobiology*, 81(2), pp.89–131.
- Morfini, G.A. et al., 2009. Axonal Transport Defects in Neurodegenerative Diseases. *Journal of Neuroscience*, 29(41), pp.12776–12786.
- Mori, S. & van Zijl, P., 2002. Fiber tracking: principles and strategies-a technical review. *NMR in Biomedicine*, 15(7-8), pp.468–480.
- Mori, S. et al., 2002. Brain white matter anatomy of tumor patients evaluated with diffusion tensor imaging. *Annals of Neurology*, 51(3), pp.377–380.
- Mori, S. et al., 1999. Three-dimensional tracking of axonal projections in the brain by magnetic resonance imaging. *Annals of Neurology*, 45(2), pp.265–269.
- Mugler, J.P. & Brookeman, J.R., 1990. Three-dimensional magnetization-prepared rapid gradient-echo imaging (3D MP RAGE). *Magnetic Resonance in Medicine*, 15(1), pp.152–157.
- Murray, L.M. et al., 2008. Loss of translation elongation factor (eEF1A2) expression in vivo differentiates between Wallerian degeneration and dying-back neuronal pathology. *Journal of anatomy*, 213(6), pp.633–645.
- Murray, T.J., 2009. The history of multiple sclerosis: the changing frame of the disease over the centuries. *Journal of the Neurological Sciences*, 277 Suppl 1, pp.S3–8.
- Myles, P.S. & Cui, J., 2007. Using the Bland Altman method to measure agreement with

- repeated measures. *British Journal of Anaesthesia*, 99(3), pp.309–311.
- Nair, G. et al., 2005. Myelination and long diffusion times alter diffusion-tensor-imaging contrast in myelin-deficient shiverer mice. *NeuroImage*, 28(1), pp.165–174.
- Naismith, R.T. et al., 2012. Diffusion tensor imaging in acute optic neuropathies: predictor of clinical outcomes. *Archives of neurology*, 69(1), pp.65–71.
- Naismith, R.T. et al., 2010. Increased diffusivity in acute multiple sclerosis lesions predicts risk of black hole. *Neurology*, 74(21), pp.1694–1701.
- Narayana, P.A. et al., 2004. Multicentre proton magnetic resonance spectroscopy imaging of primary progressive multiple sclerosis. *Multiple sclerosis (Houndmills, Basingstoke, England)*, 10 Suppl 1, pp.S73–8.
- Nave, K.-A., 2010. Myelination and the trophic support of long axons. *Nature reviews Neuroscience*, 11(4), pp.275–283.
- Neumann, H., 2003. Molecular mechanisms of axonal damage in inflammatory central nervous system diseases. *Current opinion in neurology*, 16(3), pp.267–273.
- Nikić, I. et al., 2011. A reversible form of axon damage in experimental autoimmune encephalomyelitis and multiple sclerosis. *Nature medicine*, 17(4), pp.495–499.
- Noseworthy, J.H., 2003. Management of multiple sclerosis: current trials and future options. *Current opinion in neurology*, 16(3), pp.289–297.
- Noseworthy, J.H. & Kirkpatrick, P., 2005. Natalizumab. *Nature Reviews Drug Discovery*, 4(2), pp.101–102.
- Nunes, R.G., Jezzard, P. & Clare, S., 2005. Investigations on the efficiency of cardiac-gated methods for the acquisition of diffusion weighted images. *Journal of Magnetic*



*Resonance*, 177(1), pp.102–110.

Oh, J., Pelletier, D. & Nelson, S., 2004. Corpus callosum axonal injury in multiple sclerosis measured by proton magnetic resonance spectroscopic imaging. *Archives of neurology*, 61(7), p.1081.

Ovádi, J. & Saks, V., 2004. On the origin of intracellular compartmentation and organized metabolic systems. *Molecular and cellular biochemistry*, 256-257(1-2), pp.5–12.

Ozturk, A. et al., 2010. MRI of the corpus callosum in multiple sclerosis: association with disability. *Multiple Sclerosis*, 16(2), pp.166–177.

Paolillo, A. et al., 2002. A 6-year clinical and MRI follow-up study of patients with relapsing-remitting multiple sclerosis treated with Interferon-beta. *European journal of neurology*, 9(6), pp.645–655.

Parkin, J. & Cohen, B., 2001. An overview of the immune system. *The Lancet*, 357(9270), pp.1777–1789.

Patel, T.B. & Clark, J.B., 1979. Synthesis of N-acetyl-L-aspartate by rat brain mitochondria and its involvement in mitochondrial/cytosolic carbon transport. *The Biochemical journal*, 184(3), pp.539–546.

Paty, D.W. & Li, D.K., 1993. Interferon beta-1b is effective in relapsing-remitting multiple sclerosis. II. MRI analysis results of a multicenter, randomized, double-blind, placebo-controlled trial. UBC MS/MRI Study Group and the IFNB Multiple Sclerosis Study Group. *Neurology*, 43(4), pp.662–667.

Pelletier, D. et al., 2003. MRI lesion volume heterogeneity in primary progressive MS in

relation with axonal damage and brain atrophy. *Journal of Neurology, Neurosurgery & Psychiatry*, 74(7), pp.950–952.

Petkau, J. et al., 2008. Magnetic resonance imaging as a surrogate outcome for multiple sclerosis relapses. *Multiple sclerosis (Houndmills, Basingstoke, England)*, 14(6), pp.770–778.

Pettinelli, C.B. & McFarlin, D.E., 1981. Adoptive transfer of experimental allergic encephalomyelitis in SJL/J mice after in vitro activation of lymph node cells by myelin basic protein: requirement for Lyt 1+ 2- T lymphocytes. *Journal of immunology*, 127(4), pp.1420–1423.

Petzold, A. et al., 2008. Phosphorylation and compactness of neurofilaments in multiple sclerosis: indicators of axonal pathology. *Experimental neurology*, 213(2), pp.326–335.

Petzold, A., Tozer, D.J. & Schmierer, K., 2011. Axonal damage in the making: neurofilament phosphorylation, proton mobility and magnetisation transfer in multiple sclerosis normal appearing white matter. *Experimental neurology*, 232(2), pp.234–239.

Pfeuffer, J. et al., 1998. Water signal attenuation in diffusion weighted 1H NMR experiments during cerebral ischemia: influence of intracellular restrictions, extracellular tortuosity, and exchange. *Magnetic resonance imaging*, 16(9), pp.1023–1032.

Pham, D.L. & Prince, J.L., 1999. Adaptive fuzzy segmentation of magnetic resonance images. *IEEE transactions on medical imaging*, 18(9), pp.737–752.

Pierpaoli, C. et al., 1996. Diffusion tensor MR imaging of the human brain. *Radiology*,

201(3), p.637.

Polman, C.H. et al., 2011. Diagnostic criteria for multiple sclerosis: 2010 revisions to the McDonald criteria. *Annals of Neurology*, 69(2), pp.292–302.

Popescu, B.F.G., Pirko, I. & Lucchinetti, C.F., 2013. Pathology of multiple sclerosis: where do we stand? *Continuum (Minneapolis, Minn.)*, 19(4 Multiple Sclerosis), pp.901–921.

Posse, S., Cuenod, C.A. & Le Bihan, D., 1993. Human brain: proton diffusion MR spectroscopy. *Radiology*, 188(3), pp.719–725.

Provencher, S.W., 1993. Estimation of metabolite concentrations from localized in vivo proton NMR spectra. *Magnetic resonance in medicine*, 30(6), pp.672–679.

Rango, M. et al., 1995. Central nervous system trans-synaptic effects of acute axonal injury: a <sup>1</sup>H magnetic resonance spectroscopy study. *Magnetic resonance in medicine*, 33(5), pp.595–600.

Reese, T.G. et al., 2002. Reduction of eddy-current-induced distortion in diffusion MRI using a twice-refocused spin echo. *Magnetic Resonance in Medicine*, 49(1), pp.177–

Reich, D.S. et al., 2010. Automated vs. conventional tractography in multiple sclerosis: Variability and correlation with disability. *NeuroImage*, 49(4), pp.3047–3056.

Riccitelli, G. et al., 2011. Voxelwise assessment of the regional distribution of damage in the brains of patients with multiple sclerosis and fatigue. *American Journal of Neuro-radiology*, 32(5), pp.874–879.

- Rigotti, D.J. et al., 2011. Global N-acetyl aspartate declines even in benign multiple sclerosis. *American Journal of Neuroradiology*, 32(1), pp.204–209.
- Rohwer, J.M. et al., 1998. Implications of macromolecular crowding for signal transduction and metabolite channeling. *Proceedings of the National Academy of Sciences of the United States of America*, 95(18), pp.10547–10552.
- Ronen, I., Budde, M., et al., 2014. Microstructural organization of axons in the human corpus callosum quantified by diffusion weighted magnetic resonance spectroscopy of N-acetyl aspartate and post-mortem histology. *Brain Structure and Function*, 219(5), pp. 1773-1785.
- Ronen, I., Ercan, E. & Webb, A., 2013. Axonal and glial microstructural information obtained with diffusion weighted magnetic resonance spectroscopy at 7T. *Frontiers in integrative neuroscience*, 7, p.13.
- Roosendaal, S.D. et al., 2009. Regional DTI differences in multiple sclerosis patients. *NeuroImage*, 44(4), pp.1397–1403.
- Rosner, B., 2006. *Fundamentals of Biostatistics* 6 ed., Brooks/Cole.
- Rovaris, M. et al., 2005. Axonal injury and overall tissue loss are not related in primary progressive multiple sclerosis. *Archives of neurology*, 62(6), pp.898–902.
- Rudick, R.A. et al., 2009. Gray matter atrophy correlates with MS disability progression measured with MSFC but not EDSS. *Journal of the Neurological Sciences*, 282(1-2), pp.106–111.
- Rydberg, J.N. et al., 1994. Initial clinical experience in MR imaging of the brain with a fast fluid-attenuated inversion-recovery pulse sequence. *Radiology*, 193(1),

pp.173–180.

Saidha, S., Eckstein, C. & Calabresi, P.A., 2012. New and emerging disease modifying therapies for multiple sclerosis. *Annals of the New York Academy of Sciences*, 1247, pp.117–137.

Sajja, B., Wolinsky, J. & Narayana, P., 2009. Proton magnetic resonance spectroscopy in multiple sclerosis. *Neuroimaging clinics of North America*, 19(1), pp.45–58.

Sajja, B.R. et al., 2008. Longitudinal magnetic resonance spectroscopic imaging of primary progressive multiple sclerosis patients treated with glatiramer acetate: multicenter study. *Multiple sclerosis (Houndmills, Basingstoke, England)*, 14(1), pp.73–80.

Samann, P.G. et al., 2012. Brain Volume and Diffusion Markers as Predictors of Disability and Short-Term Disease Evolution in Multiple Sclerosis. *American Journal of Neuroradiology*, 33(7), pp.1356–1362.

Sati, P. et al., 2012. FLAIR\*: A Combined MR Contrast Technique for Visualizing White Matter Lesions and Parenchymal Veins. *Radiology*, 265(3), pp.926–932.

Scalfari, A. et al., 2013. Mortality in patients with multiple sclerosis. *Neurology*, 81(2), pp.184–192.

Schmidt, T. et al., 2012. Regional Heterogeneity of Cuprizone-Induced Demyelination: Topographical Aspects of the Midline of the Corpus Callosum. *Journal of Molecular Neuroscience*, 49(1), pp.80–88.

Seewann, A. et al., 2009. Diffusely abnormal white matter in chronic multiple sclerosis: imaging and histopathologic analysis. *Archives of neurology*, 66(5), pp.601–609.

- Seewann, A. et al., 2012. Postmortem verification of MS cortical lesion detection with 3D DIR. *Neurology*, 78(5), pp.302–308.
- Serafini, B. et al., 2004. Detection of ectopic B-cell follicles with germinal centers in the meninges of patients with secondary progressive multiple sclerosis. *Brain pathology (Zurich, Switzerland)*, 14(2), pp.164–174.
- Sethi, V. et al., 2013. MS Cortical Lesions on DIR: Not Quite What They Seem? I. Pirko, ed. *PloS one*, 8(11), p.e78879.
- Shea, T.B. & Lee, S., 2011. Neurofilament phosphorylation regulates axonal transport by an indirect mechanism: a merging of opposing hypotheses. *Cytoskeleton (Hoboken, N.J.)*, 68(11), pp.589–595.
- Shiee, N. et al., 2010. A topology-preserving approach to the segmentation of brain images with multiple sclerosis lesions. *NeuroImage*, 49(2), pp.1524–1535.
- Shiee, N. et al., 2012. Revisiting brain atrophy and its relationship to disability in multiple sclerosis. *PloS one*, 7(5), p.e37049.
- Simmons, M., Frondoza, C. & Coyle, J., 1991. Immunocytochemical localization of N-acetyl-aspartate with monoclonal antibodies. *Neuroscience*, 45(1), pp.37–45.
- Simon, J.H. et al., 1999. A longitudinal study of brain atrophy in relapsing multiple sclerosis. *Neurology*, 53(1), pp.139–139.
- Sinnecker, T., Dorr, J., et al., 2012a. Distinct lesion morphology at 7-T MRI differentiates neuromyelitis optica from multiple sclerosis. *Neurology*, 79(7), pp.708–714.
- Sinnecker, T., Mittelstaedt, P., et al., 2012b. Multiple Sclerosis Lesions and Irreversible Brain Tissue Damage. *Archives of neurology*, 69(6).

- Sled, J.G., Zijdenbos, A.P. & Evans, A.C., 1998. A nonparametric method for automatic correction of intensity nonuniformity in MRI data. *IEEE transactions on medical imaging*, 17(1), pp.87–97.
- Smith, S.M. et al., 2002. Accurate, Robust, and Automated Longitudinal and Cross-Sectional Brain Change Analysis. *NeuroImage*, 17(1), pp.479–489.
- Smith, S.M. et al., 2001. Normalized accurate measurement of longitudinal brain change. *Journal of computer assisted tomography*, 25(3), pp.466–475.
- Song, S. et al., 2003. Diffusion tensor imaging detects and differentiates axon and myelin degeneration in mouse optic nerve after retinal ischemia. *NeuroImage*, 20(3), pp.1714–1722.
- Sormani, M.P. & Bruzzi, P., 2013. MRI lesions as a surrogate for relapses in multiple sclerosis: a meta-analysis of randomised trials. *Lancet neurology*, 12(7), pp.669–676.
- Sormani, M.P., Arnold, D.L. & De Stefano, N., 2014. Treatment effect on brain atrophy correlates with treatment effect on disability in multiple sclerosis. *Annals of Neurology*, 75(1), pp.43–49.
- Sospedra, M. & Martin, R., 2005. Immunology of multiple sclerosis. *Annual review of immunology*, 23, pp.683–747.
- Stadelmann, C., Wegner, C. & Brück, W., 2011. Inflammation, demyelination, and degeneration - recent insights from MS pathology. *Biochimica et biophysica acta*, 1812(2), pp.275–282.
- Stejskal, E.O. & Tanner, J.E., 1965. Spin diffusion measurements: spin echoes in the

- presence of a time-dependent field gradient. *The Journal of Chemical Physics*, 42(1), p.288.
- Stidworthy, M.F. et al., 2003. Quantifying the early stages of remyelination following cuprizone-induced demyelination. *Brain pathology (Zurich, Switzerland)*, 13(3), pp.329–339.
- Stromillo, M.L. et al., 2013. Brain metabolic changes suggestive of axonal damage in radiologically isolated syndrome. *Neurology*, 80(23), pp.2090–2094.
- Suhy, J. et al., 2000. 1H MRSI comparison of white matter and lesions in primary progressive and relapsing-remitting MS. *Multiple Sclerosis*, 6(3), p.148.
- Sun, S.-W. et al., 2006. Noninvasive detection of cuprizone induced axonal damage and demyelination in the mouse corpus callosum. *Magnetic resonance in medicine*, 55(2), pp.302–308.
- Sweeney, E.M., Shinohara, R.T., Shea, C.D., et al., 2013a. Automatic Lesion Incidence Estimation and Detection in Multiple Sclerosis Using Multisequence Longitudinal MRI. *American Journal of Neuroradiology*, 34(1), pp.68–73.
- Sweeney, E.M., Shinohara, R.T., Shiee, N., et al., 2013b. NeuroImage: Clinical. *NeuroImage. Clinical*, 2(C), pp.402–413.
- Tallantyre, E.C. et al., 2010. Clinico-pathological evidence that axonal loss underlies disability in progressive multiple sclerosis. *Multiple Sclerosis*, 16(4), pp.406–411.
- Tallantyre, E.C. et al., 2009. Greater loss of axons in primary progressive multiple sclerosis plaques compared to secondary progressive disease. *Brain*, 132(Pt 5), pp.1190–1199.



- Tallantyre, E.C. et al., 2011. Ultra-high-field imaging distinguishes MS lesions from asymptomatic white matter lesions. *Neurology*, 76(6), pp.534–539.
- Teunissen, C.E. et al., 2009. Combination of CSF N-acetyl aspartate and neurofilaments in multiple sclerosis. *Neurology*, 72(15), pp.1322–1329.
- Tiberio, M. et al., 2006. Metabolite changes in early relapsing-remitting multiple sclerosis. A two year follow-up study. *Journal of Neurology*, 253(2), pp.224–230.
- Tovar-Moll, F. et al., 2009. Thalamic involvement and its impact on clinical disability in patients with multiple sclerosis: a diffusion tensor imaging study at 3T. *American Journal of Neuroradiology*, 30(7), pp.1380–1386.
- Trapp, B.D. & Nave, K.-A., 2008. Multiple sclerosis: an immune or neurodegenerative disorder? *Annual review of neuroscience*, 31, pp.247–269.
- Trapp, B.D. & Stys, P.K., 2009. Virtual hypoxia and chronic necrosis of demyelinated axons in multiple sclerosis. *Lancet neurology*, 8(3), pp.280–291.
- Trapp, B.D. et al., 1998. Axonal transection in the lesions of multiple sclerosis. *The New England journal of medicine*, 338(5), pp.278–285.
- Tu, D. & Shao, J., 1995. *The Jackknife and Bootstrap*, New York: Springer-Verlag.
- Upadhyay, J. et al., 2007. Diffusion properties of NAA in human corpus callosum as studied with diffusion tensor spectroscopy. *Magnetic Resonance in Medicine*, 58(5), pp.1045–1053.
- Upadhyay, J. et al., 2008. Diffusion tensor spectroscopy and imaging of the arcuate fasciculus. *NeuroImage*, 39(1), pp.1–9.

- Urenjak, J. et al., 1993. Proton nuclear magnetic resonance spectroscopy unambiguously identifies different neural cell types. *Journal of Neuroscience*, 13(3), pp.981–989.
- van der Toorn, A. et al., 1996. Diffusion of metabolites in normal and ischemic rat brain measured by localized <sup>1</sup>H MRS. *Magnetic resonance in medicine*, 36(6), pp.914–922.
- van Gelderen, P. et al., 1994. Evaluation of restricted diffusion in cylinders. Phosphocreatine in rabbit leg muscle. *Journal of Magnetic Resonance Series B*, 103(3), pp.255–260.
- van Waesberghe, J.H. et al., 1999. Axonal loss in multiple sclerosis lesions: magnetic resonance imaging insights into substrates of disability. *Annals of Neurology*, 46(5), pp.747–754.
- van Walderveen, M.A. et al., 1998. Histopathologic correlate of hypointense lesions on T1-weighted spin-echo MRI in multiple sclerosis. *Neurology*, 50(5), pp.1282–1288.
- van Zijl, P.C. et al., 1991. Complete separation of intracellular and extracellular information in NMR spectra of perfused cells by diffusion weighted spectroscopy. *PNAS*, 88(8), pp.3228–3232.
- van Zijl, P.C.M., Davis, D. & Moonen, C.T.W., 1994. Diffusion Spectroscopy in Living Systems. In R. J. Gillies, ed. *NMR in Physiology and Biomedicine*. San Diego, CA: Academic Press, pp. 185–198.
- Vaz, S. et al., 2013. The Case for Using the Repeatability Coefficient When Calculating

- Test–Retest Reliability S. Hempel, ed. *PLoS one*, 8(9), p.e73990.
- Venturini, G., 1973. Enzymic activities and sodium, potassium and copper concentrations in mouse brain and liver after cuprizone treatment in vivo. *Journal of neurochemistry*, 21(5), pp.1147–1151.
- Verkman, A.S., 2002. Solute and macromolecule diffusion in cellular aqueous compartments. *Trends in biochemical sciences*, 27(1), pp.27–33.
- Visser, F. et al., 2010. High-resolution magnetization-prepared 3D-FLAIR imaging at 7.0 Tesla. *Magnetic Resonance in Medicine*, 64(1), pp.194–202.
- Warach, S. et al., 1992. Fast magnetic resonance diffusion weighted imaging of acute human stroke. *Neurology*, 42(9), pp.1717–1723.
- Wattjes, M.P. et al., 2007. Axonal damage but no increased glial cell activity in the normal-appearing white matter of patients with clinically isolated syndromes suggestive of multiple sclerosis using high-field magnetic resonance spectroscopy. *AJNR American journal of neuroradiology*, 28(8), pp.1517–1522.
- Werring, D.J. et al., 1999. Diffusion tensor imaging of lesions and normal-appearing white matter in multiple sclerosis. *Neurology*, 52(8), pp.1626–1632.
- Wetzel, S.G. et al., 2002. Three-dimensional, T1-weighted gradient-echo imaging of the brain with a volumetric interpolated examination. *AJNR American journal of neuroradiology*, 23(6), pp.995–1002.
- Wheeler-Kingshott, C.A.M. et al., 2012. A new approach to structural integrity assessment based on axial and radial diffusivities. *Functional neurology*, 27(2), pp.85–90.

- Wood, E.T. et al., 2012. Investigating Axonal Damage in Multiple Sclerosis by Diffusion Tensor Spectroscopy. *Journal of Neuroscience*, 32(19), pp.6665–6669.
- Xie, M. et al., 2010. Rostrocaudal analysis of corpus callosum demyelination and axon damage across disease stages refines diffusion tensor imaging correlations with pathological features. *Journal of neuropathology and experimental neurology*, 69(7), pp.704–716.
- Yan, T., Feng, Y. & Zhai, Q., 2010. Axon degeneration: Mechanisms and implications of a distinct program from cell death. *Neurochemistry international*, 56(4), pp.529–534.
- Young, I.R. et al., 1981. Nuclear magnetic resonance imaging of the brain in multiple sclerosis. *Lancet*, 2(8255), pp.1063–1066.
- Zhang, J. et al., 2009. Diffusion tensor magnetic resonance imaging of Wallerian degeneration in rat spinal cord after dorsal root axotomy. *Journal of Neuroscience*, 29(10), pp.3160–3171.
- Zheng, D.D. et al., 2011. The Effect of Age and Cerebral Ischemia on Diffusion weighted Proton MR Spectroscopy of the Human Brain. *American Journal of Neuro-radiology*.

# 11 CURRICULUM VITAE

## **Personal Information:**

Name: Emily Turner Wood (born Emily Patricia Turner)

Birth: March 12, 1982 in Anacortes, Washington, USA

## **Contact Information:**

Email: emilytwood@gmail.com

Telephone: 410-349-7130

## **Education:**

2006-2015 M.D. & Ph.D. (Neuroscience Graduate program),  
Johns Hopkins University School of Medicine, Baltimore, MD.

2001-2006 B.S., Magna Cum Laude with distinction in Psychology.  
University of Washington, Seattle, WA.

## **Research Experience:**

2009-2014 Graduate Thesis Research: Development of magnetic resonance  
diffusion weighted spectroscopy to examine neurodegeneration in  
Multiple Sclerosis.

National Institute of Neurological Disorders and Stroke, National Institutes  
of Health.

PI: Daniel Reich, M.D., Ph.D., Collaborator: Itamar Ronen, Ph.D.

- 2008            Research Rotation: Studied diffusion tensor imaging techniques in HIV-Associated Neurocognitive Disorders. Spring 2008. Department of Radiology, Johns Hopkins School of Medicine.  
PI: Martin Pomper, M.D., Ph.D.
- 2007            Research Rotation: Examined development of olfactory receptors. Department of Neuroscience, Johns Hopkins School of Medicine.  
PI: Gabriel Ronnett, M.D., Ph.D.
- 2006            Research Rotation: Studied gene expression in the hippocampus related to neurocognitive aging. Department of Psychological & Brain Sciences, Johns Hopkins University.  
PI: Michela Gallagher, Ph.D.
- 2004-2006     Honors Theses. Senior: "The firing properties of Substantia Nigra neurons during a complex working memory task." Junior: "Dopamine: Where does it fit in a multiple memory systems theory?"  
Psychology Department, University of Washington.  
PI: Sheri Mizumori, Ph.D.
- 2002-2003     Patient Interviewer: Multicenter Hospitalist Project.  
Pritzker School of Medicine, University of Chicago Hospitals.  
PI: David Meltzer M.D., Ph.D

**Journal Publications:**

Harrison DM, Oh J, Roy S, **Wood ET**, Whetstone A, Seigo MA, Jones CK, Pham D, van Zijl P, Reich DS and Calabresi PA (2015) "Thalamic Lesions in Multiple Sclerosis by 7T MRI: Clinical Implications and Relationship to Cortical Pathology." *Multiple*

*Sclerosis*, January. doi:10.1177/1352458514558134.

An L, Li S, **Wood ET**, Reich DS, & Shen J (2013) NAAG Detection in the Human Brain at 7T by Echo Time Optimization and Improved Wiener Filtering. *Magnetic Resonance in Medicine*, 72 (4): 903–12. doi:10.1002/mrm.25007.

**Wood ET**, Ronen I, Techawiboonwang A, Jones CK, Barker PB, Calabresi P, Harrison D, & Reich DS (2012) Investigating Axonal Damage in Multiple Sclerosis by Diffusion Tensor Spectroscopy. *The Journal of Neuroscience*, 32(19): 6665–6669.

### **Manuscripts in Review / Preparation:**

**Wood ET\***, Ercan AE\*, Branzoli F, Webb A, Sati P, Reich DS and Ronen I. “Reproducibility and Optimization of In Vivo Human Diffusion weighted Spectroscopy of the Corpus Callosum at 3T and 7T”, (submitted to NMR in Biomedicine).

\* Both authors contributed equally to this work.

### **Talks:**

**Wood ET.** (September, 2014) Diffusion weighted MR spectroscopy: How to acquire, process, analyse and model metabolite diffusion weighted data. (Invited) *ESMRMB Lectures on MR*, Leiden, NL.

**Wood ET**, Ronen I, Sati P, & Reich DS (2013) Using Diffusion Weighted Spectroscopy to Detect Alterations in White Matter Microstructure and Organization: Application to the Corpus Callosum in Multiple Sclerosis. (Proffered) *ISMRM Workshop: Dynamic MR Imaging & Spectroscopy of Psychiatric Illness*, Lisbon, Portugal.

**Wood ET**, Ronen I, Sati P, & Reich DS (2013) Diffusion Weighted Spectroscopy of NAA in Multiple Sclerosis. (Proffered) *ISMRM Workshop: Multiple Sclerosis as a*

*Whole Brain Disease*, London, UK.

**Wood ET**, Ronen I, Techawiboonwang A, Jones CK, Barker PB, Harrison D, Calabresi P, & Reich DS (2012) Investigating Axonal Damage in Multiple Sclerosis by Diffusion Tensor Spectroscopy at 7T. (Proffered) *ISMRM*, 20th Scientific Meeting, Melbourne, Australia.

**Wood ET**, Reich DS, Farrell JAD, Gillen JS, Barker PB, Ronen I. (2011) Diffusion Tensor Spectroscopy of NAA and Water in the Human Brain at 7 Tesla. (Proffered) CONECT Meeting: MRI of Brain Microstructure, Tel Aviv, Israel.

### **Other Peer-Reviewed Abstracts**

**Wood ET**, Ronen I, Techawiboonwang A, Sati P, & Reich DS (2013) Diffusion Weighted Spectroscopy of NAA in Multiple Sclerosis: Studying the Microstructure, Macrostructure and Organization of Axonal Tracts in the Corpus Callosum. (Poster) *International Society for Magnetic Resonance in Medicine*, 21th Scientific Meeting, Salt Lake City, Utah, USA.

**Wood ET**, Reich DS, Farrell JAD, Gillen JS, Barker PB, Ronen I. (2010) Diffusion Tensor Spectroscopy of NAA and Water in the Corpus Callosum of the Human Brain at 7 Tesla. (Poster) *ISMRM*, 18th Scientific Meeting, Stockholm, Sweden.

Mizumori SJY, Gill KM, & **Wood ET**. (2005) Rat substantia nigra neurons exhibit context-dependent task-related firing during a working memory task. *Society for Neuroscience Abstracts*, 31.

### **Teaching and Mentoring Experience:**

2012 & 2013 Mentorship of two undergraduate NIH Summer Interns who both received



the National Institute of Neurological Disorders and Stroke Exceptional Summer Student Award for their work with me.

2009-2010 Member of curriculum committee for Nervous System & Special Senses (NSS) course for first year medical students in new Johns Hopkins Genes to Society Curriculum.

2010 & 2011 Teaching Assistant Leader for NSS course

### **Technical Experience:**

Programming experience with MATLAB (5 years).

Familiarity with MIPAV (Medical Image Processing, Analysis and Visualization, ), JIST (Java Image Science Toolbox), Osirix, DTIstudio, and STATA software packages.

Experience operating 3T and 7T Philips Achieva MRI Systems, a 7T Siemens MRI System, a 7T Bruker animal MRI system, and a 3T GE MRI system

### **Grants & Scholarships:**

2006-2015 Medical Scientist Training Grant, Johns Hopkins University Medical Scientist Training Program,

2013-2014 NINDS Intramural Competitive MD/PhD Fellowship (NRSA F31 equivalent), National Institutes of Health

2013 National Institutes of Health Fellows Award for Research Excellence (FARE)

2010,'12,'13 ISMRM Annual Meeting Educational/Training Award

- 2009-2010 Johns Hopkins NIMH Center for Novel Therapeutics of HIV-associated cognitive disorders, NeuroAIDS developmental pilot grant award
- 2009 Turock Young Scientist Award, Johns Hopkins SOM Graduate Program
- 2005 *Mary Gates Endowment for Students* Research Training Grant, U of Washington
- 2004 University of Washington Alumni Association Scholarship
- 2004 Ashley Palumbo & Tyler Mondlock Memorial Scholarship

### **Professional Memberships**

- 2009-Pres Member, International Society for Magnetic Resonance in Medicine
- 2011-2013 Student Representative to Executive Board, White Matter Study Group, ISMRM